Feedback Control of a Shape Memory Alloy Actuator for Control Surface Deflection

by

Righardt Frederick Ehlers

Thesis presented in partial fulfilment of the requirements for the degree
Master of Science in Engineering
at the Faculty of Engineering, Stellenbosch University

Supervisor: Mr. J.A.A. Engelbrecht
Department of Electrical and Electronic Engineering

March 2012

Declaration

By submitting this thesis electronically, I declare that the entirety of the work contained therein is my own, original work, that I am the sole author thereof (save to the extent explicitly otherwise stated), that reproduction and publication thereof by Stellenbosch University will not infringe any third party rights and that I have not previously in its entirety or in part submitted it for obtaining any qualification.

March 2012

Abstract

The successful design, implementation and testing of a feedback control system for tab-deflection control of a shape memory alloy (SMA) based control surface actuator is presented. The research is performed as part of the Control Surfaces in Confined Spaces (CoSICS) research project conducted at Stellenbosch University. The research group investigates ways to provide control surface actuation in size-restricted spaces in commercial aircraft such as the Airbus A320 and A330. This is achieved by investigating the concept of trailing edge tabs to reduce the required torque load, resulting in reduced actuator requirements enabling the use of smaller actuators. This thesis contributes to the project by investigating the possibility of using SMA-based actuators in reduced hinge moment requirement applications.

An SMA-based tab actuator demonstrator design is presented. Mathematical models are derived for the SMA material, thermodynamics and actuator geometry. The models are combined to formulate an SMA-based control surface actuator model. The model is utilised in four tracking feedback controller designs; two based on linear and two based on non-linear control techniques.

The manufactured prototype is presented along with the incorporated hardware for controller implementation. System identification follows and validates the three mathematical models.

Practical verification of the model and two of the controllers is conducted. The unimplemented controllers are implemented through a validated model simulation. Controller evaluation, based on the dynamic controller performance, is conducted. The results validate the concept of using an SMA actuator for tab-deflection control and indicate important limitations for the intended application.

Opsomming

Die tesis behels die ontwerp, implementering en toetsing van ’n terugvoer beheerstelsel vir hulpvlak defleksie beheer van ’n vorm-geheue allooi (SMA) gebaseerde aktueerder. Die navorsing vorm deel van die Beheervlakke in Begrensde Ruimtes (CoSICS) navorsingsprojek by Stellenbosch Universiteit. Die CoSICS navorsing behels ’n ondersoek na beheervlak aktueering in beknopte spasies in kommersiële vliegtuie soos die Airbus A320 en A330. Die probleem word aangespreek deur ’n ondersoek na aerodinamiese hulpvlakke wat ’n vermindering in skarnier moment tot gevolg het en sodoende die aktueerder vereistes verminder.

Hierdie tesis dra by tot die projek deur die moontlikheid van die gebruik van SMA-gebaseerde aktueerders in verminderde skarnier moment vereiste toepassings te ondersoek.

‘n SMA gebaseerde hulpvlak demonstrasie aktueerder ontwerp word voorgelê. Wiskundige modelle vir die SMA materiaal, termodinamika en prototipe geometrie is geformuleer en gekombineer om ‘n SMA gebaseerde beheervlak aktueerder model te ontwikkel. Die model word in vier beheerder ontwerpe toegepas. Twee ontwerpe is op liniëre en twee op nie-liniëre beheer tegnieke gebaseer.

Die prototipe en nodige hardeware vir beheerder implementasie is voorgedra. Stelsel identifikasie is toegepas en verifieer die drie wiskundige modelle.

Praktiese verifikasie van die model en twee beheerders is gedoen. Die ongeïmplementeerde beheerders is deur die geverifieerde aktueerder model gesimuleer. ‘n Beheerder evaluasie gebaseer op die dinamiese beheerder gedrag word toegepas. Die evaluasie beklemtoon kritiese aspekte en beperkinge in verband met SMA aktueering. Die resultate regverdig die gebruik van ‘n SMA aktueerder vir hulpvlak defleksie beheer en beklemtoon belangrike beperkinge ten opsigte van die voorgestelde toepassing.

Contents

Declaration **i**

Abstract **ii**

Opsomming **iii**

List of Figures **viii**

List of Tables **xii**

Nomenclature **xiii**

Acknowledgements **xvii**

1 Introduction **1**
- 1.1 Background . . . 1
- 1.2 Problem Statement and Project Goals . . . 3
- 1.3 Previous Control in SMA-based actuator Applications . . . 4
- 1.4 Project Execution . . . 6
- 1.5 Thesis Layout . . . 7

2 Modelling of the Shape Memory Alloy **9**
- 2.1 Shape Memory Alloy Theory . . . 9
  - 2.1.1 SMA History . . . 10
  - 2.1.2 The Shape Memory Effect . . . 10
  - 2.1.3 Pseudo-Elasticity . . . 13
  - 2.1.4 Transformation Temperatures and Hysteresis . . . 14
- 2.2 Existing Modelling Approaches . . . 15
  - 2.2.1 Micromechanics-Based Macroscopic Models . . . 15
  - 2.2.2 Microscopic Thermodynamic Models . . . 15
  - 2.2.3 Macroscopic Phenomenological Models . . . 15
- 2.3 Applied Modelling Approach . . . 16
  - 2.3.1 Proposed Model . . . 17
    - 2.3.1.1 Stress, Strain and Detwinned Martensite Relationship . . . 17
    - 2.3.1.2 Memory Parameters . . . 20

2.3.2 Model Behaviour . . . 21
2.3.2.1 Shape Memory Effect . . . 21
2.3.2.2 Pseudo-Elasticity . . . 24
2.3.2.3 Minor Hysteresis Loops . . . 24

3 Modelling 27
3.1 SMA Actuator Geometry . . . 28
3.1.1 Lever Configuration . . . 28
3.1.2 Pulley Configuration . . . 31
3.2 SMA Actuator Model Formulation . . . 32
3.3 Simulation Results . . . 36
3.4 SMA Actuation . . . 38
3.4.1 Lumped System Analysis . . . 38
3.4.1.1 Analysis Assumptions . . . 38
3.4.1.2 Model Derivation . . . 39
3.4.1.3 Determining the Heat transfer Coefficient . . . 40
3.4.1.4 Lumped System Analysis Criteria . . . 43
3.4.1.5 Analysis Results . . . 43

4 Controller Design and Simulation 47
4.1 Deflection Feedback PI Controller . . . 49
4.1.1 Identifying the Linearisation Point . . . 50
4.1.2 Linearised PI Controller Design . . . 55
4.1.3 PI Controller Simulation Results . . . 60
4.2 Deflection and Temperature Control with Feedforward Compensation . . . 66
4.2.1 Simplified Modelling Approach . . . 67
4.2.2 Temperature Controller Design . . . 70
4.2.3 Integral Controller Design with Feedforward Compensation . . . 71
4.2.4 Deflection & Temperature Control with Feedforward Compensation Simulation Results . . . 73
4.3 On-off Controller Design . . . 76
4.3.1 On-off Controller Simulation Response . . . 77
4.4 Feedback Linearisation . . . 79
4.4.1 Input-state Linearisation . . . 79
4.4.2 Input-output Linearisation . . . 79
4.4.3 Control System Design . . . 80
4.4.4 Determining the Gains . . . 86
4.4.5 Feedback Linearisation Controller Simulation Results . . . 88
4.4.5.1 Performance under Natural Convection . . . 88
4.4.5.2 Performance under Forced Convection . . . 93
4.4.5.3 Cyclic Performance under Forced Convection . . . 96

5 Hardware Prototype 98

5.1 Mechanical Design 98
5.2 Electronic Design 100
5.2.1 Microcontroller 101
5.2.2 Current Driver and Current Sensor 101
5.2.3 Temperature Sensors 102
5.2.4 Deflection Angle Sensor 102
5.2.5 Load Cells 102

6 Identification of Material Model Parameters 104
6.1 System Identification: Constitutive Material Model 104
6.1.1 Material Parameters to be Identified 104
6.1.2 Transformation Temperature Identification Techniques 105
6.1.3 Experimental Technique Applied 107
6.1.4 Identification Procedure 107
6.1.5 Identification Results 109
6.1.6 Fitting the Simulation Model to the Measured Data 114
6.2 System Identification: Thermodynamic Model 116
6.2.1 Measured Temperature Responses to Current Inputs 118
6.2.2 Comparison of Simulated and Measured Temperature Responses . 119
6.3 System Identification: Actuator Model 120
6.3.1 Measured Deflection Angle Responses to Current Inputs 120
6.3.2 Comparison of Simulated and Measured Deflection Responses . . 123
6.4 Actuator Capabilities 125

7 Practical Verification of Controllers 126
7.1 Practical test Setup 126
7.2 PI Controller Response 127
7.3 Inner Loop-Outer Loop Controller Response 130
7.4 Bang-Bang Controller Response 131
7.5 Feedback Linearisation Controller Response 135
7.6 Comparison of Controller Performances 136
7.7 Scalability 139

8 Conclusions and Recommendations 143
8.1 Summary 143
8.2 Conclusions 144
8.3 Improvements and Recommendations 144

A Heat Equations 146
A.1 Heat Conduction Relationship Derivation 146
A.1.1 Lumped System Analysis 146
A.1.1.1 Analysis Assumptions 146
A.1.1.2 Relationship Derivation 146

B Strain Gauge Design **148**
B.1 Mechanical Design 148
B.2 Electronic Design 150
B.3 Load Cell Calibration 153

Bibliography **154**

List of Figures

1.1 Typical fairing protrusions on a wing of a conventional aircraft 2
1.2 Trailing edge tab concept 2
1.3 SMA-based actuator prototype 4

2.1 SMA crystalline structure dependence on temperature and stress 11
2.2 The shape memory effect 12
2.3 SMA's pseudo-elasticity 13
2.4 SMA phase transformation with inherent hysteresis 14
2.5 SMA phase diagram 20
2.6 Loading unloading cycle at a constant temperature of $30°C$ 22
2.7 Loading unloading cycle illustration using phase diagram (T = $30°C$) 22
2.8 Detwinned martensite transformation curve 23
2.9 Model's illustration of the shape memory effect 23
2.10 Loading unloading cycle at a constant temperature of $53°C$ 24
2.11 Loading unloading cycle illustration using phase diagram (T = $53°C$) 25
2.12 Load cycling illustrating the minor hysteresis loops 25

3.1 SMA-based control surface actuator model block diagram 27
3.2 SMA-based actuator prototype 28
3.3 Two-dimensional lever configuration: Force free body diagram 29
3.4 Three-dimensional pulley configuration: Force free body diagram 31
3.5 SMA-based actuator model block diagram representation 35
3.6 Open-loop response of the essential states 37
3.7 Model understanding: Phase diagram & control surface deflection response 37
3.8 Forced convection: Sea level (a) , 10 000 m (b) 44
3.9 Natural Convection: Sea level (a) , 10 000 m (b) 45

4.1 Generic closed-loop block diagram 48
4.2 The three-dimensional plot of deflection versus top and bottom wire temperatures 51
4.3 SMA phase diagram 52
4.4 The three-dimensional plot of deflection versus top and bottom wire temperatures with identified planes 52

4.5 Top view of three-dimensional phase plane illustrating the favourable operating region . . . 54
4.6 Phase diagram illustrating the favourable operating region . . . 54
4.7 Closed-loop SMA actuator block diagram with PI controller . . . 57
4.8 Linearised models root locus plot indicating the dominant open-loop poles . 58
4.9 Linearised models root locus plot indicating the dominant closed-loop poles . 59
4.10 Closed-loop PI controller response for a unity step command . . . 61
4.11 PI controller states for a unity step command . . . 61
4.12 Closed-loop PI controller response for large perturbations . . . 62
4.13 Linearised systems root locus plot for large perturbations . . . 64
4.14 Closed-loop PI controller response for a variable step command . . . 64
4.15 PI controller states for a variable step command . . . 65
4.16 Phase diagram indicating region of operation . . . 66
4.17 Proposed temperature controller block diagram architecture . . . 67
4.18 Simplified model development . . . 68
4.19 Inner-loop temperature controller block diagram . . . 70
4.20 Outer-loop deflection integral controller block diagram . . . 71
4.21 Feedforward compensation block diagram . . . 72
4.22 Closed-loop temperature controller response for a dual unity step command 74
4.23 Temperature controller states for a dual unity step command . . . 75
4.24 Closed-loop temperature controller response for a random step command . . 75
4.25 Temperature controller states for a variable step command . . . 76
4.26 Closed-loop bang-bang controller response for a random step command . . . 78
4.27 Bang-bang controller states for a variable step command . . . 78
4.28 Feedback linearisation approach in block diagram format . . . 79
4.29 Third-order linearised system open-loop block diagram . . . 83
4.30 Root-locus plot illustrating open-loop poles after linearisation . . . 83
4.31 Reference introduction and rate feedback block diagram . . . 84
4.32 Closed-loop poles obtained after inner-loop feedback compensation . . . 85
4.33 Closed-loop block diagram after complete linearisation . . . 85
4.34 Root locus plot with dominant closed-loop poles after complete feedback linearisation . . . 86
4.35 Closed-loop feedback linearisation controller response for a maximum step command ($\tau = 0.1s$) . . . 89
4.36 Feedback linearisation controller states for a maximum step command ($\tau = 0.1s$) . . . 89
4.37 Closed-loop feedback linearisation controller response for a medium step command ($\tau = 0.1s$) . . . 90
4.38 Feedback linearisation controller states for a medium step command ($\tau = 0.1s$) 91
4.39 Phase diagram illustrating wire transformation path for maximum deflection 92
4.40 Closed-loop feedback-linearisation controller response for a medium step command ($\tau = 0.1s$) . . . 92

4.41 Phase diagram illustrating wire transformation path for intermediate deflection 93
4.42 Closed-loop feedback-linearisation controller response for a maximum step command under forced convection ($\tau = 0.1s$) 94
4.43 Feedback linearisation controller states for a maximum step command under forced convection ($\tau = 0.1s$) 95
4.44 Phase diagram illustrating wire transformation path for a maximum deflection at improved convectional conditions 95
4.45 Closed-loop feedback-linearisation controller response for a random step command under forced convection ($\tau = 0.1s$) 96
4.46 Feedback linearisation controller states for a random step command under forced convection ($\tau = 0.1s$) 97
4.47 Phase diagram illustrating wire transformation path for multiple step commands 97

5.1 SMA actuator mechanical setup 99
5.2 SMA actuator mechanical setup modification 99
5.3 Actuator electronic setup 100
5.4 Actuator electronic setup block diagram 100
5.5 Current driver and sensors 101
5.6 Rotary encoder and load cell configuration 103

6.1 Strain temperature response: Determining the transformation temperatures 106
6.2 Phase diagram: Parameter estimation procedure 108
6.3 Temperature strain relationship; (a) Expected response for σ below σ_s^{cr}; (b) Expected response for σ above σ_f^{cr} 109
6.4 Temperature strain relationship: Experimental response for $\sigma = 0MPa$ . . . 110
6.5 Temperature strain relationship: Experimental response for $\sigma = 160MPa$ . . 110
6.6 Temperature strain relationship: Determining the transformation temperatures 111
6.7 Parameter estimated phase diagram 112
6.8 Determining ϵ_{pre} and σ_{cr}^f 113
6.9 Residual strain obtained for the applied load 114
6.10 Simulation results versus practical results for the determined transformation temperatures 115
6.11 Simulation results versus practical results for the modified transformation temperatures 117
6.12 SMA temperature response for various constant inputs 118
6.13 SMA temperature response: Simulation versus practical results 119
6.14 Temperature sensor lag compensation block diagram 120
6.15 Control surface deflection open-loop response at incremental inputs 121
6.16 Experimental open-loop response 122
6.17 Practical versus simulation results for an open-loop response 123
6.18 Simulation versus practical open-loop state measurements 124

7.1 PI controller experimental closed-loop response 128
7.2 PI controller experimental state measurements 128
7.3 Practical versus simulation results: PI controller 130
7.4 Temperature controller closed-loop simulation results 131
7.5 Bang-bang controller experimental closed-loop response 132
7.6 Bang-bang controller experimental state measurements 132
7.7 Releaving stress by applying the On-off approach 133
7.8 Practical versus simulation results: Bang-bang controller 135
7.9 Phase diagram illustrating temperature sensor deficiency effect 136
7.10 Feedback linearisation controller closed-loop simulation results 136
7.11 Transient power consumption versus deflection rate 138
7.12 Scalable prototype 139
7.13 Bending moment free body diagram 141

B.1 Strain gauge free body diagram 149
B.2 Wheatstone bridge setup 151
B.3 Load cell response 153

List of Tables

3.1 SMA mechanical parameters applied in simulation 36
3.2 Heat transfer coefficients & time constants at various wire diameters exposed to natural and convective heat transfer conditions 46

4.1 SMA mechanical parameters applied in simulation 49
4.2 Linearisation parameters 55

6.1 Estimated parameters 115
6.2 Revised estimated parameters 116
6.3 Temperature response specifications 118
6.4 Rise time obtained for control surface deflection open-loop response at various inputs 125

7.1 PI controller time domain specifications 129
7.2 Bang-bang controller time domain specifications 134
7.3 Controller time domain specifications overview 137
7.4 Scaled down hydraulic jack versus scaled up SMA actuator 142

Nomenclature

Abbreviations and Acronyms

CPUT	Cape Peninsula University of Technology
CoSICS	Control Surfaces in Confined Spaces
DSC	Differential Scanning Calorimetry
DC	Direct Current
LQR	Linear Quadratic Regulator
NaC	National Aerospace Centre of Excellence of South Africa
NiTiNOL	Nickel-Titanium Naval Ordnance Laboratory
PID	Proportional Integral Derivative
PC	Personal Computer
PE	Pseudo-elasticity
SME	Shape Memory Effect
SUN	Stellenbosch University
3D	Three-dimensional
2D	Two-dimensional
UCT	University of Cape Town
Wits	University of the Witwatersrand

Greek Letters

β	Volume expansion coefficient
Δ	Indicating perturbation state format
δ_t	Control surface deflection
ϵ	Strain

ϵ_{pre}	Maximum residual strain
μ	Viscosity
Ω	Transformation coefficient
ρ	Material density
ρ_m	Purely martensite resistivity
ρ_a	Purely austenite resistivity
σ	Stress
σ_s^{cr}	Stress at which a detwinning transformation start at temperatures below M_s
σ_f^{cr}	Stress at which a detwinning transformation end at temperatures below M_s
Θ	Thermoelastic coefficient
θ	Angular displacement
τ	Time constant
ξ	Martensite fraction
ξ_s	Detwinned martensite fraction
ξ_t	Twinned martensite fraction
ξ_a	Austenite fraction
ξ_0	Martensite fraction memory variable
ξ_{s0}	Detwinned martensite fraction memory variable
ξ_{t0}	Twinned martensite fraction memory variable
ξ_{a0}	Austenite fraction memory variable

Lowercase Letters

c_p	Specific heat capacity
f	Force experienced in a member
g	Load effect gravity factor
h	Convectional heat transfer coefficient
i	Current
k	Conductive heat transfer coefficient

l_0	Wire length corresponding to $\epsilon = 0$
r	Lever arm length
s	Arc length
t_r	Rise time
t_s	Settling time
u	Control system input
v	Kinematic viscosity
w	Externally applied force

Uppercase Letters

A	Surface area
A_c	Cross sectional area
A_f	Transformation temperature at which a transformation to austenite ends
A_s	Transformation temperature at which a transformation to austenite starts
B	Damping and frictional constant
Bi	Biot number
C_a	Gradient of the austenite transformation region in a stress temperature dimension
C_m	Gradient of the martensite transformation region in a stress temperature dimension
D	Diameter
E	Young’s modulus
E_m	Pure martensite Young’s modulus
E_a	Pure austenite Young’s modulus
Gr	Grashof number
$\dot{H}_O$	Time rate of change of angular momentum
I	Inertia
K	Position feedback gain
K_{ss}	Steady-state gain

K_{ff}	Feedforward gain
L_c	Characteristic length
M_p	Overshoot
M_f	Transformation temperature at which a detwinning transformation ends
M_O	Sum of moments about the fixed point O
M_s	Transformation temperature at which a detwinning transformation starts
M_t	Externally applied moment
Nu	Nusselt number
Pr	Prandtl number
R	SMA wire resistance
Re	Reynolds number
Ra	Rayleigh number
T	Temperature
T_f	Film temperature
T_I	Integral time
T_s	Surface temperature
T_0	Temperature memory variable
V	Volume

Subscripts

b	Bottom wire
t	Top wire
∞	Free-stream value

Syntax and Style

$\frac{df}{dx}$	Derivative of function, f, with respect to x
$\frac{\partial f}{\partial x}$	The partial derivative of function, f, with respect to x

Acknowledgements

Completing a project of this magnitude would have been impossible without any guidance, assistance and motivation. The following people played an important role in me completing this project and deserves my humblest gratitude.

- Mr Japie Engelbrecht for all his support, guidance and motivation throughout the entire duration of this project. He's determination is highly appreciated.

- Airbus for sponsoring the CoSICS project. The personnel involved: Keith Bohannen, David Hills, Sylvain Boye, Ian Whitehouse, Etienne Coetzee and Stephane Boissenin are thanked for promoting such a fascinating scope.

- NAC for helping in funding the project.

- Professors Greame Oliver and Oscar Philander and Messrs Lubabalo Mathoba, Velapi Msomi, Ardene Cupido and Jaques Matolla, our colleagues at the Cape Peninsula University of Technology, for providing critical information regarding smart materials.

- Professor Thomas Jones and Doctor Iain Peddle for their valuable inputs during research meetings.

- Ruan De Hart for all his effort in the electronics setup.

- My colleagues at the Electronic System Laboratory (ESL): Anton Runhaar, AM de Jager, Chris Jaquet and Francois Rupert for their assistance, inputs and many laughs during this project.

- My parents for all their emotional support.

- Lastly I would like to thank the lady in my life, Luhanie Visser, for all the emotional support and belief.

Chapter 1

Introduction

1.1 Background

The research documented in this thesis was performed as part of the larger Control Surfaces in Confined Spaces (CoSICS) research project sponsored by Airbus and the National Aerospace Centre of Excellence of South Africa (NAC), working in collaboration with Stellenbosch University (SUN) and the Cape Peninsula University of Technology (CPUT). The research investigates ways to provide control surface actuation in size-restricted spaces in commercial aircraft such as the Airbus A320 and A330.

Control surfaces are a crucial part of any aircraft as they produce the aerodynamic moments that are used to control the attitude and motion of the aircraft

These surfaces can be found on the wings and tail of any conventional aircraft. Control surfaces are accompanied by an actuator responsible for moving the control surface to its desired position. Hydraulic jacks are currently the main actuators responsible for control surface actuation on commercial airliners. In some space- restricted cases the position and size of these actuators often cause protrusion through the skin of the wing, which induces additional aerodynamic drag. In order to minimise the drag caused by the protrusion, it is encased in a fairing. Although this fairing decreases the amount of drag imposed on the wing, the drag is still notably greater than for a clean-wing configuration. Typical flap fairings are illustrated in Figure 1.1 by the coned-shape protrusions. A reduction in the control surface actuator size and therefore the accompanied protrusion can lead to decreased fairing sizes which will improve the aerodynamic performance of the wing considerably, resulting in better fuel consumption and weight savings.

The CoSICS research group addresses the problem by investigating ways to reduce the size of current control surface actuators. This is achieved by investigating the concept of trailing edge tabs to reduce the required torque load, resulting in reduced actuator requirements, in turn enabling the use of smaller actuators. Smart material research is combined with the trailing edge tab concept to investigate the possibility of smaller smart-material-based actuators for trailing edge actuation. The trailing edge

Figure 1.1 – Typical fairing protrusions on a wing of a conventional aircraft

tab concept, which consists of attaching a smaller tab to an existing control surface, is illustrated in Figure 1.2. The addition of a trailing edge operated in the opposite direction to that of the control surface can result in a reduced moment about the control surface hinge. Adding the tab results in two additional hinge moments compared to that for a conventional control surface only configuration. The aerodynamic forces acting on the tab produce a tab-induced hinge moment about the tab hinge and an additional tab-induced hinge moment about the control surface hinge. Likewise a control surface-induced hinge moment is experienced about the control surface hinge. The superiority of this configuration lies in the fact that the two hinge moments induced about the control surface hinge are opposite in direction, resulting in a reduced or even zero effective control surface hinge moment requirement. Ideally the tab hinge moment is

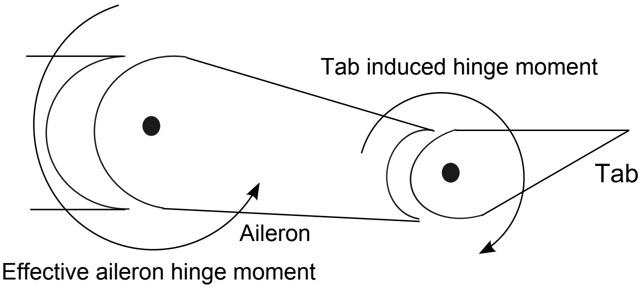

Figure 1.2 – Trailing edge tab concept

counteracted by a smart material actuator in conjunction with a smaller conventional actuator for control surface actuation.

A specific control surfaces case was selected to standardise the research. The control surface considered is that of the aileron, as noted in Figure 1.2, accompanied with its actuator. The necessary information on the aileron and the aileron actuator was supplied by Airbus.

Additional aerodynamic support, if required, is provided by NAC through students from the University of Cape Town (UCT) and the University of the Witwatersrand (Wits).

SUN is focusing on the optimisation and control aspects. C.D. Jaquet initiated the first stage of the research considering "The optimisation of trailing edge tabs to reduce control surface hinge moments". The focus was the geometric optimisation of the control surface trailing edge configuration. The findings concluded that tab-like configurations are "promising to reduce primary control surface hinge moments [1]."

F.J. Rupert, also from SUN, continued the research by considering various control strategies for the aileron-tab configuration. The approach taken was to consider the actuation of both the tab and aileron to produce the required deflections.

CPUT focuses on the actuator development and incorporation of smart materials to achieve control surface actuation. Various smart materials are being considered. Material characteristics are being determined and analysed based on the required application.

This thesis combines the smart actuator and control aspects by investigating the smart actuation and control of the trailing edge tab by considering a shape memory alloy-based actuator.

1.2 Problem Statement and Project Goals

The goal of this Master's project is to design, implement and test a feedback control system to control the deflection of a shape memory alloy-based control surface actuator. This research forms part of a wider investigation into the control and smart material aspects of the CoSICS project. Other smart materials of interest considered by CPUT are piezo-electric and magneto-strictive. The specific aspect being investigated here is the control of an alternative trailing edge actuator. The feature distinguishing the investigated actuator from the current actuator, i.e. the hydraulic jack, is the means of actuation. The actuator being investigated achieves actuation by using smart materials; in this specific case shape memory alloys (SMAs) are considered. SMAs are a special type of alloy classified as a smart material because of its unique characteristic of being able to change its shape in the presence of a temperature stimulus. The research focuses on incorporating SMA material in an actuator configuration to obtain trailing edge actuation, or for that matter any other control surface. The SMA-based actuator in mind is shown in Figure 1.3. The first objective of the thesis is to illustrate an operational SMA-based actuator able to demonstrate control surface actuation. The

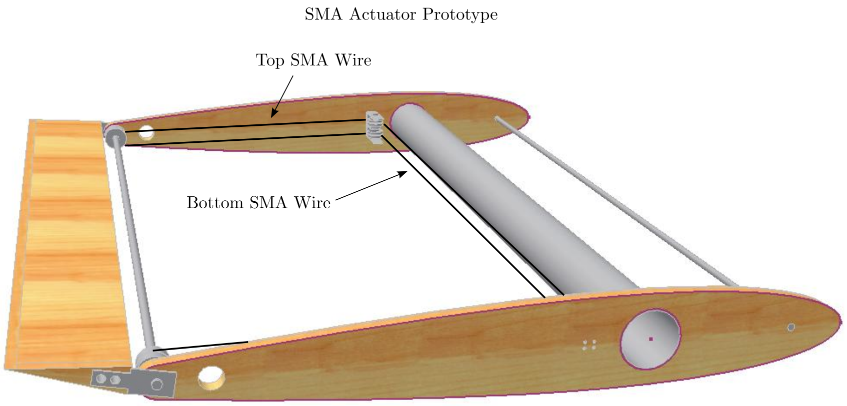

Figure 1.3 – SMA-based actuator prototype

scope of this thesis was limited to constructing a basic demonstrator and not a practical actuator. Research into a practical, full-scale actuator will build on the basis of the knowledge gained from constructing the basic demonstrator. The second objective is to evaluate the performance of the actuator in terms of the maximum obtainable deflection, actuation rate, power consumption, critical operational conditions and actuator restrictions. In order to evaluate these parameters, a control system is required. The major part of the research focuses on developing a suitable controller actuator system to obtain the required actuation.

1.3 Previous Control in SMA-based actuator Applications

The ability of shape memory alloys to produce large recovery forces and regain large deformations makes them suitable candidates in various actuator applications. Unfortunately SMAs also demonstrate highly non-linear behaviour with inherent hysteresis, which presents certain challenges when applying control to these actuators. In order to successfully manipulate these abilities, a capable control system is required in conjunction with the SMA-based actuator. Most of the SMA actuators encountered in the literature are applied to either obtain linear [2; 3; 4; 5] or rotational actuation [6; 7; 8]. Most applications only consider a single-wire actuator, while some investigate bundled SMA wire actuators [2; 9]. The ability of the SMA to regain its shape after it has been stretched is a one-way effect. A bias force is required to stretch the wire back to its original shape after contraction has occurred. Most actuators encountered in the literature are spring-biased to ensure continued actuation, but there are also examples of actuators that use another counteracting SMA element to provide the bias force.

A number of control techniques have been proposed for SMA actuators. Most of the control techniques encountered in the literature fall into the following categories: conventional PID feedback controllers, feedforward and inverse-based controllers, fuzzy logic controllers, robust control techniques such as sliding control, linearised model-based controllers, controllers based on hysteresis models, perturbation theory-based controllers, adaptive controllers and feedback linearisation-based controllers. A brief discussion of the encountered controller architecture types is presented below.

Barooah et al. applied conventional PID control with logical switches in an attempt to control a variable area fan nozzle [10]. Dickenson et al. applied similar conventional feedback PID control for position control of a beam applying a single SMA wire actuator [5]. It is shown that a pure proportional gain controller results in a steady-state error, which can be compensated for with the correct controller adaptation. Majima et al. presented a tracking control system for a spring-biased linear actuator applying PID control in conjunction with a feedforward controller [11]. The designed controllers are based on an existing SMA model, while the hysteresis is modelled applying a modified Preisach hysteresis model. A similar control technique applying feedback PID and feedforward control was applied by Howe et al. for a tactile shape display [12]. Lee et al. presented a Linear Quadratic Regulator (LQR) controller based on a simplified SMA model for position control of a single-wire linear actuator [9]. Teh et al. investigated a rapid heating strategy by applying force control to an antagonistic SMA-based actuator using a PID controller [13]. The PID controller design is based on a model obtained from a frequency response analysis. The rapid heating strategy aims to increase the heating rate of the SMA wires without causing them to overheat.

A few hysteresis model-based controllers were encountered. Gorbet et al. presented a controller based on the Preisach hysteresis model for an antagonistic wire actuator [6]. Dutta et al. considered a spring-biased linear actuator and implemented a position control system based on an experimentally developed hysteresis model [14].

Robust-type controllers were encountered quite frequently. Sana et al. applied a robust-based controller for a smart structural system, where the control input is limited [15]. The un-modelled dynamics are considered as an additive uncertainty in the controller design. Song et al. considered the position control of a composite beam with embedded SMA wires by applying robust control to compensate for the uncertainty in the SMA hysteresis [16]. Grant et al. applied variable structure control, a robust controller type, to obtain linear actuation for a wire-based actuator [2]. The actuator consisted of multiple woven SMA wires to generate a pulling force. Robust non-linear control was applied to a micro-actuator for the control of the flap positioning system by Lechevin et al [7]. The applied sliding mode control ensures robustness, while a PD controller was added to compensate for the hysteresis delay. Choi et al. applied a H_∞ robust controller to ensure force tracking of a robotic gripper [17]. Kai et al. also presented a robust variable structure controller for a rotary spring-biased micro-actuator [18]. The model used in the control design was obtained from open-loop experiments.

Arai et al. applied a feedback linearisation controller based on an actuator model developed by the authors [19]. They attached their SMA wire actuator to a plate in order to control its strain. Moallem et al. introduced an input-output-based feedback linearisation controller in order to regulate the force exerted by the SMA-based actuator on a flexible beam [20].

Various other control techniques were encountered and are briefly mentioned below. Gorbet et al. applied a dissipativity approach in developing a controller for a linear position control system to guarantee L_2 stability [18]. Ahn et al. introduced a self-tuning fuzzy logic PID controller for a single-wire actuator [4]. Fuzzy logic control was also applied by Bizdoaca el al. in an attempt to control SMA tendons [21]. Ge et al. considered a tracking control problem and applied a perturbation theory-based controller for a trajectory tracking problem of a flexible robot [22]. Moallem et al. applied an inversion controller based on an approximate SMA model with time-varying gains for tracking control [23]. They applied torque control to achieve the required position of an antagonistic SMA-based actuator.

Now that a brief overview of the control techniques applied to similar SMA related control projects have been introduced, the focus shifts to the specific project execution.

1.4 Project Execution

In order to successfully achieve the project goals, a plan to address each required aspect was developed. After becoming familiar with the CoSICS research group's objective and the relevant research already conducted within the group, the specific thesis objectives were addressed.

The initial goal was to establish the required knowledge on SMAs and to understand the phenomena that classify SMAs as smart material. This investigation led to the understanding of SMA operation and the existing theoretical models describing their fundamental characteristics. A suitable SMA model was identified for the SMA-based actuator modelling requirements.

In order to investigate the SMA's ability as an actuator, an actuator prototype was designed. It was decided to apply the SMA material in wire format in an antagonistic-type actuator. One configuration was investigated with two attaching mechanisms to ensure the simplest actuator kinematics. With an established actuator configuration, the modelling of the actuator was conducted. An accurate actuator model was required as it formed the basis from which the control system was designed.

The SMA-based actuator's ability to actuate is triggered by a temperature change within the SMA wire. It was therefore decided to investigate the possible heat transfer mechanisms and the way that these conditions would influence the actuator's ability to operate. This investigation is also relevant because of the possible application of the specific actuator at higher altitudes, where the heat transfer mechanism differs from that at sea level.

With the theoretical model established, the controller design commenced. The following controller types were considered and investigated.

- A PI controller based on a linearised model

- An on-off controller based on the fact that the fastest actuation could be obtained by applying the maximum input

- An inner-loop temperature feedback controller accompanied by an outer-loop deflection feedback controller with feedforward compensation

- A model-based feedback linearisation type controller

The feedback linearisation types of controllers were rarely encountered in the literature and not yet applied to the specific type of actuator being considered.

In order to validate the theoretical actuator model, practical verification was required to determine some of the unknown parameters found in the SMA model and apply any required model alterations. With an accurate model, the controller design was adapted for the practical application.

In order to evaluate the actuator's ability, the controllers were applied to the developed SMA-based actuator prototype. Initially the actuator was operated in an open-loop manner to investigate the dynamic response of the actuator to various constant inputs. This resulted in an indication of the rate of actuation that can be achieved. The maximum obtainable deflection was evaluated from these results. The final step was to apply the designed controllers to the practical actuator setup. The PI and on-off controllers were successfully applied on the prototype. Unfortunately time constraints and unforeseen hardware issues made it impossible to thoroughly test the temperature and feedback linearisation controllers. Nonetheless, sufficient other practical results were obtained to answer the questions raised in this thesis.

1.5 Thesis Layout

Chapter 2 describes the SMA phenomenon by introducing the capabilities of the material and the characteristics classifying it as a smart material. A thorough investigation and evaluation of existing models is undertaken, and the most suitable model for control system design is identified. The selected SMA model is presented and implemented in a simulation model. Simulations are performed and the results are analysed to show that they agree with the theory.

Chapter 3 incorporates the SMA model into the actuator prototype dynamics to establish an actuator model. The modelling is a crucial part of effectively designing a controller. The thermodynamic model of the SMA actuator is derived to model the heating and cooling mechanisms that drive the actuation of the SMA material.

Chapter 4 introduces the controller design procedures. First a short background of basic control systems architecture is presented, followed by the various controller designs.

Chapter 5 presents the practical setup available for verification. It highlights the strengths and weaknesses of the current setup, identifies the electronic hardware and sensors used, and identifies some pitfalls when working practically with SMA wires.

Chapter 6 presents the actuator system identification to identify some of the required parameters to implement the applied SMA model. At this stage the model is also compared to the practical results. The shortcomings of the model are identified and some adjustments are presented.

Chapter 7 presents the practical controller results. The practical and simulation results are evaluated and discussed, and the chapter concludes with a brief summary evaluating the different controllers followed by a brief scalability analysis.

Chapter 8 concludes the thesis with the recommendations and deductions derived from the study as well as an indication of topics for future research.

Chapter 2

Modelling of the Shape Memory Alloy

This chapter describes the mathematical representation of the fundamental characteristics captured in SMA behaviour. A mathematical representation is required to accurately model the control surface actuator in an approach to investigate its control capabilities. Firstly the reader is introduced to SMAs and the characteristics classifying it as a smart material; this is followed by a basic overview of existing modelling approaches. The overview aids in the identification of a suitable model, which is presented in detail. The SMA's fundamental characteristics, namely the shape memory effect, pseudo-elasticity and hysteresis, which will be described beforehand, are illustrated by simulation results obtained by applying the identified SMA model. Further experimental requirements needed for the practical model implementation are also mentioned.

2.1 Shape Memory Alloy Theory

A smart material is classified as a material that can significantly change its mechanical properties, such as shape, stiffness or viscosity, or its thermal, optical or electromagnetic properties, in a predictable, useful and controllable manner, in a response to an external stimulus [24]. Shape memory alloys fall under this category as they are able to change their shape, stiffness and thermal properties in a controlled environment.

SMAs exhibit two attractive characteristics that classify them as smart materials, namely the shape memory effect (SME) and pseudo-elasticity (PE). The SME is the ability of a deformed SMA specimen to return to its original shape in the presence of a temperature stimulus. In other words, an SMA can be trained to remember a specific shape. The SMA can then be deformed, to an extent, and will return to the shape it was trained to remember, if the necessary heat is applied. Pseudo-elasticity, on the other hand, is the rubber-like phenomenon of the SMA to regain large elastic strains at high temperatures. SMAs can therefore undergo large amounts of strains, at high temperatures, without plastically deforming, like pulling and releasing a rubber band.

2.1.1 SMA History

The shape memory phenomenon was initially discovered by the Swedish physicist Arne Olander while working with a gold (Au) cadmium (Cd) alloy in the early 1930s [25]. He observed the ability of the alloy to remember its shape when heated after being deformed at lower temperatures. It was not until the discovery of the shape memory effect (SME) in nickel titanium alloys that SMAs were extensively applied in engineering applications.

In 1962 William Buehler and his co-workers at the Naval Ordnance Laboratory discovered the SME in a nickel titanium alloy, they named NiTiNOL (after nickel-titanium Naval Ordnance Laboratory) [26][27]. At an earlier stage Buehler was working on finding suitable materials for the use in nose cones of re-entry vehicles. While working with NiTiNOL he took some bars from a melting furnace and left them to cool. He then intentionally dropped one bar on the floor and heard a bell-like sound as the bar hit the floor. He took another bar and quenched it in water and continued with the same procedure. The quenched bar indicated a thud-like sound when hitting the floor, resulting in the identification of curious acoustic damping qualities for the specific alloy. Buehler knew that the acoustic damping qualities were as a result of a change in the atomic structure of the material caused by a change in the material's temperature [26][27].

It was only at a later stage, when Raymond Wiley joined Buehler's research group, that the SME was identified in NiTiNOL. Wiley was illustrating the fatigue properties of NiTiNOL to management, when one of the directors decided to test how well the material would react under heat. When heat was applied to the NiTiNOL, it stretched out completely revealing another NiTiNOL property. When Buehler was informed about the findings, he linked the change in shape to his previous acoustic findings, resulting in the explanation of the SME as a result of an internal atomic structure change related to temperature [26][27]. The introduction of NiTiNOL sparked the use of SMAs in engineering practice as it was less expensive, easier to work with and more easily manufactured than previously identified alloys demonstrating the SME [28].

2.1.2 The Shape Memory Effect

The one-way SME is the ability of an unconstrained deformed SMA specimen to return to its original shape in the presence of a temperature stimulus. Strains of up to 8% have been reported in certain SMA types [29]. If a constrained specimen undergoes the SME, the SMA material exhibits large recovery stresses enabling the material to exert large forces. This grants the SMA an impressive power to weight ratio. The two-way SME indicates the ability of an SMA specimen to recover to a specific shape upon heating and transforming to a different shape when cooled down [30]. Given the scope of this thesis, the two-way SME won't be considered as the control surface actuator will be operated using only the one-way SME.

Microscopic Explanation

The SME is a result of an internal temperature- and stress-dependent shift in the material's crystalline structure between the high-temperature austenite (parent phase) and the low-temperature martensite phase [28]. These two phases along with the R-phase are the three possible phases that an SMA can consist of [30]. The R-phase can either be temperature- or stress-induced and will not be considered in this investigation as the amount of strain developed during the R-phase transformation is insignificant compared to that of the stress-induced martensite transformation process [31]. In order to visually illustrate the difference in crystalline structure for the various phases, the following simplified two-dimensional representations are shown in Figure 2.1. The crystalline structures are represented in a stress (y-axis) temperature (x-axis) plane to illustrate the conditions in which they occur. Each block represents a grain of the material with its respective grain boundaries. The austenite phase (Figure 2.1a) consists of a stable crystalline structure in cubic form resulting in grains with approximated right angles [28]. Martensite is the low-temperature phase, which may consist of two variants, namely twinned (the temperature-induced) and detwinned (the stress-induced) martensite. If the austenite phase is allowed to cool under a no-load condition, temperature-induced or twinned martensite is generated. The twinned martensite crystalline structure is

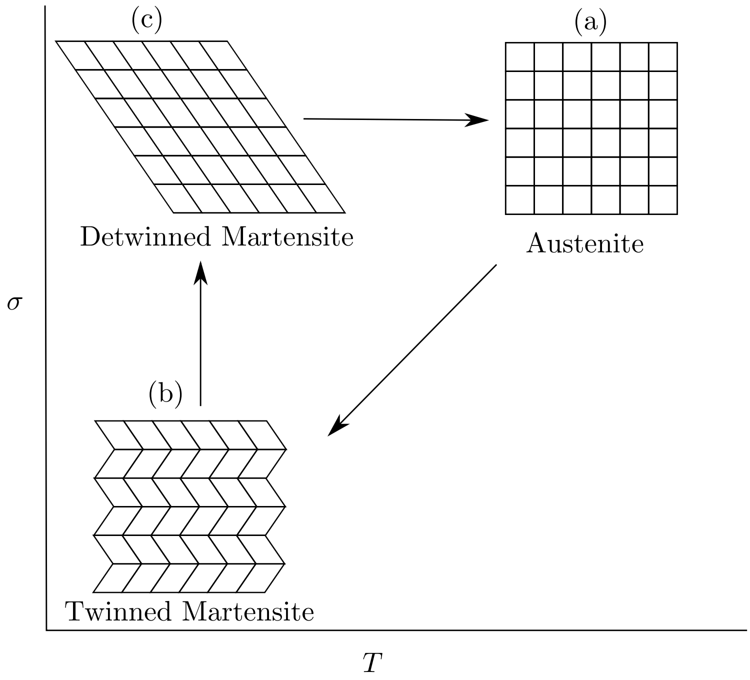

Figure 2.1 – SMA crystalline structure dependence on temperature and stress. (Source: Constantinos, et all [28])

shown in Figure 2.1b. Twinned means that the crystalline structure is orientated symmetrically across grain boundaries [28]. In the twinned martensite state the material is malleable and soft. Note that the macroscopic dimensions of the material remain unchanged during the transformation from austenite to twinned martensite. Heating the twinned martensite would only result in the formation of austenite with no subsequent macroscopic change. The twinned boundaries can easily move with the application of stress. When sufficient stress is applied, the twinned martensite starts detwinning, a process in which the twin boundaries move to accommodate the applied stress [32]. In this state the material is said to be detwinned martensite and is visually illustrated in Figure 2.1c. Applying heat in the detwinned phase results in the transformation of austenite. During this transformation the SMA returns to its original macroscopic dimensions.

Macroscopic Explanation

Another way to describe the SME is to investigate the stress-strain temperature curve of an SMA specimen undergoing a loading-unloading cycle, after which the specimen is subjected to heat. This relationship is shown in Figure 2.2. The x, y and z axes represent the strain, temperature and stress respectively. At stage 1, a low-temperature state, the specimen is in the twinned martensite phase. During the loading from stage

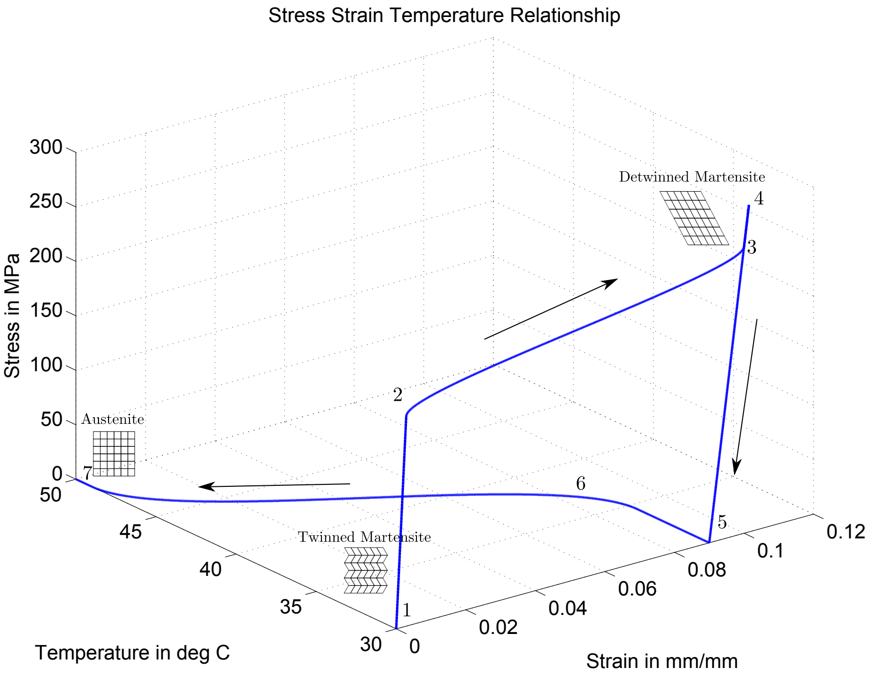

Figure 2.2 – The shape memory effect

1 to stage 2 the material undergoes elastic twinned deformation. At stage 2 the detwinning process commences until completely detwinned, at stage 3. During the detwinning process the stress only increases slightly. If load is applied beyond this point, the material undergoes elastic detwinned deformation. The load reaches a maximum at stage 4. Relieving the load results in the residual strain seen at stage 5. Upon heating, the specimen will then regain the residual strain and return to its original shape as indicated by stages 6 to 7. The specimen will return to its original state if left to cool from stage 7 to its initial temperature thus completing the loading and heating cycle.

2.1.3 Pseudo-Elasticity

Pseudo-elasticity is the elastic property of the SMA to regain its transformation strain at high temperatures [33]. Large loads, resulting in large strains, can be applied to the SMA specimen and the strain can still be recovered completely upon unloading. Pseudo-elasticity is illustrated in Figure 2.3. At stage 0 the SMA is at a high temperature and completely austenite. A load is applied and detwinning starts at stage 1. At stage 2 the material is completely detwinned. As the load decreases a hysteresis curve is visible as the SMA returns to the austenite phase thus completely recovering from the stress-induced strain.

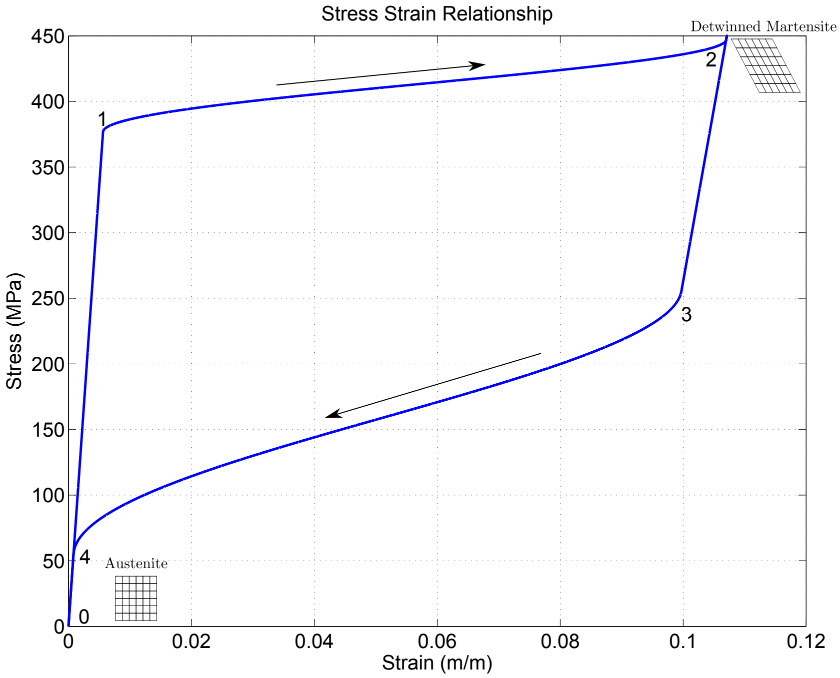

Figure 2.3 – SMA's pseudo-elasticity

2.1.4 Transformation Temperatures and Hysteresis

The SME is directly related to the temperature of the SMA. In order to describe this relationship four critical transformation temperatures are identified [34]. These transformation temperatures correspond to the respective start and completion temperatures for the various phase changes induced by heating and cooling a SMA and are commonly encountered in SMA literature. The symbols A_s and A_f correspond respectively to the temperature at which the transformation to austenite starts and the temperature at which the full austenitic state is achieved. These two symbols describe the transformation induced by a heating cycle. The symbols M_s and M_f correspond respectively to the temperature at which the formation of martensite starts and the temperature at which the full martensitic state is achieved. These two symbols describe the transformation induced by a cooling cycle. Figure 2.4 shows the phase transformation temperatures visually in terms of the temperature versus martensite fraction relationship of an SMA for a heating and cooling cycle. The SMA is initially at a temperature below M_f and consists completely of martensite. A martensite fraction of one corresponds to the full martensite state, while a martensite fraction of zero indicates the full austenite state. As the temperature increases above A_s, the martensite fraction decreases until it is reduced completely to zero at temperatures above A_f, resulting in a full austenite state. When the temperature is decreased again, martensite will only start forming once the material temperature drops below M_s. Decreasing the temperature further will result in the formation of martensite which will continue until the material is completely transformed to the full martensitic state at temperatures below M_f. Transformation temperatures are known to depend on the stress condition of the SMA, but this characteristic will be discussed at a later stage. Figure 2.4 also indicates that the heating

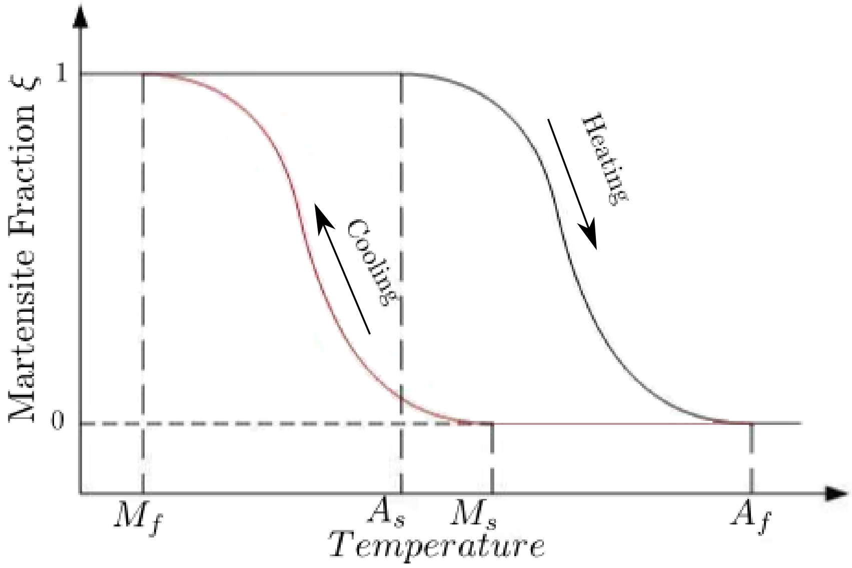

Figure 2.4 – SMA phase transformation with inherent hysteresis

and cooling curves follow different paths, indicating a hysteresis effect which is directly relatable to a hysteresis effect in the stress-strain relationship. This hysteresis effect along with its non-linear nature makes modelling and developing control schemes for SMA applications challenging. Typical hysteresis loop widths vary between 10 to $50°C$ [28]. Now that the basic properties of SMA have been presented, the focus moves to existing modelling approaches and their ability to effectively describe these properties.

2.2 Existing Modelling Approaches

From the literature study conducted one can distinguish between three existing SMA modelling approaches, namely the macroscopic phenomenological, the micromechanics-based macroscopic and the microscopic thermodynamic [35] modelling approaches. As the name suggests, the macroscopic-based modelling approaches try to capture the SMA response at a macroscopic scale, while the microscopic approaches consider the phenomena at a molecular level. A very broad description is given for the microscopic-based models, after which the focus shifts to the macroscopic models. For an in-depth explanation of the existing modelling approaches the reader is referred to [30].

2.2.1 Micromechanics-Based Macroscopic Models

These models apply thermodynamic laws to describe the material transformation and utilize micromechanics, the analysis of composite materials on their phase composition [30], to estimate the interaction energy as a result of the specific transformation. These models are fairly complicated and computationally time consuming.

2.2.2 Microscopic Thermodynamic Models

These models use phenomenological thermodynamics to describe an infinitesimal SMA volume and are usually more complicated than the other model types, thus requiring far more computational power. These models help in understanding the SMA phenomenon, but are difficult to apply in engineering applications. For a thorough description of available microscopic models refer to [30].

2.2.3 Macroscopic Phenomenological Models

This method describes material behaviour by fitting experimental data and/or using phenomenological thermodynamics to quite accurately predict the SMA's uniaxial response. Many of these models are based on the phase diagram of SMA transformation, which describes the transformation regions from martensite to austenite and vice versa in a temperature-stress dimension. These transformation regions are determined experimentally. This approach is well suited for engineering practice as it is usually very simple, as it makes use of parameters of measurable quantities based on experimental data. These models usually consist of a mechanical law, relating the stress-strain behaviour, and a kinetic law, describing the material phase transformation.

A brief description on the evolution of macroscopic phenomenological models will be presented as identified in the literature. Initially Tanaka developed a model to describe the three-dimensional behaviour of SMAs [36]. The model considered an exponential function to describe the transformation kinetics. Phase transformations from austenite to martensite are considered as well as the reverse transformation, martensite to austenite. The austenite to martensite transformation is given by

$$\xi_{A->M} = f(M_s, T, \sigma, \xi_0) \tag{2.2.1}$$

where M_s is the martensite start temperature, T and σ are the temperature and stress of the SMA and ξ_0 is the initial martensite volumetric fraction when the transformation starts. The transformation equation also contains material constants, namely C_m, C_a, σ_{cr}^s and σ_{cr}^f, which are encapsulate in the function and therefore not listed as arguments. The reverse transformation from martensite to austenite is given by

$$\xi_{M->A} = f(A_s, T, \sigma, \xi_0) \tag{2.2.2}$$

and is similar to equation 2.2.1 except that the austenite start temperature A_s replaces the martensite start temperature M_s as one of the arguments of the function. Tanaka also presented the constitutive relationship relating the stress strain and temperature to the internal variable, the martensite fraction, of the specific SMA. This constitutive relationship is found in most phenomenological models. Note, however, that Tanaka's model was restricted to the one-dimensional case.

Boyd and Lagoudas developed a three-dimensional model [37] based on the one developed by Tanaka. In order to evaluate their model against Tanaka's, the restricted one-dimensional case was considered. The conclusion was that the transformation kinetics were identical in the one-dimensional case, except for different estimations of certain constant parameters in the expression.

Laing and Rogers subsequently developed a model describing the transformation kinetics with sinusoidal functions [38] using the same parameters as shown in equations 2.2.1 and 2.2.2. Laing and Rogers's model was improved by Brinson using similar sinusoidal representations and distinguishing between the two martensite variants, twinned and detwinned martensite, when describing the internal variable. Brinson also described the elastic modulus as a function of the internal variable, whereas the other approaches approximated it as an average value [39]. The Brinson model is the model of choice for this specific application. An in-depth representation of the model is presented next.

2.3 Applied Modelling Approach

Among the modelling approaches described in the previous section, the macroscopic phenomenological model types were found to be best suited for use in the modelling of an SMA-based control surface actuator. Their relative simplicity, the fact that they are expressed in terms of measurable quantities, and the relatively large amount of literature available on these model types make them attractive candidates. Various macroscopic phenomenological model types have been developed, but very few differ in the modelling of the constitutive relationship relating the stress to the various state variables. The constitutive relationship developed by Tanaka [36] is expressed in rate form as

$$\dot{\sigma} = E\dot{\epsilon} + \Omega\dot{\xi} + \Theta\dot{T} \tag{2.3.1}$$

where σ, ϵ, ξ and T are the stress, strain, martensitic fraction and temperature of the SMA material and E, Ω and Θ are its Young's modulus, transformation coefficient and thermoelastic coefficient.

Several functions describing the transformation of the material composition, ξ, are found in the literature [31]. This transformation function is the factor which distinguishes most existing models. The transformation kinetics used in this project are those developed by Brinson et al. [33] and have the unique characteristic of distinguishing between the two martensitic variants, namely the stress-induced detwinned martensite and the temperature-induced twinned martensite. This model is thoroughly explained in the following subsection, as it leads to the formulation of the actuator model that is used for the control design process.

2.3.1 Proposed Model

The Brinson model, part of the macroscopic phenomenological type, was chosen because of its simplicity and ability to implement. The model consists of two stages namely,

- Relating the stress to the strain, temperature and detwinned martensite fraction
- Modelling temperature change inside the SMA due to electrical power input and convectional heat losses to the environment

The mathematical representation of the two different stages is presented below. Emphasis is placed on the following explanation as is gives insight into SMA behaviour and a glimpse of what to expect from the SMA behaviour in the actuator setup.

2.3.1.1 Stress, Strain and Detwinned Martensite Relationship

The model [33] describes three phases namely, (i) twinned martensite, the martensite material fraction induced by temperature, (ii) detwinned martensite, the martensite material fraction induced by stress, and (iii) austenite, the parent phase induced during heating. The phase compositions are described in equations 2.3.2 and 2.3.3 respectively,

$$\xi = \xi_s + \xi_t \tag{2.3.2}$$

$$\xi + \xi_a = 1 \tag{2.3.3}$$

where ξ_s and ξ_t are the detwinned (stress-induced) and twinned (temperature-induced) martensite fraction respectively and ξ and ξ_a are the martensite and austenite compositional fractions respectively. The one-dimensional constitutive law relating the stress, σ, to the strain, ϵ, temperature, T, and detwinned martensite fraction, ξ_s, is given by equation 2.3.4 and is expressed in rate form by equation 2.3.5.

$$\sigma = E\epsilon + \Omega\xi_s + \Theta T \tag{2.3.4}$$

$$\dot{\sigma} = E\dot{\epsilon} + \Omega\dot{\xi}_s + \Theta\dot{T} \tag{2.3.5}$$

with,

$$\Omega(\xi) = -\epsilon_L E(\xi) \tag{2.3.6}$$

$$E = E^a + \xi(E^m - E^a) \tag{2.3.7}$$

where ϵ_L is the maximum residual strain (prestrain), E^a is the pure austenite Young's modulus, and E^m is the pure martensite Young's modulus. The Young's modulus depends on the current material composition as shown in equation 2.3.7. The stress, strain, martensite fraction relationship shown in equation 2.3.4 was further simplified by Brinson et al. [40] as follows:

$$\dot{\sigma} = \dot{E}(\dot{\epsilon} - \epsilon_L\dot{\xi}_s) + \Theta\dot{T} \tag{2.3.8}$$

This can further be simplified to,

$$\dot{\sigma} = \dot{E}(\dot{\epsilon} - \epsilon_L\dot{\xi}_s) \tag{2.3.9}$$

since the magnitude of the thermal strain component is significantly smaller than the transformation strain components [40].

The following set of cosine functions, presented by Brinson et al. [33], describes the material composition during specific transformations.

For the conversion to detwinned martensite

for T > M_s and $\sigma_s^{cr} + C_m(T - M_s) < \sigma < \sigma_f^{cr} + C_m(T - M_s)$

$$\xi_s = \frac{1-\xi_{s0}}{2}cos(\frac{\pi}{\sigma_s^{cr} - \sigma_f^{cr}}(\sigma - \sigma_f^{cr} - C_m(T - M_s))) + \frac{1+\xi_{s0}}{2} \tag{2.3.10}$$

$$\xi_t = \xi_{t0} - \frac{\xi_{t0}}{1-\xi_{s0}}(\xi_s - \xi_{s0}) \tag{2.3.11}$$

for T < M_s and σ_s^{cr} < σ < σ_f^{cr}

$$\xi_s = \frac{1-\xi_{s0}}{2}cos(\frac{\pi}{\sigma_s^{cr} - \sigma_f^{cr}}(\sigma - \sigma_f^{cr})) + \frac{1+\xi_{s0}}{2} \tag{2.3.12}$$

$$\xi_t = \xi_{t0} - \frac{\xi_{t0}}{1-\xi_{s0}}(\xi_s - \xi_{s0}) + \Delta_t \tag{2.3.13}$$

where for M_f < T < M_s and T < T_0

$$\Delta_t = \frac{1-\xi_{t0}}{2}(cos(a_M(T-M_f))+1) \tag{2.3.14}$$

otherwise,

$$\Delta_t = 0 \tag{2.3.15}$$

For the conversion to austenite

for T > A_s and $C_a(T-A_f) < \sigma < C_a(T-A_s)$

$$\xi = \frac{\xi_0}{2}[cos(a_A(T-A_s-\frac{\sigma}{C_a}))+1] \tag{2.3.16}$$

$$\xi_s = \xi_{s0} - \frac{\xi_{s0}}{\xi_0}(\xi_0 - \xi) \tag{2.3.17}$$

$$\xi_t = \xi_{t0} - \frac{\xi_{t0}}{\xi_0}(\xi_0 - \xi) \tag{2.3.18}$$

where

$$a_M = \frac{\pi}{M_s - M_f} \tag{2.3.19}$$

$$a_A = \frac{\pi}{A_f - A_s} \tag{2.3.20}$$

The parameters C_m, C_a, σ_s^{cr} and σ_f^{cr}, are material constants which are either determined from a set of stress-strain tests at different constant temperatures, or supplied to the user by the supplier. The subscript m and a refers to martensite and austenite while σ_s^{cr} and σ_f^{cr} refers to the critical stress at which a transformation start and finish at temperatures below M_s respectively. The meaning of these material constants are made clear by a phase diagram [33], illustrating the relationship between the stress in the SMA material and the current temperature state, as shown in Figure 2.5, while the zero subscript parameters will be addressed in section 2.3.12.

The phase diagram shown in Figure 2.5 captures the stress versus temperature dependencies for the different phase compositions of an SMA material. There are four transitional strips indicated by the numbers 1, 2, 7 and 6. Strip 1 indicates the transitional area where transformation from a mixed martensite and austenite to a pure detwinned martensite state occurs. Strip 2 indicates the transitional area where transformation from a mixed martensite and austenite to a pure austenite state occurs. Strip 7 indicates the transitional area where transformation from a mixed twinned and detwinned martensite to a pure detwinned martensite state occurs. Strip 6 indicates the transitional area where transformation from a mixed martensite and austenite state to a twinned and detwinned martensite state occurs. It is only in these transformational strips in which the twinned and detwinned martensite as well as the austenite fractions can change. It is also very important to note that transformation only occurs if

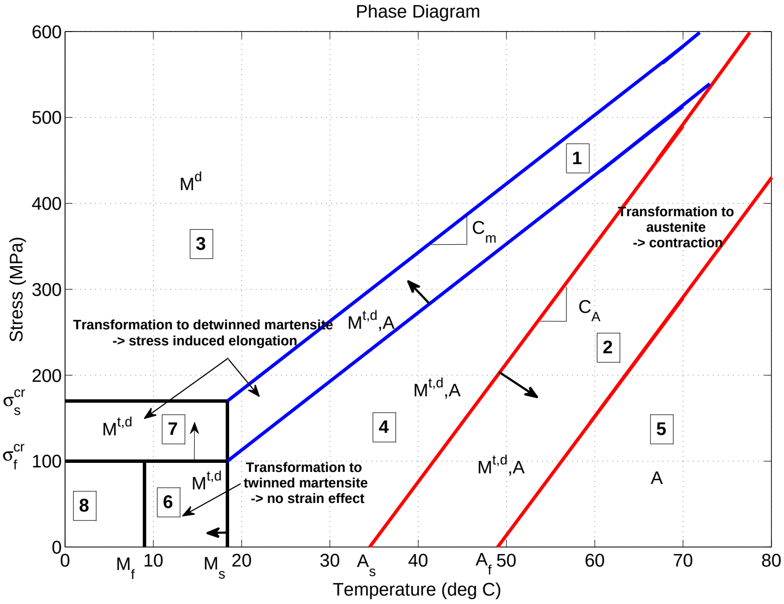

Figure 2.5 – SMA phase diagram (Source: Brinson, et all [33])

the time derivative of the temperature-stress vector has a positive component in the direction of the local transformational vector (indicated by the arrows in the respective transformation strips in Figure 2.5). In regions 5, 4, 3 and 8 the material composition remains constant. The unknown material properties C_m, C_a, σ_s^{cr} and σ_f^{cr} are indicated on the figure as the gradient of strip 1, the gradient of strip 2, the critical stress start and the critical stress finish respectively. Figure 2.5 indicates that the transformation temperatures increase as the stress increases, as mentioned in the introduction to transformation temperatures. The material constants C_m and C_a are in fact the rates at which the transformation temperatures increases for an increase in stress, for the martensite and austenite transformation strips respectively. Figure 2.5 also indicates that the detwinning process starts and ends at constant stress magnitudes at temperatures below M_s. The stress at which the detwinning starts is known as σ_s^{cr} while the stress at which the transformation completes is known as σ_f^{cr}.

2.3.1.2 Memory Parameters

The zero subscript variables indicated in equations 2.3.10 to 2.3.18 are memory variables. These variables contain the initial conditions of the twinned and detwinned martensitic and austenitic volumetric fraction at the start of the material transformation and may only change when one of the following events occurs.

- The material composition enters one of the four transformational strips in the direction of the transformational vector (indicated by the arrows on Figure 2.5)

- The material transformation direction changes sign inside any of the four transformational strips, i.e. if the component of the temperature-stress rate vector that is parallel to the local transformation direction changes from positive to negative or vice versa.

The memory variables, together with the equations and the accompanying phase diagram presented in the previous section, now provide the basis for a thorough understanding of the Brinson model. The Brinson model will form one component of the SMA-based control surface actuator model that will be developed in Chapter 3.

2.3.2 Model Behaviour

The Brinson model was implemented in a simulation model and simulations were performed to verify its ability to model the SMA characteristics and behaviour, including the shape memory and pseudo-elasticity effects. This verification was conducted to make sure that the SMA model behaves as predicted by the theory before the model is used in the actuator and controller configurations.

2.3.2.1 Shape Memory Effect

Figure 2.6 shows a basic loading-unloading cycle at a constant temperature below A_s. The SMA material is initially at a relaxed, zero-strain state, after which stress is applied. Upon unloading, a residual strain is evident in the material, which can be regained if the SMA material is heated. Figure 2.7 shows the same loading-unloading cycle by means of a phase diagram described earlier. At marker 0 the SMA is at a relaxed state with zero strain. A loading cycle is applied. When the stress reaches marker 1, the transformation of detwinned martensite starts. By the time the transformation reached marker 2 the SMA composition consists fully of detwinned martensite. The stress continues to increase until marker 3 is reached, after which the stress is gradually decreased until marker 4 is reached. These markers correspond to those shown in Figure 2.6.

Figure 2.8 is also included to illustrate the way in which the model mathematically describes the transformation process occurring during the transformation from markers 1 to 2. The sinusoidal shape of the curve clearly shows the transformation from 0% to 100% detwinned martensite.

Figure 2.9 shows the same loading-unloading cycle as mentioned above, but includes a heating process, after the SMA has undergone the stress cycle, to above A_f. The figure clearly illustrates the ability of the model to account for the shape memory effect as one can see the strain being reduced from 9% to 0%.

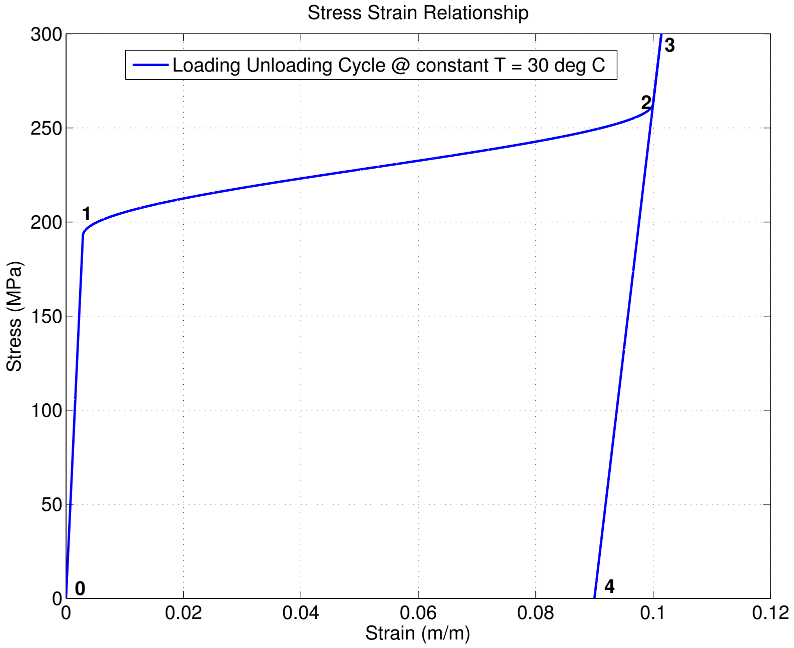

Figure 2.6 – Loading unloading cycle at a constant temperature of $30°C$

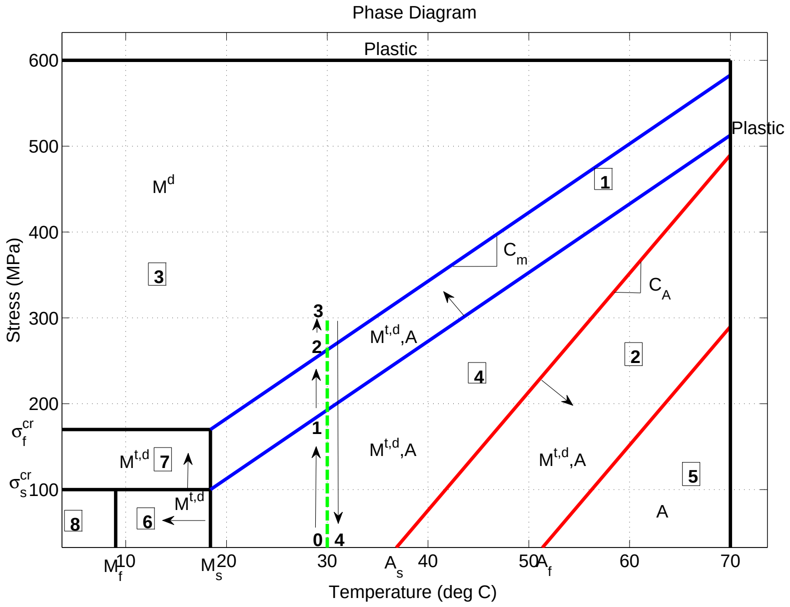

Figure 2.7 – Loading unloading cycle illustration using phase diagram (T = $30°C$)

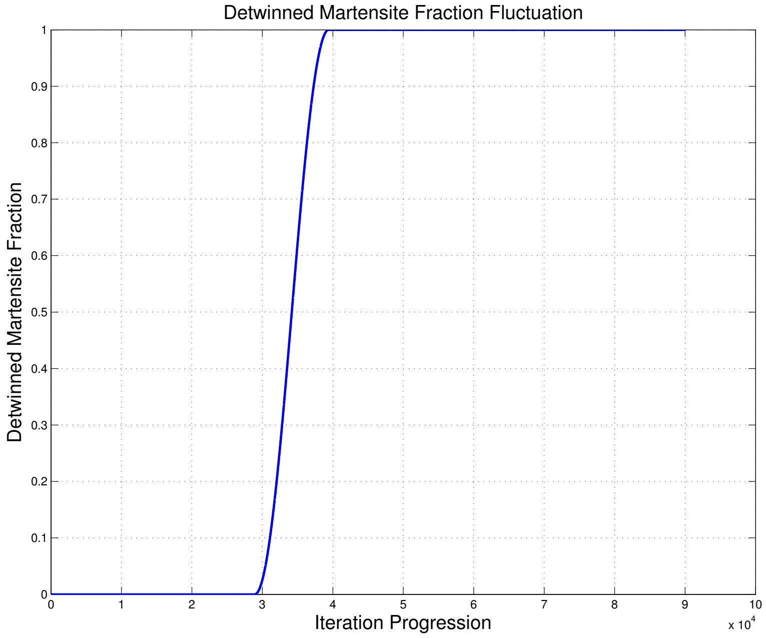

Figure 2.8 – Detwinned martensite transformation curve

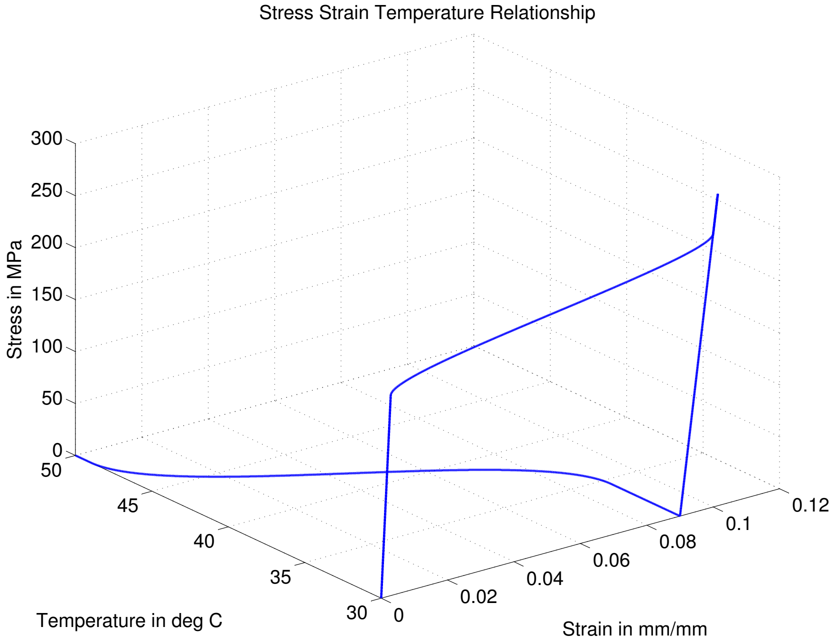

Figure 2.9 – Model's illustration of the shape memory effect

2.3.2.2 Pseudo-Elasticity

Figure 2.10 shows the stress-strain curve of a loading-unloading cycle for an SMA at a constant temperature above A_f. Initially the SMA is at a 100% austenite phase composition. The property pseudo-elasticity, the ability to regain transformation strains upon unloading, is captured in this figure. Figure 2.11 illustrates this transformation using the phase diagram. The SMA is initially in the parent phase (marker 0), after which stress is applied. Stress increases until detwinned martensite starts forming (marker 1). After the detwinned martensite transformation (marker 2), the stress is decreased. As austenite starts forming (marker 3), the strain is fully regained until the SMA is at 100% austenite again (marker 4). The stress continues to decrease until the initial condition is reached (marker 0).

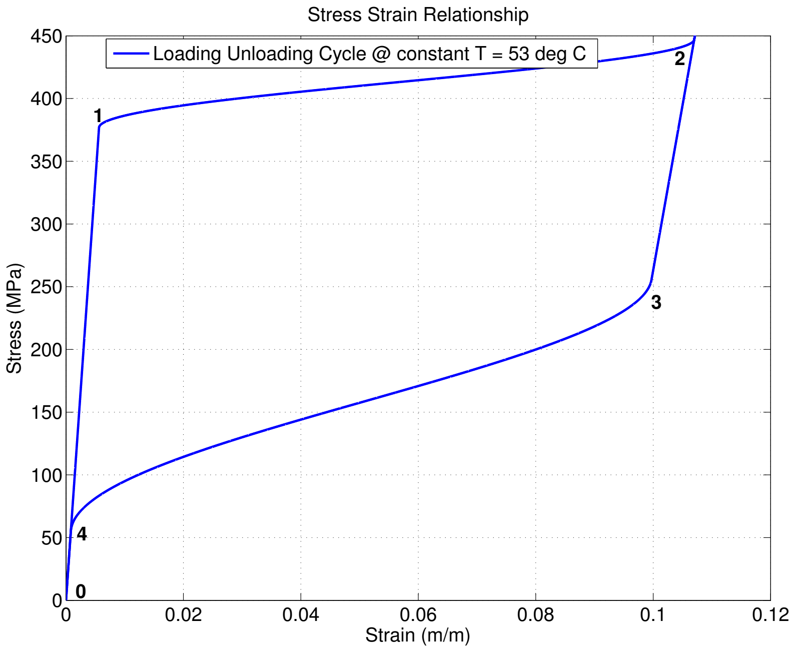

Figure 2.10 – Loading unloading cycle at a constant temperature of $53°C$

2.3.2.3 Minor Hysteresis Loops

The final step was to investigate the ability of the model to describe the minor hysteresis loops and whether the model indeed takes them into account. Minor hysteresis loops can be considered as transformations in which the phase transformation has only completed partially. Figure 2.12 shows the stress-strain relationship for a stress-strain cycle at a constant temperature above A_f. Initially the stress is increased to result in a completed detwinned transformation. The stress is then cycled between two fixed

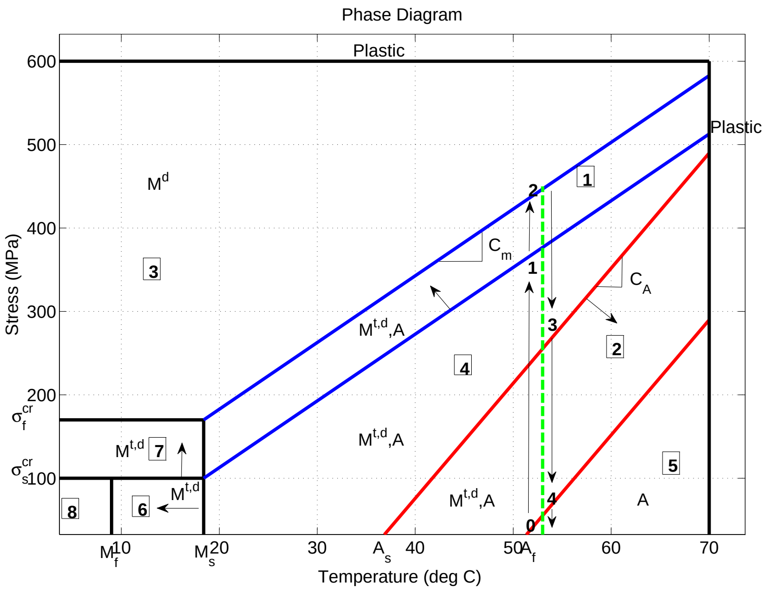

Figure 2.11 – Loading unloading cycle illustration using phase diagram (T = $53^{\circ}C$)

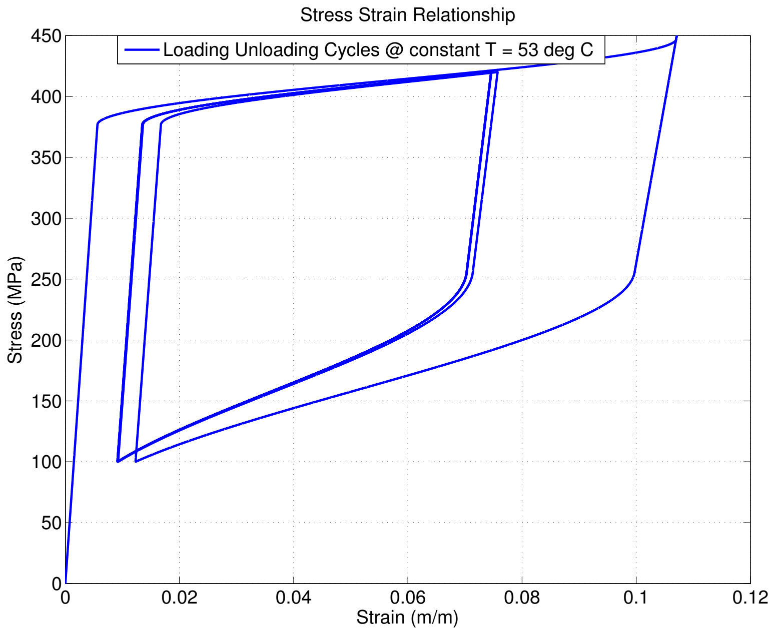

Figure 2.12 – Load cycling illustrating the minor hysteresis loops

values to induce constant partial transformations. The figure illustrates the minor hysteresis loops and shows how these loops initially differ for the same stress cycle, after which they eventually settle to a specific stress-strain hysteresis cycle.

Now that the smart material behaviour is understood and sufficiently modelled, the control surface actuator model, which incorporates the SMA model, can be developed.

Chapter 3

Modelling

This chapter captures the dynamics of the SMA-based control surface actuator in order to derive a suitable actuator model. The actuator configuration is presented by evaluating one configuration with two different wire attaching mechanisms. The evaluation results in the selection of a suitable configuration. The dynamics and kinematics of the chosen actuator configuration is developed and combined with the SMA constitutive relationship, phase transformation kinetics and temperature dynamics to formulate the differential model describing the control surface actuator dynamics. Combining the modelling components results in the following SMA-based control surface actuator block diagram model relating the current input, u, to eventually obtain a control surface deflection, δ_t. An accurate actuator model is required in order to analyse and develop suitable control solutions. Simulation results obtained by implementing the derived actuator model is also presented to illustrate basic actuator operation. The chapter concludes with an in depth investigation into the thermodynamic model governing the ohmic heating and convective cooling of the SMA wire, which drives the temperature variable that serves as an input to the constitutive material model.

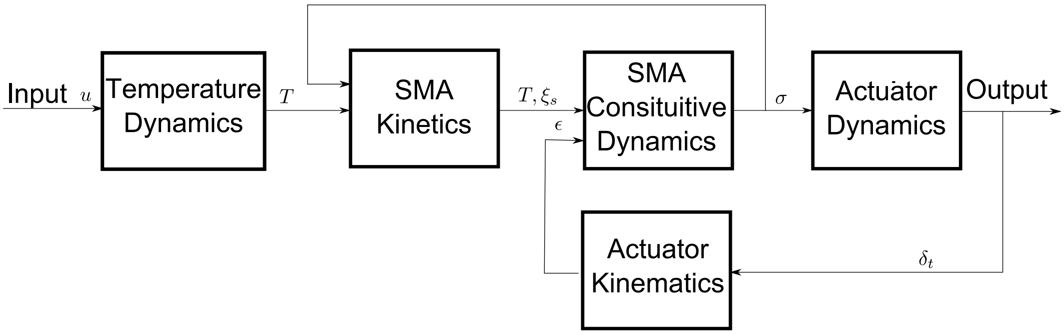

Figure 3.1 – SMA-based control surface actuator model block diagram

3.1 SMA Actuator Geometry

A one-degree-of-freedom SMA actuated control surface is considered. In order to obtain actuation in an SMA actuator a bias force is required. The bias force ensures that the wire returns to its original position or shape after a SME cycle has been completed. In this application a second SMA wire provides the required bias force, resulting in the actuator classification as an antagonistic type SMA actuator. A basic prototype of the counteracting two-wire actuator is shown in Figure 3.2. During operation one wire will be active, being heated and contracting thus resulting in actuation, while the other will react passively, because it is exposed to natural convection. Heating is achieved through resistive electrical heating and can only be applied to one wire at an instance. The outcome of the configuration modelling is to investigate the kinematic relationship between the strains in the respective wires and the control surface deflection variable. Such a relationship will simplify the actuator dynamics considerably. One actuator configuration will be considered with two different attaching mechanisms. The attaching mechanisms refer to the method used to attach the SMA wire to the control surface shaft. Each wire is attached at two separate ends of the shaft. A pulley system is used to guide each wire from one attaching point to another. The kinematics for both configurations is developed, followed by the identification of the preferred choice.

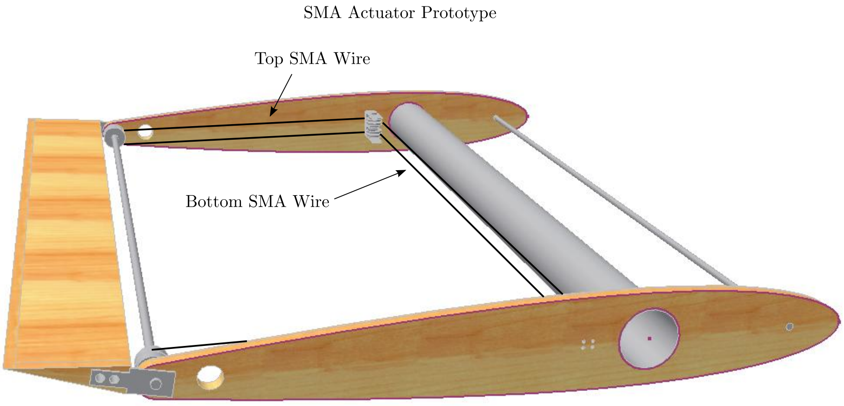

Figure 3.2 – SMA-based actuator prototype

3.1.1 Lever Configuration

One of the attaching configurations under consideration is illustrated in Figure 3.3. The configuration consists of an arm constrained to move in an arc. Two SMA wires will be attached to either end of the lever arm to achieve movement in the positive and negative movement directions as the wires either contract or elongate. The relevant parameters are the lever arm length, r, the force in the top and bottom SMA wires, f_t and f_b, the external applied moment, M_t and the control surface deflection, δ_t.

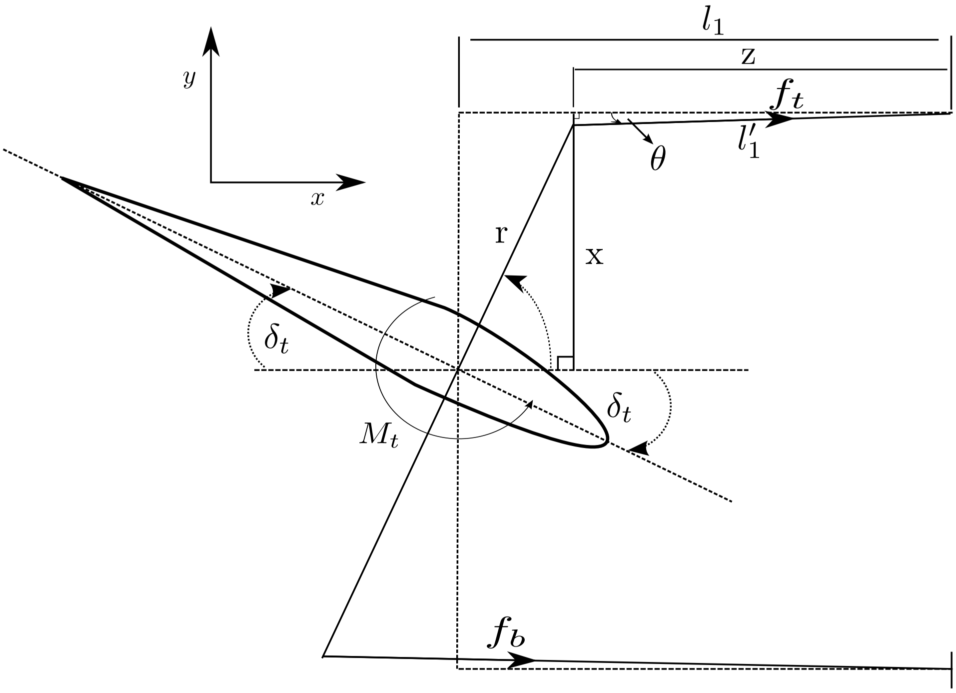

Figure 3.3 – Two-dimensional lever configuration: Force free body diagram

Relating the Control Surface Deflection to Strain

The kinematic relationship between the strain in the SMA wires epsilon and the control surface deflection δ_t can be derived from Figure 3.3 as follows. The strain induced in a wire can be expressed as

$$\epsilon = \frac{l_{new} - l_0}{l_0} \tag{3.1.1}$$

where l_{new} and l_0 are the wire lengths after and prior to the application of strain respectively. Before attaching the SMA wire to the actuator, at a control surface deflection of $0°$, it is given a pre-strain. In other words its being stretched. The pre-strain is set equal to half of the maximum residual strain, allowing symmetrical maximum deflection in either direction. At a maximum positive deflection the bottom wire length will be at a minimum, completely austenite, while the top wire length will be at a maximum, completely de-twinned . A maximum negative deflection will result in the equal but opposite effect. At $\delta_t = 0°$ the lengths of both the top and the bottom wires are equal and can be represented as,

$$l_{\delta_{t0}} = 2l_1 + l_2 \tag{3.1.2}$$

where l_1 and l_2 are the wire lengths situated parallel and perpendicular to the air foil ribs as shown in Figure 3.2. Together these lengths describe the current total length of the respective top and bottom wires. Because of the pre-strained condition of the wires at $\delta_t = 0°$, $l_{\delta_{t0}}$ could be expressed as follows:

$$l_{\delta_{t0}} = l_0 + l_0 \frac{\epsilon_{pre}}{2} \tag{3.1.3}$$

where l_0 is the un-deformed, $\epsilon = 0$, wire length and ϵ_{pre} the maximum residual strain, as mentioned earlier. With reference to Figure 3.3, applying small angle approximation resulted in the development of the required strain control surface deflection relationship. For the case at hand the control surface deflection is related to the strain in the top wire for a negative control surface deflection as shown in Figure 3.3. Note that an upward deflection corresponds to a negative angle resulting in the following trigonometrical relationships:

$$z = l_1 + r\sin(\delta_t) \tag{3.1.4}$$

$$\cos(\theta) = \frac{z}{l'_1} \tag{3.1.5}$$

Applying small angle approximation to equation 3.1.5 results in,

$$l'_1 = z \tag{3.1.6}$$

and the new total wire length, l', could be determined as.

$$l' = 2l'_1 + l_2 \tag{3.1.7}$$

Substituting equation 3.1.7 into equation 3.1.1 for the top wire case where $l' = l_{new}$ and then equation 3.1.6 into the result yields the following:

$$\epsilon_t = \frac{2l' + l_2 - l_0}{l_0} \tag{3.1.8}$$

$$\epsilon_t = \frac{2(l_1 + r\sin(\delta_t)) + l_2 - l_0}{l_0} \tag{3.1.9}$$

Recalling equation 3.1.2 and substituting equation 3.1.3 into the result yields the following.

$$\epsilon_t = \frac{l_{\delta_{t0}} + 2r\sin(\delta_t)) - l_0}{l_0} \tag{3.1.10}$$

$$\epsilon_t = \frac{\epsilon_{pre}}{2} + \frac{2r}{l_0}\sin(\delta_t) \tag{3.1.11}$$

The equation developed in equation 3.1.11 is a direct relationship between the control surface deflection and the strain in the top wire. The stain in the bottom wire can also be derived in similar fashion. The result is shown in equation 3.1.12.

$$\epsilon_b = \frac{\epsilon_{pre}}{2} - \frac{2r}{l_0}\sin(\delta_t) \tag{3.1.12}$$

It is clear that the relationship is of a non-linear nature because of the visible cosine functions. Unfortunately small angle approximation won't be sufficient to linearly approximate these equations as angles of up to $30°$ will be considered. This non-linear nature is an identified disadvantage of the considered configuration.

3.1.2 Pulley Configuration

The second attaching configuration consists of a counteracting pulley system guiding the SMA wire on the arc of the pulley as rotation occurs. The control surface is attached to these pulleys resulting in a direct relationship between the pulley rotation and the control surface deflection. The configuration is illustrated in Figure 3.4. Considering the same pre-strain condition as in the lever configuration, half of the maximum residual strain at $\delta_t = 0°$, the required kinematics could be developed.

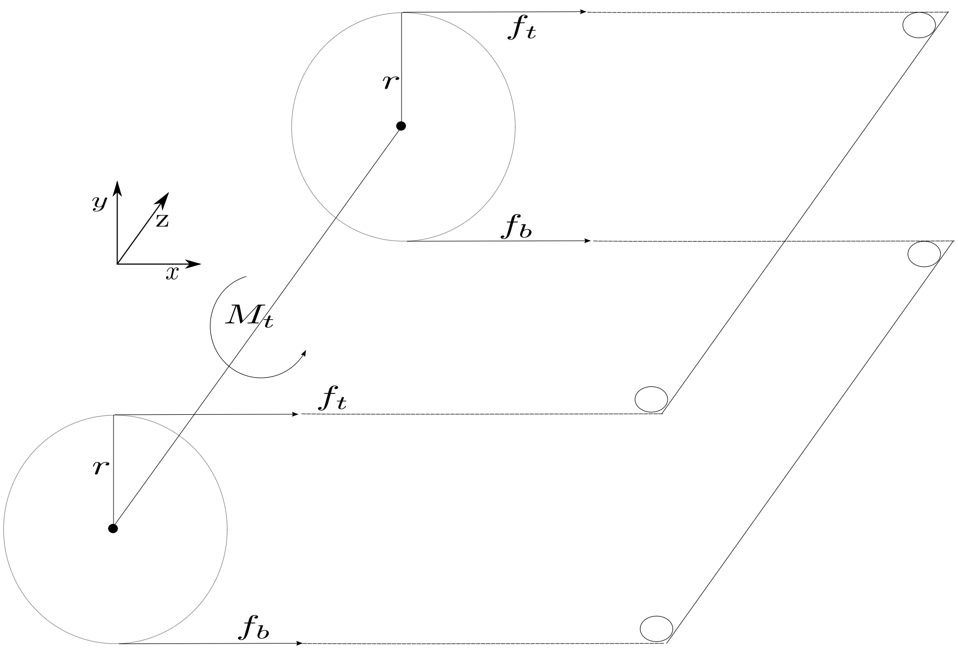

Figure 3.4 – Three-dimensional pulley configuration: Force free body diagram

Relating the Control Surface Deflection to Strain

By applying simple geometry the strain in both wires could be related to the pulley deflection and thus the control surface deflection. Recalling that the arc, s, with a fixed radius, r, performing a fraction of a revolution can be represented as follows:

$$s = r\delta_t \tag{3.1.13}$$

and using the same notation as in the lever configuration, with a positive deflection being upwards, the following strain-control surface deflection relationship could be developed. The new wire length, l', as a result of the current control surface deflection, can be represented as follows:

$$l' = l_{\delta_{t0}} + 2r\delta_t \tag{3.1.14}$$

Substituting equation 3.1.14 into the original definition of strain, equation 3.1.1, along with the definition of $l_{\delta_{t0}}$ as shown in equation 3.1.3, results in the final relationship.

$$\epsilon_t = \frac{\epsilon_{pre}}{2} + \frac{2r}{l_0}\delta_t \tag{3.1.15}$$

Similarly the relationship for the bottom wire can be developed.

$$\epsilon_b = \frac{\epsilon_{pre}}{2} - \frac{2r}{l_0}\delta_t \tag{3.1.16}$$

Differentiating equations 3.1.15 and 3.1.16 yields the rate form representation, which results in a direct top wire bottom wire strain relationship, as shown in equation 3.1.19.

$$\dot{\epsilon}_t = \frac{2r}{l_0}\dot{\delta}_t \tag{3.1.17}$$

$$\dot{\epsilon}_b = -\frac{2r}{l_0}\dot{\delta}_t \tag{3.1.18}$$

$$\dot{\epsilon}_t = -\dot{\epsilon}_b \tag{3.1.19}$$

One might notice that the relationships developed for the two configurations are similar. The major difference is the non-linear nature inherent in attaching configuration 1. Small angle approximation was applied in the lever configuration and would thus yield results susceptible to error. Because of the differences mentioned it was decided to model the actuator according to the pulley configuration, mainly because of its linear nature and ability to relate the two strains directly.

3.2 SMA Actuator Model Formulation

This subsection presents the actuator dynamics. The SMA statics are incorporated into the presented dynamic relationship to develop a system representation suitable for control system design and system analysis. The SMA constitutive relationship, statics and actuator dynamics, presented earlier, will be utilized and simplified further to result in a suitable SMA actuator model. The relevant SMA statics are displayed again to capture the actuator system as a whole and aid in the derivation of a suitable model.

Actuator Dynamics

An alternative way to model the angular displacement of a static body rotating about an fixed axis is by implementing the sum of moments relation [41], which states that the sum of moments about a fixed axis O, of all the forces acting on m, the mass of the system, equals the time rate change of angular momentum ($\dot{H}_O$) of the mass about the axis O [41]. This relation is stated in equation 3.2.1.

$$\sum M_O = \dot{H}_O \tag{3.2.1}$$

Assuming the configuration has a known inertia, I, some damping or frictional constant B and some load effect gravity factor, g, the following dynamic relationship can be derived as stated in equation 3.2.2.

$$I\ddot{\theta} + B\dot{\theta} + g\theta = f + w \tag{3.2.2}$$

Where f and w are the external forces and disturbances acting on the mass respectively. In the context of the actuator, the external forces are those exerted by the respective SMA wires acting on the control surface. Initially no external disturbances will be considered. The free body diagram of the current configuration, illustrated in Figure 3.4, is considered next in order to develop a relationship for the externally applied force, f. Summing the moments about the axis of rotation and taking the sign convention into consideration results in the following moment relationship:

$$f = 2r(f_b - f_t) + M_t \tag{3.2.3}$$

with f_b, f_t and M_t equal to the force in the bottom and top wire, and the externally applied moment respectively, though the latter can be considered as a disturbance and neglected for current purposes . Knowing $\sigma = \frac{f}{A_c}$, where A_c is the cross-sectional area of the wires, and replacing θ with δ_t results in the dynamic relationship of the actuator.

$$I\ddot{\delta}_t + B\dot{\delta}_t + g\delta_t = 2rA_c(\sigma_b - \sigma_t) \tag{3.2.4}$$

The SMA statics must be incorporated into the abovementioned equation to capture the complete actuator dynamics.

Heat Transfer Modelling

The heat conduction relationship is presented keeping in mind that the control surface actuator will be heated by applying an electrical current through a cylindrical wire. The heat conduction relationship, obtained by applying an energy balance equation for the case at hand, relates the temperature of the SMA wire to the current supplied to it in the presence of convectional heat losses from the SMA surface area to the environment. The governing equation is shown in equation 3.2.5. To view the derivation of this relationship please refer to Appendix A.

$$\dot{T} = C_1(T - T_\infty) + C_2 i^2 \tag{3.2.5}$$

with,

$$C_1 = -\frac{hA}{\rho c_p V} \tag{3.2.6}$$

$$C_2 = \frac{R}{\rho c_p V} \tag{3.2.7}$$

and ρ is the material density, c_p the specific heat capacity of the SMA, V the wire volume, h the convectional heat transfer coefficient, A the wire surface area, T the wire temperature, T_∞ the ambient temperature, R the wire resistance and i the current subjected to the wire. The convectional heat transfer coefficient is dependent on the convectional properties of the system and requires knowledge of the conductive heat transfer coefficient, k, of the SMA wire. Studies have been conducted to investigate the value of the heat transfer coefficient for various environmental conditions and these are presented at a later stage. For simulation purposes, all these parameters were acquired through manufacturers' material property data sheets obtained from the literature. Note that the specific heat, c_p, and the wire resistance, R, varies with change in temperature for an SMA material. Literature studies investigating this relationship have been conducted [42] [43] with the aim to establish mathematical parameter relationships. For this specific model these parameters are assumed to be constant for the sake of simplicity and are applicable as the focus of this study is on the model control aspects and not so much on the SMA parameter characterisation.

SMA Constitutive Modelling

$$\dot{\sigma} = E\dot{\epsilon} + \Omega\dot{\xi}_s \tag{3.2.8}$$

Note that the Young's modulus is taken as the average between the martensite and austenite Young's moduli respectively. This simplification is a general trend in modelling SMA systems.

$$E = \frac{E^a + E^m}{2} \tag{3.2.9}$$

$$\Omega = -\epsilon_{pre} E \tag{3.2.10}$$

Phase Transformation Kinetics

The phase transformation kinetics obtained from the Brinson model is summarised below.

$$\xi_s = \left\{ \begin{array}{c} \frac{1-\xi_{s0}}{2} cos(b_M(\sigma - \sigma_f^{cr} - C_m(T - M_s))) + \frac{1+\xi_{s0}}{2} \\ \text{if } T > M_s \text{ and } \sigma_s^{cr} + C_m(T - M_s) < \sigma < \sigma_f^{cr} + C_m(T - M_s) \\ \frac{\xi_{s0}}{2}[cos(a_A(T - A_s - \frac{\sigma}{C_a})) + 1] \\ \text{for } T > A_s \text{ and } C_a(T - A_f) < \sigma < C_a(T - A_s) \\ \xi_{s0}, \text{ otherwise} \end{array} \right\} \tag{3.2.11}$$

with

$$b_M = \frac{\pi}{\sigma_{cr}^s - \sigma_{cr}^f} \tag{3.2.12}$$

$$a_A = \frac{\pi}{A_f - A_s} \tag{3.2.13}$$

By taking the derivative of equation 3.2.11 the rate form is determined.

$$\dot{\xi}_s = \left\{ \begin{array}{c} \frac{\xi_{s0}-1}{2} sin(b_M(\sigma - \sigma_f^{cr} - C_m(T - M_s)))(b_M(\dot{\sigma} - C_m\dot{T})) \\ \text{if } T > M_s \text{ and } \sigma_s^{cr} + C_m(T - M_s) < \sigma < \sigma_f^{cr} + C_m(T - M_s) \\ \frac{-\xi_{s0}}{2}[sin(a_A(T - A_s - \frac{\sigma}{C_a}))][a_A\dot{T} - \frac{a_A}{C_a}\dot{\sigma}] \\ \text{for } T > A_s \text{ and } C_a(T - A_f) < \sigma < C_a(T - A_s) \\ 0, \text{ otherwise} \end{array} \right\} \tag{3.2.14}$$

Actuator Kinematic Modelling

The actuator kinematics as derived in Section 3.1.2 is summarised below.

$$\epsilon_t = \frac{2r(\delta_t)}{l_0} + \frac{\epsilon_{prestrain}}{2} \tag{3.2.15}$$

$$\epsilon_b = -\frac{2r\delta_t}{l_0} + \frac{\epsilon_{prestrain}}{2} \tag{3.2.16}$$

Equation 3.2.4 states the primary relationship describing the dynamics of the actuator. It relates the control surface deflection and its first and second derivatives to the stress state in each wire. The transformation kinetics is described by equation 3.2.11 and depends on the region of operation for each respective wire. The temperature dynamics are represented in equation 3.2.5, while the stress dynamics are described in equation 3.2.8. Figure 3.5 illustrates the block diagram of the derived actuator model and its internal dependencies. An identical top and bottom wire model is visible and incorporated into the actuator dynamics. The input is the electrical current supplied to the respective wires, while the control surface deflection serves as the required output.

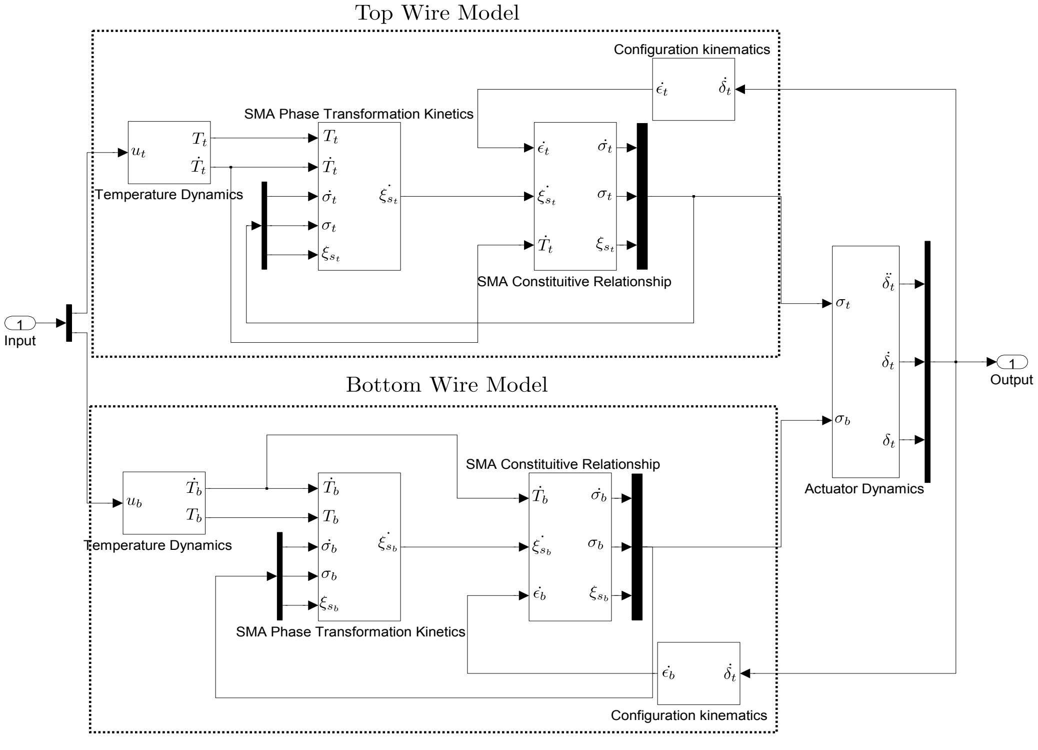

Figure 3.5 – SMA-based actuator model block diagram representation

Parameter	Units	Magnitude	Symbol
density	$\frac{kg}{m^3}$	6450	ρ
Specific Heat Capacity	$\frac{J}{kgK}$	322	c_p
M_s	$^\circ C$	18.4	M_s
M_f	$^\circ C$	9	M_f
A_s	$^\circ C$	34.5	A_s
A_f	$^\circ C$	49	A_f
Martensite Resistivity	$\mu\Omega cm$	76	ρ_m
Austenite Resistivity	$\mu\Omega cm$	82	ρ_a
Martensite E	GPa	26.3	E_m
Austenite E	GPa	67	E_a
Maximum Residual Strain	%	9	ϵ_{pre}

Table 3.1 – SMA mechanical parameters applied in simulation

3.3 Simulation Results

The presented model was put through a series of simulation runs to investigate the actuator's expected response. The SMA material parameters used in the simulation were obtained primarily from Brinson [39]. The focus of the simulation is not so much on the use of the correct material parameters, but on the general response of the actuator. The material parameters used are shown in Table 3.1. The model verification for the experimental actuator will be presented at a later stage.

Figure 3.6 shows the primary variables obtained for an open-loop response of 5 amperes input to the top wire. The term open-loop response implies a pure input-output relationship. The initial control surface deflection is constrained to 0°, implying an initial strain equal to half of the maximum residual strain, which is 5% for the simulation. This results in a detwinned martensite fraction of 0.5 to ensure equal actuation ability in both directions. The initial stress state in both wires is zero. Figures 3.6a, 3.6b, 3.6c, and 3.6d captures the control surface deflection, stress, strain and detwinned martensite fraction responses respectively. In order to explain the response the control surface deflection and phase diagram responses are shown in Figure 3.7.

Initially both wires are at the same temperature and stress. Current is applied to the top wire and the wire temperature increases. The application of current is accompanied by a dead zone, indicated by symbol **a** in Figure 3.7, in which no actuation is visible. The wire temperature has not yet reached the A_s transformation temperature resulting in the inactive state of the actuator. As the temperature increases above A_s, the active wire starts to contract, resulting in actuation. The initial actuation is illustrated by the symbol **b**. The contraction of the active wire induces stress in both the active and passive wires because of the counter acting nature of the actuator. As the active wire contracts, the passive wire stretches until it reaches the detwinning stress, symbol **c**. The exact state of detwinning is shown in Figure 3.6d. The stress-induced detwinning process causes a sudden drop in the stiffness of the passive wire, resulting in an increased actuation rate. As the active wire temperature is raised above A_f, the phase

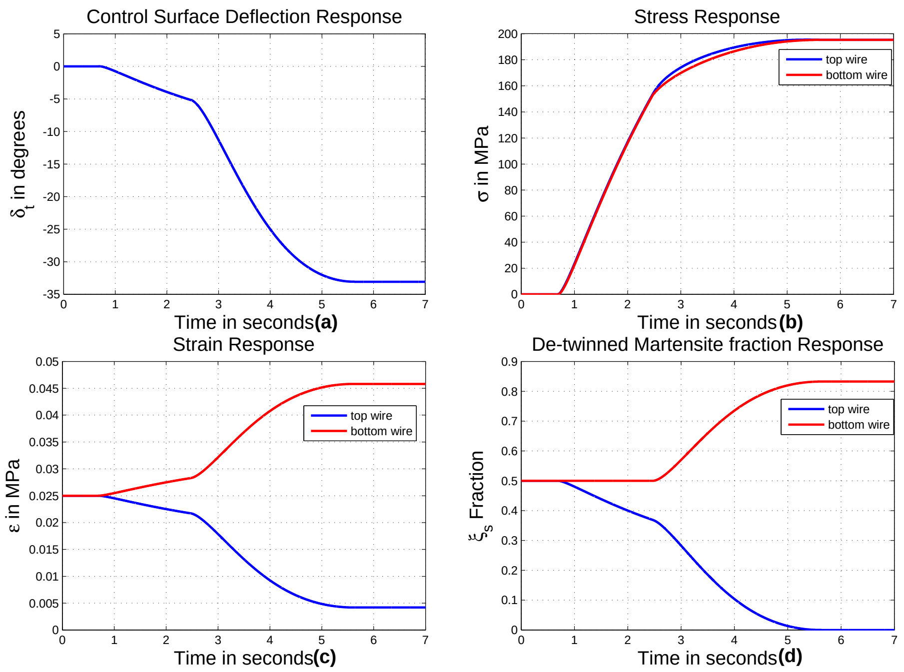

Figure 3.6 – Open-loop response of the essential states

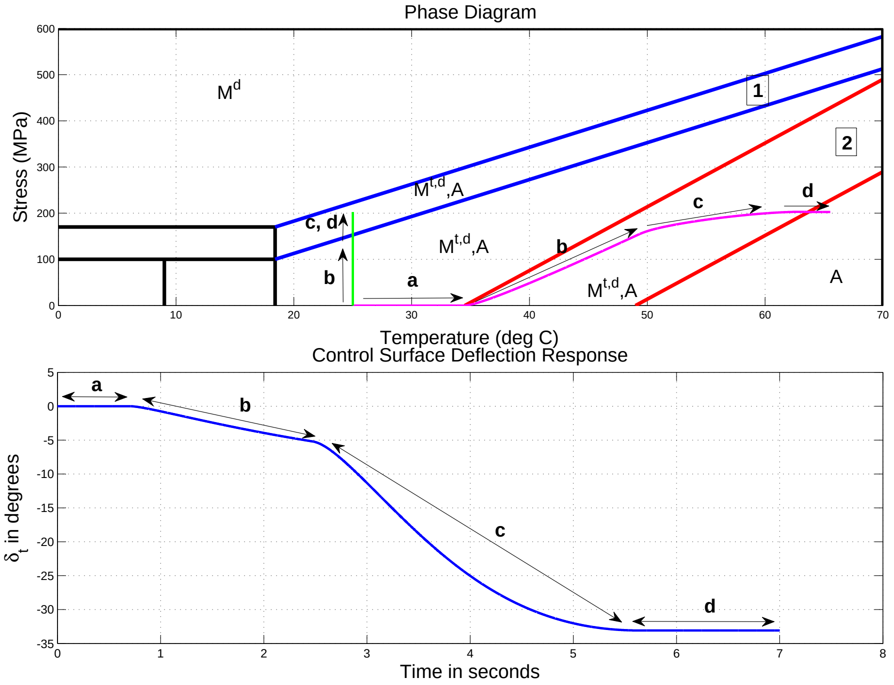

Figure 3.7 – Model understanding: Phase diagram & control surface deflection response

transformation halts and no more actuation is obtained, resulting in another dead zone. Keeping the active wire temperature in the dead zone results in constant stress levels in each wire as illustrated in Figure 3.6b. This explanation covers the driving mechanism for the basic operation of the SMA actuator according to the derived model. Actuation is achieved as a result of temperature- and stress-induced phase transformations. How to effectively manipulate these phase transformations is the challenge at hand and will be considered in the control chapter.

3.4 SMA Actuation

The advantageous ability of SMAs to contract to their trained length is triggered by a temperature change within the material which induces an internal phase transformation from martensite to austenite. Therefore a natural step in investigating the capability of SMA actuators is to understand the process which governs this temperature change. By understanding the heat transfer phenomenon and fundamentals one may discover ways in which SMA actuator responses can be increased or decreased as required. The response referred to is the control surface deflection actuation time in response to a command. The heat transfer mechanism at higher altitude is evaluated because of the possible application of SMA actuators in aircraft for control surface actuation. For this specific case a single cylindrical SMA wire will be considered and basic heat transfer fundamentals are applied in an attempt to understand the cooling and heating mechanism. Firstly the thermal analysis is explained after which some heat transfer parameters are investigated in detail followed by theoretical simulated responses illustrating the heat transfer process.

3.4.1 Lumped System Analysis

In order to determine the temperature characteristics of the SMA material it was necessary to conduct a thermal analysis. The applied method was chosen because of the SMA wire geometry and way in which it is applied in the actuator.

The method implemented treats the SMA wire as a lumped system, which entails that its internal temperature remains essentially uniform throughout the wire [44]. The temperature distribution is therefore solely a function of time and not of position. This simplifies the current heat transfer problem without sacrificing a significant amount of accuracy. Such an analysis is viable when the SMA wire's diameter is relatively small compared to its length, as is the case in our SMA actuator application. At a later stage the viability of the applied analysis will be confirmed for the configuration under consideration.

3.4.1.1 Analysis Assumptions

In order to implement the lumped system analysis the following assumptions were made. It is assumed that the SMA actuator geometry complies with the criteria for lumped system analysis (mentioned in section 3.4.1). The cross-sectional area of the SMA wire is assumed constant throughout the length of the wire. It is also assumed that the SMA wire is heated with a uniformly distributed heat source. Only convectional heat losses from the SMA wire surface to the surrounding medium, at a constant temperature, are considered. This analysis is limited to forced and natural external convection. The main difference is the different heat transfer coefficients for the convection mediums. These two convection mechanisms form the basis of the investigation as they vary quite considerably.

3.4.1.2 Model Derivation

The equation governing the temperature change inside the SMA wire, as presented in this chapter, is shown below.

$$\rho c_p V \frac{dT(t)}{dt} = -hA_s(T(t) - T_\infty) + Pe \tag{3.4.1}$$

where,

$$Pe = i^2 R \tag{3.4.2}$$

and ρ is the material density, c_p the specific heat capacity of the SMA, V the wire volume, h the convectional heat transfer coefficient, A the wire surface area, T the wire temperature, T_∞ the ambient temperature, R the wire resistance and i the current subjected to the wire.

Setting $\theta(t) = T(t) - T_\infty$ simplifies to the following first-order non-homogeneous ordinary differential equation:

$$\frac{d\theta(t)}{dt} + m\theta(t) = n \tag{3.4.3}$$

with,

$$m = \frac{hA}{\rho c_p V}$$

$$n = \frac{I^2 R}{\rho c_p V}$$

with the initial condition supplied below.

$$\theta(0) = \theta_0 = T_0 - T_\infty \tag{3.4.4}$$

where T_0 equals the initial temperature of the SMA wire at t = 0. Equation 3.4.3 is the standard differential equation for the specific case considered and governs the temperature change inside an SMA wire for a specific current input. An analytical analysis of this equation can now be conducted to give some insight into the heat distribution of a singular SMA wire exposed to electrical resistive heating. The general solution of equation 3.4.3, obtained when the input, i, is considered to be a constant, is shown below.

$$\theta(t) = \frac{n}{m} + (\theta_0 - \frac{n}{m})e^{-mt}, t > 0 \tag{3.4.5}$$

From equation 3.4.5 one can extract the time constant, τ, of the system.

$$\tau = \frac{1}{m}$$

The time constant of a system is the corresponding time the system requires to reach 62.3% of its final settling value in response to a step command. It is usually applied to specify the time specification of a first-order system. A small time constant suggests a system with faster dynamics, while a larger one suggest a system with slower dynamics. In our case the larger the variable m, the faster the system will tend towards the steady state value. By inspecting the parameter m analytically, one can identify that it can be increased by increasing the surface area exposed to heat convectional losses. This is a logical statement as larger heat losses would be expected from a larger exposed surface. The only other notable variable which can be altered to increase m is the convectional heat transfer coefficient, h. Section 3.4.1.3 is dedicated to investigating this parameter and its effect on the heat transfer conditions. The steady-state temperature as $t- > \infty$, for a specific set of conditions, can also be deduced from equation 3.4.5 and is shown below.

$$\theta(t) = \frac{n}{m} = \frac{I^2R}{hA} \tag{3.4.6}$$

Furthermore, it is noted that increasing the input will only increase the steady-state temperature and will have no effect on the time constant of the system. The time constant depends solely on the heat transfer conditions. Increasing the input will only increase the magnitude of the steady-state temperature. Theoretically any temperature can be obtained within any time constraint by increasing the current supply to the required magnitude. The heating ability of the actuator is therefore constrained to the practical limitations of the hardware used to drive the actuator. The limiting dynamic in the heat convection mechanism is the cooling procedure, which is limited by the time constant and therefore depends solely on the heat transfer conditions. By manipulating these conditions, a faster cooling response can be obtained, improving the actuator's response time. This is better explained as follows. Actuation in an SMA actuator is obtained when the heated wire exerts a large enough force to strain the passive wire. At lower temperatures the passive wire presents less resistance when counteracting the active wire in an actuation attempt. This is because the majority of the SMA is in the softer martensite state. In this state the actuation is obtained with the least effort. At higher temperatures the passive wire presents considerably more resistance, decreasing the actuator's response time. This is because the majority of the SMA is in the stiffer austenite state. This suggests that it is necessary to cool the passive wire in the fastest possible time in order to reduce the passive wire resistance to a minimum.

3.4.1.3 Determining the Heat transfer Coefficient

As mentioned above, the only other parameter in the heat transfer equation that can be altered to improve the SMA wire temperature response time is the convectional heat transfer coefficient, h. Determining the heat transfer coefficient depends on the type of convection the wire is exposed to. Two types of heat dissipation modes were investigated. The first is forced external convection which entails cooling the SMA wires by forcing air over the wire, while the second is natural convection in which cooling takes place as a result of the natural draught around the SMA wires. Both mechanisms will be discussed.

Forced External Convection

The following steps constitute the basic procedure one would follow to determine the heat transfer coefficient for a forced convection heat transfer problem, as indicated in [44]. The first step is to determine whether the flow of the cooling medium is laminar, the more streamline flow, or turbulent, the more chaotic flow regime. This phenomenon is governed by the Reynolds number, which is a ratio of the fluid's inertia forces to its viscous forces. The Reynolds number for flow across a cylindrical object, as in this case, is shown in the equation below.

$$Re = \frac{VD}{v} \tag{3.4.7}$$

where V and v, are the free-stream velocity and the kinematic viscosity of the cooling fluid, while D represents the SMA wire diameter. The expression for the kinematic viscosity is shown below:

$$v = \frac{\mu}{\rho} \tag{3.4.8}$$

where μ and ρ are equal to the viscosity and density of the cooling fluid respectively. The next step is to determine the Prandtl number, which describes the relative thickness of the velocity and thermal boundary layers at the surface boundary of the object undergoing convectional heat transfer. This relationship is shown below.

$$Pr = \frac{\mu c_p}{k} \tag{3.4.9}$$

where μ is the same as mentioned above and c_p and k represent the specific heat and thermal conductivity of the cooling fluid respectively. The final step is to determine the Nusselt number, which non-dimensionalises the heat transfer coefficient. The Nusselt number shown below is one of a few empirical formulas which calculate the parameter, depending on the magnitude of the Reynolds number.

$$Nu = \frac{hD}{k} = \left\{ \begin{array}{c} 0.989 Re^{0.330} Pr^{1/3} \text{ for } 0.4 < Re < 4 \\ 0.911 Re^{0.385} Pr^{1/3} \text{ for } 4 < Re < 40 \\ 0.683 Re^{0.466} Pr^{1/3} \text{ for } 40 < Re < 4000 \\ 0.193 Re^{0.618} Pr^{1/3} \text{ for } 4000 < Re < 40000 \\ 0.027 Re^{0.805} Pr^{1/3} \text{ for } 40000 < Re < 400000 \end{array} \right\} \tag{3.4.10}$$

By rearranging equation 3.4.10 the convectional heat transfer coefficient of the cooling medium can be determined.

Parameter Selection

Note that the convectional heat transfer coefficient derived above is a mean heat transfer coefficient of the system and therefore the cooling fluid parameters mentioned above will be evaluated at the film temperature:

$$T_f = 0.5(T_\infty + T_s) \tag{3.4.11}$$

where T_∞ is the temperature far away from the SMA wire and T_s is the surface temperature of the SMA wire. In this application film temperature will vary as the SMA wire temperature increases or decreases.

Natural Convection

The following section illustrates the calculation of the convectional heat transfer coefficient, h, for natural convection of air for a horizontal cylinder. The primary driving forces for natural convection are the temperature and the fluid buoyancy force, which is the net upward force generated in a gravitational field when a lighter fluid is placed under a heavier fluid [44]. The volume expansion coefficient, β, governs the variation of density of a fluid with a change in temperature at a constant pressure and is used to express the net buoyancy force in terms of a temperature difference. For an ideal gas β can be approximated as:

$$\beta_{idealgas} = \frac{1}{T} \tag{3.4.12}$$

where T is the temperature in Kelvin. The next step is to calculate the non-dimensionless Grashof number, which represents the ratio of the buoyancy force to the viscous force acting in on the cooling fluid.

$$Gr_L = \frac{g\beta(T_s - T_\infty)L_c^3}{v^2} \tag{3.4.13}$$

where g, L_c and v are the gravitational constant, the characteristic length of the geometry and the kinematic viscosity of the fluid respectively. The other parameters are as previously defined. Knowing the Grashof number, it is possible to calculate the Rayleigh number: the product of the Grashof and the Prandtl numbers.

$$Ra_L = Gr_L Pr \tag{3.4.14}$$

It is now possible to calculate the Nusselt number using equation 3.4.15 and then determine the convectional heat transfer coefficient by making it the subject of the equation.

$$Nu = \frac{hD}{k} = [0.6 + \frac{0.387 Ra_L^{\frac{1}{6}}}{[1 + (0.559/Pr)^{\frac{9}{16}}]^{\frac{8}{27}}}]^2 \tag{3.4.15}$$

It has been shown how to calculate the convectional heat transfer coefficient, h, for both natural and forced convection. It will be shown briefly that the lumped system analysis is a valid assumption for the specific configuration, after which some specific cases of heat transfer coefficients will be calculated and tabulated.

3.4.1.4 Lumped System Analysis Criteria

In order for the lumped system analysis to be applicable to the specific problem without adversely influencing the accuracy of the results, it has to comply to a certain degree with a certain criterion . This criterion is governed by the Biot number, which can be described as the ratio of the internal resistance of a body to heat conduction to its external resistance to heat convection and is defined as:

$$Bi = \frac{hL_c}{k} \tag{3.4.16}$$

where h is the heat transfer coefficient of the surrounding medium and k is the thermal conductivity of the SMA wire. L_c is described as the characteristic length of the system, where

$$L_c = \frac{V}{A} \tag{3.4.17}$$

and V is the wire volume, while A is the surface subjected to convectional heat transfer. Any lumped system analysis is applicable if

$$Bi \leq 0.1$$

For our specific application the Biot number is well below this requirement.

3.4.1.5 Analysis Results

The following results were obtained by implementing equation 3.4.5 in simulation for forced and natural convection using the procedure explained in Section 3.4.1.3.

Forced Convection

Figure 3.8a illustrates the change in temperature for an SMA wire subjected to a cross-flow of 100m/s at various current inputs at sea level. As expected, the larger the power supply, the higher the steady-state temperature. The transient response is similar regardless of the current supplied to the SMA wire.

Figure 3.8b is the same SMA wire subjected to the same forced convective heat transfer conditions, but at a higher altitude. One notices that for the 4 ampere input the energy entering the system is actually less than the energy leaving the system, thus resulting in a decrease in the wire temperature. At higher altitudes one would expect a decrease in the steady-state temperatures for identical current inputs because of the lower ambient temperature at high altitudes, which causes a larger temperature gradient for energy to be removed from the system. This is the case as seen in Figure 3.8b, but only up until a certain input magnitude is exceeded. Increasing the input above 6 amperes results in lower steady-state temperatures at higher altitudes. From inspection it was found that the heat transfer coefficient decreases with increasing altitude. The main contributor is the lower densities encountered at higher altitudes, which restricts the flow of heat away from the wire.

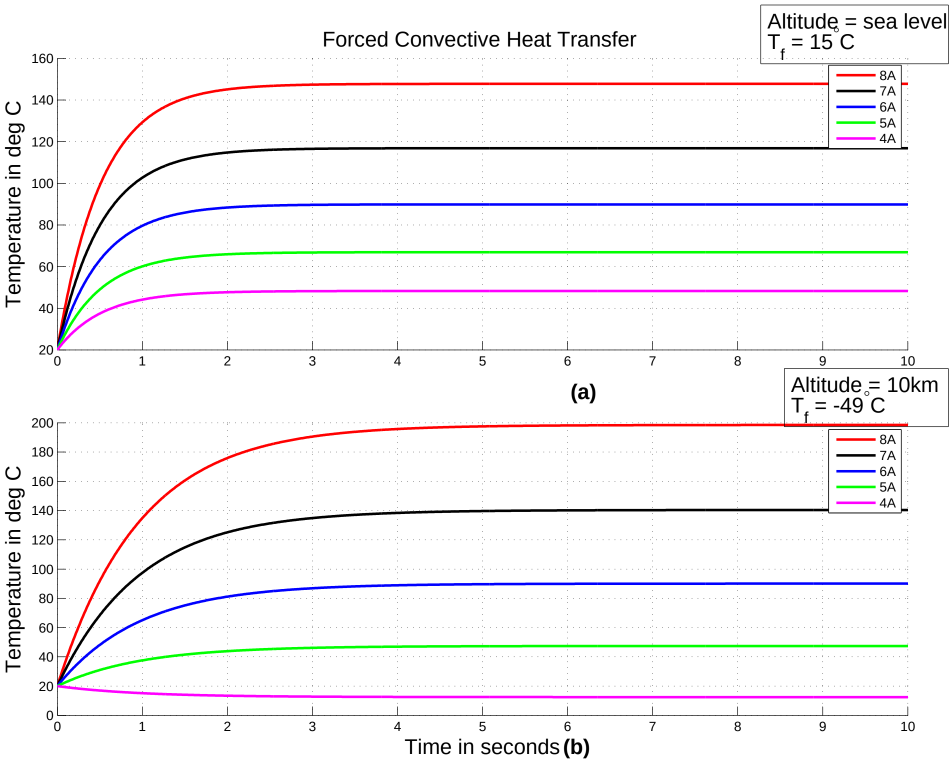

Figure 3.8 – Forced convection: Sea level (a) , 10 000 m (b)

The question arising is why lower current inputs result in lower steady-state temperatures than their equivalent sea-level results, when the higher input results do not. Inspecting the heat transfer equation could explain the phenomenon . The heat transfer equation describes the change in wire temperature as a function of the rate at which energy leaves and enters the system as depicted in equation 3.4.18. Regardless of the altitude, the rate of energy input remains constant for the same input. The rate of energy losses is governed by the heat transfer coefficient, h, and the temperature gradient between the SMA surface temperature and the surrounding temperature. At a higher altitude the temperature gradient increases, while the heat transfer coefficient decreases. At lower altitudes the temperature gradient decreases, while the heat transfer coefficient increases. The resulting steady-state temperature therefore depends on the ratio between these two values at the respective altitudes. At lower current inputs at higher altitude the temperature gradient is sufficient enough regardless of the lower heat transfer coefficient to result in a lower steady-state temperature than that achieved at lower altitudes. Increasing the current inputs results in the heat transfer coefficient dominating the abovementioned ratio, resulting in lower energy losses at high altitudes compared to those at lower altitudes.

$$\underbrace{\rho c_p V \frac{dT(t)}{dt}}_{\text{Energy Storage}} = \underbrace{-hA(T(t) - T_\infty)}_{\text{Energy Losses}} + \underbrace{I^2R}_{\text{Energy Input}} \tag{3.4.18}$$

Figure 3.8b also illustrates a slightly delayed transient response which is caused by the decreased convective heat transfer coefficients at higher altitudes.

Natural Convection

Figure 3.9a illustrates the heating curves for an SMA wire exposed to various power inputs and undergoing natural convection at sea level. One can clearly see a higher steady-state temperature being achieved than that obtained for forced convection. The time response is degraded as the heat transfer coefficient is smaller than that experienced in forced convection. Figure 3.9b illustrates the same heat transfer conditions as mentioned above but at a higher altitude. The same phenomenon of higher steady-state temperatures at higher altitudes is seen. Again this is the result of smaller heat transfer

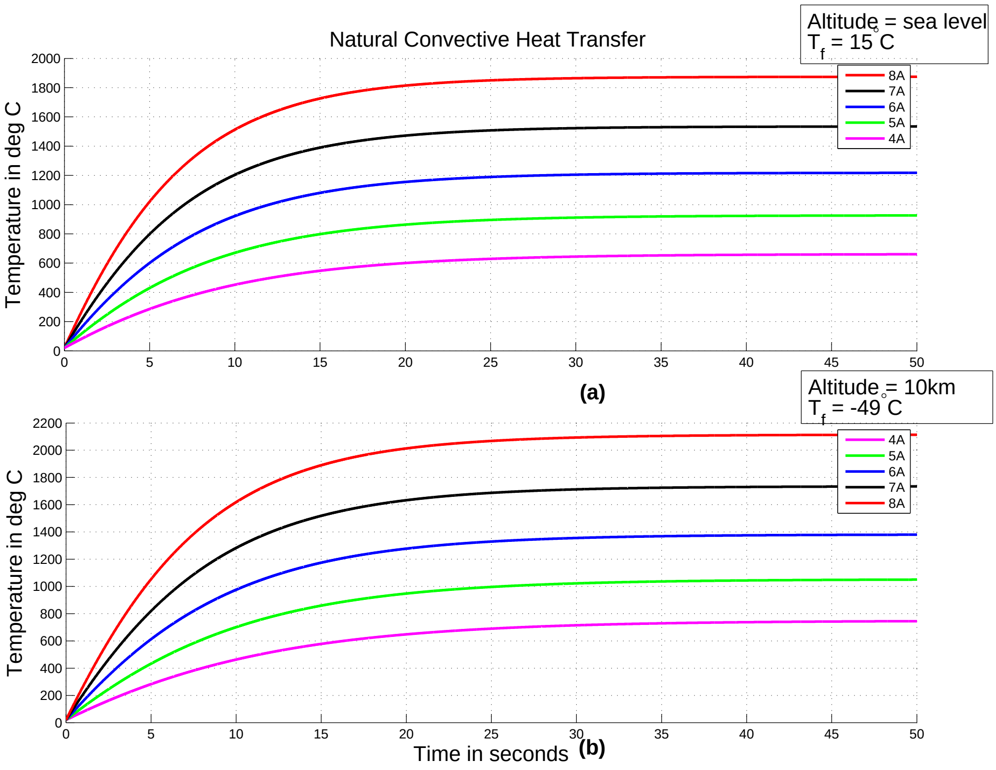

Figure 3.9 – Natural Convection: Sea level (a) , 10 000 m (b)

coefficients at higher altitudes, as explained in the forced convection case.

Table 3.2 shows the heat transfer coefficients and time constant for different wire diameters and various applied cooling mechanisms. The simulation results were conducted at sea level and at an altitude of 10 km. One can see a considerable increase in the heat transfer coefficient for a shift from natural to forced convection. The time constant of the heat transfer dynamics reduces considerably. This suggests the need for a forced convective cooling mechanism to ensure that the actuator can operate at an optimal rate. Note that the heat transfer coefficient deteriorates with increasing wire diameters. Applying a bundled actuator consisting of multiple smaller wires will thus respond quicker than a single larger SMA wire under the same convective conditions. Applying such a bundled configuration introduces various other mechanical uncertainties. Now that the basic heat transfer mechanism is better understood, some facts become clear. Forced convection is essential when the time response of the actuator is of importance, as the cooling rate governs the mechanical properties of the passive wire. Ideally a cooling mechanism able to extract energy from the wires individually would be required. Enclosing each wire in a tubular casing and rushing air through the tubing and over the wire is a possibility. In this thesis a more practical approach is applied by constantly cooling both wires simultaneously with the aid of a fan. This will not influence the rate of heating as any temperature can be obtained by simply increasing the input. High-altitude operation introduced the problem of reduced heat transfer. This can be overcome by an effective cooling mechanism, which will require increased cooling fluid speeds. The practical cooling implication for SMA actuators, especially at high altitudes, is still an undeveloped research area and poses unique challenges.

Diameter (mm)	Heat Transfer Coefficient ($\frac{W}{m^2K}$)			Time Constant (s)		
Altitude: Sea Level						
	Natural	Forced 10m/s	Forced 15m/s	Natural	Forced 10m/s	Forced 15m/s
0.5	35	460	557	8	0.5	0.46
1	28	318	384	20	1.6	1.35
2	21	220	265	50	4.9	3.9
Altitude: 10 000m						
0.5	30	246	297	9	1	0.8
1	20	170	205	26	2.5	2
2	15	117	141	72	8	7.3

Table 3.2 – Heat transfer coefficients & time constants at various wire diameters exposed to natural and convective heat transfer conditions

Chapter 4

Controller Design and Simulation

The following chapter presents the proposed controller designs for the SMA-based control surface actuator. In general a tracking control problem is considered in which the control surface is required to track a certain angular position trajectory. The SMA-based control surface actuator model, presented in Chapter 3, is applied in each controller design procedure. Four controller designs were considered.

- Conventional proportional-integral (PI) controller
- Inner-loop outer-loop PI controller with feed forward compensation
- Bang-bang type controller
- Feedback linearisation controller

The PI controller design is based on a linearised SMA control surface actuator model. Conventional proportional-integral-derivative (PID) feedback type controllers were encountered often in SMA actuator literature hence the choice off the first controller approach.

The inner-loop outer-loop PI controller with feed forward compensation is based on a simplified SMA control surface actuator model. This controller consists of an inner-loop PI controller to ensure temperature control. An outer-loop PI controller is applied in conjunction with the inner loop controller in order to ensure perfect tracking in the presence of model uncertainties. Feedforward compensation is introduced to speed up the transient response. This approach was taken to investigate the possibility of obtaining indirect deflection control by controlling the SMA temperature, the parameter driving actuation.

The bang-bang type controller applies an on-off approach. This controller approach is taken to serve as a benchmark as it should result in the fastest possible actuation.

Finally a non-linear controller design technique called feedback linearisation is presented. This model-based controller design was rarely encountered in literature and not yet applied to a deflection tracking problem. Each controller design is thoroughly presented accompanied by simulation results followed by a controller performance evaluation. The chapter starts by presenting a basic overview of control systems terminology followed by the controller design requirements and controller designs.

Basic control systems architecture

The following section will provide a short overview of control systems terminology to aid in the understanding of the control system designs to follow.

A control system can be any device that aims to influence the behaviour of a system in a preferred manner. Control systems are encountered in everyday life, from an autopilot on an airliner to the heating of a geyser. The system to which control is applied is usually referred to as the plant. The plant is driven by an input which results in a certain output. This pure input-output response is also known as the open-loop response. Theoretically a plant consists of mathematical relationships describing its dynamics. Knowing the plants dynamics enables one to apply various control techniques to ensure a desired output response. Control problems encountered can be classified as either a regulator or tracking control problem. A regulator control problem requires the plant to remain at a certain set point within acceptable limits, while a tracking problem requires the plant to follow a certain trajectory. The term "feedback control" is encountered frequently in any control systems literature. Feedback control applies feedback from sensors or mathematical models to determine the error between the desired output and the sensed output. This output error variable, e, is manipulated to determine the required input to the plant, depending on the control scheme, to achieve the desired output. When feedback control is incorporated into a system, its response is termed the closed-loop response. This is most clearly illustrated by the block diagram representation, a technique to visually illustrate the flow of information between a plant and its control system. A simple block diagram representation is shown in Figure 4.1. The measured output, y, is subtracted from the desired reference, r, which results in the output error, e. The output error serves as the input to the controller block, $D(s)$, which calculates the required input, u, to the plant, $G(s)$. Having clarified the basic terminology, the focus shifts to the development of the respective controllers.

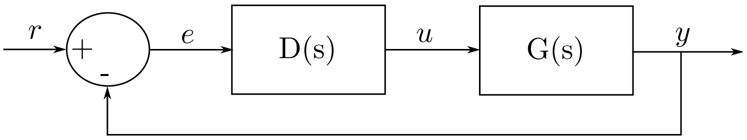

Figure 4.1 – Generic closed-loop block diagram

SMA controller design requirements

It is necessary to control the control surface deflection and obtain actuation in the fastest possible way without degrading the actuator's performance capability. It is preferred that the system be over-damped in order to avoid the dead zones inherent in the

SMA behaviour when approaching the set-point. An under-damped system will result in overshoot making it necessary to actuate the actuator in the opposite direction, which will result in the activation of the passive wire. The passive wire will most probably be in a dead zone, inducing unwanted lag in the actuator's response equivalent to the time required to move out of the dead zone. The controller effort, the power consumed during actuation, should also be considered. A maximum deflection range of $50°$ is required $25°$ in either direction. As the rate at which energy is removed from the system plays a vital role in the cyclic operability of the actuator a convective heat transfer medium is considered in all the controller designs except when mentioned otherwise.

SMA parameters

The SMA parameters used in all the control system designs and simulation results correspond to those applied in the Brinson model simulations, whilst the actuator dimensional parameters were those to be used in the practical setup. These parameters are shown in Table 4.1.

Parameter	Units	Magnitude	Symbol
density	$\frac{kg}{m^3}$	6450	ρ
Specific Heat Capacity	$\frac{J}{kgK}$	322	c_p
M_s	$°C$	18.4	M_s
M_f	$°C$	9	M_f
A_s	$°C$	34.5	A_s
A_f	$°C$	49	A_f
Martensite Resistivity	$\mu\Omega cm$	76	ρ_m
Austenite Resistivity	$\mu\Omega cm$	82	ρ_a
Martensite E	GPa	26.3	E_m
Austenite E	GPa	67	E_a
Maximum Residual Strain	%	0.05	ϵ_{pre}
C_m	$MPa/°C$	8	C_m
C_a	$MPa/°C$	13.8	C_a
σ_s^{cr}	MPa	100	σ_s^{cr}
σ_f^{cr}	MPa	170	σ_f^{cr}
Sink Temperature	$°C$	25	T_∞
Heat Transfer Coefficient	$\frac{W}{m^2K}$	50	h
$0°$ wire length	m	0.555	l_0
Wire Diameter	mm	0.508	D
Pulley Radius	mm	11	r

Table 4.1 – SMA mechanical parameters applied in simulation

4.1 Deflection Feedback PI Controller

A conventional PI controller was the first design approach investigated to obtain the necessary SMA control surface actuation. The PI controller would illustrate the inability of linear control techniques to yield sufficient performance in non-linear systems. Nonetheless it would result in a controller able to ensure performance within a certain design criteria. It is required to establish the boundaries within which the PI controller can perform. Performance will be measured for the following parameters, (i) settling time, (ii) percentage overshoot and (iii) the steady-state error.

4.1.1 Identifying the Linearisation Point

In order to apply conventional controller design techniques, such as PI control, to the SMA-based control surface actuator a linearised model was required. Because of the non-linearities and hysteresis inherent in SMAs the condition of the linearised model depended heavily on the linearisation point. A different linearised model would arise for different operating points, depending on whether the SMA is transforming to austenite, transforming to martensite or in a dead zone. To linearise the model about every possible operating condition is pointless as millions of different operating points can arise. It is therefore required to establish a single operating point to linearise the model about. The SMA control surface actuator should operate about, or as close as possible to this point for the majority of the actuation time in order to ensure the expected closed-loop response for the specific controller design. Drifting too far away from the linearisation point will result in the excitation of unmodelled dynamics resulting in unpredicted closed-loop behaviour. Having identified a suitable linearisation point the PI controller can be designed for the nominal linearised model and evaluated for various operating points in the vicinity of the linearisation point.

To identify a suitable operating point, multiple actuator open-loop responses were investigated. The purpose of the investigation was to develop a three-dimensional plot of the control surface deflection as a function of the top-and-bottom wire temperatures. Such a representation would give an indication of favourable operating regions and if any exist. The open-loop responses investigated considered heating the top wire of the actuator while keeping the bottom wire temperature constant throughout the top wire heating cycle. The bottom wire temperature would then be increased followed by the application of the exact same top wire heating cycle. By applying the above mentioned simulation, the following three-dimensional plot of deflection versus top and bottom wire temperatures, illustrated in Figure 4.2, could be constructed. The figure illustrates the top and bottom wire temperature combinations along with the resulting control surface deflection. Note that no direct time dependencies can be extracted from this diagram.

In order to explain the three-dimensional plane clearly a specific simulation case is considered. Consider a case in which both the top and bottom wire temperatures are at $25°$C. Heating the top wire will increase its temperature and the present condition will shift from the initial position [X:25 Y:25 Z:0] and eventually move to the final position [X:89.96 Y:25 Z:-22.62], which corresponds to a deflection of $-22.62°$, for a constant bottom wire temperature of $25°$C. Multiple temperature trends, for various initial conditions, can be obtained from this plane to visually illustrate the movement of the control surface. Note that the plane only illustrates the control surface deflection of a hea-

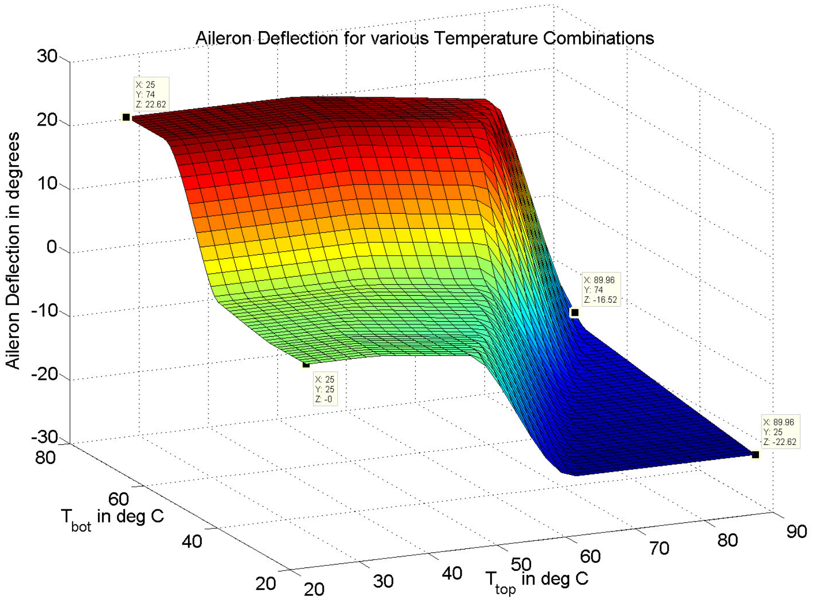

Figure 4.2 – The three-dimensional plot of deflection versus top and bottom wire temperatures

ting cycle for either the top or bottom wire for the specific initial conditions present at the start of the heating cycle. Various similar three-dimensional phase planes can be constructed for different initial de-twinned martensite fractions which is not illustrated here. No information about the cooling cycle can be obtained from the presented phase plane because of the SMA's inherent hysteresis. The cooling cycle will therefore follow a path not illustrated by the plane.

The non-linearity of the SMA control surface actuator is clearly visible in the presented three-dimensional plane. Four planes can be identified corresponding to the regions of the phase diagram presented in Chapter 2 and shown again in Figure 4.3 for explanatory purposes. These planes are indicated in Figure 4.4 by the black numbered text boxes. The condition of the current plane depends on the bottom-and-top wire temperatures.

In plane 1 on the 3D plot both bottom and top wires are in region 4 of the phase diagram. In region 4, the dead zone, no contraction or elongation has occurred and a constant zero aileron deflection is visible. This plane is unfavourable as no aileron actuation is achieved. This aspect clearly indicates a need for a minimum temperature in order to avoid the dead zone as it will hamper the actuating ability of the actuator.

In plane 2 on the 3D plot the active wire has entered region 2 of the phase diagram. The transformation to austenite starts, resulting in contraction, while the passive wire, still in region 4, is undergoing elastic deformation. The stiffness of the passive wire

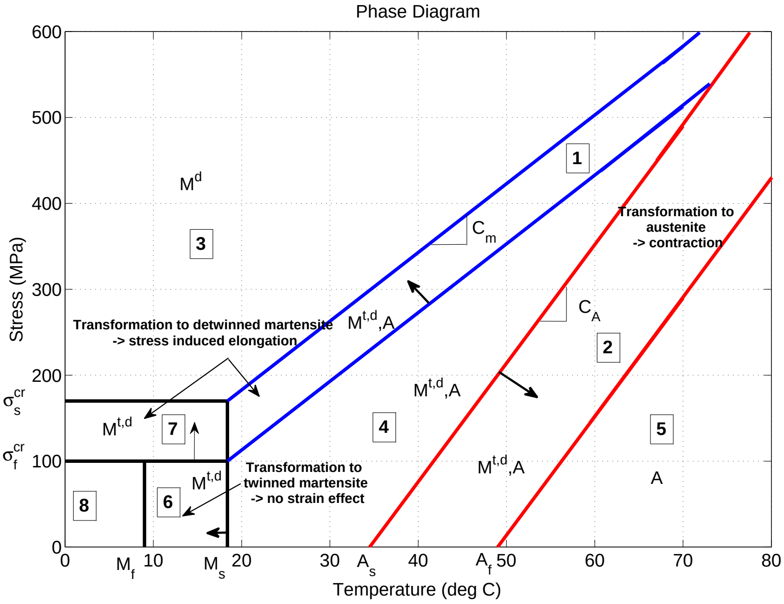

Figure 4.3 – SMA phase diagram

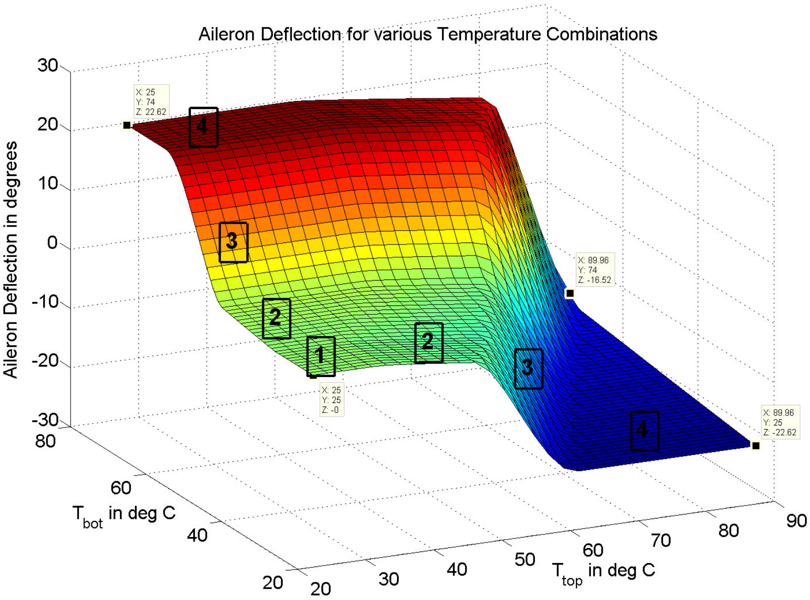

Figure 4.4 – The three-dimensional plot of deflection versus top and bottom wire temperatures with identified planes

is still relatively large at these low stresses causing the slow gradual movement of the control surface as indicated by the small slope of the plane.

In plane 3 on the 3D plot, the active wire is still contracting in region 2 of the phase diagram while the increase in stress has forced the passive wire to enter region 1. As the passive wire moves into region 1 the transformation to detwinned martensite causes the stiffness of the passive wire to decrease extensively causing a rapid change in aileron deflection. This plane illustrates a large actuation range for a rather small temperature range, labelling it as the most favourable plane to operate in. Another encouraging aspect of this plane upon inspection is its rather linear behaviour. This plane is a favourable candidate for the linearisation point.

In plane 4 on the 3D plot, the active wire has moved out of region 2 and into region 5 of the phase diagram where no more contraction is obtainable. The passive wire is in either region 1 or 3 depending on the maximum stress experienced during the process. The aileron thus settles at the maximum obtainable angle and cannot increase the deflection any further.

Although only one of the many hysteresis curves in the SMA control surface actuator has been presented in the three-dimensional phase plane, a general idea on the favourable areas of operation could be developed. The important detail concluded from this investigation can be illustrated by a top view of the created phase plane. This is shown in Figure 4.5. The top view illustrates a favourable region of operation indicated by the white oval. This region is favourable for its large control surface deflection range for a rather narrow temperature range. This region of operation coincides with the state at which the top wire is contracting, in region 2, while the bottom wire is detwinning, in region 1. It would be beneficial to operate the actuator within this vicinity as it would result in the maximum obtainable control surface deflection for the smallest temperature change. Operating in this regions will also improve the cyclic performance of the actuator due to the decrease in the dead zone size, between the transformation regions, at the increased stress levels.

The linearisation operating point is therefore chosen at a relatively large stress level where the respective austenite and detwinning transformations start. Ideally the initial detwinned martensite fraction should be 0.5 for both wires to ensure the same actuating potential in both directions. In order to achieve this initial de-twinned martensite state it is necessary to increase the stress in the wire gradually while increasing the temperature of both wires without causing either wire to enter the austenite transformation or detwinning zones. To practically achieve this state might prove difficult. One might apply a tensioning mechanism to increase the stress in both wires while increasing the temperatures gradually while keeping the control surface deflection at 0°. This process is illustrated in the phase diagram, Figure 4.6. Both wires start at identical initial conditions. The stresses are increased gradually, at a constant rate, while each wires temperature is increased. It would be necessary to heat the wires at different rates in order to achieve the required operating condition. The oval indicates the favourable

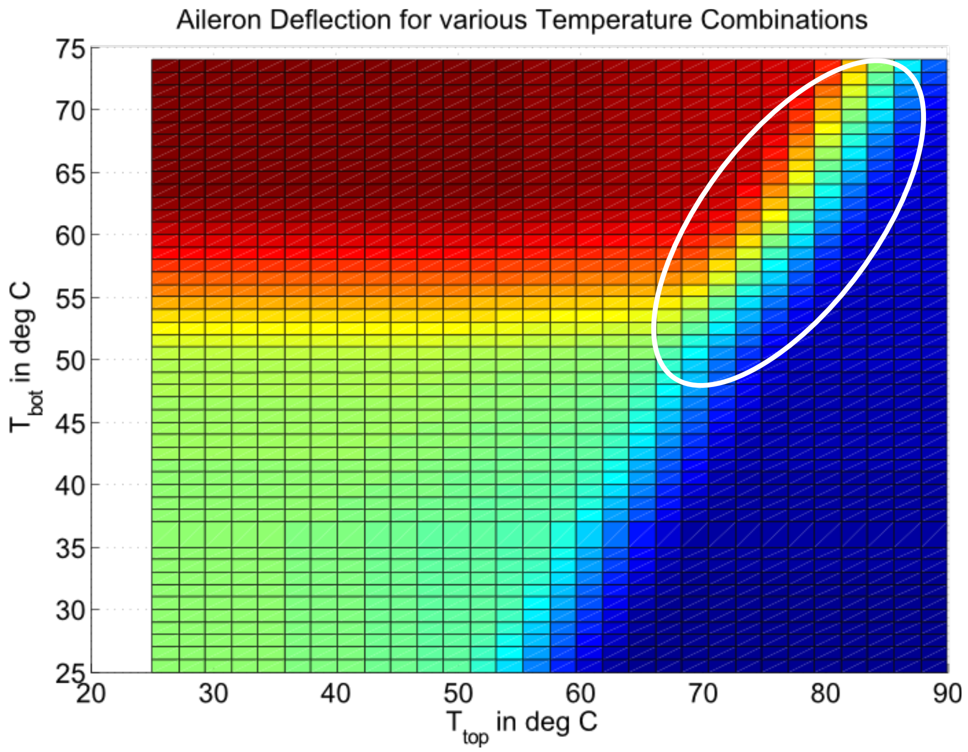

Figure 4.5 – Top view of three-dimensional phase plane illustrating the favourable operating region

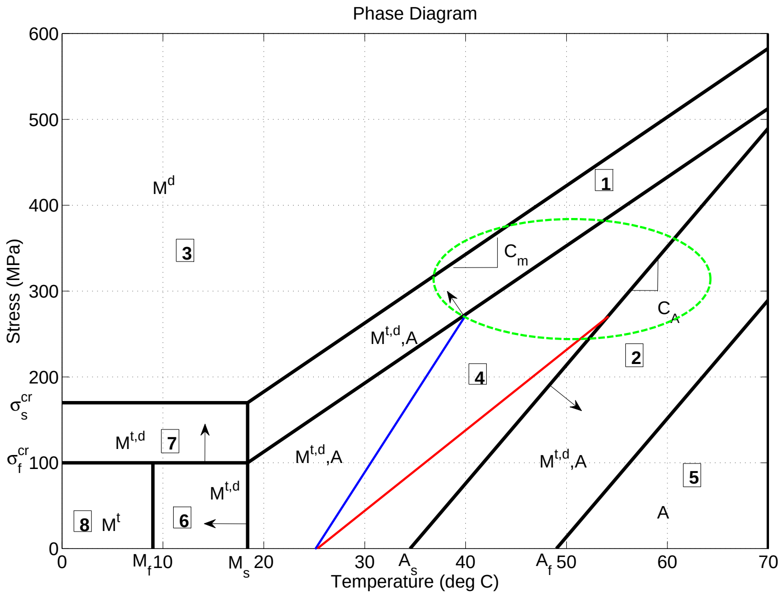

Figure 4.6 – Phase diagram illustrating the favourable operating region

region of operation. For the practical implementation this procedure will not be applied as the designed actuator configuration does not allow the ability to mechanically tension the wires. Nonetheless this state will be assumed obtainable and will serve as the linearisation point for the PI controller design. The material parameters decided upon for the identified linearisation point is shown in Table 4.2.

Parameter	Units	Magnitude
σ_{t0}	MPa	272
σ_{b0}	MPa	272
$\xi_{s0_{t0}}$	dimensionless	0.5
$\xi_{s0_{b0}}$	dimensionless	0.5
T_{t0}	$^\circ C$	40
T_{b0}	$^\circ C$	54.3

Table 4.2 – Linearisation parameters

4.1.2 Linearised PI Controller Design

In order to commence with the controller design a linearised model representation is required. This is achieved by identifying the non-linearities in the model and linearising it about a fixed operating point. The SMA non-linearities are present in the transformation kinetics. In order to relieve the model from these non-linearities the transformation kinetics where linearised with respect to its dependents, stress and temperature, as shown in equation 4.1.1.

$$\xi_s = \xi_s(T_0, \sigma_0) + \frac{\partial \xi_s}{\partial T}\Big|_{T_0,\sigma_0}(T - T_0) + \frac{\partial \xi_s}{\partial \sigma}\Big|_{T_0,\sigma_0}(\sigma - \sigma_0) \tag{4.1.1}$$

Applying the linearisation on equation 3.2.11 resulted in the following,

$$\xi_s = \xi_{s0} + f_1 \times (T - T_0) + f_2 \times (\sigma - \sigma_0) \tag{4.1.2}$$

with the functions f_1 and f_2 defined in equations 4.1.7 and 4.1.8. Equation 4.1.2 could further be simplified to perturbation state format where the zero subscript indicates the linearisation point for the various parameters,

$$\Delta\xi_s = f_1 \Delta T + f_2 \Delta\sigma \tag{4.1.3}$$

with,

$$\Delta\xi_s = \xi_s - \xi_{s0} \tag{4.1.4}$$

$$\Delta T = T - T_0 \tag{4.1.5}$$

$$\Delta\sigma = \sigma - \sigma_0 \tag{4.1.6}$$

and,

$$f_1(\xi_{s0}, \sigma_0, T_0) = \left\{ \begin{array}{c} \frac{\xi_{s0}-1}{2} sin(b_M(\sigma - \sigma_f^{cr} - C_m(T - M_s)))b_M \\ \text{for } M_{t,s}, A- > M_s \\ \frac{\xi_{s0}}{2} sin(a_A(T - A_s - \frac{\sigma}{C_a}))\frac{a_A}{C_a} \\ \text{for } M_{t,s}, A- > A \\ 0, \text{ otherwise} \end{array} \right\} \tag{4.1.7}$$

$$f_2(\xi_{s0}, \sigma_0, T_0) = \left\{ \begin{array}{c} \frac{\xi_{s0}-1}{2} sin(b_M(\sigma - \sigma_f^{cr} - C_m(T - M_s)))b_M C_m \\ \text{for } M_{t,s}, A- > M_s \\ \frac{\xi_{s0}}{2} sin(a_A(T - A_s - \frac{\sigma}{C_a}))a_A \\ \text{for } M_{t,s}, A- > A \\ 0, \text{ otherwise} \end{array} \right\} \tag{4.1.8}$$

Having linearised the transformation kinetics equation 4.1.3 could be substituted into the perturbation state format of equation 3.2.8. The perturbation state format equation and result of substitution are shown below.

$$\Delta\sigma = E\Delta\epsilon + \Omega\Delta\xi_s \tag{4.1.9}$$

$$\Delta\sigma = \frac{E\Delta\epsilon - \Omega f_2 \Delta T}{1 - \Omega f_1} \tag{4.1.10}$$

Equation 4.1.10 could further be simplified by substituting the perturbation state format of the actuator kinematics, equations 3.2.15 and 3.2.16, which resulted in the two linearised perturbation state format relationships for the stress in the respective top and bottom SMA wire.

$$\Delta\sigma_t = \frac{\frac{2rE}{l_0}\Delta\delta_t - \Omega f_{2t}\Delta T_t}{1 - \Omega f_{1t}} \tag{4.1.11}$$

$$\Delta\sigma_b = \frac{-\frac{2rE}{l_0}\Delta\delta_t - \Omega f_{2b}\Delta T_b}{1 - \Omega f_{1b}} \tag{4.1.12}$$

Substituting equations 4.1.11 and 4.1.12 into the perturbation state format of the actuator dynamics, equation 3.2.4, would result in the following linearised second order differential.

$$I\Delta\ddot{\delta}_t + B\Delta\dot{\delta}_t + g(\Delta\delta_t) = 2rA_c(\Delta\sigma_b - \Delta\sigma_t) \tag{4.1.13}$$

By substituting equations 4.1.11 and 4.1.12 into equation 4.1.13 a linearised dynamic relationship is obtained which relates the control surface deflection to the respective top and bottom SMA wires temperatures. The final linearised representation is shown below,

$$I\Delta\ddot{\delta}_t + B\Delta\dot{\delta}_t + g(\Delta\delta_t) = Z_1\Delta\delta_t + Z_2\Delta T_b + Z_3\Delta T_t \tag{4.1.14}$$

with.

$$Z_1 = \frac{\frac{-4r^2A_cE}{l_0}(2 - \Omega(f_{1t} + f_{1b}))}{(1 - \Omega f_{1b})(1 - \Omega f_{1t})} \tag{4.1.15}$$

$$Z_2 = \frac{-2rA_c\Omega f_{2b}}{1 - \Omega f_{1b}} \tag{4.1.16}$$

$$Z_3 = \frac{2rA_c\Omega f_{2t}}{1-\Omega f_{1t}} \tag{4.1.17}$$

The linearised actuator dynamics, equation 4.1.14, could be used to develop a state space representation, in perturbation state format, as shown below. The need for the perturbation state format is also to accommodate some of the states that are non-zero at the linearisation point.

$$\underbrace{\begin{bmatrix} \Delta\ddot{\delta}_{tab} \\ \Delta\dot{\delta}_{tab} \\ \Delta\dot{T}_{top} \\ \Delta\dot{T}_{bot} \end{bmatrix}}_{\dot{X}} = \underbrace{\begin{bmatrix} -\frac{B}{I} & \frac{Z_1}{I} & \frac{Z_3}{I} & \frac{Z_2}{I} \\ 1 & 0 & 0 & 0 \\ 0 & 0 & C1 & 0 \\ 0 & 0 & 0 & C1 \end{bmatrix}}_{F} \underbrace{\begin{bmatrix} \Delta\dot{\delta}_{tab} \\ \Delta\delta_{tab} \\ \Delta(T_{top}-T_\infty) \\ \Delta(T_{bot}-T_\infty) \end{bmatrix}}_{X} + \underbrace{\begin{bmatrix} 0 & 0 \\ 0 & 0 \\ C_2 & 0 \\ 0 & C_2 \end{bmatrix}}_{G} \underbrace{\begin{bmatrix} \Delta u_1 \\ \Delta u_2 \end{bmatrix}}_{U}$$

$$\Delta y = \underbrace{\begin{bmatrix} 0 & 0 & 0 & 0 \\ 0 & 1 & 0 & 0 \\ 0 & 0 & 1 & 0 \\ 0 & 0 & 0 & 1 \end{bmatrix}}_{H} \begin{bmatrix} \Delta\dot{\delta}_{tab} \\ \Delta\delta_{tab} \\ \Delta(T_{top}-T_\infty) \\ \Delta(T_{bot}-T_\infty) \end{bmatrix}$$

with,

$$u_1 = I_{top}^2$$

$$u_2 = I_{bot}^2$$

Having established a linearised state space model the controller design could commence. The block diagram of the closed loop system is illustrated in Figure 4.7 indicating the feedback loop. A certain reference, r, serves as an input to the system. In this case the required control surface deflection will serve as the command variable. The error, e, between the reference command and the actual control surface deflection is then fed into the PI controller block, D(s). The controller block determines the required input, u, which serves as the input to the plant, G(s), which then results in an output control surface deflection, y. The transfer function of the linearised plant about the linearisation point is presented next. For the linearisation the bottom wire is considered active while the top wire will operate passively. The state space representation was converted to a transfer function relating the input, the current squared supplied to the bottom wire, to the output, the control surface deflection.

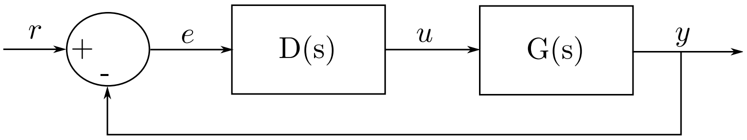

Figure 4.7 – Closed-loop SMA actuator block diagram with PI controller

$$G(s) = \frac{Y(s)}{U(s)} = \frac{2565}{(s+304)(s+82)(s+0.95)} \tag{4.1.18}$$

The linearised system transfer function shown in equation 4.1.18 consists of three real poles. The poles consist of a pole relatively far to the left in the left half plane and two poles closer to the origin. The two poles far to the left in the left half plane represents the spring-damper dynamics, as a result of the systems frictional damping and torsional stiffness, of the antagonistic wires connected to the control surface while the slowest pole is in fact induced by the temperature dynamics of the active wire. The root locus plot of the transfer function is shown in Figure 4.8. The real pole far to the left in the left half plane is not shown in the figure, but will be non-dominant since it's dynamics are much faster than the other two poles. The root locus shows the closed-loop poles as a function of gain if proportional feedback is used. The specific closed-loop poles indicated on the root locus are for a unity gain. The open-loop poles dominating the closed-loop dynamics of the system are the two poles situated near the origin. The root locus around the dominant poles departs from each pole, heads towards each other, and meets halfway after which the root locus departs from the real axis and tends to the right half plane. Increasing the gain would result in instability as the dominant closed-loop poles shifts to the right half plane illustrating that a pure proportional controller would be insufficient. A pure proportional controller would also result in a steady state error and unrealisable high input requirements in order to achieve a small steady state error.

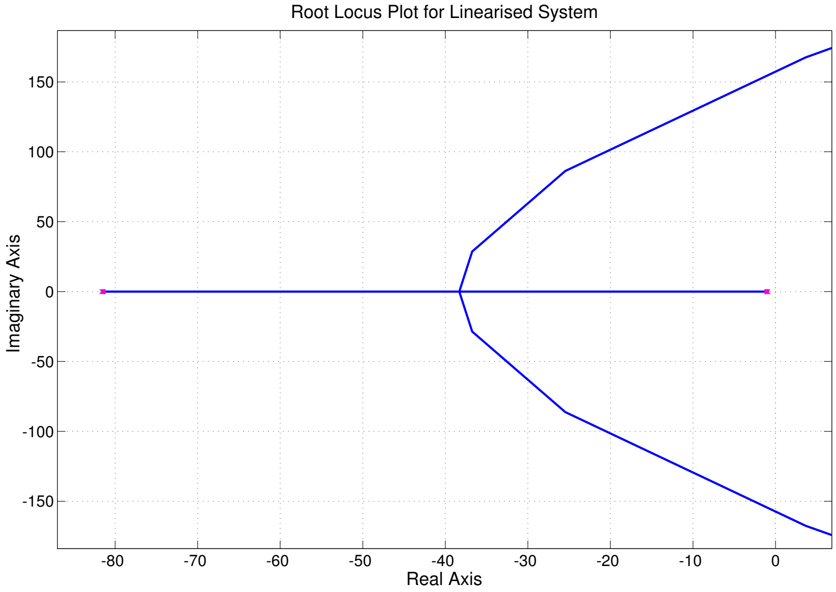

Figure 4.8 – Linearised models root locus plot indicating the dominant open-loop poles

The open-loop pole limiting the closed-loop dynamics of the actuator is the one closest to the origin. From previous investigations it was found that this pole is in fact the pole introduced by the temperature dynamics of the active wire. By applying proportional feedback control a large unwanted steady state error and overshoot will arise stressing the requirement for another approach. It is therefore decided to introduce a PI controller resulting in a zero in the vicinity of the temperature pole to cancel its effect, and an integrator at the origin to ensure perfect tracking. The proportional term is determined based on the required settling time. The PI controller format is shown in equation 4.1.19 along with its Laplace format in equation 4.1.20.

$$u(t) = K[e(t) + \frac{1}{T_I}\int_0^t e(t)dt] \tag{4.1.19}$$

$$D(s) = \frac{u(s)}{e(s)} = K(1 + \frac{1}{T_I s}) \tag{4.1.20}$$

Where K is the position feedback gain and T_I the integral time. The closed loop poles, for a 1 second settling time and critically damped system requirements achieved by introducing such a controller is illustrated by the root locus plot in Figure 4.9. The dominant closed loop pole limiting the transient response is situated at approximately -4 on the real axis. Applying this controller about the linearisation point will ensure an over damped response with perfect tracking. For a settling time requirement of 1 second and critically damped response the following controller gains arise.

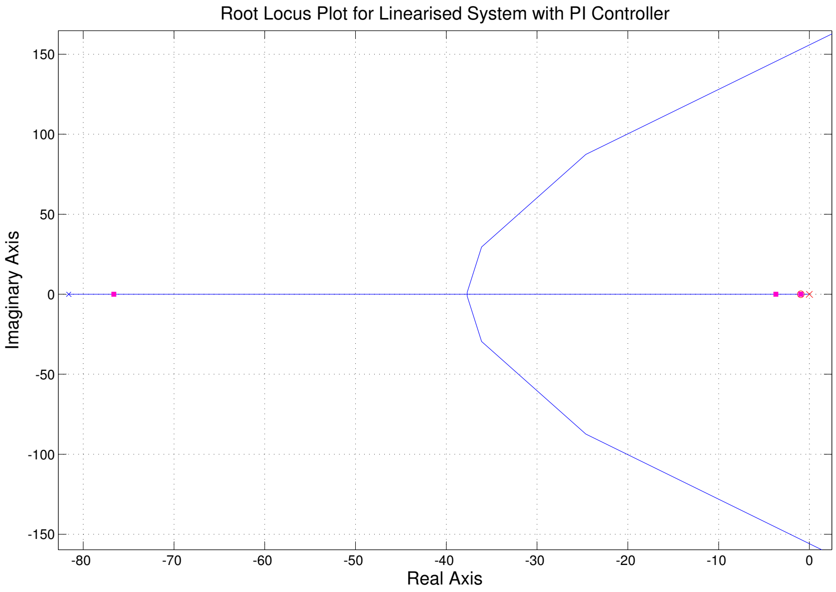

Figure 4.9 – Linearised models root locus plot indicating the dominant closed-loop poles

$$K = 32$$

$$T_I = 1.1$$

It is required to evaluate the response of the designed PI controller on the SMA control surface actuator to determine the controllers effectiveness and validity.

4.1.3 PI Controller Simulation Results

The PI controller was added to the SMA control surface actuator simulation model and simulations were performed to evaluate its performance. The PI controller is evaluated for small perturbations from the linearisation point to validate the controller design procedure after which the controller response at the extremes, the maximum required deflections, are evaluated. In order to evaluate the controllers performance at the extremes of operation the system is linearised about these extremes in order to determine the new open loop poles. The designed controller is then applied to the new open loop system to investigate the change in the closed loop poles of the system. In order to determine the linearisation parameters of the plant, at the extremes, the closed loop system is commanded to the extremes, from the initial linearisation point, through simulation.

PI controller under small perturbations

Figure 4.10a shows the closed loop response of the control surface actuator in conjunction with the PI controller for a small control surface step command of 1°. From closer inspection a 2% settling time of 1.12s is achieve as opposed to that of 1s as designed for. An overdamped response as well as a zero steady state error is achieved as expected from the controller design. The results shown in Figure 4.10a shows that the designed PI controller does in fact ensure the expected response at small perturbations in the vicinity of the linearisation point. Figure 4.10b shows the inputs to the respective wires indicating a smooth input requirement for the bottom wire.

Figure 4.11 shows the change in states for the specific step response from the linearisation point. Figure 4.11a shows the change in temperature while Figure 4.11b shows the change in the stress present in both wires. Figure 4.11c shows the symmetric change in strain while Figure 4.11d shows the change in the detwinned martensite fraction for each wire. Figure 4.11 illustrates the small perturbations of the stress and temperature states from the linearisation point parameters which ensures the relative accuracy of the controller. Having illustrated successful small perturbation responses the focus shifts to larger perturbation requirements.

PI controller response at large perturbations

In order to investigate the performance of the PI controller at large perturbations the plant was re-linearised at control surface deflections of 25° and -25° respectively, the two extreme deflection requirements, in order to investigate the change in closed-loop dynamics in conjunction with the designed controller. The re-linearisation parameters were obtained by commanding the actuator model to a control surface of 25° and thereafter to -25°, from the initial linearisation point, and taking the parameters at the state were the respective deflections were reached.

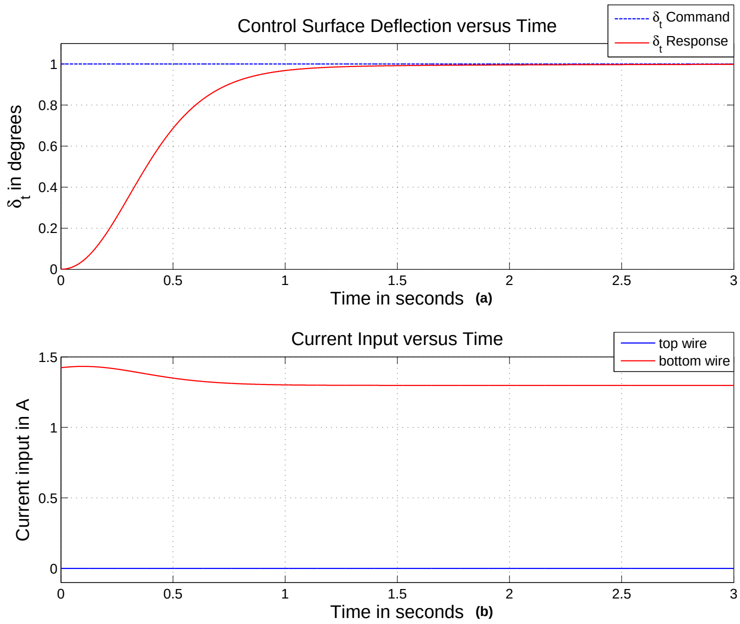

Figure 4.10 – Closed-loop PI controller response for a unity step command; (a) Deflection response; (b) Input requirement response

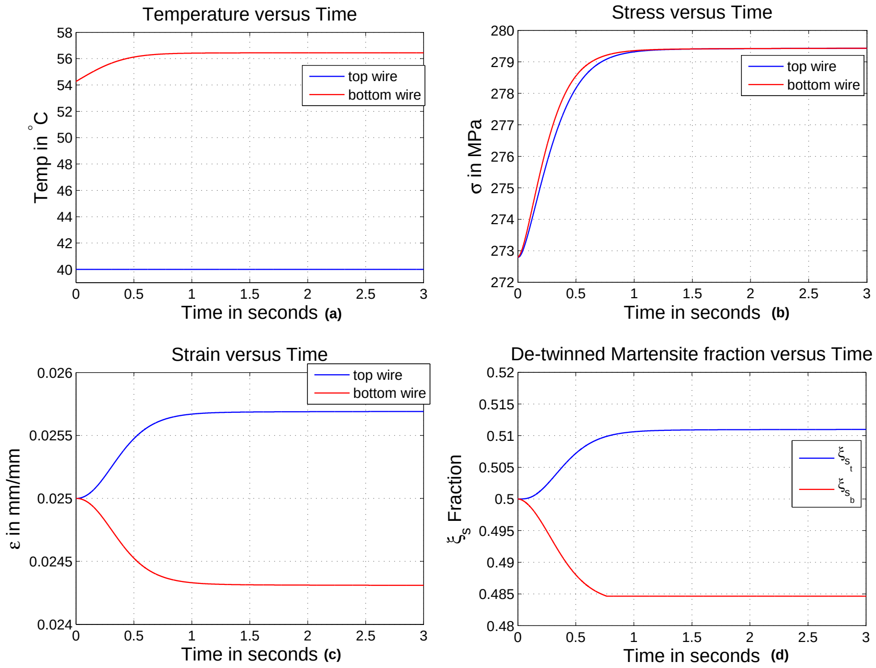

Figure 4.11 – PI controller states for a unity step command ; (a) Temperature response ; (b) Stress response ; (c) Strain response ; (d) Detwinned martensite response

Figure 4.12a shows the transient response of the actuator for the extreme control surface commands from the initial linearisation point conditions. Different than for small perturbations the transient response illustrates a large amount of overshoot , approximately 15% for the $25°$ command and 20% for the $-25°$ command, and a settling time larger than 5 seconds. The change in control surface deflection at about 2.5 and 8.5 seconds is as a result of the previously active wire cooling and entering the detwinning stage resulting in the gradual stress relaxation within the wire. The corresponding current inputs are shown in Figure 4.12b indicating an input saturation of 3 amperes followed by a gradual decrease in input for both commands. The obtained response illustrates the shortcomings of applying the designed PI controller at large perturbations without using active cooling . The unwanted overshoot illustrates the need for the passive wire to be actuated in order to obtain actuation in the opposite direction as the cooling of the previously active wire is not sufficient to ensure the required actuation rate in the opposite direction. The overshoot also induces an unwanted lag in the system as a result of the integrator present in the controller. An anti-windup component needs to be incorporated to compensate for this effect.

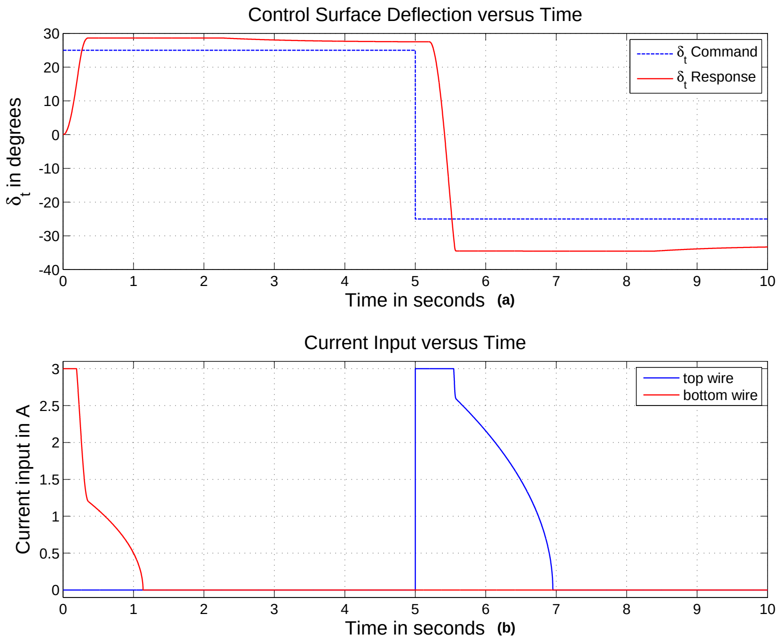

Figure 4.12 – Closed-loop PI controller response for large perturbations ; (a) Deflection response; (b) Input requirements response

In order to understand the response obtained at large perturbations the change in the open-loop poles of the plant for both extremes were investigated. The system was re-linearised at the control surface deflection of $25°$ and $-25°$ respectively after which the open loop transfer functions could be determined as shown in equations 4.1.21 and 4.1.22 for the extreme positive and negative commands respectively.

$$G(s) = \frac{Y(s)}{U(s)} = \frac{2680}{(s+373)(s+0.95)(s+13)} \tag{4.1.21}$$

$$G(s) = \frac{Y(s)}{U(s)} = \frac{2600}{(s+368)(s+0.95)(s+18)} \tag{4.1.22}$$

Note that the middle pole is considerably slower that its counterpart at the linearisation point. The generic linearised transfer function is shown to aid in determining the reason for this change.

$$G(s) = \frac{Y(s)}{U(s)} = \frac{\frac{Z_2}{I}}{(s^2 + \frac{B}{I}s - \frac{Z_1}{I})} \tag{4.1.23}$$

The only changeable term in the characteristic equation is the $\frac{Z_1}{I}$ term. The Z_1 term, shown in equation 4.1.15, depends on the f_1 and f_2 functions which in turn depends on the magnitude of the martensite transformation in the respective wires. These transformations directly affect the torsional stiffness of the system when referring to equation 4.1.14, the actuator dynamics. A change in the torsional stiffness will result in a change in the un-damped natural frequency and therefore the damping ratio of the system. The fairly complete transformations, which are brought about by large control surface deflection requirements, are the direct cause for the change in the open-loop system poles.

Equations 4.1.21 and 4.1.22 clearly indicate different linearised transfer functions than that obtained at the linearisation point. There still exists three real poles. Similarly than at the linearisation point the two open-loop poles dominating the closed-loop poles are the two closest to the origin with the identical open-loop temperature pole still limiting the systems closed-loop transient response. Applying the same controller to the linearised models resulted in the following dominant closed loop poles as indicated by the root locus plots in Figure 4.13a and 4.13b respectively. Figure 4.14 clearly indicates the reason for the experienced overshoot. The shift in the open-loop pole positions result in the dominating closed loop poles moving away from the real axis and resulting in a conjugate pole pair. An expected overshoot of approximately 13.5%, very close to the overshoot of 15% experienced in the simulation for the $25°$ command, is predicted by the root locus plot. The expected overshoot for the $-25°$ command is approximately 24%, also very close to the overshoot of 20% as experienced in the simulation. The findings above clearly illustrates the shortcomings of one wire control versus two wire control. It was shown that the designed controller is able to perform as designed for small perturbation in the vicinity of the linearisation point. At large perturbations however, the closed loop system exhibits a large amount of overshoot and a quicker rise time than expected. The overshoot and uncertainty in the model behaviour at large perturbations for the designed PI controller requires the need for a on-off approach in order to apply the PI controller effectively. As soon as unwanted overshoot occurs the active wire will switch to passive and vice versa in order to minimise the overshoot. In doing so the PI controller will ensure better performance for large perturbations. When nearing the

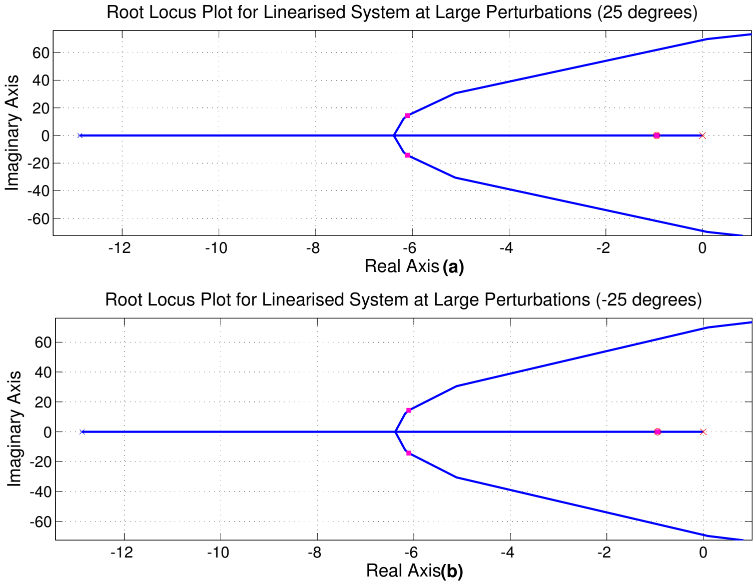

Figure 4.13 – Linearised systems root locus plot for large perturbations; (a) Dominating closed-loop poles for a maximum command of 25°; (b) Dominating closed-loop poles for a maximum command of -25°

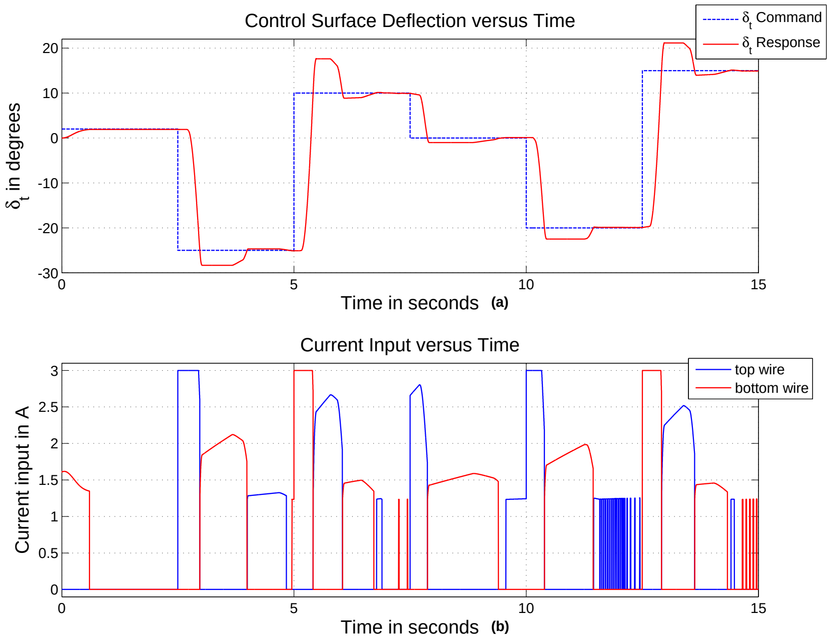

Figure 4.14 – Closed-loop PI controller response to a variable step command ; (a) Deflection response; (b) Input requirements response

required set point the on-off approach might result in excessive control effort, switching the active state between the top-and-bottom wires in order to keep the control surface at the required set-point. This will result in an unwanted increase in both wire temperatures and in effect increase the stresses in both wires which will hinder further actuation and increase the chance of overheating the wires. In order to account for this effect both wire inputs will be set to zero when the control surface deflection is near the required set-point. This will result in both wire temperatures cooling down ensuring future actuation.

In order to illustrate the effect of the modifications applied in conjunction with the PI controller the SMA-based control surface actuator model was put through a random series of control surface deflection step responses. The transient response obtained by such a simulation is shown in Figure 4.14a. The transient response clearly indicates the ability of the controller to deliver the expected response for small perturbations, as illustrated by the first step response, followed by the expected overshoot at larger perturbation requirements. The required set point is met in all the step responses although not at the designed settling time of 1 second. Figure 4.14b shows the inputs for the required control surface trajectory. For the last two step responses the controller is switched between the on and of state continuously resulting in the input spikes in order to keep the control surface deflection at the required set point. Figure 4.15 captures the change in temperature, stress and strain states as well as the detwinned

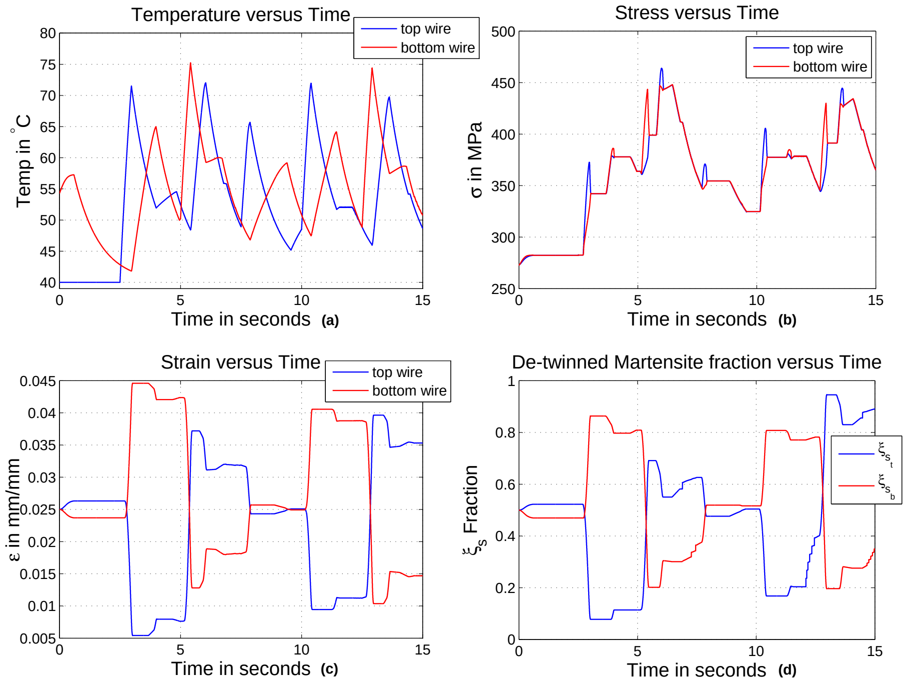

Figure 4.15 – PI controller states for a variable step command ; (a) Temperature response ; (b) Stress response ; (c) Strain response ; (d) Detwinned martensite response

martensite fraction for the required control surface trajectory. Finally the stress temperature relationship for the respective wires is shown in the phase diagram in Figure 4.16. The reason for illustrating this cluttered relationship is to indicate that the region of operation is in fact reasonably within the operating oval as identified in Figure 4.6.

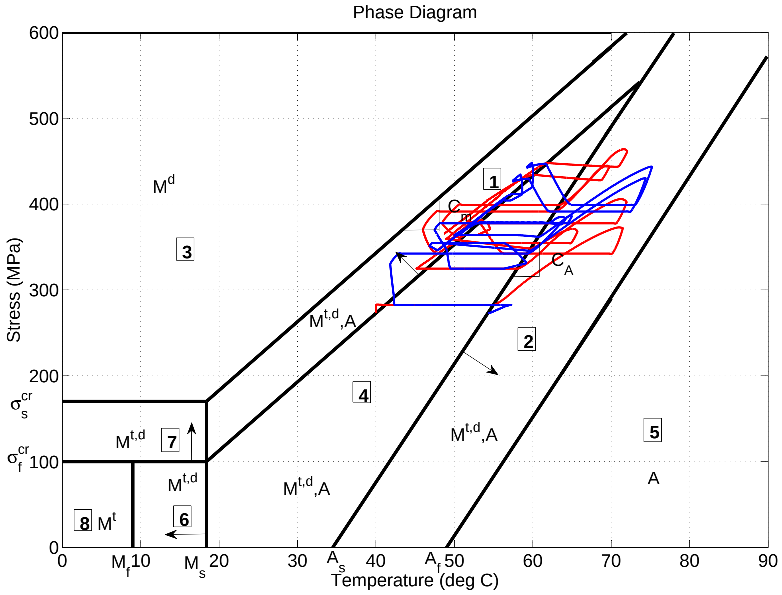

Figure 4.16 – Phase diagram indicating region of operation

In this subsection a PI controller was designed which illustrated satisfactory performance for small perturbations from the identified linearisation point. The PI controller however struggled to perform as designed for large perturbations and illustrated unwanted overshoot of up to approximately 23%. A zero steady state error was eventually achieved although not at the required rate. In order to improve the PI controller a few adjustments were made as mentioned above. This resulted in an improved PI controller performance. After applying the adjustments the required 1 second settling time was obtainable at small perturbations but increased up to three folds for larger perturbations.

This concludes the design and evaluation of the PI controller able to ensure control surface command tracking although not at the required specifications.

4.2 Deflection and Temperature Control with Feedforward Compensation

The fact that the actuator driving force is governed by a temperature change within the SMA wires led to the choice of controller approach considered in this section. Rather than to solely apply deflection feedback, the controller design incorporates an inner-loop temperature feedback PI controller to obtain the required deflection. An outer-loop integral controller is applied in conjunction with the inner-loop temperature controller to ensure adequate tracking. The integral controller degrades the closed-loop transient response considerably which is compensated for by means of a feedforward component. The feedforward component is calculated online by means of a simplified SMA actuator model. The proposed block diagram architecture is shown in Figure 4.17. The simplified modelling approach aims to relieve some of the non-linearities in the system by replacing the sinusoidal transformation kinetics with linear representations. Firstly the simplified model is presented. The inner-loop temperature controller design is presented next, followed by the outer-loop integral controller design in conjunction with the feedforward controller. The controller designs are followed by closed-loop simulation results illustrating the controller response. The section is concluded by evaluating the following controller performance parameters: (i) settling time, (ii) percentage overshoot and (iii) the steady-state error.

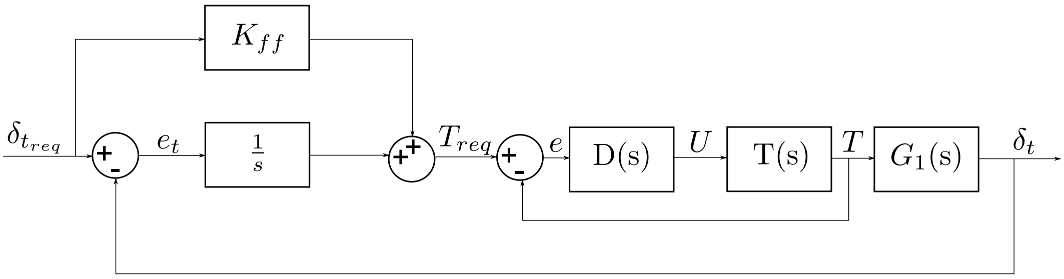

Figure 4.17 – Proposed temperature controller block diagram architecture

4.2.1 Simplified Modelling Approach

As mentioned above a simplified model is obtained by replacing the non-linear transformation kinetics, as shown in equation 3.2.11, with linear approximations. A simplified modelling approach will ensure less computational effort and easier controller design in exchange for degraded system modelling.

The phase diagram was implemented as a tool to aid in the development of the simplified functions. Figure 4.18 is a section of the phase diagram illustrating the phase transformation from a fully twinned ($\xi_s = 0$) to a fully detwinned ($\xi_s = 1$) martensite composition. It is required to describe this transformation using a linear representation. Consider a partial transformation, from T_0 to T_{cur}, where T_{cur} is the current temperature T, and a completed transformation, from T_0 to T_1, as illustrated in Figure 4.18. The current state of transformation can sufficiently be described by equation 4.2.1, the current transformation state as a fraction of the complete transformation.

$$\frac{T_0 - T_{cur}}{T_0 - T_1} \tag{4.2.1}$$

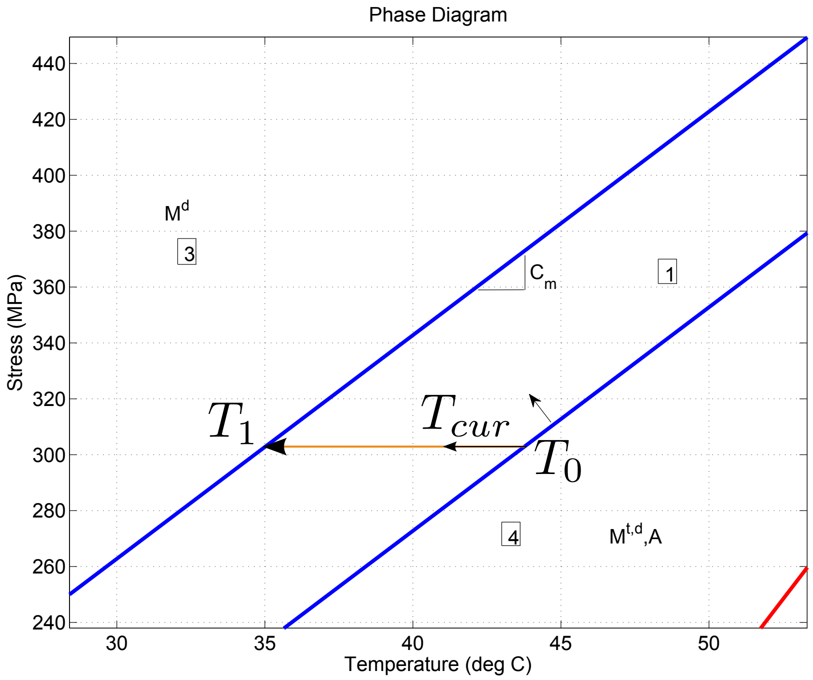

Figure 4.18 – Simplified model development

Integrating the memory variable ξ_{s0} into equation 4.2.1 results in the following linear representation for the de-twinning process.

$$\xi_s = (1-\xi_{s0})\frac{T_0 - T_{cur}}{T_0 - T_1} + \xi_{s0} \tag{4.2.2}$$

Thus at half a transformation and $\xi_{s0} = 0$ the detwinned martensite fraction will be the following,

$$\xi_s = (1-0)(0.5) + 0 = 0.5$$

as expected. This relationship can further be expanded by substituting the relationship for T_0 and T_1, the equations for the respective de-twinning transformation curves, as presented by the Brinson model into equation 4.2.2. The transformation curve relationships are shown below.

$$T_0 = \frac{\sigma - \sigma_s^{cr}}{C_m} + M_s \tag{4.2.3}$$

$$T_1 = \frac{\sigma - \sigma_f^{cr}}{C_m} + M_s \tag{4.2.4}$$

Substituting the transformation curves, equations 4.2.3 and 4.2.4, into equation 4.2.2 and knowing $T_{cur} = T$ resulted in the newly identified linear transformation relationship relating the de-twinned martensite fraction to the stress, temperature and initial de-twinned martensite fraction for a de-twinning process.

$$\xi_s = (1-\xi_{s0})\frac{\frac{\sigma-\sigma_s^{cr}}{C_m} + M_s - T}{\frac{\sigma_f^{cr}-\sigma_s^{cr}}{C_m}} + \xi_{s0} \tag{4.2.5}$$

The same procedure was applied to a heating transformation and resulted in the following relationship relating the de-twinned martensite fraction to the stress, temperature and initial de-twinned martensite fraction for a austenite transformation.

$$\xi_s = \xi_{s0} \frac{T - (\frac{\sigma}{C_a} + A_f)}{A_s - A_f} \tag{4.2.6}$$

By combining equations 4.2.5 and 4.2.6 a new set of transformation kinetics could be developed as shown in equation 4.2.7.

$$\xi_s = \left\{ \begin{array}{c} \xi_s = (1 - \xi_{s0}) \frac{\frac{\sigma - \sigma_s^{cr}}{C_m} + M_s - T}{\frac{\sigma_f^{cr} - \sigma_s^{cr}}{C_m}} + \xi_{s0} \\ \text{for } M_{t,s}, A- > M_s \\ \xi_s = \xi_{s0} \frac{T - (\frac{\sigma}{C_a} + A_f)}{A_s - A_f} \\ \text{for } M_{t,s}, A- > A \\ \xi_{s0}, \text{ otherwise} \end{array} \right\} \tag{4.2.7}$$

Which if simplified could be presented in the following format.

$$\xi_s = f_1 \sigma + f_2 T + f_3 \tag{4.2.8}$$

With,

$$f_1(\xi_{s0}) = \left\{ \begin{array}{c} \frac{1 - \xi_{s0}}{8.75 C_m} \\ \text{for } M_{t,s}, A- > M_s \\ \frac{-\xi_{s0}}{C_a (A_s - A_f)} \\ \text{for } M_{t,s}, A- > A \\ 0, \text{ otherwise} \end{array} \right\} \tag{4.2.9}$$

$$f_2(\xi_{s0}) = \left\{ \begin{array}{c} \frac{\xi_{s0} - 1}{8.75} \\ \text{for } M_{t,s}, A- > M_s \\ \frac{\xi_{s0}}{A_s - A_f} \\ \text{for } M_{t,s}, A- > A \\ 0, \text{ otherwise} \end{array} \right\} \tag{4.2.10}$$

$$f_3(\xi_{s0}) = \left\{ \begin{array}{c} (1 - \xi_{s0}) \frac{M_s - \frac{\sigma_s^{cr}}{C_m}}{8.75} + \xi_{s0} \\ \text{for } M_{t,s}, A- > M_s \\ -\xi_{s0} \frac{A_f}{A_s - A_f} \\ \text{for } M_{t,s}, A- > A \\ \xi_{s0}, \text{ otherwise} \end{array} \right\} \tag{4.2.11}$$

Eliminating the sinusoidal functions in the transformation kinetics enabled the creation of the above shown set of linear transformation kinetics which could be applied to establish a simplified linear actuator model.

4.2.2 Temperature Controller Design

The first step in the controller development was the inner-loop temperature controller design. Figure 4.19 illustrates the inner-loop temperature controller block diagram representation with $G_2(s)$, the transfer function relating the temperature, T, to the current squared input, U, and $G_1(s)$, the transfer function relating the temperature, T, to the control surface deflection, δ_t. Recalling the temperature dynamics, shown in equation 3.2.5, $G_2(s)$ could be developed.

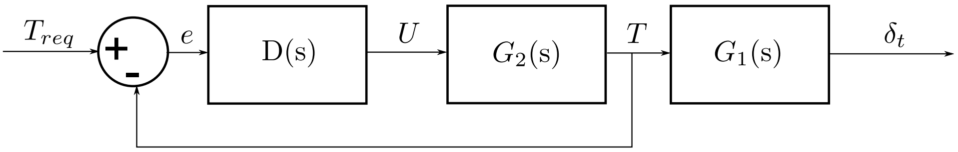

Figure 4.19 – Inner-loop temperature controller block diagram

$$G_2(s) = \frac{T(s)}{U(s)} = \frac{C_2}{s + C_1} \tag{4.2.12}$$

with,

$$C_1 = \frac{hA}{\rho c_p V} \tag{4.2.13}$$

$$C_2 = \frac{R}{\rho c_p V} \tag{4.2.14}$$

A simple PI controller could be used to ensure a critically damped closed loop temperature response at the required settling time. The controller format is shown below.

$$D(s) = \frac{U(s)}{e(s)} = K(1 + \frac{1}{T_I s}) = \frac{K(s + \frac{1}{T_I})}{s} \tag{4.2.15}$$

By choosing $T_I = \frac{1}{C_1}$, to eliminate the temperature pole, results in a closed-loop first order transfer function with closed-loop pole at $\sigma = -C_2 K$. The value of K can be determined based on the settling time requirement, t_s, as shown below.

$$K = \frac{4.6}{t_s \sigma} \tag{4.2.16}$$

The presented controller design results in the closed-loop transfer function shown in equation 4.2.17.

$$T_{cl}(s) = \frac{KC_2}{s + KC_2} \tag{4.2.17}$$

The inner-loop temperature controller will ensure a first order temperature response to a temperature command depending on the required settling time.

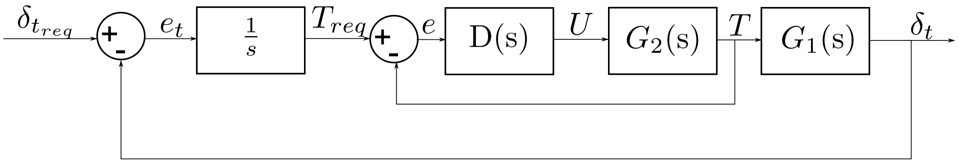

Figure 4.20 – Outer-loop deflection integral controller block diagram

4.2.3 Integral Controller Design with Feedforward Compensation

The introduction of the outer-loop integral controller is illustrated in Figure 4.20. In order to establish the influence of the integral controller on the closed-loop response the transfer function, $G_1(s)$, needs to be available. Recalling the actuator dynamic relationship in perturbation format, equation 4.2.18, and substituting the respective stress relationships, equations 4.2.19 and 4.2.20, with the newly acquired linear representation for ξ_s, equation 4.2.8, results in the second order simplified piecewise linear system dynamics, equation 4.2.21. The reason for using perturbation format is to eliminate the f_3 term in the newly developed transformation kinetics.

$$I\Delta\ddot{\delta}_t + B\Delta\dot{\delta}_t + g(\Delta\delta_t) = 2rA_c(\Delta\sigma_b - \Delta\sigma_t) \tag{4.2.18}$$

$$\Delta\sigma_t = \frac{\frac{2rE}{l_0}\Delta\delta_t + \Omega(f_{2t}\Delta T_t)}{1 - \Omega f_{1t}} \tag{4.2.19}$$

$$\Delta\sigma_b = \frac{-\frac{2rE}{l_0}\Delta\delta_t + \Omega(f_{2b}\Delta T_b)}{1 - \Omega f_{1b}} \tag{4.2.20}$$

$$\Delta\ddot{\delta}_t + \frac{B}{I}\Delta\dot{\delta}_t + A_1\Delta\delta_t = A_2\Delta T_b + A_3\Delta T_t \tag{4.2.21}$$

With,

$$A_1 = \frac{4r^2A_cE(2 - \Omega(f_{1t} + f_{1b}))}{l_0I(1 - \Omega f_{1b})(1 - \Omega f_{1t})} \tag{4.2.22}$$

$$A_2 = \frac{2rA_c\Omega f_{2b}}{I(1 - \Omega f_{1b})} \tag{4.2.23}$$

$$A_3 = -\frac{2rA_c\Omega f_{2t}}{I(1 - \Omega f_{1t})} \tag{4.2.24}$$

Considering the bottom wire to be active and assuming no change in the top wire temperature the transfer function, $G_1(s)$, can be determined by performing the Laplace transformation of equation 4.2.21 with respect to the active wire temperature. The resulting second order transfer function is showed below.

$$G_1(s) = \frac{A_2}{s^2 + \frac{B}{I}s + A_1} \tag{4.2.25}$$

During the PI deflection feedback controller design it was established that the poles of $G_1(s)$ are far to the left in the left half plane. Due to the rapid nature of these poles their dynamic contribution are neglected and only the steady state gain considered when determining the new closed-loop dynamics. $G_1(s)$ can therefore be approximated as,

$$G_{1ss}(s) = \frac{A_2}{A_1} \tag{4.2.26}$$

resulting in the following simplified closed-loop transfer function with second order characteristic equation.

$$G_3(s) = \frac{KC_2\frac{A_2}{A_1}}{s^2 + s(KC_2) + KC_2\frac{A_2}{A_1}} \tag{4.2.27}$$

The roots of the characteristic equation can easily be determined by simplifying the closed-loop transfer function as follow,

$$G_3(s) = \frac{KC_2\frac{A_2}{A_1}}{(s+\sigma_1)(s+\sigma_2)} \tag{4.2.28}$$

with,

$$\sigma_1 = \frac{-KC_2 + \sqrt{(KC_2)^2 - 4KC_2\frac{A_2}{A_1}}}{2} \tag{4.2.29}$$

$$\sigma_2 = \frac{-KC_2 - \sqrt{(KC_2)^2 - 4KC_2\frac{A_2}{A_1}}}{2} \tag{4.2.30}$$

In order for real poles to exist the following constraint needs to be satisfied.

$$KC_2 \geq \frac{4A_2}{A_1} \tag{4.2.31}$$

Assuming a set of real poles is obtainable a feedforward controller can be incorporated to eliminate the effect of the slow dominant real pole introduced into the system by using the integral controller. Figure 4.21a illustrates the feedforward controller block diagram. By applying block diagram manipulation it is possible to illustrate the effect

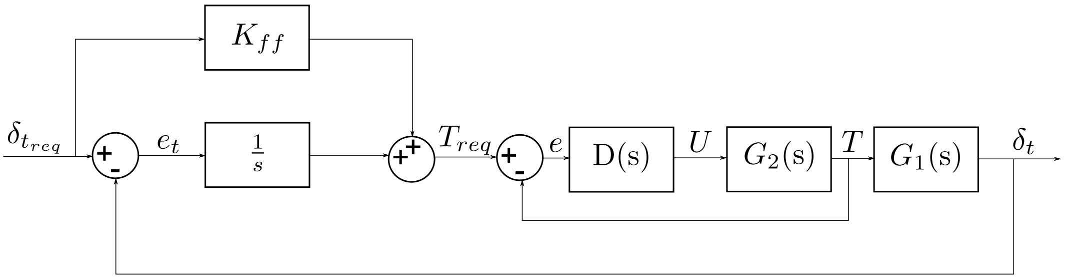

(a) Introduction of feedforward compensation

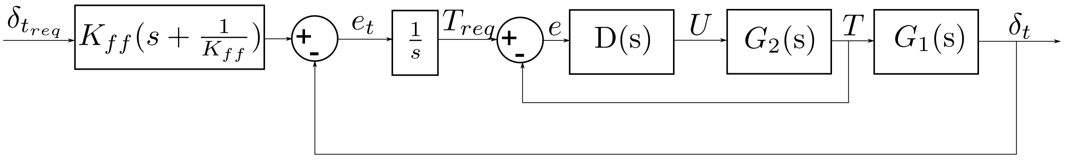

(b) Equivalentfeedforward influence

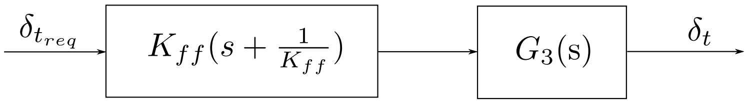

(c) Equivalentsystem block diagram

Figure 4.21 – Feedforward compensation block diagram

of the feedforward controller on the system dynamics, as shown in Figure 4.21b with,

$$N = K_{ff}(s + \frac{1}{K_{ff}}) \tag{4.2.32}$$

The feedforward introduces a real zero into the system. One can therefore choose K_{ff} to cancel the effect of the slow closed loop pole introduced by applying the integral controller by setting,

$$K_{ff} = \frac{1}{\sigma_s} \tag{4.2.33}$$

where σ_s is the slower of the two closed loop poles σ_1 and σ_2 of equation 4.2.28. The equivalent system block diagram is illustrated in Figure 4.21c which if K_{ff} is chosen correctly will result in the following system transfer function,

$$G_{sys}(s) = \frac{K_{ff}KC_2\frac{A_2}{A_1}}{(s + \sigma_f)} \tag{4.2.34}$$

where σ_f is the faster of the two closed loop poles σ_1 and σ_2 of equation 4.2.28. It should be noted that the controller will only be activated once the active wire is contracting. If the active wire is in a dead zone $G_1(s)$ will equal zero causing the controller to be ineffective for that region of operation. To overcome this obstacle the active wire will be forced into the active region by applying the maximum allowable current after which the designed controller will take over. To prevent the controller from being over active about the set point, switching the maximum current between the two wires and causing overheating, a lower input will be applied to the active wire about the set point. This will result in a gradual wire temperature relaxation. Having completed the controller design, simulation results are presented.

4.2.4 Deflection & Temperature Control with Feedforward Compensation Simulation Results

The controller design presented in the previous section was implemented in simulation to illustrate the controller ability. The initial conditions are similar to that used for the linearisation point in the PI deflection feedback controller simulation results.

Firstly the controller was subjected to a sequence of small step commands as illustrated in Figure 4.22. The deflection response for a positive followed by a negative unity step command is shown in Figure 4.22a accompanied by the input supplied to the respective wires in Figure 4.22b. The controller was designed to have a critically damped response with a 2% settling time of 1 second. The first step command clearly illustrates that the design requirements are met. The second step response illustrates a deviation from the expected response. On inspection it was determined that this deviation is the result of the passive wire cooling down and entering the de-twinning region hence accelerating the response. During the control design constant passive wire temperatures were assumed. This is not the case as a previously active passive wire will cool down. This is not a problem while the wire is in a dead zone as wire stiffness will stay constant.

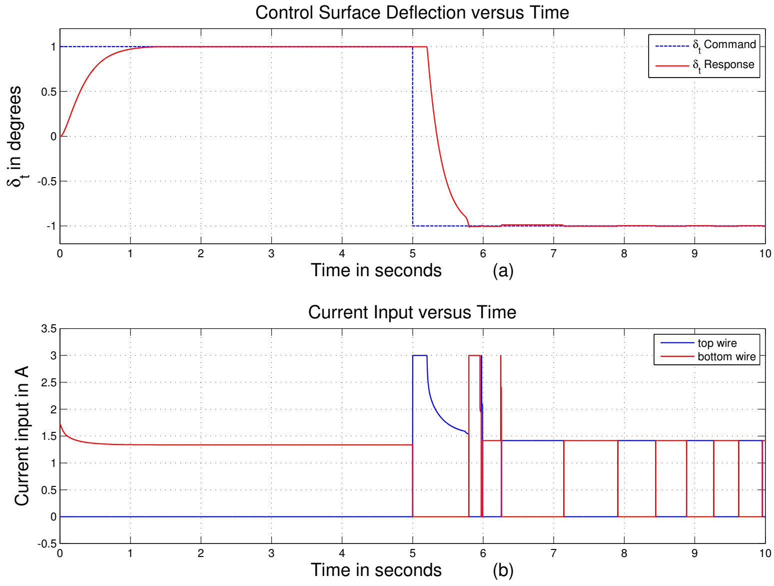

Figure 4.22 – Closed-loop temperature controller response for a dual unity step command ; (a) Deflection response; (b) Input requirements response

When entering the de-twinning region de-twinned martensite will start forming resulting in a softer material. The softer wire will therefore exert less resistance against which the active wire is pulling resulting in the increase in deflection rate. This effect is confirmed by the evolution of the passive wire de-twinned martensite fraction shown in Figure 4.23d. The bottom wire which was previously active is now cooling down, as shown in Figure 4.23a, and entering the de-twinning region resulting in the slight increase in the de-twinned martensite fraction. This increase, although very small, is sufficient to push the deflection over the set-point resulting in the active status alternating from the top to the bottom wire. This effect will always increase the response of the actuator with the negative effect of inducing unwanted overshoot. This suggest the benefit of investigating a double wire controller in which two wires are controlled simultaneously.

Figure 4.22b further illustrates the method of forcing the active wire into the region in which the controller can take over. It also illustrates the controller conditioning at which a lower current is supplied to the wire occupying the active state when the deflection is near the set-point. Additional information is shown in Figure 4.23b and 4.23c, indicating the stress and strain magnitudes respectively.

Lastly the controller is subjected to a random step command, similar to that applied to each controller design to evaluate its response to multiple step requirements. Figure 4.24a shows the deflection for the respective step commands. In all cases a zero steady state error is obtained. The result of neglecting the effect of the passive wire cooling

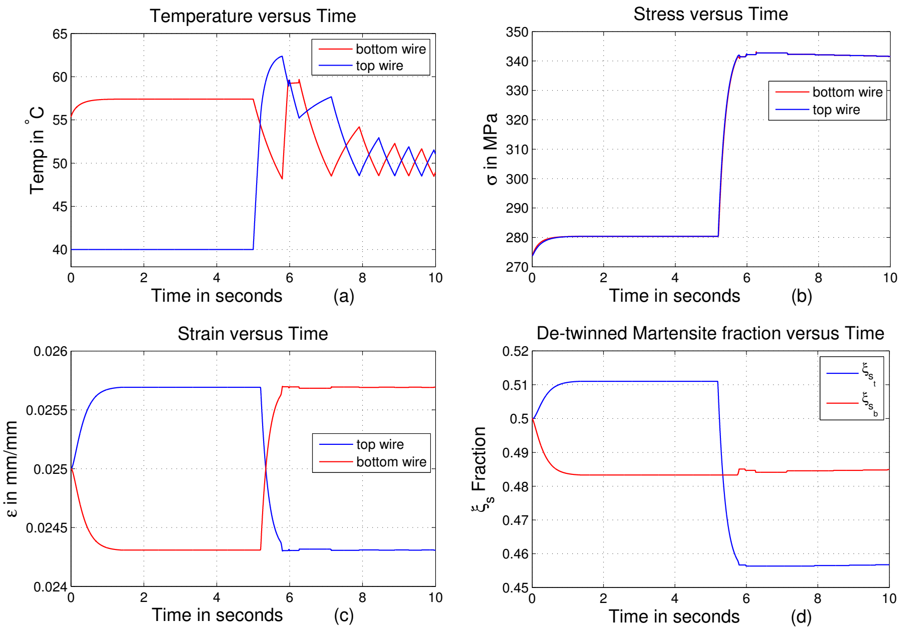

Figure 4.23 – Temperature controller states for a dual unity step command; (a) Temperature response ; (b) Stress response ; (c) Strain response ; (d) Detwinned martensite response

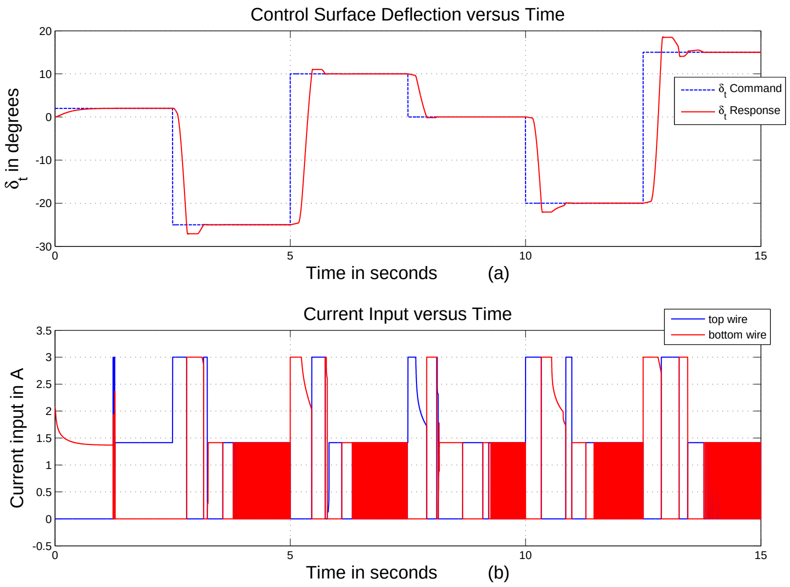

Figure 4.24 – Closed-loop temperature controller response for a random step command ;(a) Deflection response; (b) Input requirements response

down on the response of the actuator is more prominent in the larger step commands with larger amounts of overshoot. Figure 4.24b shows the inputs indicating overactive switching of the active state between the top and bottom wire. This might be overcome by incorporating a dead zone or hysteresis component into the controller. The controller amounts to a bang-bang type controller at later commands due to the required input increasing above the maximum allowable limit.

Figure 4.25a captures the temperature response with temperatures reaching up to approximately $80^{\circ}C$. The stress magnitudes are shown in Figure 4.25b indicating a maximum experienced stress of approximately $550MPa$. Figure 4.25c indicates the symmetric strain response while the de-twinned martensite evolution is shown in Figure 4.25d. The temperature controller illustrates sufficient capability. A maximum overshoot of 12% was recorded with a maximum 2% settling time of 1 second.

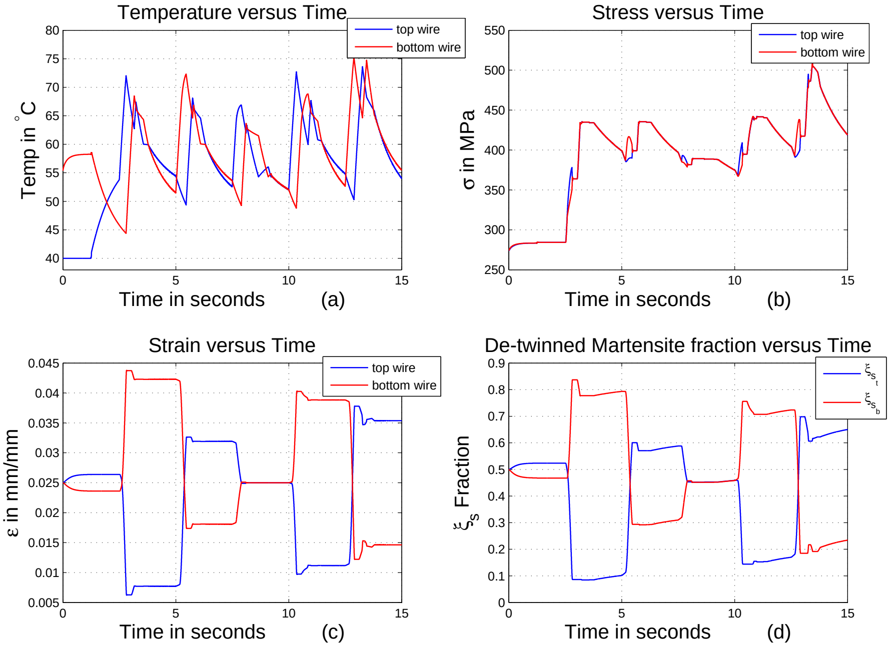

Figure 4.25 – Temperature controller states for a variable step command ; (a) Temperature response ; (b) Stress response ; (c) Strain response ; (d) Detwinned martensite response

4.3 On-off Controller Design

The on-off controller approach is based on the fact that the fastest obtainable actuation would be achieved when the maximum obtainable input is supplied to the appropriate SMA wire. The actuator would therefore be operated in a on-off approach consisting of the following switching laws:

- Only one wire will be active at an instance

- The sign of the deflection error would determine which wire occupies the active state

- The input in the active wire is a maximum when the command is not met (On)

- The input in the both wires are zero when the command is met (Off)

This control approach is applicable to the specific system as the energy input has zero temperature momentum. Switching the current supply to zero would ensure an immediate decrease in the wire temperatures. Unfortunately inertial momentum does induce control surface deflection overshoot even after the current input has been switched to zero. Nonetheless the on-off approach will indicate the maximum obtainable rise time corresponding to a specific maximum control input. The straightforward on-off approach was applied and resulted in the following closed-loop simulation results.

4.3.1 On-off Controller Simulation Response

Although non-linear control techniques such as phase-plane analysis exists, simulation was the preferred method of measuring controller performance. In order to obtain a degree of certainty in the controller performance the same random step input response, as applied in the PI and temperature controller designs, were applied to the on-off controller through simulation. Figure 4.26a shows the deflection response obtained by applying the on-off approach. The on-off approach yields satisfactory tracking ability but induces overshoot of up to 20%. The flat tops of the overshoot peaks is as a result of both wires being in a dead zone. A 2% settling time of approximately 1.5 seconds is obtained. Figure 4.26b do however illustrate the extensive control effort for the applied control approach switching the active state between the top and bottom wires quite rapidly when nearing the required command.

Figure 4.27 shows the temperature and stress states as well as the respective top and bottom wire strain and de-twinned martensite fraction. The temperature response illustrates the zigzag nature of the response induced by the controller choice when nearing the command setpoint. Rather large stress levels are obtained when applying the on-off approach compared to that of the previously designed controllers.

The on-off controller approach considered yield a faster rise time than the PI controller but induces unwanted overshoot. This transient response does however come with increased control effort and higher operating stresses. A 2% settling time of 1.5 seconds is achieved while overshoot of up to 20% can be expected. This concludes the non-linear on-off control technique design.

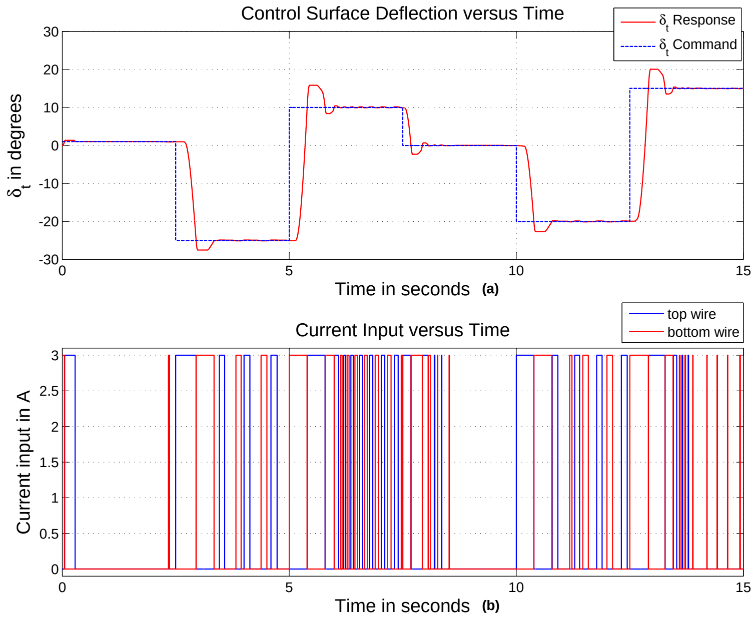

Figure 4.26 – Closed-loop bang-bang controller response for a random step command ; (a) Deflection response; (b) Input requirements response

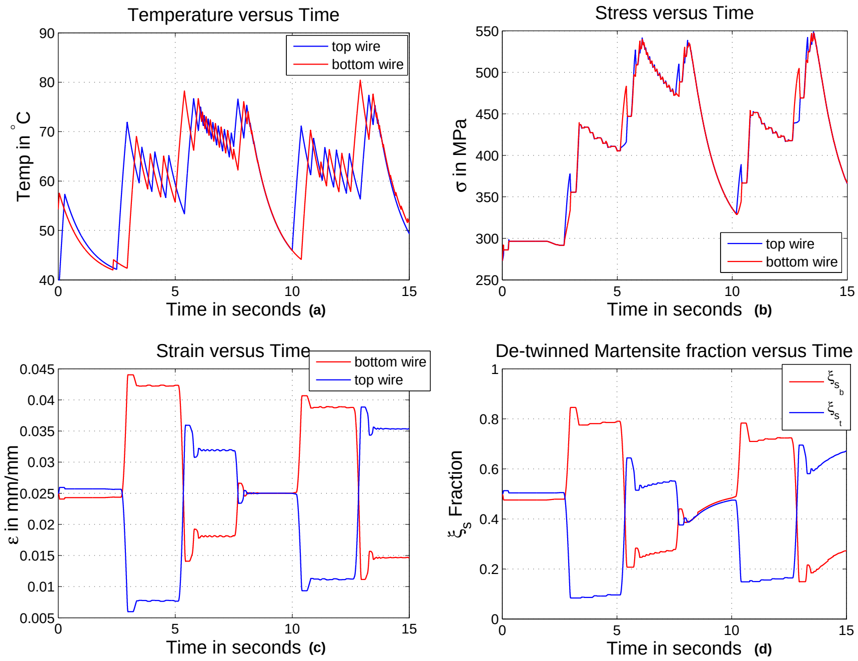

Figure 4.27 – Bang-bang controller states for a variable step command ; (a) Temperature response ; (b) Stress response ; (c) Strain response ; (d) Detwinned martensite response

4.4 Feedback Linearisation

The fundamental idea behind feedback linearisation is to algebraically transform a set of non-linear system dynamics into a fully or partly linear set [45]. Once such a model has been developed, linear control techniques can be applied in order to obtain the desired response. Figure 4.28 illustrates the basic feedback linearisation approach where state feedback is applied to convert a non-linear system into a linear one after which linear control techniques can be applied. The state-variable form shown in the figure will be presented shortly. This linearisation technique differs from conventional linearisation in the sense that linearisation is achieved by exact state transformations and feedback, whilst conventional linearisation only approximates the non-linear system as a linear system at the current work point. To summarise, feedback linearisation applies feedback in order to cancel the non-linearities of the system, hence transforming the closed-loop dynamics into the linear form. There are two types of feedback linearisation techniques, namely, input-state and input-output linearisation, of which only one technique is applied.

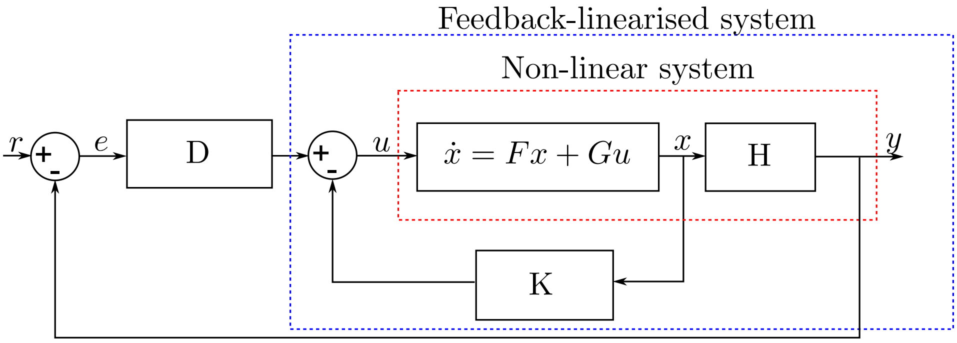

Figure 4.28 – Feedback linearisation approach in block diagram format (Source: Slotine, et all [45])

4.4.1 Input-state Linearisation

Input-state linearisation aims to find a state transformation and an input transformation in order to transform the non-linear system dynamics into equivalent linear time-invariant dynamics [45]. Once this has been achieved, a classical linear control law can be applied to design a linear controller. A detailed description of the input-state linearisation technique can be found in [45], but will not be considered here as it is not applied in this control problem.

4.4.2 Input-output Linearisation

Input-output linearisation can be applied to a non-linear system of the following form:

$$\dot{x} = f(x, u) \tag{4.4.1}$$

$$y = h(x) \tag{4.4.2}$$

where the non-linear dynamics, $\dot{x}$, are dependent on the input and current states of the system. The output, y, on the other hand, depends only on the states and is therefore indirectly related to the input, u, through the states , x. The technique attempts to establish a direct relationship between the system output and the control input by differentiating the output equation until the control input, u, appears. The number of times the output has to be differentiated for the control input to appear is said to be the relative degree, r, of the system [45]. This value indicates the number of states rendered "unobservable" in the input-output linearisation and plays a role in investigating the stability of the internal dynamics of the system.

4.4.3 Control System Design

The following section combines the SMA-based actuator model to derive the system's linearised differential state space model. The linearised state space representation is developed to illustrate that the system output, δ_t, is not directly related to the inputs u_t and u_b. The state and output vectors are shown below.

$$\dot{x} = \begin{bmatrix} \dot{x}_1 \\ \dot{x}_2 \\ \dot{x}_3 \\ \dot{x}_4 \\ \dot{x}_5 \\ \dot{x}_6 \end{bmatrix} = \begin{bmatrix} \ddot{\delta}_t \\ \dot{\delta}_t \\ \dot{\sigma}_t \\ \dot{\sigma}_b \\ \dot{T}_t \\ \dot{T}_b \end{bmatrix} x = \begin{bmatrix} x_1 \\ x_2 \\ x_3 \\ x_4 \\ x_5 \\ x_6 \end{bmatrix} = \begin{bmatrix} \dot{\delta}_t \\ \delta_t \\ \sigma_t \\ \sigma_b \\ T_t \\ T_b \end{bmatrix} y = \begin{bmatrix} \delta_t \\ T_t \\ T_b \end{bmatrix}$$

with,

$$\dot{x}_1 = f(x_1, x_2, x_3, x_4) \tag{4.4.3}$$

$$\dot{x}_2 = x_1 \tag{4.4.4}$$

$$\dot{x}_3 = f(x_3, x_5, u_1) \tag{4.4.5}$$

$$\dot{x}_4 = f(x_4, x_6, u_2) \tag{4.4.6}$$

Having identified the system states, it was possible to transform the system into the linearised state space form as depicted below.

$$\begin{bmatrix} \ddot{\delta}_t \\ \dot{\delta}_t \\ \dot{\sigma}_t \\ \dot{\sigma}_b \\ \dot{T}_t \\ \dot{T}_b \end{bmatrix} = \underbrace{\begin{bmatrix} \frac{B}{I} & \frac{g(\delta_{tab})}{I} & -\frac{2rA_c}{I} & \frac{2rA_c}{I} & 0 & 0 \\ 1 & 0 & 0 & 0 & 0 & 0 \\ \frac{\partial\dot{\sigma}_t}{\partial\dot{\delta}_{tab}} & \frac{\partial\dot{\sigma}_t}{\partial\delta_{tab}} & \frac{\partial\dot{\sigma}_t}{\partial\sigma_t} & \frac{\partial\dot{\sigma}_t}{\partial\sigma_b} & \frac{\partial\dot{\sigma}_t}{\partial T_t} & \frac{\partial\dot{\sigma}_t}{\partial T_b} \\ \frac{\partial\dot{\sigma}_b}{\partial\dot{\delta}_{tab}} & \frac{\partial\dot{\sigma}_b}{\partial\delta_{tab}} & \frac{\partial\dot{\sigma}_b}{\partial\sigma_b} & \frac{\partial\dot{\sigma}_b}{\partial\sigma_b} & \frac{\partial\dot{\sigma}_b}{\partial T_t} & \frac{\partial\dot{\sigma}_b}{\partial T_b} \\ 0 & 0 & 0 & 0 & C1 & 0 \\ 0 & 0 & 0 & 0 & 0 & C1 \end{bmatrix}}_{F} \begin{bmatrix} \dot{\delta}_t \\ \delta_t \\ \sigma_t \\ \sigma_b \\ T_t \\ T_b \end{bmatrix} + \underbrace{\begin{bmatrix} 0 & 0 \\ 0 & 0 \\ \frac{\partial\dot{\sigma}_t}{\partial u_1} & \frac{\partial\dot{\sigma}_t}{\partial u_2} \\ \frac{\partial\dot{\sigma}_b}{\partial u_1} & \frac{\partial\dot{\sigma}_b}{\partial u_2} \\ C_2 & 0 \\ 0 & C_2 \end{bmatrix}}_{G} \begin{bmatrix} u_1 \\ u_2 \end{bmatrix}$$

$$y = \underbrace{\begin{bmatrix} 0 & 1 & 0 & 0 & 0 & 0 \\ 0 & 0 & 0 & 0 & 1 & 0 \\ 0 & 0 & 0 & 0 & 0 & 1 \end{bmatrix}}_{H} \begin{bmatrix} \dot{\delta}_t \\ \delta_t \\ \sigma_t \\ \sigma_b \\ T_t \\ T_b \end{bmatrix}$$

with,

$$u_1 = I_t^2$$

$$u_2 = I_b^2$$

As one can deduce from the system representation above, there is no direct relationship between the required output y_1 and the inputs, u_2 and u_1. They are only related through the states. One could differentiate the output until the input introduces itself. The procedure mentioned was applied, but led to a need for parameters that were unavailable through measurement , thus rendering the controller unable to linearise the system. The control system setup only measures the control surface deflection, whilst the rate of control surface deflection was required. Differentiating this measurement twice would result in inaccurate values as a result of the sensor noise. One could introduce a low-pass filter to reduce the sensor noise, but this would induce a phase lag in the required parameter, which is undesirable. Thus the investigation shifted into another direction.

Clearly the non-linearities enter the system through the stress state, as depicted in equation 3.2.8 through the non-linear SMA kinetics, equation 3.2.14, which can be rearranged as shown in equation 4.4.7.

$$\dot{\xi}_s = f_1\dot{\sigma} - f_2\dot{T} \tag{4.4.7}$$

With,

$$f_1(\xi_{s0}, \sigma_0, T_0) = \left\{ \begin{array}{c} \frac{\xi_{s0}-1}{2} sin(b_M(\sigma - \sigma_f^{cr} - C_m(T - M_s)))b_M \\ \text{for } M_{t,s}, A- > M_s \\ \frac{\xi_{s0}}{2} sin(a_A(T - A_s - \frac{\sigma}{C_a}))\frac{a_A}{C_a} \\ \text{for } M_{t,s}, A- > A \\ 0, \text{otherwise} \end{array} \right\} \tag{4.4.8}$$

$$f_2(\xi_{s0}, \sigma_0, T_0) = \left\{ \begin{array}{c} \frac{\xi_{s0}-1}{2} sin(b_M(\sigma - \sigma_f^{cr} - C_m(T - M_s)))b_M C_m \\ \text{for } M_{t,s}, A- > M_s \\ \frac{\xi_{s0}}{2} sin(a_A(T - A_s - \frac{\sigma}{C_a}))a_A \\ \text{for } M_{t,s}, A- > A \\ 0, \text{otherwise} \end{array} \right\} \tag{4.4.9}$$

Rather than try and linearise the input-output relationship, an attempt is launched to linearise the stress state to obtain linear actuator dynamics. The top wire stress relationship can be simplified, as presented below, by substituting equation 4.4.7 and the temperature dynamics, equation 3.2.5, into equation 2.3.9.

$$\dot{\sigma}_t = A + B + Cu_t \tag{4.4.10}$$

Where the A, B and C representations are shown below.

$$A = \frac{2rE\dot{\delta}_t}{l_0(1 - \Omega f_{1t})} \tag{4.4.11}$$

$$B = \frac{-\Omega f_{2t} C_1 (T_t - T_\infty)}{1 - \Omega f_{1t}} \tag{4.4.12}$$

$$C = \frac{-\Omega f_{2t} C_2}{1 - \Omega f_{1t}} \tag{4.4.13}$$

Similarly the bottom wire stress can be simplified as follow,

$$\dot{\sigma}_b = D + E + Fu_b \tag{4.4.14}$$

Where the D, E and F representations are shown below.

$$D = \frac{-2rE\dot{\delta}_t}{l_0(1 - \Omega f_{1b})} \tag{4.4.15}$$

$$E = \frac{-\Omega f_{2b} C_1 (T_b - T_\infty)}{1 - \Omega f_{1b}} \tag{4.4.16}$$

$$F = \frac{-\Omega f_{2b} C_2}{1 - \Omega f_{1b}} \tag{4.4.17}$$

It is required to choose the input, either u_t or u_b depending on which wire is active, in order to linearise our stress-state dynamics. To gain more insight into how to choose our input, we investigate the effect our linearised stress state will have on our actuator dynamics. As evident in both equations 4.4.10 and 4.4.14, the inputs enter the system through $\dot{\sigma}$. In order to determine their effect we need to differentiate our system dynamics, equation, 4.1.13, thus resulting in the following relationship:

$$I\dddot{\delta}_t + B\ddot{\delta}_t = 2rA_c(\dot{\sigma}_b - \dot{\sigma}_t) \tag{4.4.18}$$

Equation 4.4.18 clearly illustrates where the non-linearities enter the system, namely the $(\dot{\sigma}_b - \dot{\sigma}_t)$ term. By replacing this term with a linear representation, the system's response would be transformed to a linear third-order system. The following input is chosen, for the case where the top wire is active, in an attempt to linearise the non-linear stress relationship induced by both SMA wires.

$$u_t = \frac{1}{C}(v - A - B - \dot{\sigma}_b) = \frac{1}{C}(v - A - B - (D + E)) \tag{4.4.19}$$

Substituting equation 4.4.19 into equation 4.4.10 and subsequently equation 4.4.10 into equation 4.4.18 results in a linear third-order system representation as shown below.

$$I\dddot{\delta}_t + B\ddot{\delta}_t = 2rA_c v \tag{4.4.20}$$

Figure 4.29 shows the newly linearised system's block diagram by choosing the input as stated above. With the linearised model developed, it was possible to design a linear

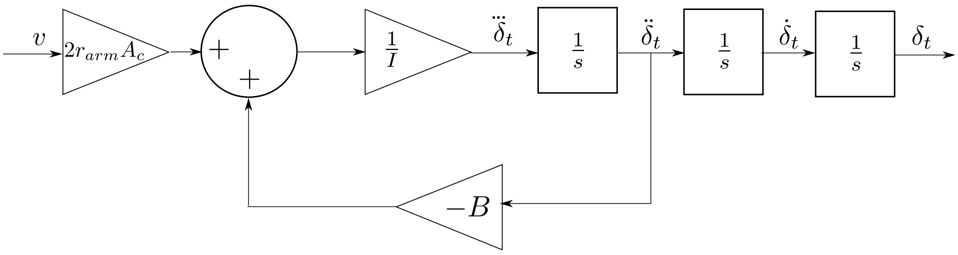

Figure 4.29 – Third-order linearised system open-loop block diagram

controller to force the closed-loop poles to the desired position. In order to do so the root locus of linearised system will be investigated to determine the position of the open-loop poles, followed by choosing the relevant controller parameters to stabilise the closed-loop response. A conventional proportional controller will be applied. Figure 4.30 illustrates the root locus plot for the linearised model with a unity proportional feedback controller. Two open-loop poles are situated at the origin, while another is situated far to the left in the left-half plane. By increasing the proportional gain the root locus of the poles situated at the origin tends to the right-half plane, while the one situated at the far left departs horizontally to the left. For a gain greater than 1 the closed-loop response is unstable because of the dominant poles departing to the right-half plane. For a gain of 1 the closed-loop poles are marginally stable and will result in infinite actuator oscillation.

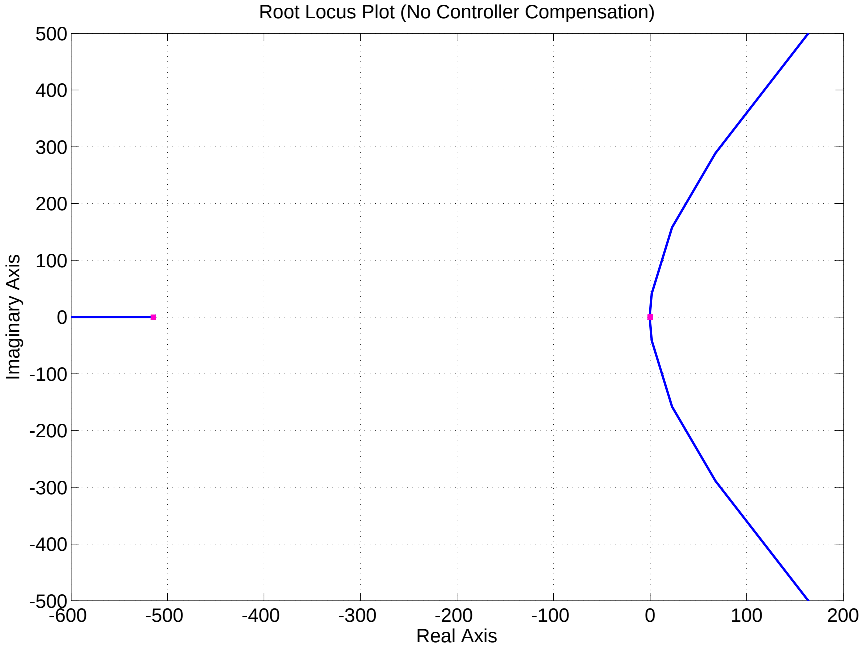

Figure 4.30 – Root-locus plot illustrating open-loop poles after linearisation

In order to stabilise the third-order system rate and position, feedback is required. The approach is to apply inner-loop rate feedback to effectively cancel the effect of one of the poles at the origin. An outer-loop consisting of a proportional position feedback with an introduced reference will be applied. In order to implement this approach, it would be ideal to separate v, of equation 4.4.19, into two parts as follows:

$$v = v_1 + v_2 \tag{4.4.21}$$

where v_1 and v_2 are the respective inner-loop and outer-loop controller signals. The inner-loop controller is considered first and illustrated by Figure 4.31 in block diagram format: where k_1, the feedback gain, is a positive constant. From the diagram the representation of the inner-loop controller is clearly seen as stated below.

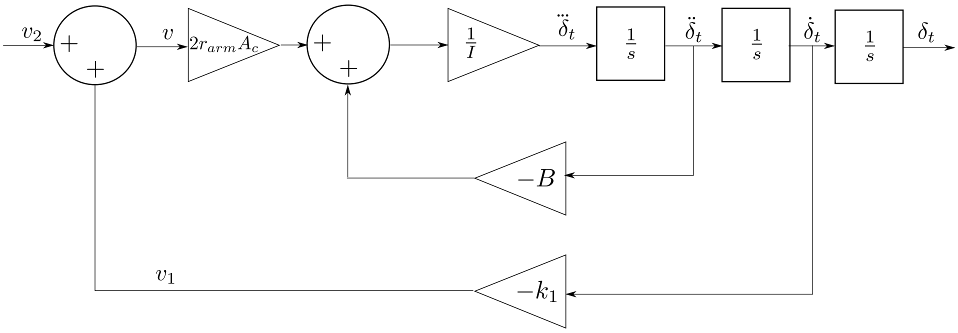

Figure 4.31 – Reference introduction and rate feedback block diagram

$$v_1 = -k_1\dot{\delta}_t \tag{4.4.22}$$

Note that $\dot{\delta}_t$ is not measured directly and will be obtained by differentiating the δ_t measurement. This is considered as bad practice, but will suffice in this application as the δ_t measurement contains very little noise.

The new open-loop poles obtained by applying the inner-loop feedback controller are illustrated in the root locus plot, Figure 4.32. By introducing the rate feedback the effect of one of the poles at the origin is eliminated. This results in an equivalent system consisting of two open-loop poles, one at the origin and one far to the left in the left-half plane. The root locus departs from the two equivalent open-loop poles and heads toward their midpoint, after which they depart perpendicular to the real axis as indicated by the arrows in Figure 4.32. By varying the feedback gain k_1, the necessary closed-loop poles can be achieved.

In order to introduce a reference to the system an outer-loop position feedback controller is considered. A pure proportional controller is applied as shown below.

$$v_2 = k_2 e \tag{4.4.23}$$

where e is the error between the required and actual control surface deflection.

$$e = \delta_{t_{req}} - \delta_t \tag{4.4.24}$$

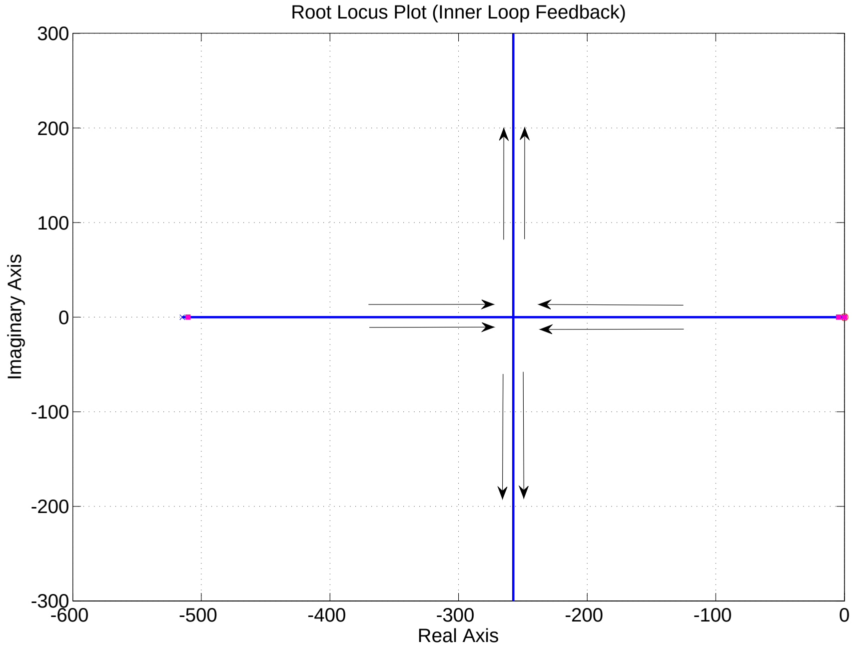

Figure 4.32 – Closed-loop poles obtained after inner-loop feedback compensation

The block diagram of the completed system is illustrated in Figure 4.33. The figure illustrates the outer-loop position feedback controller and the introduction of the reference input, the required control surface deflection.

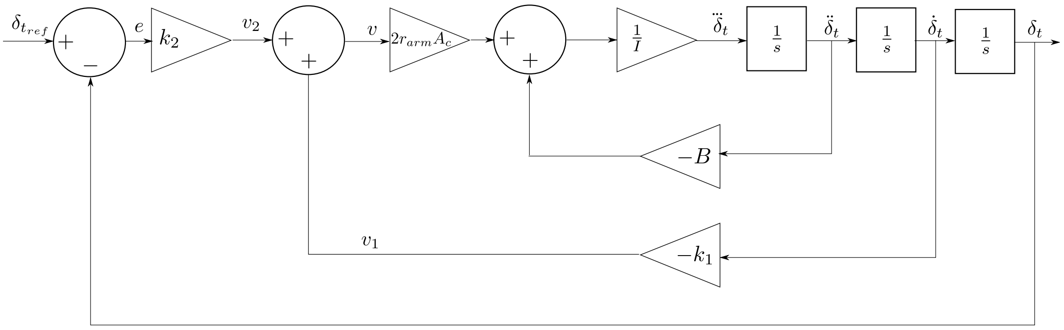

Figure 4.33 – Closed-loop block diagram after complete linearisation

Figure 4.34 illustrates the root locus plot of the system after applying the outer-loop feedback controller. Up to this point the equivalent system consists of three poles, one at the origin, one far to the left in the left-half plane and one depending on the magnitude of the gain, k_1, of the inner-loop controller. The closed-loop poles of the system are influenced by the two controller gains, k_1 and k_2 respectively. The magnitude of k_1

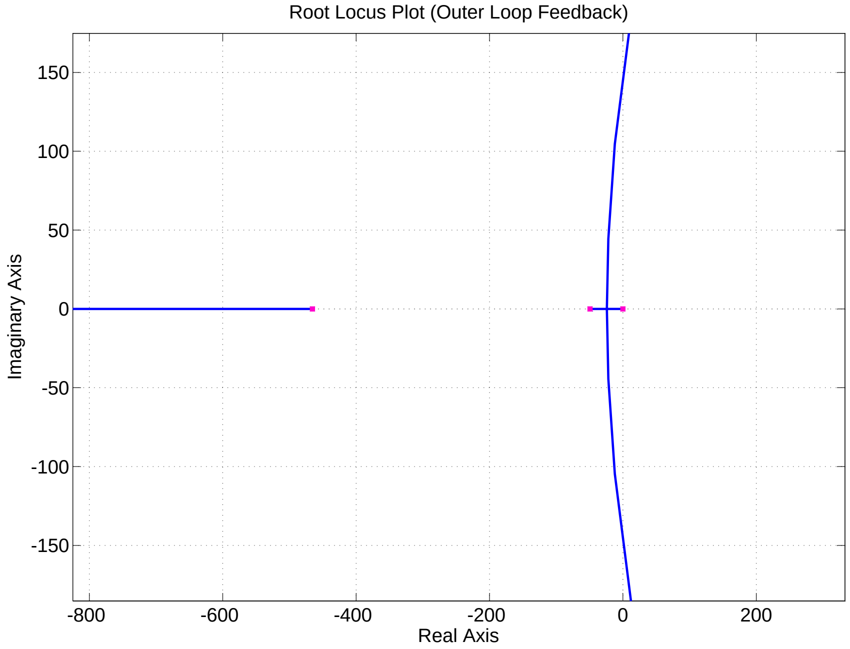

Figure 4.34 – Root locus plot with dominant closed-loop poles after complete feedback linearisation

influences the position of the middle open-loop pole of the final system, which enables it to drag the closed-loop poles to the left and thus increasing the actuation transient response. The k_2 gain determines where exactly the closed-loop poles are situated, depending on the specific magnitude of k_1. For the illustrative example, there can be either three real or one real and one imaginary closed-loop pole set . As the k_2 gain increases, the closed-loop pole far to the left departs horizontally to the left, while the closed-loop poles near to the origin move towards each other until they depart perpendicular to the real axis. By choosing the correct gain combination, the required response can be obtained. The following section investigates the transfer function of the system after the control solution, as described above, has been applied. The focus is on determining the correct gain combinations.

4.4.4 Determining the Gains

Substituting v into the system's third-order dynamics yields the following third order polynomial:

$$I\dddot{\delta}_t + B\ddot{\delta}_t + 2rA_ck_1\dot{\delta}_t + 2rA_ck_2\delta_t = 2rA_ck_2\delta_{t_{req}} \tag{4.4.25}$$

Taking the Laplace transforms of equation 4.4.25, assuming the initial conditions are at zero, results in the closed-loop transfer function for the required control surface deflection.

$$\frac{Y(s)}{R(s)} = \frac{2rA_ck_2}{Is^3 + Bs^2 + 2rA_ck_1s + 2rA_ck_2} \tag{4.4.26}$$

The transfer function thus developed contains known variables except the positive control gains k_1 and k_2. The closed-loop steady-state gain of the system is 1, which indicates perfect input tracking. A procedure to choose the gains, k_1 and k_2, is needed to result in the required time specifications. As a critically-damped response is required, a characteristic equation consisting of three real roots, of which one is dominant and the other two more than ten times the magnitude of the dominant pole, will be needed. Thus,

$$(s + p_1)(s + p_2)(s + p_3) = 0 \tag{4.4.27}$$

which, if set equal to our actual characteristic equation, yields the following set of equations. Setting

$$(s + p_1)(s + p_2)(s + p_3) = Is^3 + Bs^2 + 2rA_ck_1s + 2rA_ck_2 \tag{4.4.28}$$

and solving yields the following:

$$\frac{B}{I} = p_1 + p_2 + p_3 \tag{4.4.29}$$

$$\frac{2rA_ck_1}{I} = p_2p_3 + p_1p_3 + p_1p_2 \tag{4.4.30}$$

$$\frac{2rA_ck_2}{I} = p_2p_3p_1 \tag{4.4.31}$$

Knowing the time constant requirement of the first order dominant pole, $p_3 = \frac{1}{T_C}$, and knowing that the middle pole should be at least ten times larger as shown below,

$$p_2 = 10p_3$$

the magnitude of remaining pole can be determined by rearranging equations 4.4.29 to 4.4.31.

$$p_1 = \frac{B}{I} - p_2 - p_3$$

The gains can be determined by substituting the values of the real poles into the following equations;

$$k_1 = \frac{I(p_2p_3 + p_1p_3 + p_1p_2)}{2rA_c} \tag{4.4.32}$$

$$k_2 = \frac{I(p_2p_3p_1)}{2rA_c} \tag{4.4.33}$$

The procedure developed linearises the non-linear system. The required time constant for the closed-loop response can then be achieved by calculating the gains by applying the abovementioned procedure. The procedure results in rather large gains. The large gain values should however not be misinterpreted as resulting in unobtainable inputs. The controller results in reasonable required input magnitudes, as will be illustrated in the simulation results section.

4.4.5 Feedback Linearisation Controller Simulation Results

The stress feedback linearisation controller designed in the preceding sections was implemented in simulation to investigate whether its behaviour is indeed as expected by the design. Closed-loop simulations for various time constants and control commands were conducted, after which the response was analysed.

Firstly, the controller response in the presence of natural convective cooling conditions is considered, followed by an analysis of increased heat transfer conditions. The simulation results are wrapped up by an illustration of the actuator tracking an arbitrary command to ensure that the controller yields satisfactory results for the specific application.

Questions to be answered by the simulation results are whether the expected first-order response is obtained, whether the time constant constraint is met, and whether the required maximum deflection in either direction can be met. If any unforeseen elements are identified, they should be addressed.

4.4.5.1 Performance under Natural Convection

Initially the performance of the controller actuator combination under natural convective conditions was investigated. Multiple-step responses were applied for various required time responses to evaluate the controller's ability to ensure the necessary actuation. Note that the initial conditions applied in the non-linear controller simulation differs from that applied in the preceding controller designs. This is purely because of the non-linear controller design not being restricted to a certain set-point, like the other controller designs, but rather being valid through the whole operating range.

Maximum deflection: $\tau = 1$ second

Figure 4.35 shows the transient response of the actuator after the integration of the designed control system for a time constant requirement of 1 second. The command, the deflection at which the time constant must be met, and the transient response are shown in Figure 4.35a. The command varies between $25°$ and $-25°$ to illustrate the entire range of operation. As expected, a first-order response is obtained.

Figure 4.35b shows the applied current to the respective wires. Initially the actuator is in a dead zone, clearly illustrated by the initial zero actuation, which results in the maximum allowable input to force the actuator into the transformation region as quickly as possible. Once the transformation region is reached, the controller stabilises the system, followed by a steady decrease of the required input. One notices a slightly larger time constant than designed for. This is as a result of input saturation occurring either due to the SMA actuator being in a dead zone or the controller requiring inputs above the maximum allowable input. By increasing the maximum allowable input this effect can be minimised.

Figure 4.36 shows the SMA material properties during the actuation for the respective wires. Figure 4.36a shows the temperature response. Figure 4.36b shows the stress

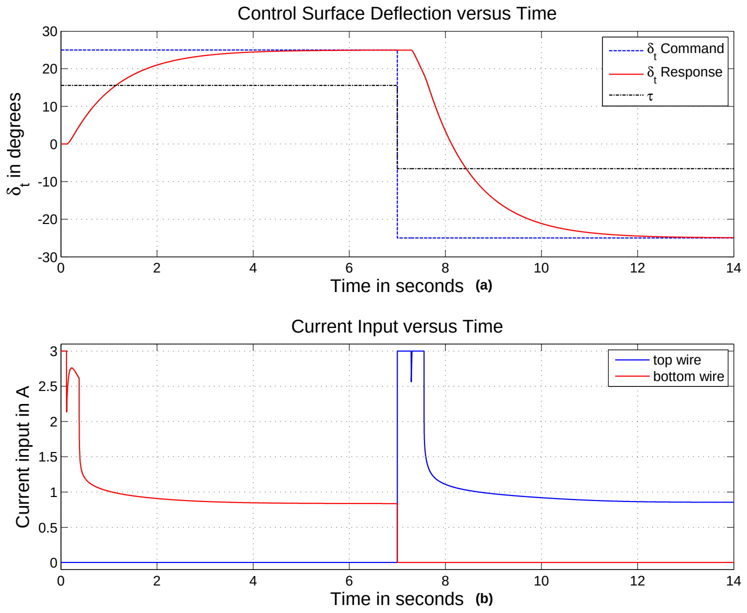

Figure 4.35 – Closed-loop feedback-linearisation controller response for a maximum step command ($\tau = 0.1s$) ; (a) Deflection response; (b) Input requirements response

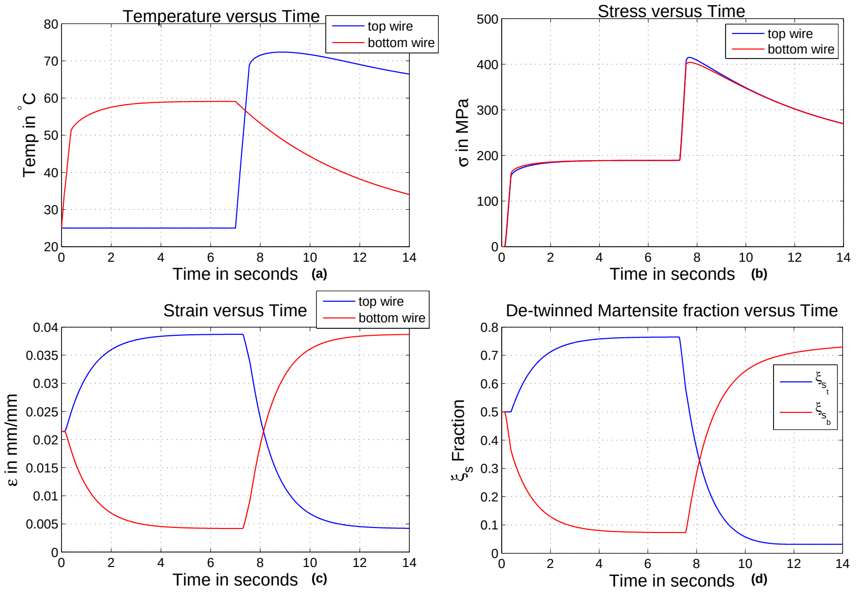

Figure 4.36 – Feedback linearisation controller states for a maximum step command ($\tau = 0.1s$); (a) Temperature response ; (b) Stress response ; (c) Strain response ; (d) Detwinned martensite response

resulting from the actuation, while Figure 4.36c shows the strain in the respective wires. The detwinned martensite fraction for both wires are shown in Figure 4.36d.

Maximum deflection: $\tau = 0.1$ seconds

Figure 4.37 shows the transient response of the actuator for a time constant requirement of 0.1 seconds. As can be seen in Figure 4.37a, the time constant requirement deteriorates further due to the increase in duration of the input saturation. It seems as if the actuator failed to reach the final value of the second step response within specification. After an investigation, it was found that the actuator reached saturation caused by the slow extraction of energy from the system as a result of the relatively small heat transfer coefficient present in natural convective cooling. In other words, the passive wire is too stiff for the active wire to overcome the stress to contract and ensure actuation. Once this saturation point has been reached, the controller interprets it as a dead zone and forces maximum current into the respective wire, as seen in Figure 4.37b by the second saturation command for the second step response. The second step command is eventually met but causes overshoot resulting in the activation of the previously passive wire. This phenomenon illustrates the importance of ensuring a suitable heat transfer mechanism, especially in counteracting SMA actuators requiring cyclic operation.

Figure 4.38 shows the SMA parameters of the respective wires, as previously mentioned. The saturation effect is seen as the top wire temperature increases rapidly after

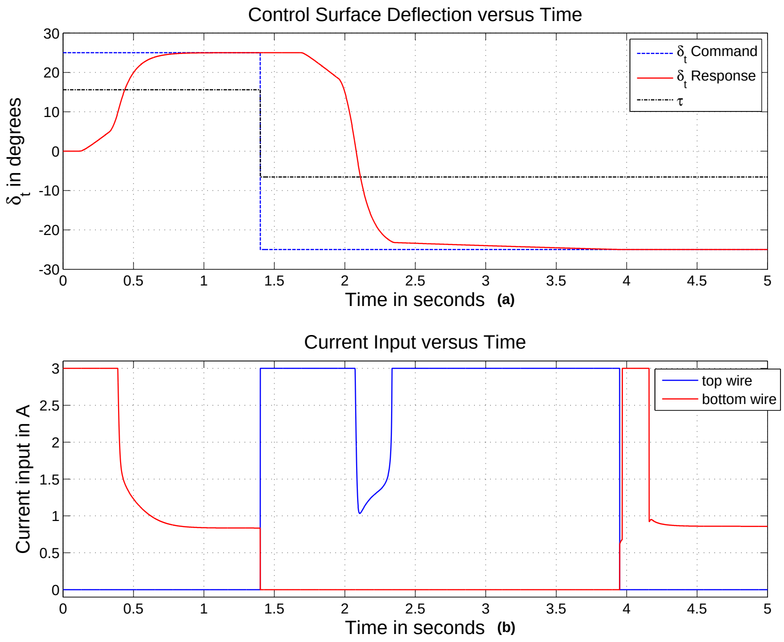

Figure 4.37 – Closed-loop feedback-linearisation controller response for a medium step command ($\tau = 0.1s$) ; (a) Deflection response; (b) Input requirements responses

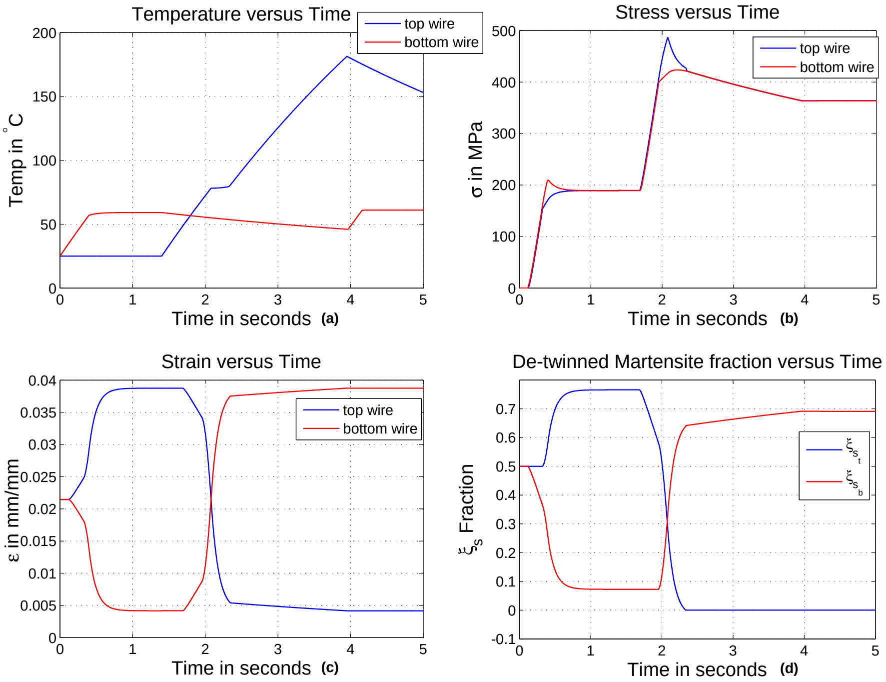

Figure 4.38 – Feedback linearisation controller states for a medium step command ($\tau = 0.1s$) ; (a) Temperature response ; (b) Stress response ; (c) Strain response ; (d) Detwinned martensite response

saturation occurs. This is an unwanted effect, as it will result in the SMA being heated to above the re-training temperature, thus removing the shape memory effect. In order to accommodate for this effect, a maximum temperature limit will be placed on the actuator, resulting in a zero input when the temperature limit is exceeded. The increased stress levels are as a result increased top wire temperature caused by the saturation effect. It is evident from the simulation results that the actuator struggles to obtain large control surface deflections at low heat transfer coefficients.

Figure 4.39 shows the respective stress-temperature relationships in the phase diagram for both wires. The phase diagram clearly shows why saturation occurs. After being heated, the passive wire cools too slowly, resulting in an increased stress required to obtain the required deflection command. This increased stress is large enough to restrict the active wire from contracting, thus producing the actuation deficiency.

Half the maximum deflection: $\tau = 0.1$ seconds

The following test case requires smaller actuation intervals to investigate whether saturation occurs at smaller control surface deflection requirements. The command varies between $12°$ and $-12°$. For the case at hand, the time constant requirement was set to 0.1 seconds. Once again a first-order response is obtained, as illustrated in Figure 4.40a. It is noted that the actuator does indeed reach the required deflection for both cycles, suggesting that saturation did not occur. The input command is shown in Figure

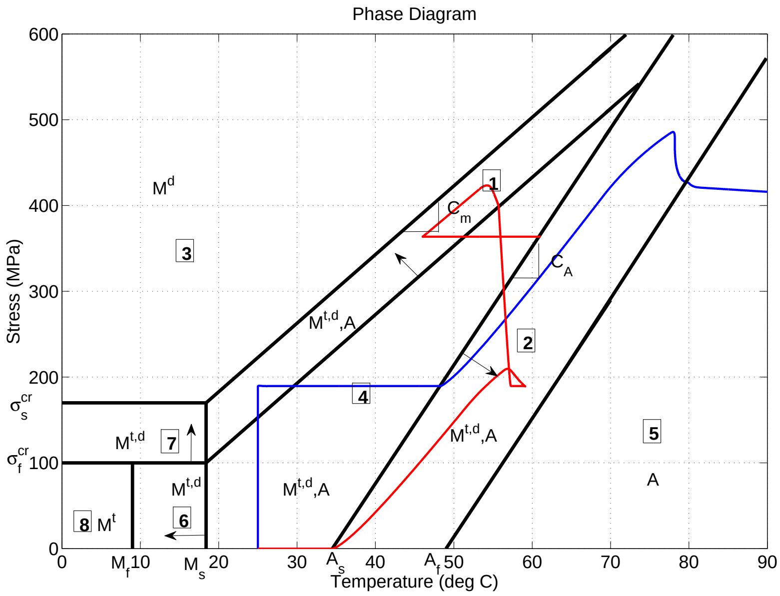

Figure 4.39 – Phase diagram illustrating wire transformation path for maximum deflection

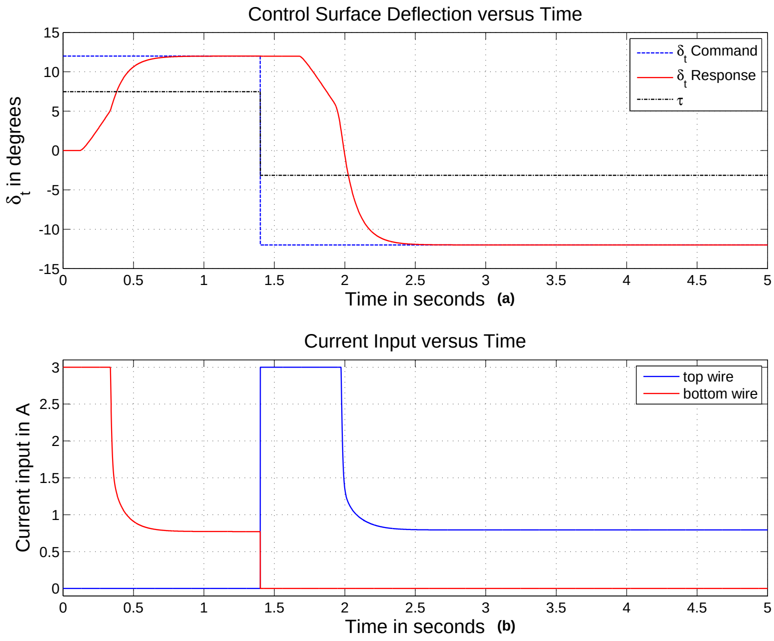

Figure 4.40 – Closed-loop feedback-linearisation controller response for a medium step command under ($\tau = 0.1s$) ; (a) Deflection response; (b) Input requirements response

4.40b and illustrates an initial maximum input to force the actuator out of the dead zone, followed by a steady decrease in the required input.

The respective SMA wire parameters are not taken into consideration, but the phase diagram is shown to illustrate that saturation has not occurred. The phase diagram, shown in Figure 4.41, clearly indicates a lower stress level in both wires, resulting in a lower resistance for the active wire to pull against when contracting. Therefore the required control surface deflection can be met. The above controller simulation results indicate the importance of the heat transfer mechanism when applying control to an SMA actuator when cyclic operation is required. At insufficient heat transfer conditions saturation will eventually occur in cyclic loadings whether at the third fourth or tenth cycle. The rate at which the energy is removed governs the ability of the controller to command the actuator to obtain the maximum required deflection. The following simulations will therefore be conducted at improved heat transfer conditions to investigate whether any improvements in the ability of the actuator to operate under cyclic loadings are visible.

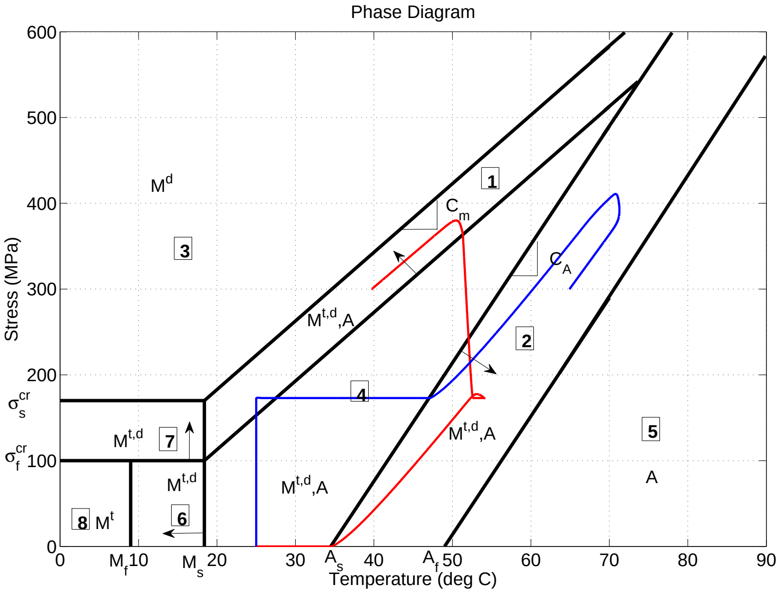

Figure 4.41 – Phase diagram illustrating wire transformation path for intermediate deflection

4.4.5.2 Performance under Forced Convection

The following simulation investigates whether the controller performance will improve under improved convectional heat transfer conditions. The actuator and SMA parameters used are identical to those used during the natural convective condition, except for a 5-times improved convectional heat transfer coefficient, h. Figure 4.42a shows the transient response of the actuator for a maximum deflection command in either direction. It is in fact shown that saturation doesn't occur. It is noticed that increased inputs are required compared to the same simulation conducted at natural convective heat transfer, as expected because of the improved heat transfer conditions. This is shown in Figure 4.42b. Figure 4.43 shows the respective SMA wire parameters obtained for the improved heat transfer conditions. It is noticed that the cooling response is much faster, as illustrated in Figure 4.43a, which in turn results in lower stresses, Figure 4.43b, for the equivalent simulation at reduced heat transfer conditions.

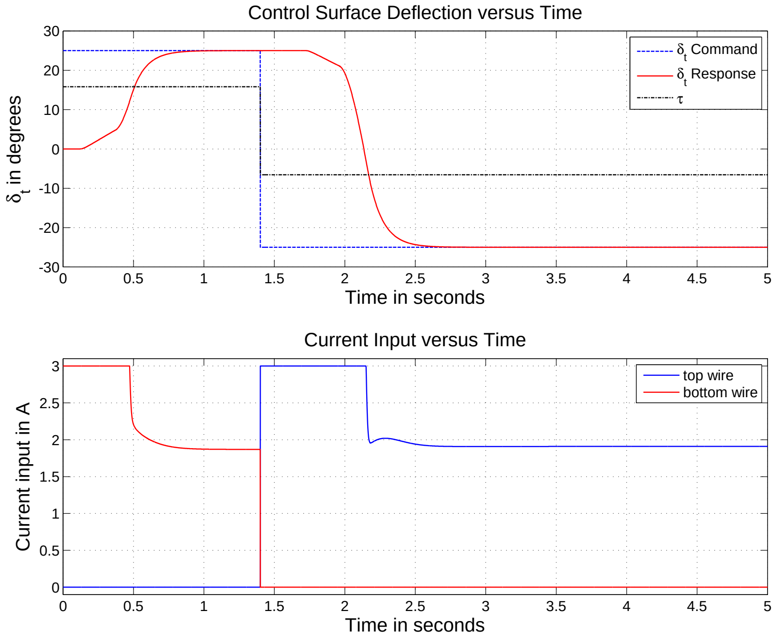

Figure 4.42 – Closed-loop feedback-linearisation controller response for a maximum step command under forced convection ($\tau = 0.1s$) ; (a) Deflection response; (b) Input requirements response

The phase diagram shown in Figure 4.44 indicates the lower stress levels, which will ensure that the current controller can produce the required cyclic response.

The above simulation results indicate the ability of the designed controller to ensure the required actuator control. In general, counteracting SMA actuators has limitations when applied in cyclic operations because of the dependence of the passive wire's stiffness on temperature. This factor degrades the actuator's response when large deflections and a rapid transient response are required. This limitation can be addressed by introducing improved heat transfer mechanisms as illustrated by the forced convective heat transfer simulation results. Other configurations - for example, spring -biased actuators - might not illustrate this deficiency.

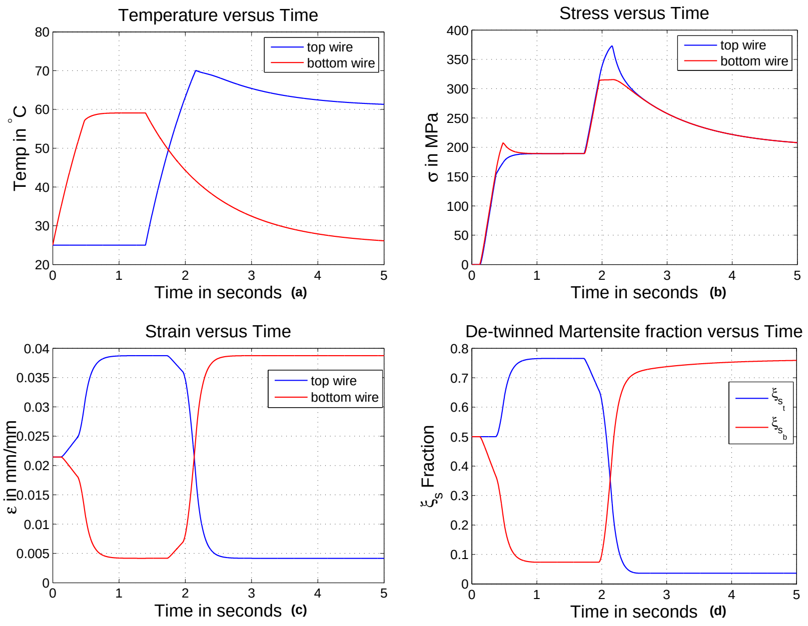

Figure 4.43 – Feedback linearisation controller states for a maximum step command under forced convection ($\tau = 0.1s$) ; (a) Temperature response ; (b) Stress response ; (c) Strain response ; (d) Detwinned martensite response

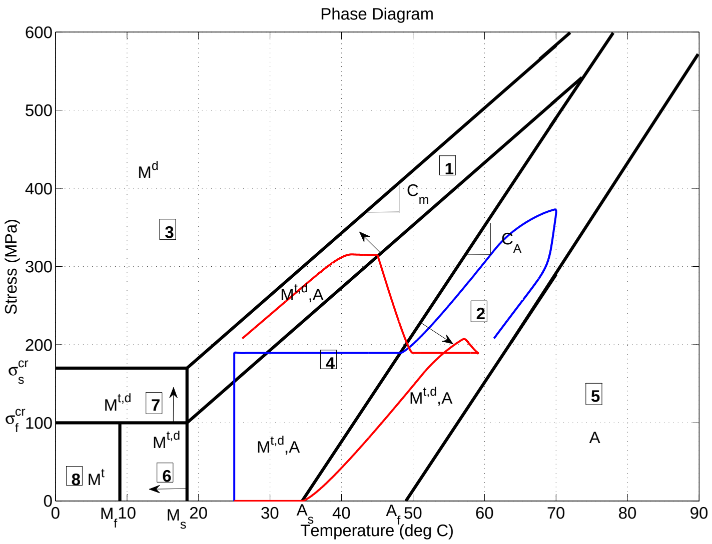

Figure 4.44 – Phase diagram illustrating wire transformation path for a maximum deflection at improved convectional conditions

4.4.5.3 Cyclic Performance under Forced Convection

The final simulation conducted ensures the ability of the designed control system to command the actuator to various control surface deflections at a fast transient response in the necessary heat transfer conditions. The actuator is commanded to follow random step inputs with a time constant requirement of 0.1 seconds, which will ensure fast actuation. Figure 4.45a shows the transient response of the actuator for various control surface deflection commands. A first-order over-damped response is obtained for every command. The input required for the actuation is shown in Figure 4.45b for each respective wire. Most of the inputs required resemble a first-order response, while some have minor deviations. The required inputs are well capable of producing in practice. Figure 4.46 shows the respective SMA wire material parameters during the actuator run. The temperature for either wire never exceeds $68°C$, while the stress is rarely above $380MPa$. The strain developed in the respective wires is shown in Figure 4.46c, while the martensite fraction progression is shown in Figure 4.46d.

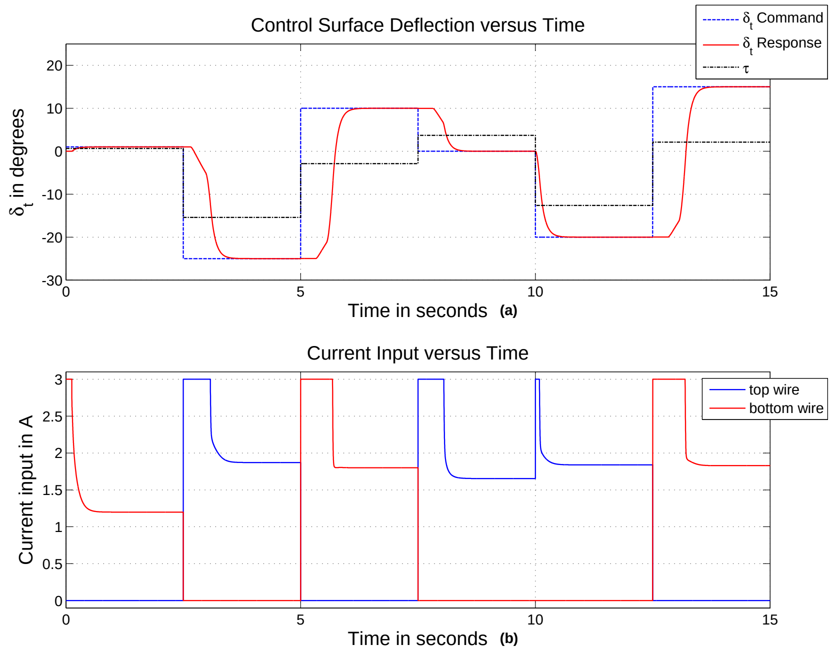

Figure 4.45 – Closed-loop feedback-linearisation controller response for a random step command under forced convection ($\tau = 0.1s$) ; (a) Deflection response; (b) Input requirements response

Figure 4.47 shows the phase diagram for the current simulation run. It illustrates the region of operation for the actuator. The two wires vary between the predominantly austenite and predominantly martensite states. Keeping within these boundaries will ensure satisfactory actuation. The final simulation results illustrate the controller's ability to ensure accurate and satisfactory actuation. The rest of the thesis focuses on the practical results obtained from implementing the designed controllers.

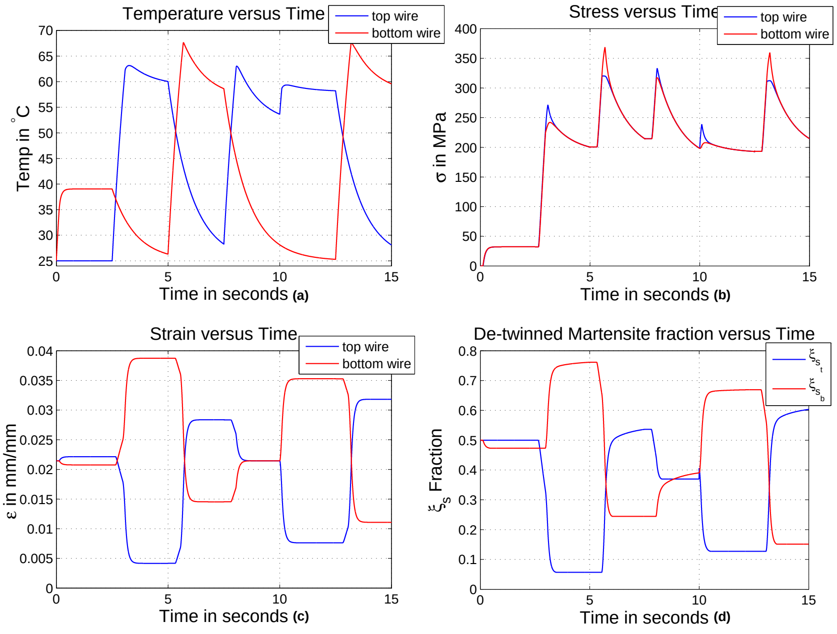

Figure 4.46 – Feedback linearisation controller states for a random step command under forced convection ($\tau = 0.1s$) ; (a) Temperature response ; (b) Stress response ; (c) Strain response ; (d) Detwinned martensite response

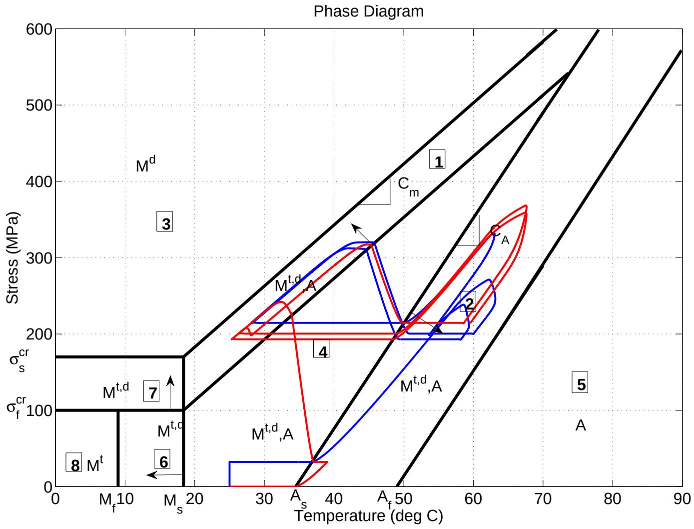

Figure 4.47 – Phase diagram illustrating wire transformation path for multiple step commands

Chapter 5

Hardware Prototype

This section covers the hardware prototype used in the practical control system implementation. The idea is to familiarize the reader with the equipment available. Firstly, the physical actuator is described, followed by a presentation of the accompanied sensors, drivers and hardware used in the control system implementation. Limitations encountered during the practical setup will also be discussed.

5.1 Mechanical Design

The SMA controller consists of two aileron ribs manufactured by laser-cutting technology. These two ribs are joined by a wooden shaft, with machined shoulders for structural support, and a threaded rod in order to improve the structural stability. The threaded rod is used to align the two ribs accordingly. The aileron shaft runs on two ball-bearings situated within the respective aileron ribs. Attached to the shaft are the pulleys required to attach the respective SMA wires and the aileron ribs required to attach the aileron control surface. One U-bracket is attached to each aileron rib. These U-brackets are required to attach the pulleys used to guide the respective SMA wires. Figure 5.1 illustrates the initial mechanical setup. At the time the photo was taken load cells were not incorporated into the system. The attachment is also not the pulley type as applied during the model development, controller designs and practical implementation. In order to accommodate the use of load cells the U-brackets had to be shifted to the other side of the wooden shaft in order to allow the use of the increased SMA wire length to obtain the required deflection. Due to the insertion of load cells in the SMA wire path it was required elongate the SMA guide path by attaching the U-brackets on the other side of the wooden shaft by drilling guiding holes through the shaft to allow frictionless movement. This modification and pulley configuration are shown in Figure 5.2. The SMA wire applied in the prototype development was purchased from Dynalloy. The supplier specialises in the manufacturing of SMA wire which they term "flexinol" a nickel-titanium based SMA with the ability to regain strains of up to 5%. "Flexinol" can be purchased at various diameters and lengths as either a low or high temperature type. The type refers to either a lower or higher set of transformation temperatures.

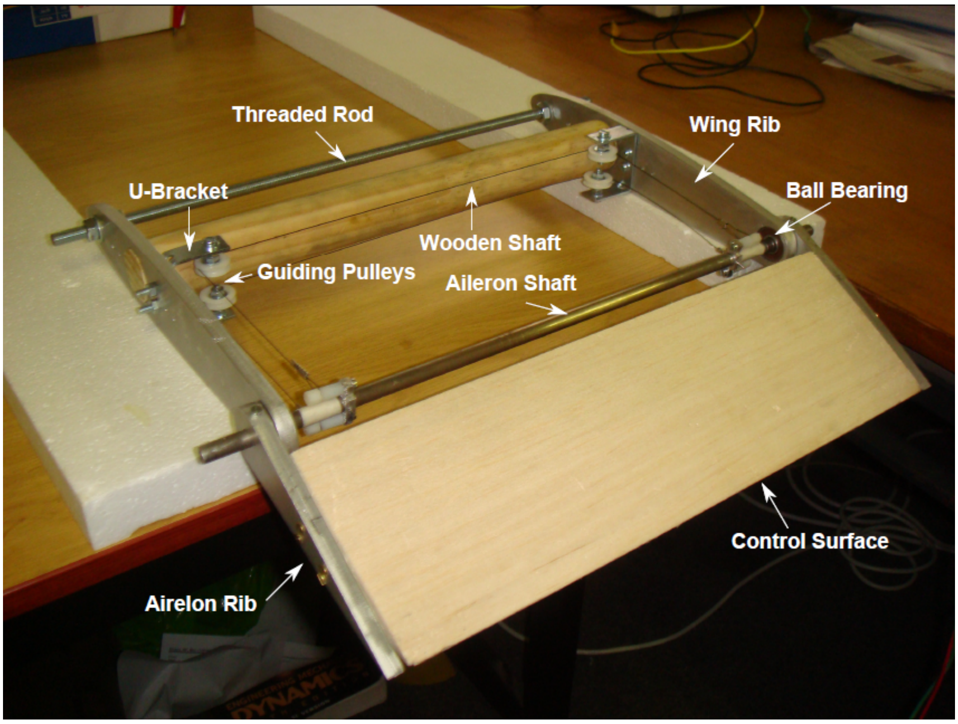

Figure 5.1 – SMA actuator mechanical setup

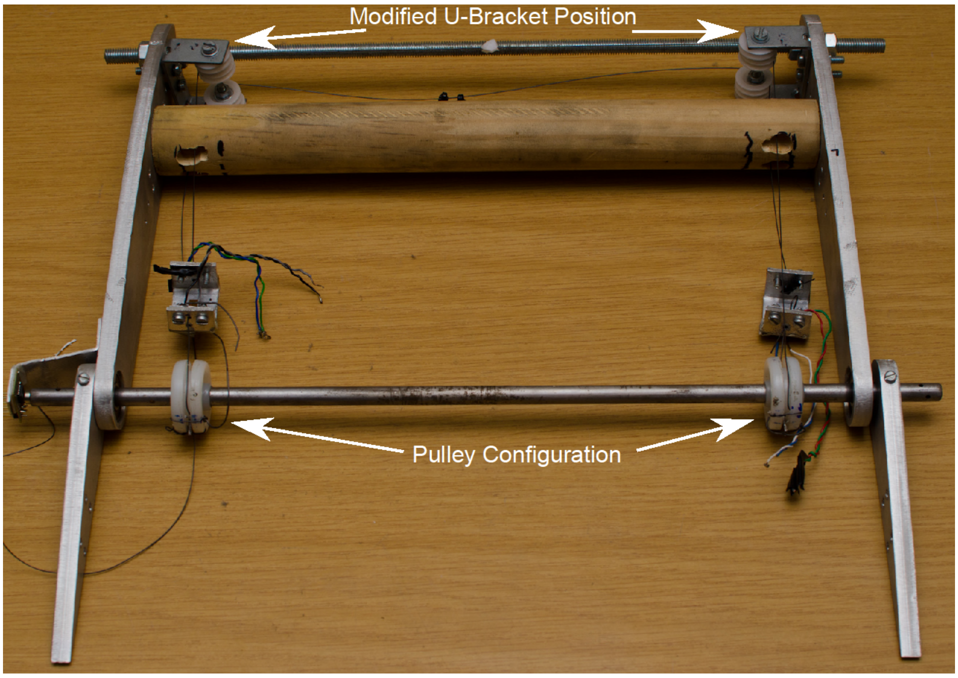

Figure 5.2 – SMA actuator mechanical setup modification

The SMA purchased was of the lower type transformation temperatures at a diameter of 0.508mm. For further information on the supplier and "flexinol" refer to [46].

5.2 Electronic Design

The actual actuator system with all the sensors is shown in Figure 5.3. The primary electronic components consists of a microcontroller, current drivers and sensors, temperature sensors, angle deflection sensor and load cells. A block diagram illustrating the overview and flow of information between the components is shown below. Only one SMA wire setup, illustrated by the red line, is shown to simplify the diagram.

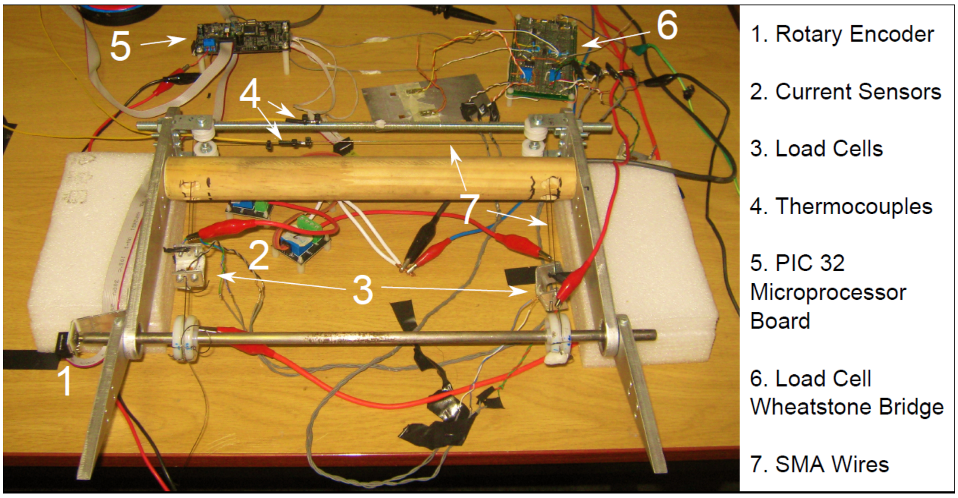

Figure 5.3 – Actuator electronic setup

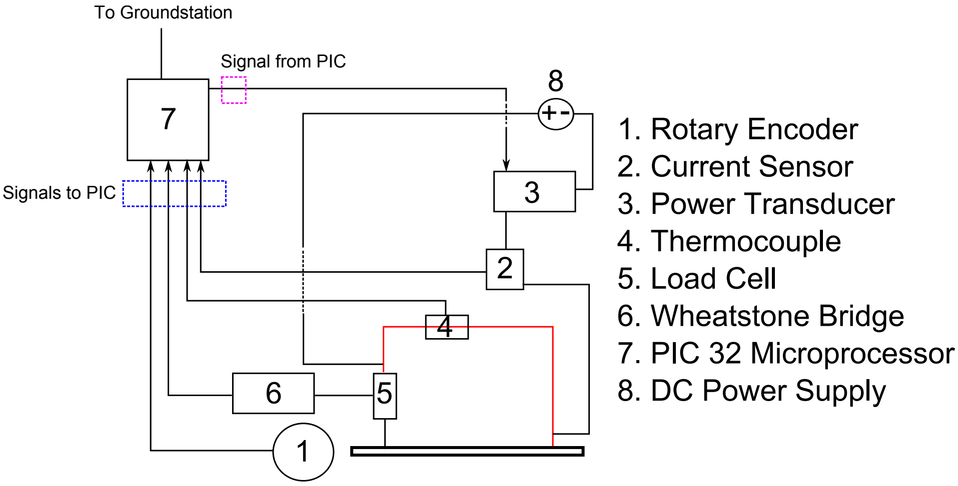

Figure 5.4 – Actuator electronic setup block diagram

5.2.1 Microcontroller

All the sensors and current drivers are connected to a PIC32 Microcontroller. All the relevant sensor manipulations can be done on board the microcontroller. The control algorithms will also be performed by the microcontroller. The PIC32 is able to receive and transmit data from and to the ground station on the PC through a serial communications cable; the data can be logged on the PC, if required. QT Creator was the software applied to develop the ground station software.

5.2.2 Current Driver and Current Sensor

The SMA actuator is driven by a pulse-width modulated voltage signal of constant amplitude. In order to vary the current supplied to the wire, the on time of the pulse-width modulated voltage signal is varied. This results in an overall average current supplied to the wire. A n-channel power transducer is used to switch the voltage supply on and off over the SMA wire. Each wire has its own current driver. In order to switch the transducer, a pulse-width modulated signal is used. This pulse-width modulated signal is obtained directly from the microcontroller. A current transducer based on the Hall Effect is used to measure the current supplied to the respective SMA wires. The current measurement is essential, as it is the control system input to the actuator. The pulse-width modulated voltage is supplied by a regular DC power supply. The current driver and sensors are shown in Figure 5.5 accompanied by the electrical connection diagram.

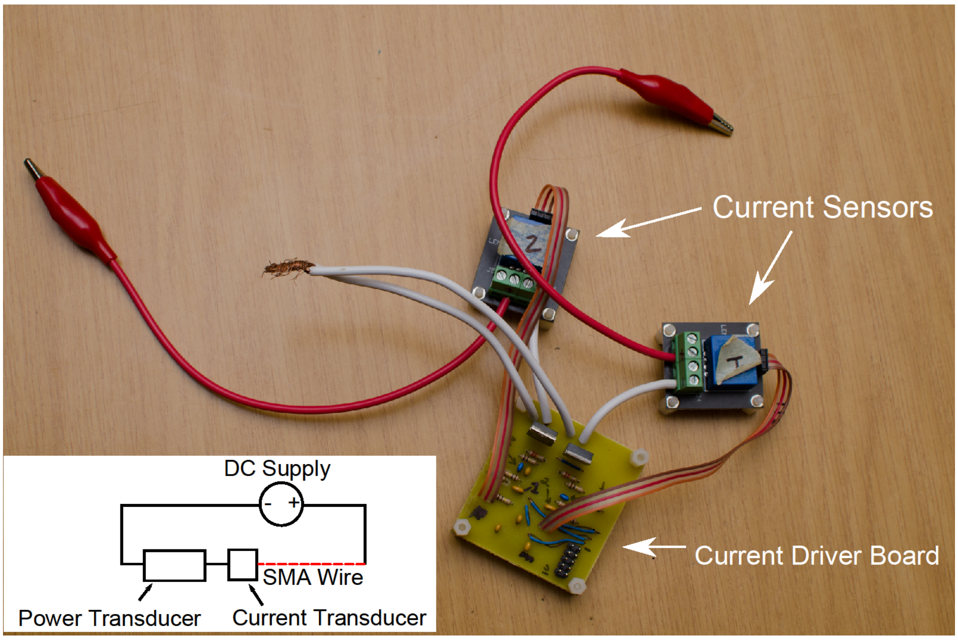

Figure 5.5 – Current driver and sensors

5.2.3 Temperature Sensors

Temperature measurement was essential as SMA operation is directly related to it. The temperature measurement also serves as a safety precaution against overheating the wire above its retraining temperature. Above this temperature the wire will lose its ability to actuate. A type-K thermocouple was used to measure the temperature. Insulation problems occurred when the measurement tip was applied to the SMA wire. Because of the current flowing through the wire, the measurement tip needed to be insulated to prevent current from flowing through it rather than through the SMA wire. A suitable epoxy, H61, was attached to the measurement tip to electrically insulate it, but still allow sufficient heat transfer, thus not degrading the temperature measurement accuracy. Initially additional noise was induced in the temperature measurement. It was found that the noise was induced by magnetic interference from the current flowing through the wire. In order to overcome this obstacle, tin foil was placed over the tip to protect the sensor from magnetic interference.

5.2.4 Deflection Angle Sensor

The output variable to be controlled is the control surface deflection angle. The deflection angle is measured using a contactless magnetic rotary encoder. The sensor, also based on the Hall Effect, measures the change in magnetic field. The change in magnetic field is brought about by a magnet attached to a shaft. As the shaft rotates the magnetic field will follow. The change in magnetic field is sensed and results in an output voltage. The rotary encoder and attaching mechanism are shown in Figure 5.6.

5.2.5 Load Cells

The stresses in both SMA wires were measured with load cells. Each load cell consists of three strain gauges, 2 active and 1 passive, in a Wheatstone configuration. The linear strain gauges were obtained from HBM. The detailed design and calibration of the load cells are described in Appendix B. A photograph of one of the two load cells that were used in the actuator prototype is shown in Figure 5.6.

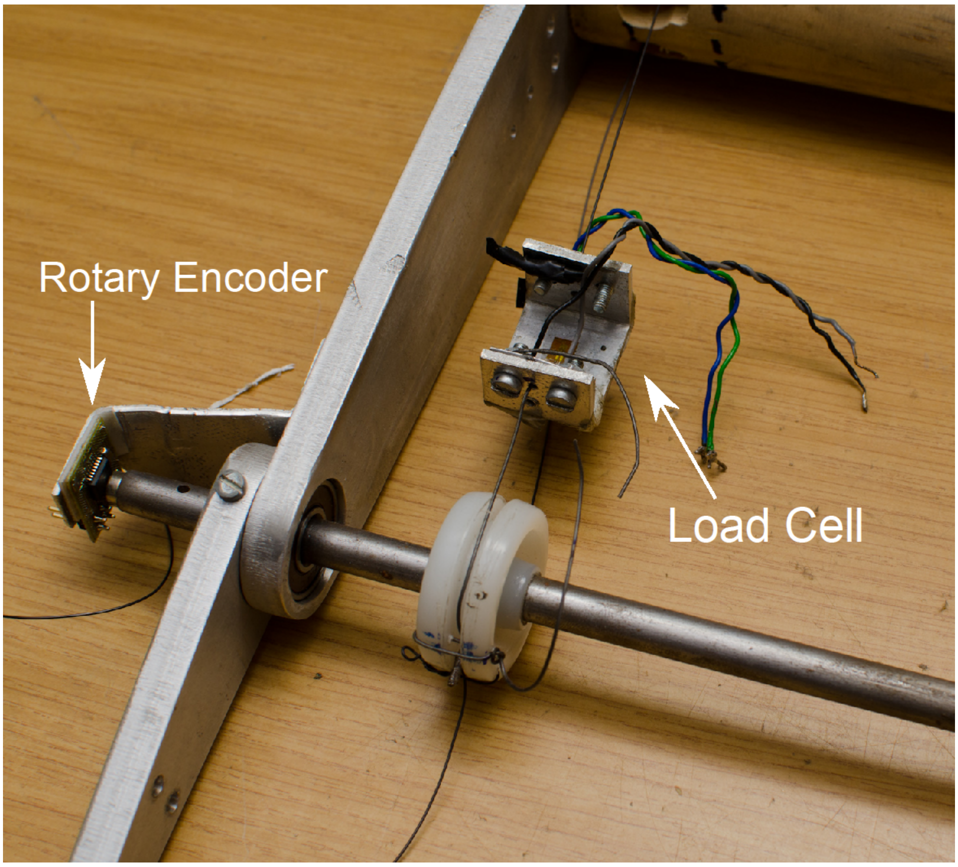

Figure 5.6 – Rotary encoder and load cell configuration

Chapter 6

Identification of Material Model Parameters

System identification was required to determine the constitutive material model and thermodynamic model parameters. By successfully determining these parameters the actuator model can be validated against the practically obtained actuator results. After the successful validation the actuator capabilities are addressed.

6.1 System Identification: Constitutive Material Model

System identification was required to determine some of the unknown parameters of SMA used for the practical setup. These parameters were required to successfully apply the SMA-based actuator model in some of the controller designs. These parameters serve as constant parameters for the Brinson constitutive SMA model. The goal of the system identification is to enable the simulation results to match the practical results to eventually be applied in the relevant controllers. In this section the nine parameters required are briefly discussed with reference to their importance and role in the phase diagram. Because of the current setup, practical limitations and materials at hand, a resourceful method to estimate these parameters was required. Firstly, the common method to determine these parameters is presented along with the precautions required when implementing the transformation temperatures obtained with the current model. The method decided upon and procedures followed are presented next, followed by some simulation results. Finally, the simulation results are compared to the practical results to validate the system identification procedure.

6.1.1 Material Parameters to be Identified

Eight parameters needed identification in order to successfully apply the Brinson model. These parameters are as follows,

- C_a, the gradient of the transformation strip in which the transformation from a mixed martensite to fully austenite state occurs

- C_m, the gradient of the transformation strip in which the transformation from a mixed martensite to a fully detwinned martensite state occurs

- σ_s^{cr}, the stress required to induce a transformation from a mixed martensite to fully detwinned martensite state at temperatures below M_s

- σ_f^{cr}, the stress at which the transformation from a mixed martensite to fully detwinned martensite state at temperatures below M_s will be completed

- M_s, M_f, A_s, A_f, the four transformation temperatures at a zero load

- ϵ_{pre}, the maximum residual strain of the SMA wire

6.1.2 Transformation Temperature Identification Techniques

In practice there are two procedures to determine these parameters. One can use Differential Scanning Calorimetry (DSC), which is a thermo-analytical technique used to characterize the transformation temperatures in a stress-free transformation of an SMA material [31]. This procedure determines the heat required to increase the temperature of a small SMA sample and a reference sample. The SMA's and reference sample's temperatures are held at the same values throughout the heating cycle. The reference sample's heat capacity is known, which enables the calculation of the SMA sample's heat capacity throughout the temperature range. The drawback of the DSC technique is that one is restricted to obtaining the transformation temperatures under a no-load condition and it thus sheds no light on the transformation temperatures at higher stresses. SMA materials are seldom applied in this condition and therefore another technique is required.

The other procedure uses standard stress-strain tests which can be divided into two categories: isobaric tests and isothermal tests. The isobaric test consists of applying a constant stress to the SMA material and then applying a very slow-moving heating and cooling cycle to shift between the martensite and austenite phases. From this test the transformation temperatures for that specific constant load can be determined. This test is applied for various constant loads to obtain the transformation temperature over a broad stress spectrum. The isothermal test entails loading and unloading an SMA specimen while keeping it at a constant temperature. This test is then conducted for a range of temperatures in order to determine the transformation temperatures over the entire temperature range. This test is also ideal to determine the critical stresses at temperatures below M_s.

The SMA actuator model applied in the simulation constrains transformation and therefore actuation to the transformation strips. The way in which the transformation temperatures are calculated and presented by the SMA supplier can sometimes be misunderstood when applied in these types of models. Figure 6.1 shows the strain-temperature relationship obtained from a typical isobaric stress-strain test as well as how these transformation temperatures are typically determined. Initially the specimen is in an elongated state at a temperature below A_s. Heat is applied which transforms the specimen to the full austenite state, forcing the specimen to contract. When cooled, the constant stress applied to the specimen is large enough to cause a detwinning process, forcing the specimen to elongate.

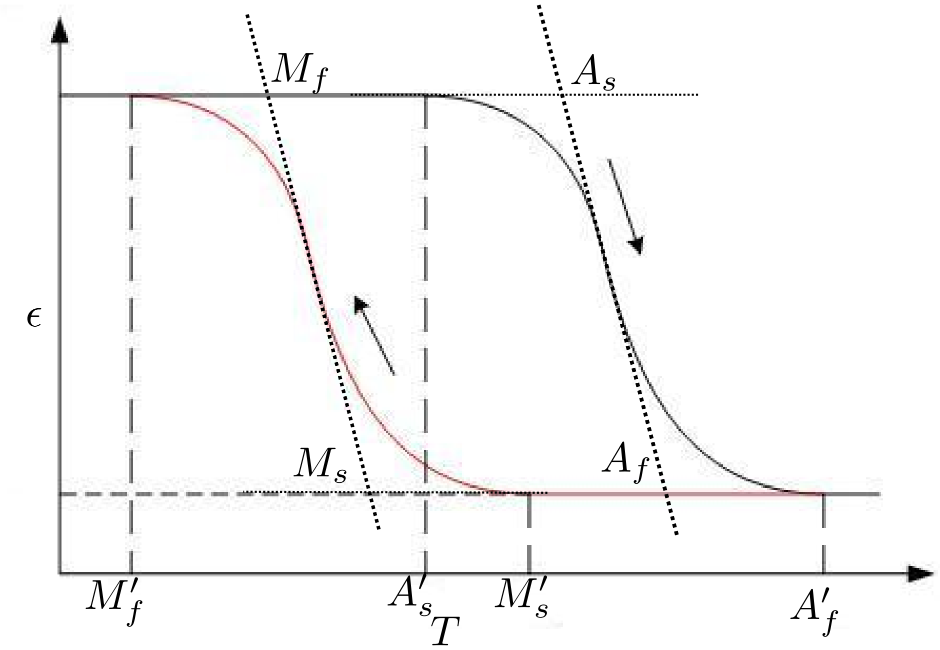

Figure 6.1 – Strain temperature response: Determining the transformation temperatures

A common technique in determining the transformation temperatures entails drawing tangent lines to the heating and cooling segments and taking the transformation temperature as the point at which these lines intersect. This technique is illustrated by the dashed lines in Figure 6.1. One can easily see the pitfall in using this technique for the specific SMA model applied in the simulation. According to this technique, transformation occurs between the respective transformation temperatures illustrated by the diamond shape in Figure 6.1. One can clearly see a small amount of strain still visible below A_s and above A_f respectively. The same applies to the cooling curve transformation temperatures M_s and M_f. Not taking this strain into account will cause the model to under-predict the temperature at which actuation occurs and ends, whether in the cooling or heating phase. One generally wants the transformation temperatures to indicate the exact temperature at which transformation occurs. This results in the transformation temperatures on the y-axis in Figure 6.1 indicated by the accents. One notices that the A'_s temperature is below the M'_s temperature. In order to incorporate this problem into the applied model, the transformation temperatures are slightly modified to include these small strain gains into the model. Keeping this problem in mind, the A_s and M_s temperatures are expected to be much lower and higher respectively than specified by the supplier. The error needs to be taken into account, otherwise the SMA actuator model will indicate that no transformation has occurred, while the actuator has already been actuated, thereby causing a lag in the model's prediction.

6.1.3 Experimental Technique Applied

In order to estimate the unknown parameters of the macroscopic model, the actuator had to be put through a series of actuation runs. The procedure chosen to determine these parameters depended heavily on the specific setup and sensors at hand. The parameters to be identified describe the stress temperature plane and thus call for temperature and stress measurements. Ultimately it was decided to imitate the isobaric stress heating and cooling cycle. For this procedure the bottom wire of the actuator was disconnected from the pulley, leaving only the top wire able to actuate. To simulate a load, a constant weight was attached to the aileron to achieve a relatively constant load in the top wire. This is called a relative constant load as the stress would vary as the aileron position would change during the heating cycle due to contraction. This effect was taken into account when determining the stress levels at which the transformation occurred. The top wire was allowed to be pre-strained by the stress generated in it by the mass attached to the aileron. In some cases where these loads were too small to induce elongation, the wire was pre-strained by hand ensuring a visible amount of pre-strain. After completing the pre-strain procedure the heating and cooling cycle was applied. As a result of the lag in the temperature sensors caused by a 250 milliseconds measurement conversion time, it was decided to force the top wire to follow a slow varying, constant rate, temperature curve of approximately $\frac{7^{\circ}C}{min}$. Knowing the temperature measurement varies slowly ensures that the measured temperature will quite accurately describe the actual temperature state. The slow varying temperature curve is also required to indicate the transformation temperatures more clearly. The corresponding stress - which is known because of the constant applied load and control surface deflection measurements, which can be related to the strain in the SMA wire through the configuration kinematics - is also logged. Applying these tests and combining the logged variables allow for the proper estimation of the unknown parameters. It should be noted that the maximum stress applied to the wire is rarely above $172MPa$ as this is the maximum safe stress, as stated in the supplier data sheet, for operation without inducing degradation in the maximum recoverable strain.

6.1.4 Identification Procedure

The aim of the procedure is to determine the transformation temperatures at which contraction start and ends and detwinning start and ends for the specific loads applied through each run. The typical phase diagram presented earlier (Chapter 2) is shown again in Figure 6.2. This phase diagram was created according to the transformation temperatures specified by the supplier of the SMA used in the practical setup. The critical stress transformation stresses, σ_f^{cr} and σ_s^{cr}, and rate of transformation temperature

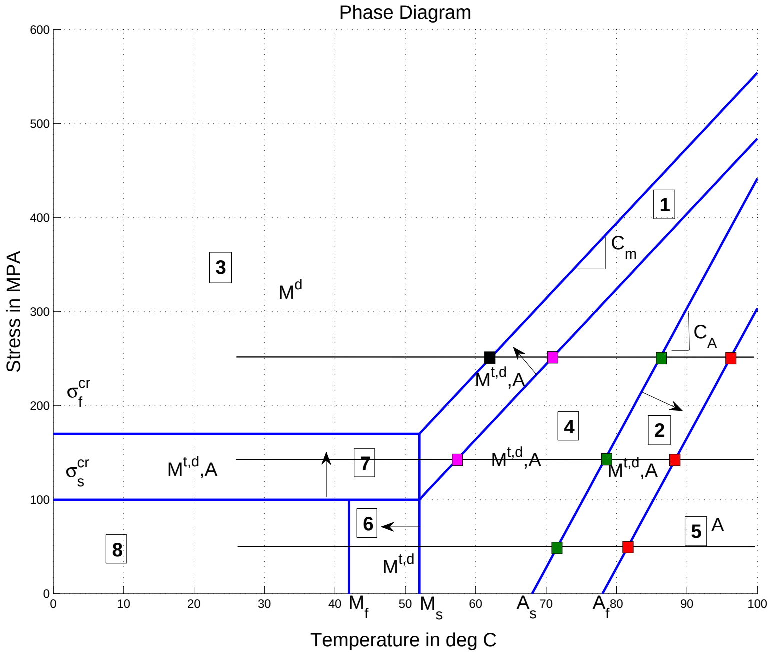

Figure 6.2 – Phase diagram: Parameter estimation procedure

increases, C_m and C_A, are shown but not known . It is necessary to determine these unknown parameters.

Figure 6.2 also illustrates the process occurring during the heating and cooling cycle for various constant stresses. The results will give as a good indication of the temperature at which actuation starts, indicated by the green squares, and at which it finishes, indicated by the red squares. It will also tell us at which temperature the detwinning starts, indicated by the pink squares, and whether de-twinning actually occurred. If it did not occur, it indicates that we are below the σ_s^{cr} stress. In the same way the transformation temperature at which detwinning finishes can be determined, indicated by the black square, and whether it actually occurred. If not, we are currently operating at a stress below the σ_f^{cr} magnitude. In that way information about the transformation stresses can be extracted from the results. Typical temperature-strain relationships which can be expected are shown in Figure 6.3. These responses were obtained from the transformation temperatures provided by the suppliers. Figure 6.3a indicates the temperature-strain relationship for a constant stress below σ_s^{cr}, which means that no detwinning will occur as the stress is too small. Figure 6.3b illustrates a total transformation for a constant stress above σ_f^{cr}. The arrows in the figure indicate the direction of the transformation. Practical results in the same form as those indicated by Figure 6.3 are expected.

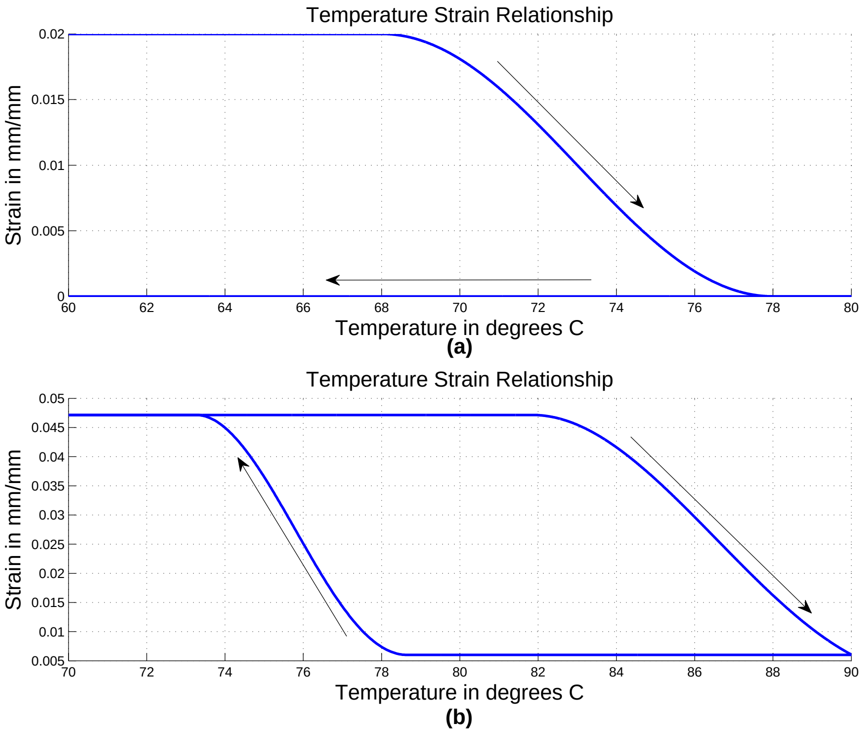

Figure 6.3 – Temperature strain relationship; (a) Expected response for σ below σ_s^{cr}; (b) Expected response for σ above σ_f^{cr}

6.1.5 Identification Results

Heating and cooling cycles were applied for 7 different constant stresses. Before each heating cycle was applied, the wire was allowed to detwin as a result of the constant load subjected to it. By doing this, the majority of the wire's composition was forced to consist of detwinned martensite. After the de-twinning process was completed, the wire was left to cool to room temperature, after which the heating and cooling cycle could commence.

Figures 6.4 and 6.5 shows the results obtained for the zero and maximum load respectively. Figure 6.4, as expected, resembles Figure 6.3a as both stresses are below σ_s^{cr}. The heating transformation can be divided into three distinct parts. An initial transformation where the transformation starts, a linear transformation where the transformation is mainly linear and the end of transformation, where the transformation stops. These regions are indicated by the numbers 1, 2 and 3 on Figure 6.4 respectively. The regions indicated are very similar to those predicted by the model in Figure 6.3a, the only noticeable difference is the magnitude of the temperature range in which the transformation occurs. The tail of the transformation dies away over a large temperature range compared to that of the initial transformation. This suggests that the model

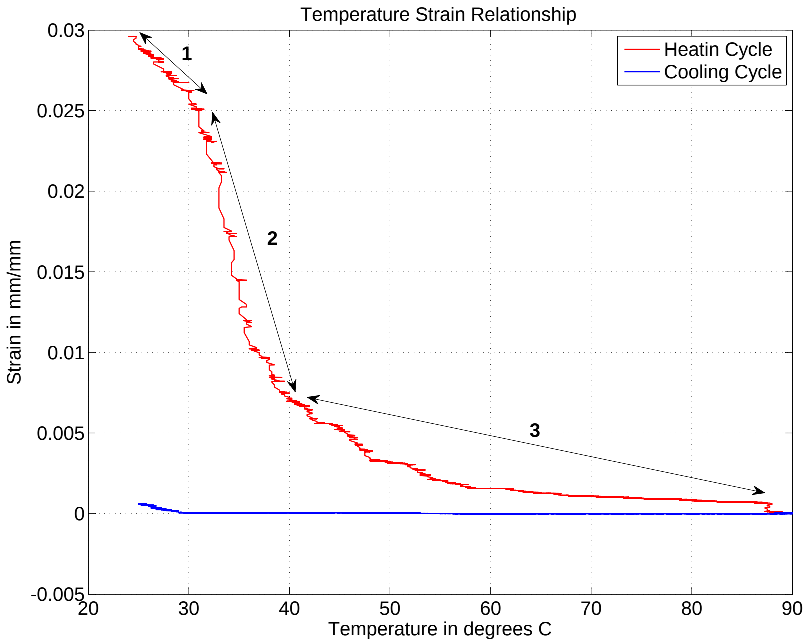

Figure 6.4 – Temperature strain relationship: Experimental response for $\sigma = 0MPa$

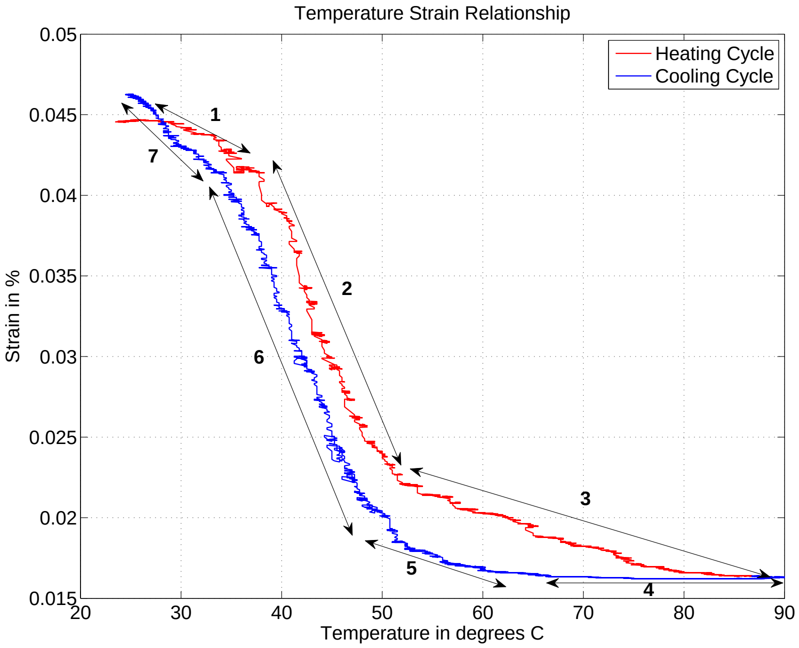

Figure 6.5 – Temperature strain relationship: Experimental response for $\sigma = 160MPa$

will not be able to predict the actual transformation because of the model's symmetrical nature. But more on this in Section 6.1.6. Figure 6.5, as expected, resembles Figure 6.3b as its constant load is above σ_f^{cr}. It therefore illustrates a full transformation, indicating all four transformation temperatures. Four additional regions are visible other than those mentioned for Figure 6.4: (i) a dead zone in which no transformation occurs, (ii) an initial detwinning stage, (iii) a linear detwinning stage and (iv) an end of de-twinning stage. These regions are indicated by the letters 4, 5, 6 and 7 in Figure 6.5 respectively.

By using the data gathered from the heating and cooling cycles, the transformation temperatures could be determined at the respective stresses. The technique of drawing tangent lines for determining the transformation temperatures is illustrated in Figure 6.6. The transformation temperatures can be approximated as $A_s = 31°C$ and $A_f = 40°C$, which already differs from those provided by the supplier. One can also notice considerable amount of strain being regained at temperatures below A_s and above A_f. Figure 6.6 sheds no light on the detwinning transformation temperatures. When the cooling cycle commences, the wire does have a tendency to relax resulting in a minor strain loss, as shown at approximately $30°C$, although the literature states that no strain loss will occur after a specimen has undergone a heating cycle under no load.

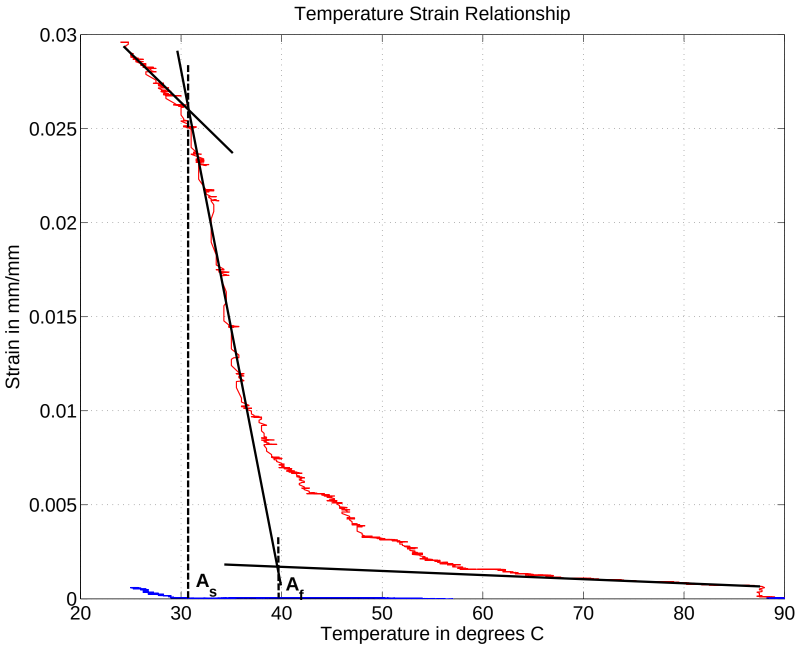

Figure 6.6 – Temperature strain relationship: Determining the transformation temperatures

By applying the tangents procedure mentioned above, the required transformation temperatures could be extracted from all the results. A few assumptions are made before illustrating the practical results. It is assumed that the parameters C_a and C_m are constant for both the start and finish transformation temperatures curves respectively. In other words, the gradient of transformation strip 2, as indicated by Figure 6.2, is constant for both the A_s and A_f transformation lines. This applies to transformation strip 1 as well. Figure 6.7 shows the results obtained after applying all the heating and cooling cycles. The temperatures and relevant stresses for the specific transformation temperature are indicated as well as their linear approximations. As one can see, the results are linear as expected. One interesting fact is that the M_s transformation curve intersects the A_s transformation curve at higher stresses resulting in these two regions overlapping. The gradients of the two heating transformation temperatures are relatively similar and an average value will be implemented. Unfortunately very little data describing the M_f transformation curve could be collected as the detwinning transformation didn't complete successfully because of the low stress the wire was subjected to. As can be seen at the beginning of the M_s transformation curve, three temperature are bunched at approximately the same temperature, giving an indication of the σ_s^{cr} position as indicated by Figure 6.7.

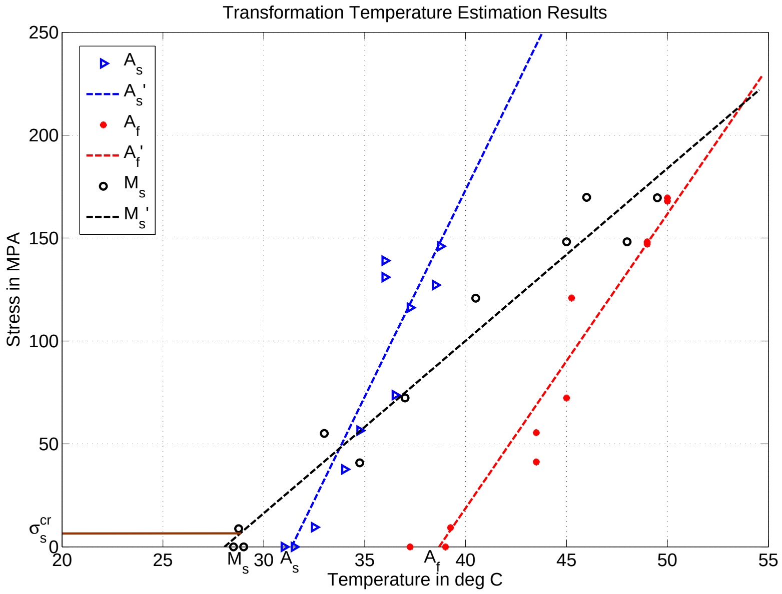

Figure 6.7 – Parameter estimated phase diagram

As mentioned above, insufficient data were collected to determine σ_f^{cr}, therefore an alternative method was required to determine this parameter. In order to get an indication of this parameter, various loading-unloading tests, at incremental maximum stresses, were applied to the SMA wire at a constant temperature below M_s. The wire was heated to the fully austenite state and left to cool to room temperature prior to the loading cycle. After unloading, a heating cycle is applied to determine the residual strain for the specific load applied during the loading cycle. The procedure will result in two outcomes, namely determining σ_f^{cr} and the maximum residual strain, ϵ_{pre}, the wire is capable of. Investigating the residual strain will indicate whether the wire was fully detwinned during the loading stage and can be identified by the stage where constant residual strain is recorded even after increasing loads are applied. The procedure is better explained by Figure 6.8. It shows the stress-strain relationship for various maximum stresses. In the interest of clarity, only four loading cycles are shown, as indicated by the numbers. A load is applied to the wire, which will induce a stress resulting in a certain amount of residual strain after unloading, indicated by ϵ_1 and ϵ_2 for cases 1 and 2 respectively. The goal of this technique is to induce a load forcing a full detwinning transition, case 4, which will indicate the maximum residual strain, the other outcome of this procedure. Increasing the stress above that of marker 4 will induce the same residual strain, thus indicating the maximum stress required for a full detwinning process, or σ_f^{cr}.

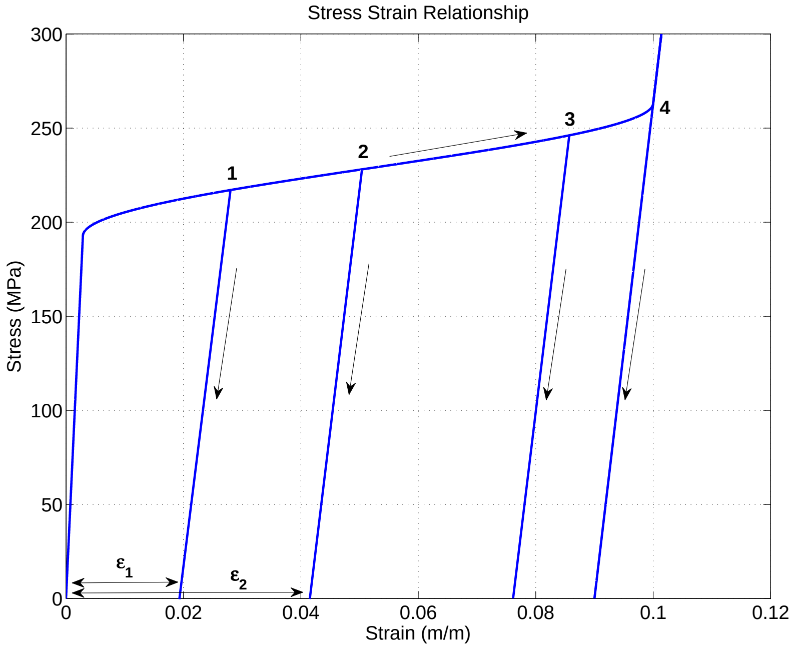

Figure 6.8 – Determining ϵ_{pre} and σ_{cr}^{f}

Ten different maximum stresses were applied and the residual strains measured. The maximum load was limited to $210MPa$, as previously mentioned, staying below the maximum recommended safe stress, not wanting to degrade the wire's performance. The results obtained are shown in Figure 6.9. The response obtained is approximated as a linear response, indicating that the stress levels are between the maximum and minimum critical stresses. All we can deduce from the results is that $\sigma_f^{cr} > 210MPa$ and

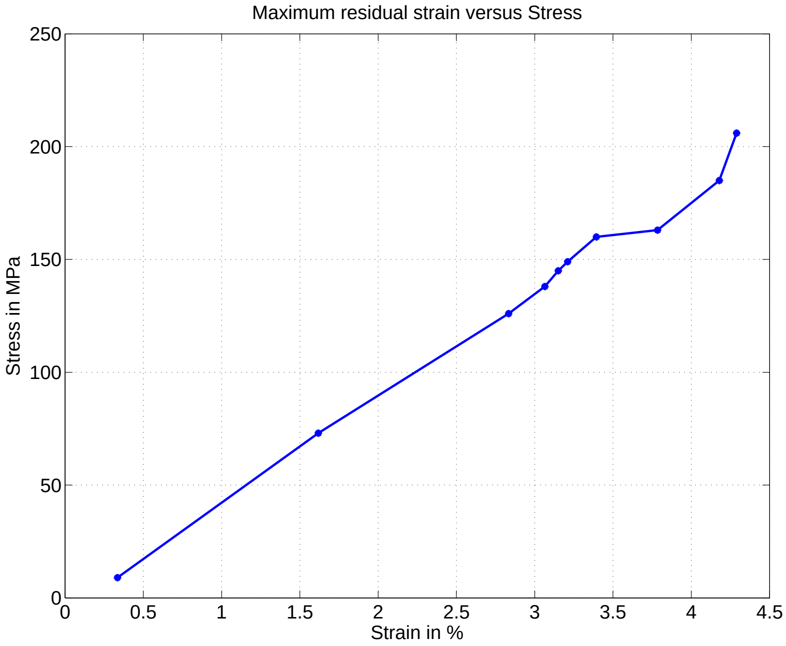

Figure 6.9 – Residual strain obtained for the applied load

that the maximum residual strain is larger than 4.3%. The σ_f^{cr} parameter will therefore be selected as $210MPa$ and will not influence the accuracy of the model greatly as practical stresses in the prototype will rarely exceed that magnitude. The maximum residual strain will be tweaked to ensure the simulation results corresponds to the practical results.

6.1.6 Fitting the Simulation Model to the Measured Data

From the results obtained the required values of M_s, M_f, A_s and A_f at zero load as well as C_a, C_m, σ_s^{cr} and σ_f^{cr} could be determined. In order to obtain the same C_a and C_m values for the finish and start transformation temperatures respectively, the average of the two gradients were taken. The following results were obtained as shown in Table 6.1.

It was necessary to validate the experimental calibration data with the model in order to evaluate its performance. In order to illustrate this, three heating-cooling cycles at three different constant stress magnitudes were investigated, a zero-stress case and two cases between the two critical stresses. From these results the performance of the Brinson model to describe the SMA behaviour can be evaluated and adjustments can be made, if required. Figure 6.10 shows the zero stress, $135MPa$ and $150MPa$ cases respectively. For the zero-load case the wire is initially in an elongated state. As the temperature increases, the wire contracts to zero strain. Figure 6.10a does indicate

Parameter Estimation Data	
M_s	$27.8°C$
M_f	$21.6°C$
A_s	$31.9°C$
A_f	$38.1°C$
C_m	$9.1MPa/°C$
C_a	$17.2MPa/°C$
σ_s^{cr}	$15MPa$
σ_f^{cr}	$210MPa$
ϵ_{pre}	0.043

Table 6.1 – Estimated parameters

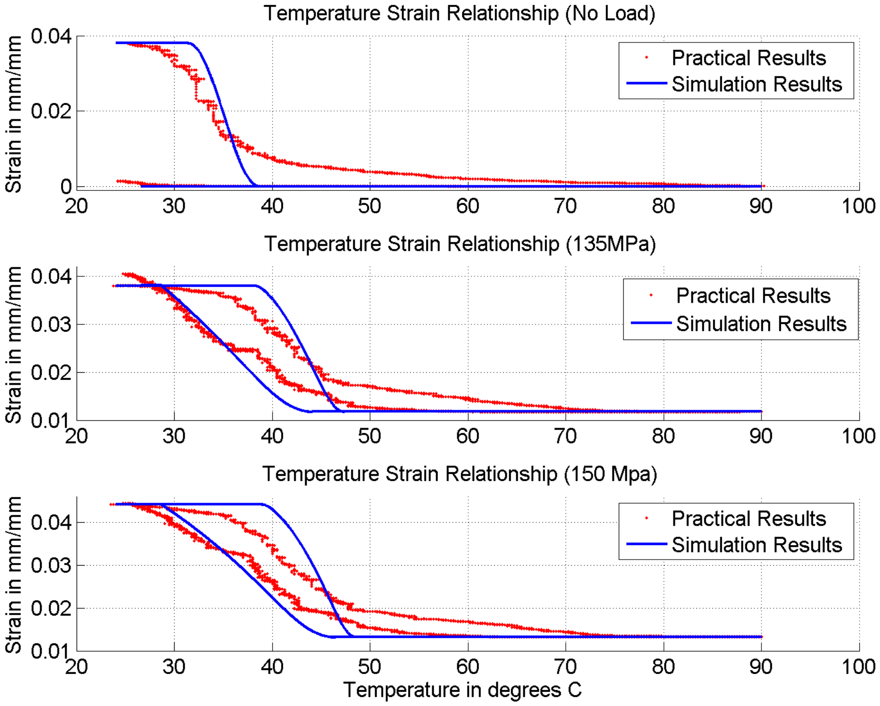

Figure 6.10 – Simulation results versus practical results for the determined transformation temperatures

that the current model can capture the transformation to a certain degree, although not 100% accurately. The model under-predicts the start of the transformation and over-predicts the end of the transformation because of the relatively long tail, as mentioned in Section 6.1.5. The linear part of transformation is not exactly matched. Figure 6.10b illustrates the transformation from a partially detwinned state to a fully austenite state and back to a partially detwinned state at a load of approximately $135MPa$. Again the same under- and over-prediction is noted in the heating transformation, while a similar trend is seen in the cooling transformation. Figure 6.10c shows the applied heating and cooling cycle at a constant stress of $150MPa$. This is the best prediction, but reveals the same short comings as the previous cases.

From an evaluation of the practical and simulation results one can make the following deductions: the model is capable of predicting the transformation to an extent; the model does predict the correct amount of residual strain, albeit not at the right temperature. A feature noticed is the offset in the predicted response and the actual response during the linear part of the transformation. This is because of the method used when the transformation temperatures were determined. As mentioned previously, the method neglects a small amount of strain at the start end of the transformation cycles. By modifying the transformation temperatures, the linear transformation can be matched to an extent and a better response can be obtained. By decreasing and increasing the A_s and A_f respectively, a better match to the practical results could be found. Similarly, the M_s transformation was increased slightly. The tweaked parameters are shown in Table 6.2. The results after changing the transformation temperatures, as mentioned above, are shown in Figure 6.11. This clearly illustrates a much better response, resulting in the transformation temperatures that will be applied in the control implementation. This stresses the importance of the technique adopted for determining the transformation temperatures when applying these temperatures to the specific model.

Parameter Estimation Data	
M_s	$28.7°C$
M_f	$21.6°C$
A_s	$31.4°C$
A_f	$38.7°C$
C_m	$9.1MPa/°C$
C_a	$17.2MPa/°C$
σ_s^{cr}	$15MPa$
σ_f^{cr}	$210MPa$
ϵ_{pre}	0.043

Table 6.2 – Revised estimated parameters

6.2 System Identification: Thermodynamic Model

The final step before theoretical SMA model and controller validation could commence was to ensure that the temperature dynamics correspond to the practically obtained measurements. In order to achieve this a single SMA wire was subjected to various constant current inputs while recording its temperature. This was done under forced convectional conditions. By doing this the first order response time constant and steady state gain for the various inputs could be determined. In turn this would enable the identification of the convectional heat transfer constant, h. The transfer function of a

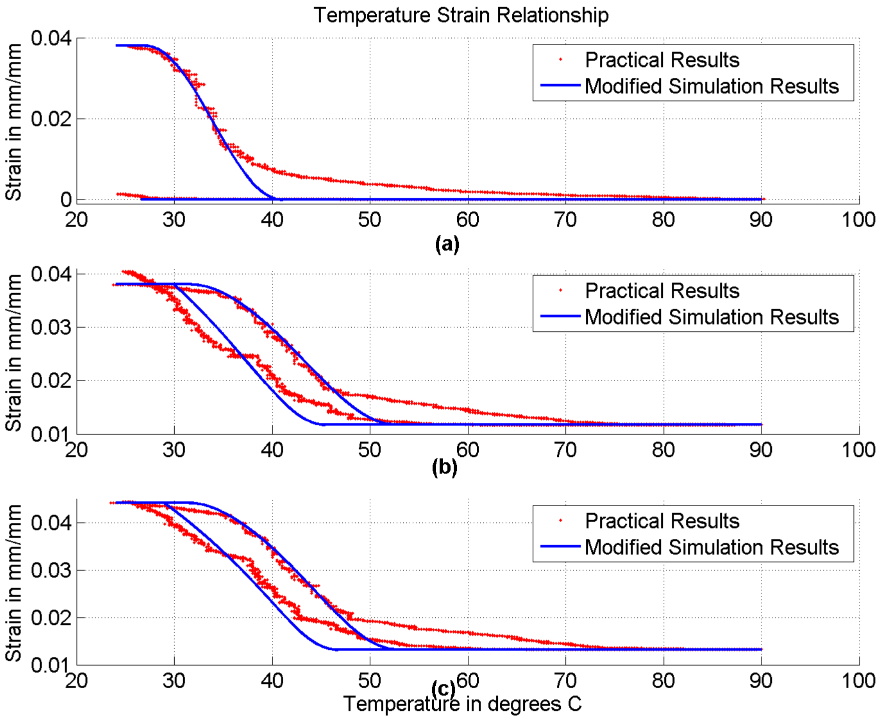

Figure 6.11 – Simulation results versus practical results for the modified transformation temperatures

general first order system is shown in equation 6.2.1, with K_{ss} being the steady state gain and τ the time constant.

$$\frac{G(s)}{U(s)} = \frac{K_{ss}}{\tau s + 1} \tag{6.2.1}$$

The temperature dynamics, shown in equation 6.2.2, can be converted to a first order transfer function resulting in relationships for K_{ss} and τ as shown in equations 6.2.6 and 6.2.7 respectively. The temperature dynamics

$$\dot{T} = C_1(T - T_\infty) + C_2 u \tag{6.2.2}$$

with,

$$C_1 = -\frac{hA}{\rho c_p V} \tag{6.2.3}$$

$$C_2 = \frac{R}{\rho c_p V} \tag{6.2.4}$$

$$u = i^2 \tag{6.2.5}$$

results in,

$$\tau = \frac{\rho c_p V}{hA_s} \tag{6.2.6}$$

$$K_{ss} = \frac{R}{hA} \tag{6.2.7}$$

By determining K_{ss} and τ experimentally one can determine the heat transfer coefficient, h, and specific heat, c_p, as the other parameters are all known.

6.2.1 Measured Temperature Responses to Current Inputs

Figure 6.12 shows the temperature measurements for various inputs, as indicated, under forced convection. As expected a first order response is obtained. The time constants and steady state gains with respect to the current and current squared are shown in the Table 6.3. According to the differential equation one expects a constant steady state gain with respect to the current squared. This is not the case as seen in the practical results. There is however relatively constant steady state gains with respect to the current. This is most probably caused by assuming constant parameters in equation 6.2.2 when they in fact fluctuate. The resistance, R, of the wire and specific heat, c_p,

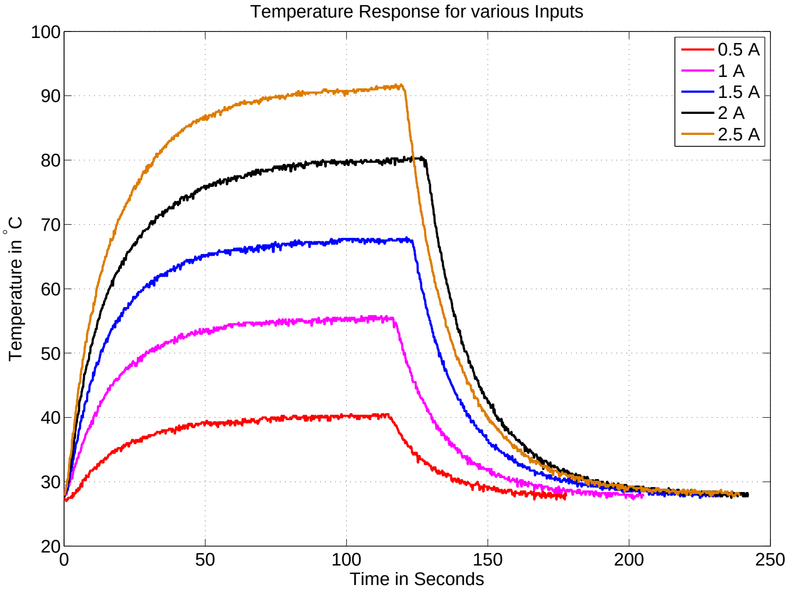

Figure 6.12 – SMA temperature response for various constant inputs

	$0.5A$	$1A$	$1.5A$	$2A$	$2.5A$
τ	$18.1s$	$17.3s$	$16.2s$	$17.2s$	$17.45s$
K_{ss} with respect to (I^2)	49.2	27.5	17.6	13	10.2
K_{ss} with respect to (I)	26.6	27.5	26.4	26.1	25.4

Table 6.3 – Temperature response specifications

changes with temperature. Modelling these parameters introduces a completely new challenge and is therefore neglected in this study.

6.2.2 Comparison of Simulated and Measured Temperature Responses

In order to ensure the simulation results match the practically obtained results the temperature dynamics will be adapted to be a function of i and not i^2. By applying this alteration the correct temperature response is obtained during the simulation. The revealed contradiction is as a result of assuming constant parameters when they in fact fluctuate. The SMA's electrical resistance, r, and specific heat, c_p, fluctuates with temperature. Generally a SMA's resistivity will increase during a heating cycle. This corresponds to the observed decrease in steady state gains at larger input magnitudes inducing higher temperatures. Applying the modification for $\tau = 17.3$ and $K_{ss} = 26$ resulted in accurate simulation and practical result correlation as illustrated in Figure 6.13.

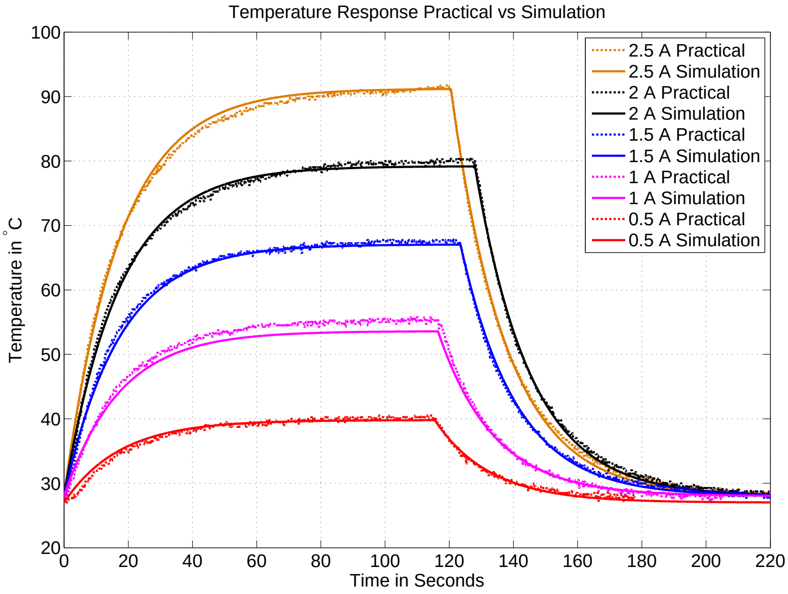

Figure 6.13 – SMA temperature response: Simulation versus practical results

When performing the first open-loop response comparisons a temperature sensor deficiency was observed. It was noticed that the temperature reading at the start of aileron movement differed from the corresponding transformation temperature which would initiate that movement. In other words the temperature sensor indicated actuation at much lower temperatures than anticipated by the practically obtained transformation temperatures. This suggests the temperature sensor is lagging the actual SMA wire temperature. This is probably caused by the rapid temperature increase in the wire and the method applied when attaching the sensor to the wire. The fact that a minor air gap exists between the thermocouple and wire, and the isolation adhesive used between the wire and the thermocouple could have contributed to this lag. The air gap and adhesive will act as a thermal barrier resulting in a delayed measurement. Keeping in mind that the steady state temperature is indeed correct, as the thermocouple would eventually reach the temperature of the wire, it was decided to decrease the time constant, τ, of the first order temperature dynamics until the practically acquired control surface deflection results were matched by simulation. Figure 6.14 illustrates the approach taken. The temperature dynamics now consists of two first order transfer functions, one with a faster time constant τ_2, to speed up the transient response, in conjunction with the practically obtained steady state gain and the other consisting of the practically obtained time constant, τ_1, and a steady state gain of one. The output of the first transfer function will be considered as the actual temperature reading while the output of the second will correspond to the measured temperature reading. By applying this approach the simulation results could be applied to successfully match the practically obtained results.

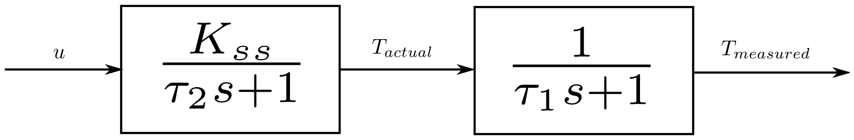

Figure 6.14 – Temperature sensor lag compensation block diagram

6.3 System Identification: Actuator Model

This section focuses on validating the theoretical actuator model. Firstly practically obtained open-loop responses are presented. This will offer some insight into the actuator capabilities in terms of speed of response and maximum obtainable deflection which will be summarised in the actuator capabilities section. The open-loop responses were measured by applying current cycles of constant magnitude to the respective SMA wires while they are subjected to both forced and natural convection. A cycle would be applied to the bottom wire followed by a current cycle in the top wire resulting in the open-loop response over the entire region of operation.

Secondly the theoretical actuator model is evaluated against the practically obtained open-loop results. This is conducted to verify the applied model's validity and accuracy.

6.3.1 Measured Deflection Angle Responses to Current Inputs

In order to obtain multiple open-loop responses the actuator was subjected to various current inputs at forced and natural convective conditions. Figure 6.15 shows the open-loop control surface response at various constant current inputs while subjected to forced convectional conditions. The input ranges from 0.5 to 2.5 amperes in increments of 0.5 amperes. Initially the control surface is in the vicinity of $-21°$. The reason for the inconsistent starting deflections is due to the procedure applied to obtain the initial condition. In all the cases the actuator was forced to a maximum negative deflection and then left to cool prior to applying current in the opposing wire. During the cooling stage stress relaxation occurs which causes the control surface to move in the opposite direction which resulted in the starting deflections as seen in Figure 6.15. Due to the nature of the configurations mechanical integrity the experienced stress relaxation would never be identical resulting in the inconsistent starting deflection.

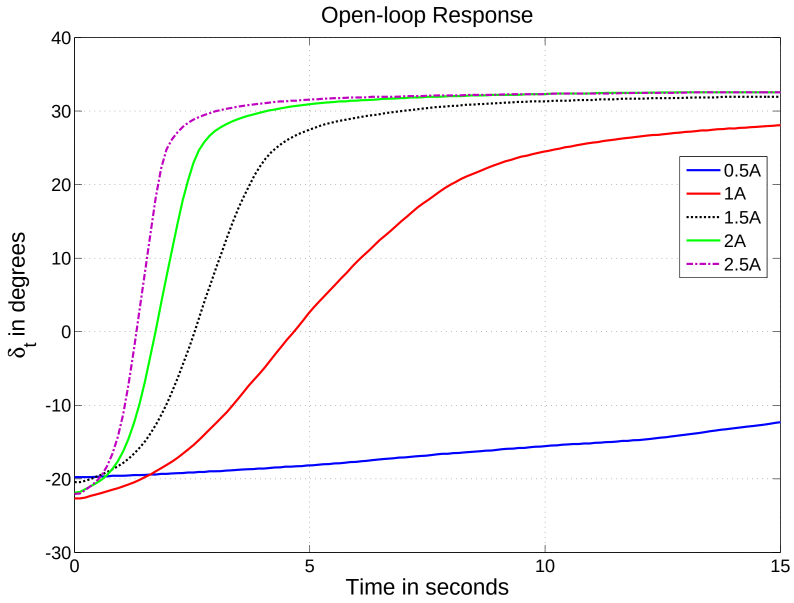

Figure 6.15 – Control surface deflection open-loop response at incremental inputs

With the introduction of current the control surface progresses to the maximum positive deflection of approximately $32°$. Note that the slow response of the 0.5 ampere input is due to the energy input being only slightly larger than that being removed from the system through convectional heat losses. Therefore only a small increase in temperature is experienced resulting in the very slow control surface response.

In order to later on determine the maximum obtainable deflection or stroke of the prototype the actuator was forced to the maximum obtainable positive deflection followed by actuation in the opposite direction in order to determine the maximum obtainable negative deflection. This procedure was conducted for various constant current inputs with the wires being subjected to natural and forced convectional conditions. For illustrative purposes only a 2 ampere input cycle is considered.

Figure 6.16 shows the sensor measurements for an open-loop response subjected to a 2 ampere input cycle. Initially the actuator is in a relaxed state at approximately $-22°$ with relatively small equivalent stresses, approximately 35MPa, in both wires due to the actuators pre-strained condition. Forced convectional conditions were achieved by a fan blowing air over both wires simultaneously. For this specific open-loop response the actuator was subjected to current cycles of 2 amperes, as shown in Figure 6.16c, to obtain the maximum deflection in either direction. Note that the actuator was allowed to cool down after saturating to prevent over stressing and heating the wires.

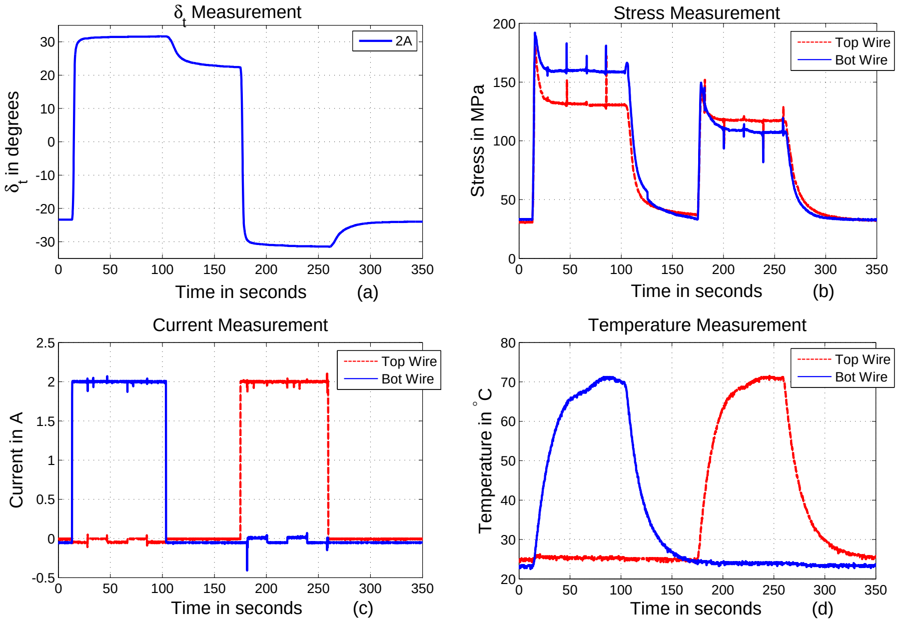

Figure 6.16 – Experimental open-loop response; (a) Control surface deflection ; (b) Stress measurement ; (c) Current measurement ; (d) Temperature measurement

The measured temperature response is shown in Figure 6.16d, illustrating very similar first-order behaviour for both the top and bottom wire heating cycle. A steady state temperature of approximately $70°C$ is recorded.

An interesting phenomenon noticed is the tendency of the actuator to relax when zero current is applied. This is caused by the stress release within the heated wire, starting at approximately 100 seconds in Figure 6.16b, as a result of the decrease in temperature which triggers the transformation of austenite into de-twinned martensite, the softer material state. The softening of the active wire enables the passive wire, which remains at a constant stiffness, to pull the control surface in the opposite direction. This phenomenon will further be referred to as stress relaxation.

The stress measurements are shown in Figures 6.16b. The stress measurements illustrate a rapid increase in stress as actuation starts followed by stress stabilisation in both wires. The rapid increase in stress corresponds to the ongoing formation of austenite while the followed constant stress level indicates a complete austenite transformation. After the complete austenite transformation, the active SMA wire enters a dead zone which results in no change in stress. It is observed that the maximum recorded stress is less for a negative deflection than that experienced during a positive deflection. This might indicate a balancing error resulting from one wire being slightly more tensioned than the other at the start of the simulation.

6.3.2 Comparison of Simulated and Measured Deflection Responses

In order to verify that the mathematical model agrees with the practical system, the simulations were performed using the same conditions as applied during the practically obtained open-loop responses. Only the first step command of the $2A$ open-loop cycle will be shown to demonstrate the similarities between the simulation and practical open-loop results. Figure 6.17 illustrates the comparison between the practically obtained control surface deflection and the simulation response. The model approximates the actual response with relative accuracy during the majority of the response but struggles during the starting and finishing stages of the transformation. During the start of actuation the model lags the actual response while it precedes the response during the final stages. The model predicts the linear part of actuation quite accurately. The lagging and leading of the simulation response is directly related to method by which the transformation temperatures were determined. During the transformation

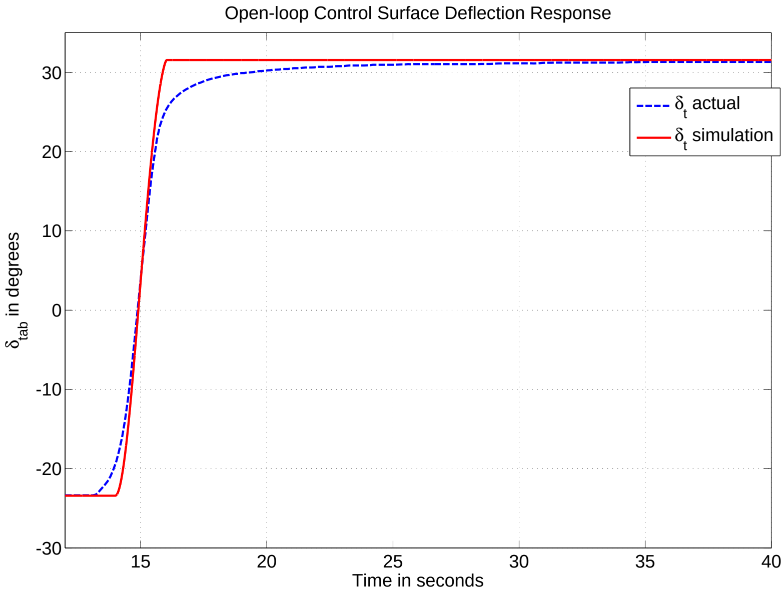

Figure 6.17 – Practical versus simulation results for an open-loop response

temperature estimation in section 6.1 it was noted that using the tangent lines method could result in under- and overpredicting the A_s and A_f transformation temperature respectively. This is the exact case as seen in the simulation results. Nonetheless the model predicts the actual response accurately enough to be implemented as it captures the key elements of the response.

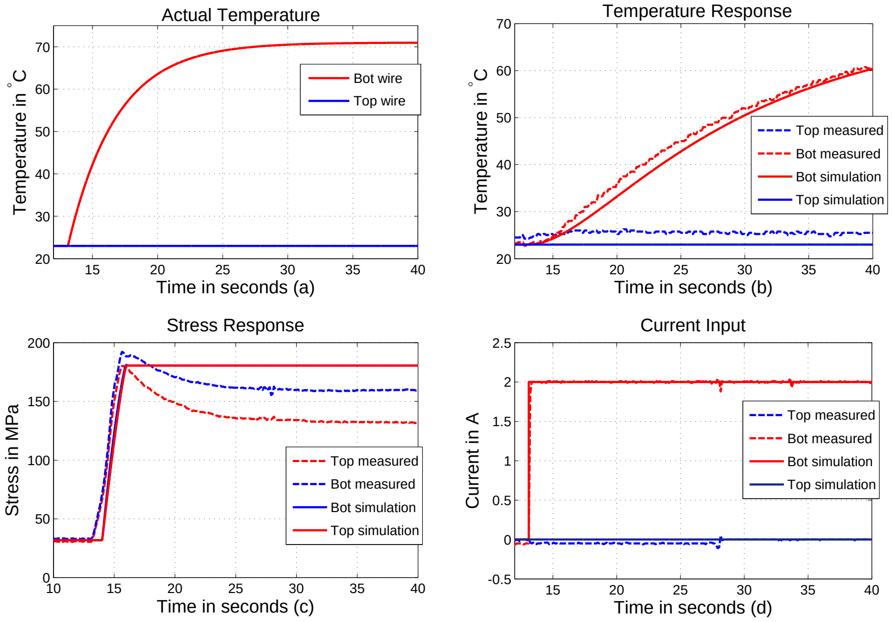

Figure 6.18 – Simulation versuss practical open-loop state measurements; (a) Actual temperature ; (b) Temperature measurement ; (c) Stress measurement ;(d) Current measurement

Figure 6.18 shows the simulated sensor measurements along with the practically obtained values. Figure 6.18a shows the actual temperature response obtained after applying the abovementioned temperature dynamics modifications. The temperature response is accelerated as intended and can be compared to the measured values as shown in Figure 6.18b. The correlation between the simulated and measured stress levels are shown in Figure 6.18c. It can be seen that the simulation predicts the maximum stress quite accurately but does not allow for stress relaxation as indicated by the sensor measurement. This discrepancy won't be elaborated on as the load cells were self manufactured and intended to give insight on the stress trend. It does however give sufficient knowledge during the initial actuation and therefore deemed accurate for use. Lastly the supplied current is shown in Figure 6.18d.

6.4 Actuator Capabilities

By conducting the practical open-loop responses two valuable questions could be answered namely: (i) what is the maximum obtainable deflection and (ii) what is the achievable transient response.

Table 6.4 illustrates the decrease in rise time with an increase in input for the open-loop responses. This result shows that a rise time of approximately 1.37 seconds is achievable. Increasing the input above 2.5 ampere will further decrease the rise time though one must consider the drawbacks of overheating-and-stressing the SMA wire.

Input (Amphere)	t_r (seconds)
1	10.5
1.5	3.7
2	1.93
2.5	1.37

Table 6.4 – Rise time obtained for control surface deflection open-loop response at various inputs

The open-loop deflection response, shown in Figure 6.16a, clearly indicates the actuator ability to achieve a maximum deflection of approximately $30°$ in both directions which results in a stroke of approximately $60°$. The actuator therefore meets the requirement of achieving a maximum deflection of $25°$ in both direction.

From the open-loop response it can be concluded that a rise time of at least 1.37 seconds is achievable and that a maximum stroke of $60°$ is obtainable.

Chapter 7

Practical Verification of Controllers

With a validated theoretical SMA-based control surface actuator model the controllers was re-designed for practical implementation. Unfortunately only the PI and bang-bang controller's practical results will be presented. Due to a temperature sensor limitation identified in the practical controller implementation of the project the practical results of the temperature and feedback linearisation controllers are deemed inadequate. Both of these controllers require a temperature measurement to determine the control action and the sensor limitation resulted in incorrect controller commands.

The PI and bang-bang controller evaluation will be based on the practical results accompanied by simulation results for comparison. Although the temperature and feedback linearisation controllers were not practically implemented, the simulation models were updated using the parameters identified through the system identification and the controllers were redesigned and re-simulated to verify their potential for practical implementation. The chapter start by describing the test setup procedure applied prior to each practical test. The chapter concludes with a recap on the practically determined time domain specifications of the various controllers followed by a scalability analysis.

7.1 Practical test Setup

Before conducting the practical results the actuator was pre-strained by applying the following procedure. This setup is critical as it ensure equal deflection in both directions.

- Remove both the top and bottom wires from their respective guide pulleys
- Apply heat to both wires to ensure a composition of purely austenite and the shortest possible length
- Leave the wires to cool to room temperature resulting in the formation of temperature induce twinned martensite

- Put each wire on its respective guide pulley.
- Tighten each pulley to increase the stress in each wire which will result in elongation and the formation of stress induced de-twinned martensite

The procedure described above results in two SMA wires consisting of identical ξ_s, ξ_t and ξ_a fractions with an initial control surface deflection of zero. The initial material compositions are all determinable by using the constitutive SMA relation as the temperatures and stresses during each step are known. It is crucial to apply this procedure before conducting any tests as it ensures symmetric actuation in both the positive and negative directions.

Note that a forced convective cooling environment was achieved during each test by a fan blowing air over both wires. This was applied to ensure a valid controller comparison.

7.2 PI Controller Response

The PI controller design, presented in section 4.1, was reproduced taking the practically obtained SMA parameters into consideration. The controller was designed as to produce a settling time of 1.5 seconds with no resulting overshoot. Although the open-loop response indicated a rise time of 1.37 seconds for a 2.5 ampere input this optimistic settling time requirement is considered as a larger current limit is placed on the actuator. This optimistic settling time requirement will also result in a more aggressive controller even if the settling time is not met. The controller design followed the practical implementation by commanding the actuator to track a step response sequence. The sequence consists of a positive step command followed by the same magnitude negative step and a final step to zero. This sequence was applied at 20, 10 and 5 degree commands in order to cover the majority of the deflection range. For illustrative purposes only the 10 degree step commands are considered.

Figure 7.1 shows the closed-loop response of the PI controller to a deflection angle step command. In all three step instances the required deflection is reached indicating the power of using feedback. The response shows very little indication of any dead zone in both the forward and reverse transformations. This is evident as control surface movement occurs directly after the application of current to the previously passive wire with no apparent dead zone. This is similar for the reverse transformation evident in the event of overshoot. This suggests that the forward and reverse transformation regions overlap quite extensively as determined in Chapter 6 during parameter estimation. Figure 7.2 is included in the results to show the various sensor measurements recorded during the practical implementation. Figure 7.2b illustrates the recorded stress levels in the respective wires which, as expected, are relatively similar in both wires throughout the practical run. The maximum stress is experienced in the second step command, as expected, since it is the largest step requirement. The larger the step

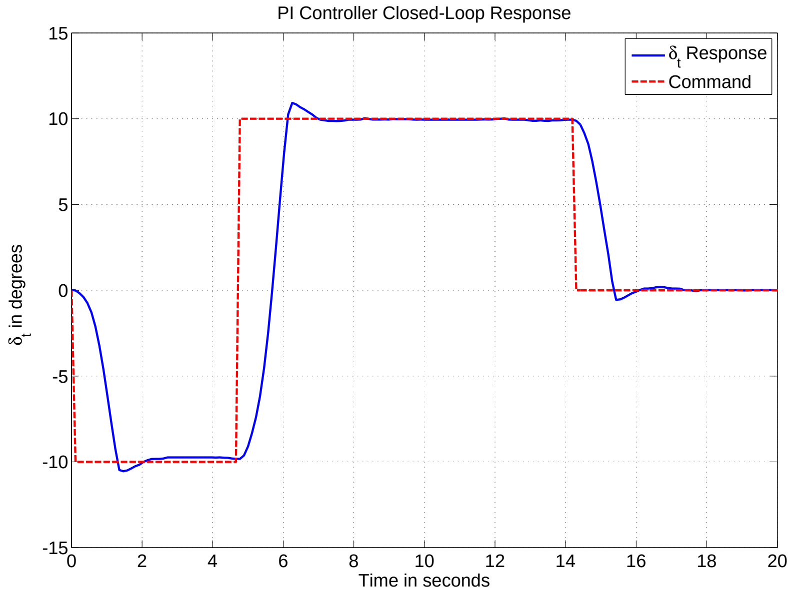

Figure 7.1 – PI controller experimental closed-loop response

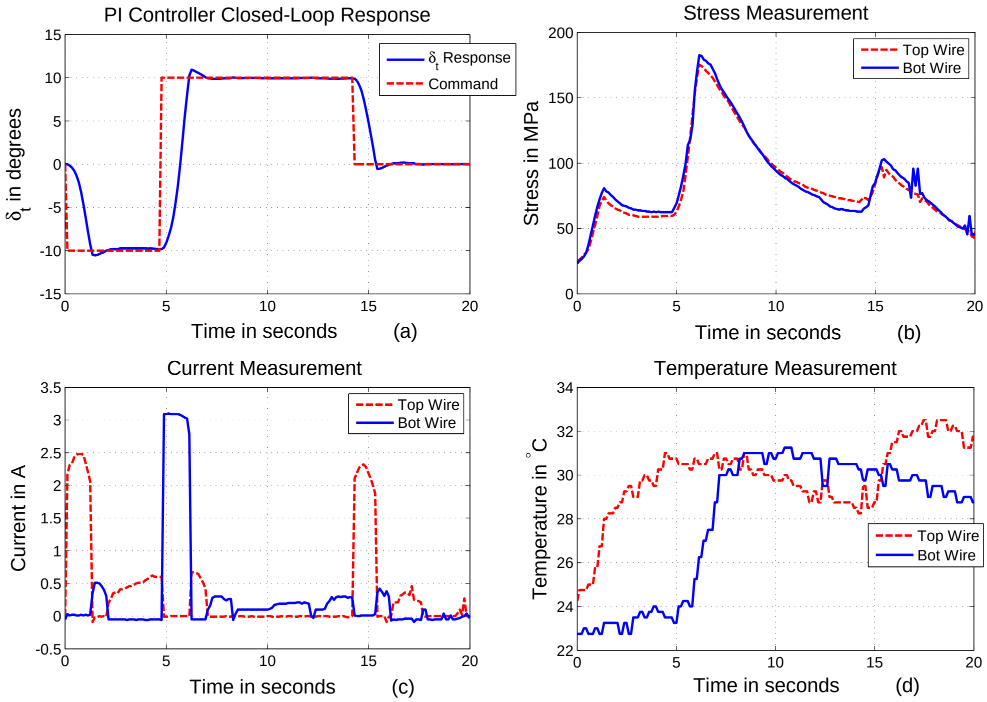

Figure 7.2 – PI controller experimental state measurements ; (a) Control surface deflection ;(b) Stress measurement ; (c) Current measurement ; (d) Temperature measurement

requirement, the more complete the austenite transformation will be and therefore the higher the resulting stress levels.

The respective inputs are shown in Figure 7.2c which indicates larger control effort to get the control surface near the required set-point and less effort to keep it fluctuating about the set-point.

Figure 7.2d shows the respective temperature measurements where an increase corresponds to control surface movement. The temperature increases rapidly while the control surface deflection is far from the required set-point with the temperature staying approximately constant while fluctuating about the set-point.

The PI controller transient response characteristics recorded during the practical results are tabulated below. The parameters considered are the maximum percentage overshoot, 3% settling time and rise time. Throughout the results the overshoot never exceeded 6.8% with the maximum overshoot occurring at the $5°$ step response sequence. The settling time fluctuates about the 2 seconds mark for all obtained results which is relatively close to the designed requirement of 1.5 seconds. The difference can be contributed to the optimistic settling time requirement placed on the controller. The rise time, probably the most accurate parameter to indicate the ability of the actuator, is near the 0.9 seconds vicinity except for the $20°$ step response sequence. This delayed rise time is due to the large step requirement resulting in large resultant stresses in both wires therefore hindering the actuation process. This imposes challenges when considering cyclic actuation but can be prevented by introducing an improved cooling mechanism in order to remove the heat in the passive wire more rapidly. The practical results suggest that the PI controller illustrates sufficient capability with a maximum overshoot of 6.8% and a 3% settling time of 2 seconds.

Specification	$5°$ sequence	$10°$ sequence	$20°$ sequence
M_p	6.8%	5.6%	6.5%
$t_s(3\%)$	$1.97s$	$2s$	$2.2s$
t_r	$0.87s$	$0.85s$	$2.2s$

Table 7.1 – PI controller time domain specifications

Figure 7.3 illustrates the comparison between the simulation and practically obtained results for the PI controller for a similar step command. The simulation results predict the actual response quite accurately except at the start of the first step command. The simulation exhibits a clear dead zone which is not evident in the practical results. This suggests that the A_s temperature is lower than anticipated. This phenomenon relates directly to the method by which the transformation temperatures were determined. The tangent method applied, as mentioned in Chapter 6, resulted in a higher A_s temperature than actually observed in the practical results. This dead zone is again evident in the overshoot of the $-10°$ command, suggesting that the two transformation regions

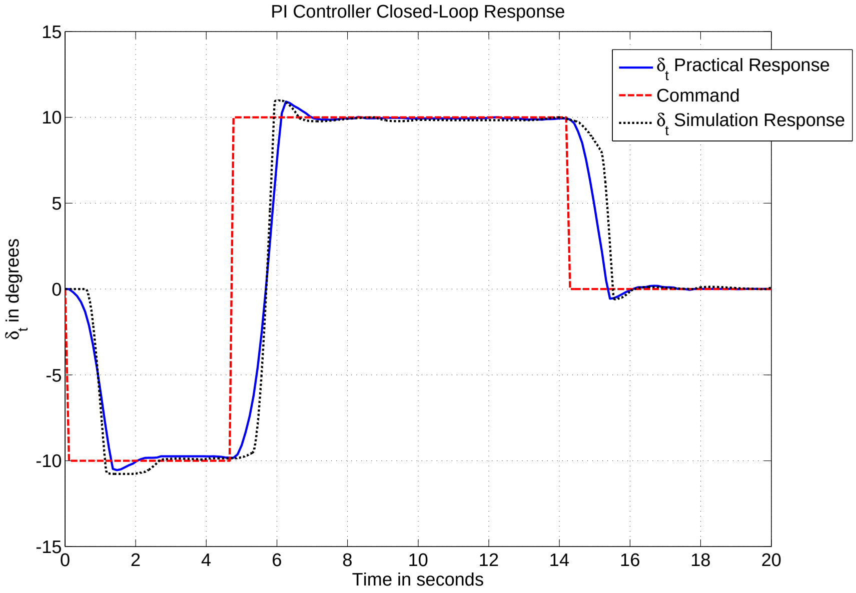

Figure 7.3 – Practical versus simulation results: PI controller

overlaps to a great extent. The initial slower actuation obtained in simulation for both the $10°$ and $0°$ commands are induced by stress relaxation as mentioned in the open loop results in Chapter 6. During this stage the decrease in passive wire temperature results in detwinning, the softer material, while the active wire is heating up but not yet in the austenite transformation region. The stress in the active wire will therefore remain constant while the passive wire will relax. This stress imbalance results in the initial deflection. The faster actuation rate corresponds to the active wire entering the forward transformation region resulting in the transformation of austenite hence contraction occurs more rapidly. The simulation results model the overshoot rather accurately while the settling time corresponds to a certain extent.

7.3 Inner Loop-Outer Loop Controller Response

The temperature measurement is a critical part in applying the temperature controller successfully. The shortcomings of the temperature sensor hindered applying the controller practically. The temperature controller is therefore, similarly than the feedback linearisation controller, evaluated on a simulation basis for a 2% settling requirement of 1.5 seconds. Figure 7.4 shows the response of the temperature controller on a similar command sequence as applied to the previous controller. The controller response is satisfactory as there is no resulting steady state error. A maximum overshoot of 5.5% is achieved with a 2% settling time of 2 seconds. Applying the temperature controller on a more suitable system is recommended as a topic for further research.

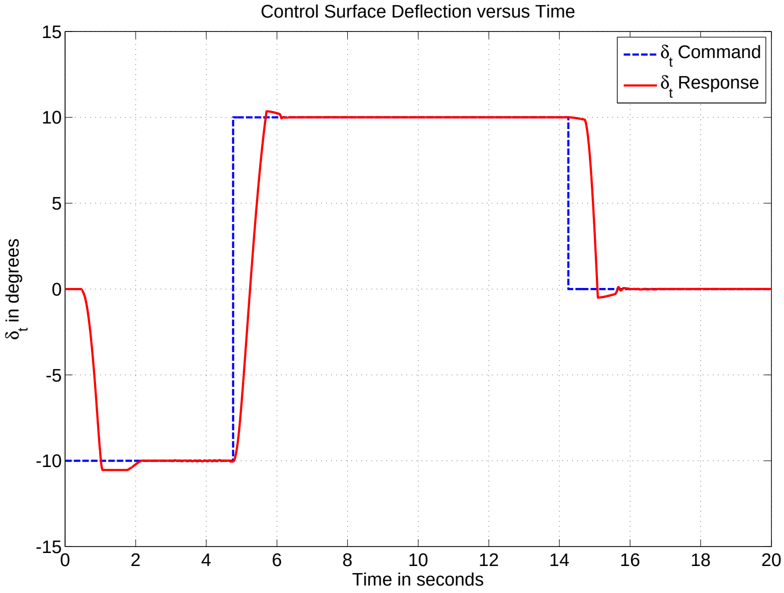

Figure 7.4 – Temperature controller closed-loop simulation results

7.4 Bang-Bang Controller Response

The bang-bang controller was subjected to identical step response sequences than that applied to previous controllers. Similarly only the 10° step sequence will be discussed.

The closed-loop response obtained by applying the bang-bang controller for a 10° step sequence is shown in Figure 7.5. The response shows that the measured deflection follows the commanded deflection for all three step inputs. The dead zone, which was absent in the PI controller results, is more evident in the bang-bang controller results and especially noticeable in the overshoot of the 10° command where the control surface remains stationary at a deflection of approximately 11° for 0.4 seconds. This is as a result of the manner in which the bang-bang controller was implemented. In the practical implementation an on-off approach was applied which entails only one wire being active at a given step command. The controller will bang the control surface to within a certain margin about the set-point and then supply zero current until the deflection drops outside these boundaries followed by another bang to keep it fluctuating at the required set point. The approach is evident in Figure 7.6c, the current supplied to the respective wires, in which only one wire receives input for a given command. By not activating the passive wire to counter-act the overshoot one solely relies on the cooling of the active wire to reduce the deflection error. The rate of control surface deflection is much slower for a cooling cycle than that obtained by activating the passive wire and therefore results in more prominent dead zones in the bang-bang controller results. The reason for applying the approach was to prevent overstressing and heating the SMA wires which would occur when alternating the maximum allowable current

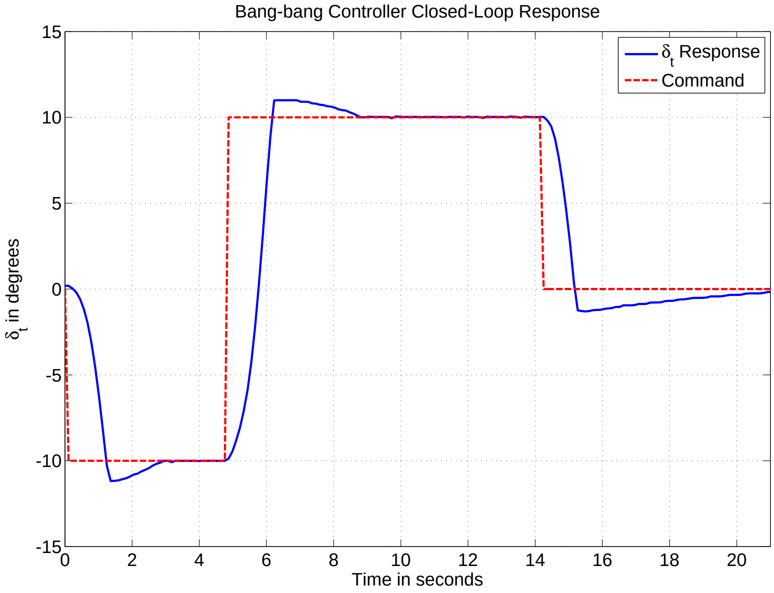

Figure 7.5 – Bang-bang controller experimental closed-loop response

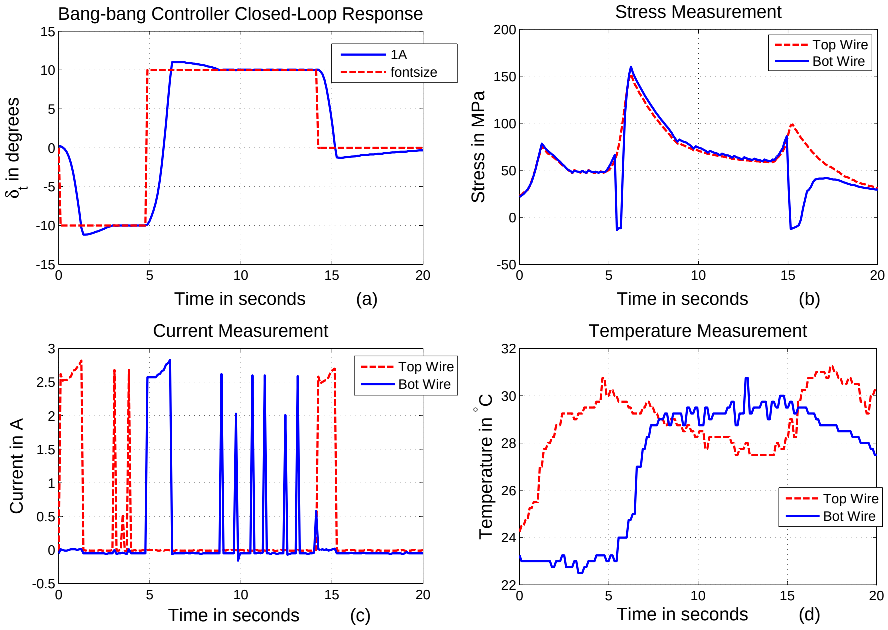

Figure 7.6 – Bang-bang controller experimental state measurements ; (a) Control surface deflection ; (b) Stress measurement ; (c) Current measurement ; (d) Temperature measurement

between the two wires as the deflection fluctuates about the set-point resulting in degraded cyclic responses.

Figure 7.7 illustrates the overstressing effect by evaluating the results obtained from the PI and bang-bang controller implementation. The top wire stress levels, shown in Figure 7.7b, are approximately equal at the beginning of actuation. During the first step command the stress levels reaches identical peaks followed by a general decrease in stress. Due to the on-off approach applied lower stress levels are recorded in the bang-bang controller results. There is a definitive trade-off between the experienced stress levels and actuator transient response. Faster actuation will result in larger stress levels which will hinder actuation during later cycles. The net change in stress for the second command is identical for both cases although the PI results experiences higher peak stresses. This is caused by the stress carried over from the previous command. This suggests that the PI controller will carry over approximately $20MPa$ for each subsequent step command which will amount considerably during future cycles resulting in loss of actuation. The identified problem can again be alleviated by improving the heat transfer mechanism.

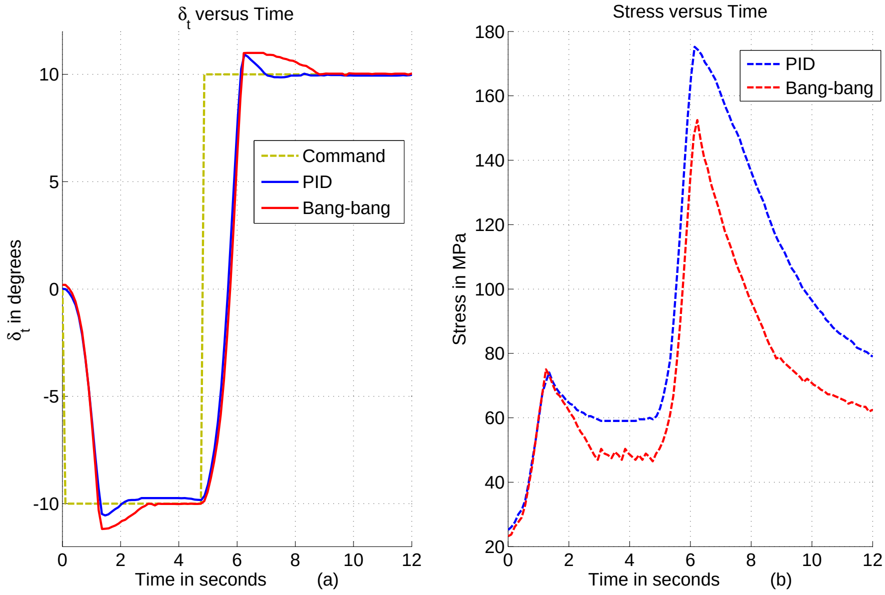

Figure 7.7 – Releaving stress by applying the On-off approach

The rest of the sensor measurements are shown in Figure 7.6. It is observed that the last step response tends to the set-point slower than the first two instances. This can be attributed to the large amount of austenite present in both wires during the last cycle. During the last step response the temperature of the passive wire, shown in Figure 7.6d, is still high from the previous step command which entails that it consists of a considerable amount of austenite, the harder material type. The active wire is also still relatively hot because it has already undergone actuation during the first step also resulting in a considerable amount of austenite present in the wire. The harder parent phase present in both wires results in a slower stress relaxation, as illustrated in Figure 7.6b, resulting in the degraded response. This problem can again be overcome by improving the heat transfer conditions. At this stage of implementation one of the load cells started degrading as seen in Figure 7.6b by the two spikes visible in the stress measurement. The load cell was still used regardless of this degradation.

The current inputs, shown in Figure 7.6c, seem to deviate with time and not stay constant as intended. This is due to the dependency of the SMA wire's resistance on the temperature of the wire. For this implementation the controller was required to provide $3A$ inputs. It is seen that only a mean current of approximately $2.6A$ is supplied. This is due to the current controller being calibrated at higher temperatures than induced in this result. This problem can be overcome by implementing a current feedback controller to ensure that the required input is in fact subjected to the wire as indicated by the current sensors.

The time domain specifications resulting from the practical implementation are shown in Table 7.2 for all three applied step response sequences. Throughout the results the overshoot never exceeds 16% with the maximum overshoot occurring at the $5°$ step response sequence. It was found that the application of the bang-bang controller resulted in the inertia of the control surface contributing considerably to the amount of overshoot experienced and that the overshoot increases with a decrease in step command. The settling time is different for all obtained results due to the non-linear nature of SMAs. The rise time, probably the most accurate parameter to indicate the ability of the actuator, is generally below 1 second except for the $20°$ step response sequence. This higher rise time, similar than that experienced during the PI controller results, is caused by the large stresses generated in both wires in response to the large step requirement.

Specification	$5°$ sequence	$10°$ sequence	$20°$ sequence
M_p	15.8%	13%	7.4%
$t_s(3\%)$	$3.2s$	$5.2s$	$3.8s$
t_r	$0.67s$	$0.86s$	$1.86s$

Table 7.2 – Bang-bang controller time domain specifications

Figure 7.8 shows the comparison between the simulation and practically obtained results for the bang-bang controller for a similar step command. The bang-bang simulation results are slightly less accurate than that obtained for the PI controller. Nonetheless it still captures the general control surface deflection trend. Again one notices a dead zone in the simulation results, at the beginning of each step command, which is not present in the practical results. The simulation results obtained for the $0°$ step command does not indicate the slow decay to the set point as obtained in the results. This suggests an incorrect M_f transformation temperature.

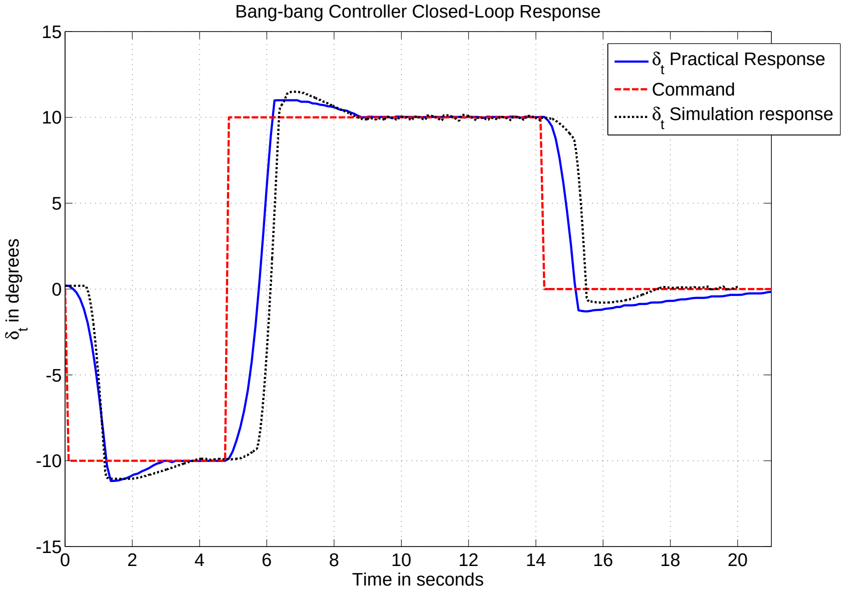

Figure 7.8 – Practical versus simulation results: Bang-bang controller

7.5 Feedback Linearisation Controller Response

Due to the temperature sensor limitation the feedback linearisation controller could not be practically implemented. The lag in the temperature measurement would cause the controller to incorrectly identify regions of transformation which are critical for calculating the controller output. Figure 7.9 illustrates the situation. The temperature and stress measurements would suggest that the active SMA wire, indicated in red, is undergoing a de-twinning process while it should in fact be transforming to austenite as suggested by the green line. The incorrectly identified regions would therefore result in undesirable controller calculations resulting in unwanted behaviour. Having acknowledged this problem, it would still be useful to evaluate the feedback linearisation controller in simulation using the practically measured material properties in order verify its operation and to be able to compare its performance to that of the other controllers. Figure 7.10 shows the actuator behaviour in response to the similar step response sequence as applied in the preceding controller evaluations. The time constant requirement was set to $\tau = 0.5$ seconds which is the case in all three step responses with a resulting overshoot of zero. It is still unknown how this controller would respond in the presence of model uncertainties and is recommended as a topic for further research.

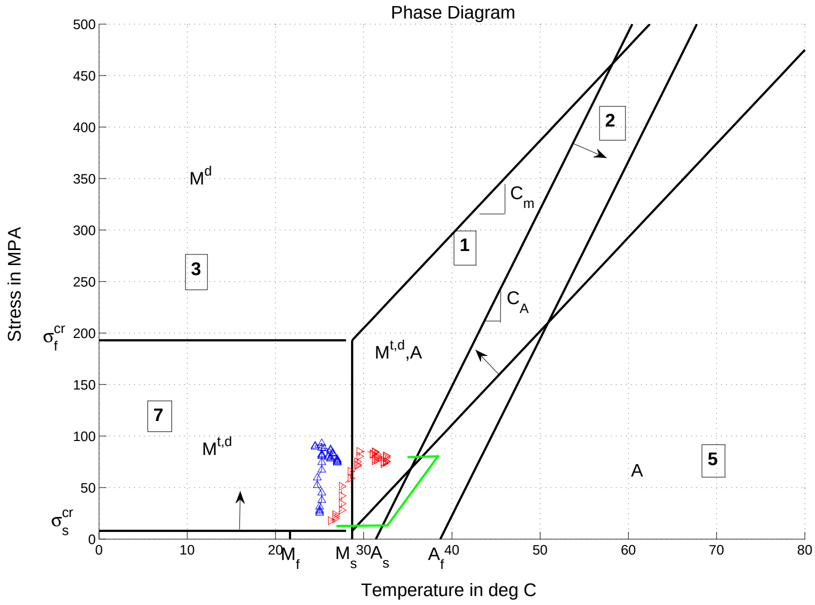

Figure 7.9 – Phase diagram illustrating temperature sensor deficiency effect

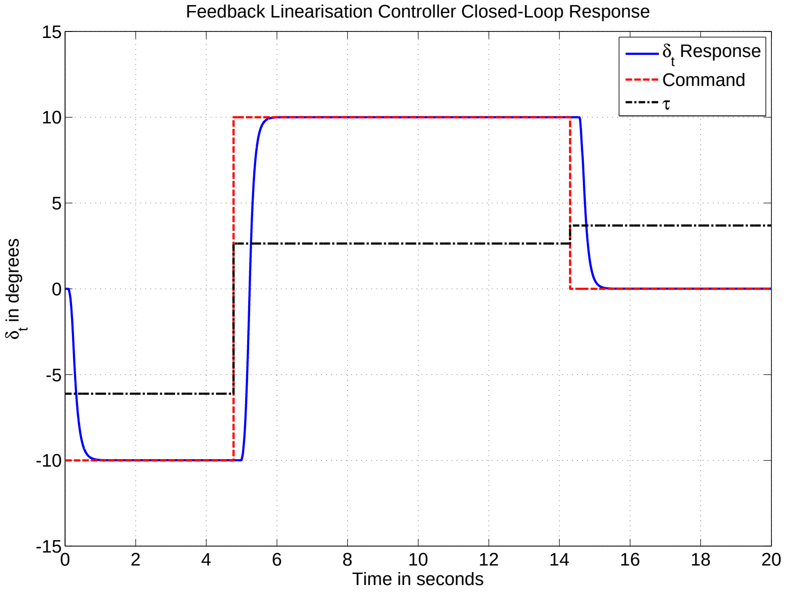

Figure 7.10 – Feedback linearisation controller closed-loop simulation results

7.6 Comparison of Controller Performances

This section briefly summarises and compares the transient response characteristics and steady-state errors of the various controllers. The four controllers are evaluated for the time constant, τ, settling time, t_s, rise time, t_r and overshoot, M_p, as tabulated in Table 7.3. In the case of absent parameters the specification is irrelevant to the specific controller.

The feedback linearisation controller illustrates by far the most promising time domain specifications. The settling time is in line with that required for aileron actuation with zero overshoot. The feedback linearisation controller specifications are solely obtained from simulation and it is therefore required to apply the controller to a suitable actuator system in order to validate the theoretical performance.

Specification	PI	Bang-bang	Temperature	Feedback-linearisation
τ	–	–	–	$0.5s$
t_s	$2.2s$	$5.2s$	$2.38s$	$0.96s$
t_r	$2.2s$	$1.86s$	$0.65s$	–
M_p	6.8%	15.8%	5%	0%

Table 7.3 – Controller time domain specifications overview

The PI and temperature controllers display similar specifications with the only noticeable difference in the rise time specification. The large rise time was experienced during large deflection commands where large stresses were apparent in the respective wires. The settling time and overshoot is of the same order. The PI and temperature controller illustrates sufficient time domain specifications although not completely at the speed required for aileron actuation.

The bang-bang controller illustrates, against expectation, the worst time domain specifications of the presented controllers. The large settling time and overshoot is as a result of the on-off approach taken during the practical implementation. The large rise time is also not an accurate representation of that obtainable by implementing a bang-bang type controller as the large stresses induced during larger deflection requirements resulted in the slower response.

The time domain specifications presented are by no means the limit of SMA actuators. The primary obstacle limiting the transient response is the method of heat transfer applied to cool down the wires. Improving these conditions will alleviate most of the limiting factors encountered in this thesis. For one it will prevent overstressing of SMA wires at larger deflection requirements as faster cooling will result in exiting the dead zone quicker resulting in reaching the de-twinning transformation strip faster.

Another aspect of interest addressed in this section is the power consumption of SMA-based actuators. Note that this analysis is controller independent and will address the transient and steady-state power consumption of the SMA-based actuator demonstrator. The transient power consumption is defined as the power required to get the tab to the required set-point while the steady-state power corresponds to the power required to keep the tab deflection at the set-point.

In order to investigate the instantaneous transient power consumption the practically obtained open-loop results, shown in Figure 6.15, are recalled. A first order approximation was conducted by calculating the average deflection rate corresponding to the respective input. This resulted in an indication of the required power consumption for a specific deflection rate. The instantaneous power consumption was calculated using equation 7.6.1. The current was known while the resistance of the wire was obtained from the supplier data sheet [47] and held constant irrespective of the wire temperature.

$$P = I^2R \tag{7.6.1}$$

The deflection rate was calculated by dividing 80% of the respective open-loop deflection ranges by the recorded rise time, as shown in equation 7.6.2, to capture the linear part of actuation.

$$\dot{\delta}_t = \frac{0.8\delta_{t_{tot}}}{t_r} \tag{7.6.2}$$

The results are shown in Figure 7.11 illustrating an approximately linear relationship. Clearly an increased deflection rate corresponds to an increase in the power requirement. A maximum deflection rate of approximately $32°s^{-1}$ is achievable which corresponds to a power requirement of approximately $15W$. To investigate the steady-state

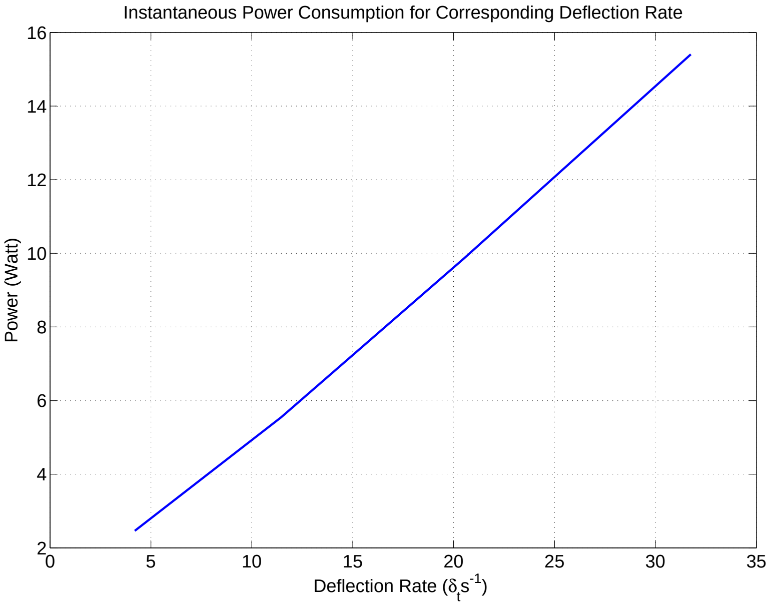

Figure 7.11 – Transient power consumption versus deflection rate

power consumption an SMA actuator with the ability to actively choose to cool or insulate an SMA wire is considered. This is the ideal case. Once the tab deflection is at the required set-point and the active SMA wire is properly insulated there should be minimal heat losses to the surrounding environment. This suggests that the active wire will stay at the required temperature to keep the tab at the set-point deflection. The steady state power consumption will therefore ideally be zero or directly related to the thermal insulation of the SMA wires. No quantitative information regarding the steady-state power consumption can be made as it is highly dependent upon thermal properties of the actuator.

There are a few qualitative conclusions that can be made regarding the respective controllers power consumption. Note that only the two practically implemented controllers are considered. The Bang-bang controller implementation results in the maximum transient power consumption as it applied the maximum allowable input. It can however result in chattering about the set-point which can result in a excessive steady-state power consumption. The PI controller illustrates improved steady state power consumption due to the on-off approach taken near the set-point. Incorporating a dead-zone into the controller near the set-point can result in a reduced steady-state power consumption.

7.7 Scalability

This project placed emphasis on demonstrating feedback control of an SMA-based demonstrator. Naturally the next step would be to investigate the scalability of the demonstrator considering its intended application. The following section is a first order approximation to serve as a starting point when considering a thorough scalability analysis. Note that the scalability analysis is intended for a tab actuator. Evaluation will prove difficult as very little tab actuator data is available. The scalability analysis will therefore make use of aileron actuator data to provide an estimate for a possible tab actuator size and requirements.

The model is scaled according to the initial considered prototype shown in Figure 7.12 with b the length between sequential actuators. A set of actuators are placed in parallel. For the purpose of the approximation it is assumed that a pulley type mechanism is obtainable. The number of required actuator segments will depend on the maximum required hinge moment. According to C.D Jaquets trailing edge tab optimisation [1] the worst gain in applying the trailing edge concept may result in a factor 17 reduction

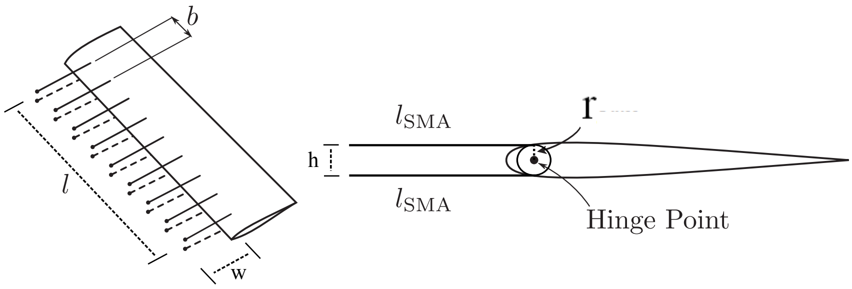

Figure 7.12 – Scalable prototype

in the aileron hinge moment coefficient. In addition the maximum resulting tab hinge moment coefficient was approximately 8.5 times smaller than the equivalent aileron coefficient. The tab actuator hinge moment requirement will therefore be scaled according to the aileron hydraulic jack hinge moment requirement, $2225N$m, by a factor of approximately 145. This approximation results in a maximum tab hinge moment requirement of $15.4N$m. This requirement is the primary input driving the scalability of the actuator.

The geometric scalability is started by referring to the actuator kinematic equation for a pulley type configuration as shown in equation 7.7.1. Note that a factor 2 is missing from the second term due to the wire only being attached to one pulley and not two as in the demonstrator prototype.

$$\epsilon = \frac{r\delta_t}{l_0} + \frac{\epsilon_{pre}}{2} \tag{7.7.1}$$

From this equation the moment arm to original SMA wire length ratio can be determined for the actuator requirements. For a top wire strain, ϵ, of 0 a control surface deflection, δ_t, of $-25°$ is required. Allowing a maximum residual strain, ϵ_{pre}, of 5% results in the following ratio.

$$\frac{r}{l_0} = \frac{\epsilon_{pre}}{2\delta_t} = 0.0572 \tag{7.7.2}$$

Any SMA wire length moment arm ratio satisfying the abovementioned constraint will result in the required control surface deflection. The reason for mentioning the ratio is due to the dependence of the moment arm, r, on the obtainable hinge moment for a singular actuator. There is a direct correlation between the obtainable hinge moment and the actuator size. Increasing hinge moment requirements will result in longer moment arm requirements resulting in increased amounts of SMA wire length to obtain the required deflection.

A moment is the tendency of a force to rotate an object and is defined as the force times the perpendicular distance from the force line of action to the point of interest, in this case the tab hinge point. The actuator needs to supply the net moment required to overcome the hinge moment created by the aerodynamic forces acting on the tab. In this particular setup there are three forces resulting in moments about the hinge, namely the two forces in the top and bottom SMA wires and the aerodynamic induced force acting on the tab. It is noted that the active wire induced moment must overcome the hinge moment induced by the aerodynamic forces as well as the moment induced by the passive wire element as illustrated in Figure 7.13a. Taking the sum of moments about the hinge results in equation 7.7.3 where M_t is the top wire induced moment, M_b the bottom wire induced moment and M_h the aerodynamic induced hinge moment.

$$M_t = M_b + M_h \tag{7.7.3}$$

For this analysis the obtainable hinge moment, M_{tot}, will be considered as the hinge moment induced by the force created in the active wire to overcome the aerodynamic and passive wire induced moments as illustrated in Figure 7.13b and expressed in equation

7.7.4.

$$M_{tot} = M_b + M_h = M_t \tag{7.7.4}$$

The moment obtainable is expressed in equation 7.7.5 and needs to overcome M_{tot} in order to induce movement. Equation 7.7.5 also indicates the direct relationship between the obtainable hinge moment and moment arm.

$$M_t = F_1 r \tag{7.7.5}$$

The SMA wire manufacturer suggests a safe contracting load, F_1 of approximately $35N$ per wire to ensure adequate cyclic behaviour [47] while loads of up to $60N$ were recorded during the practical implementation. Note that the safe contracting load is for the specific SMA wire size applied in the demonstrator. For the scaling purpose a maximum contracting load of $35N$ will be considered. In order to start scaling the SMA tab actuator a geometric constraint is required. There are two choices, either a constraint on the maximum allowable moment arm length, r, or a constraint on the maximum allowable SMA wire length, l_0 or w as indicated in Figure 7.12, both as a result of the available space. For this analysis the maximum allowable SMA wire length will be constrained. The reason for choice is due to the availability of the aileron jacks geometric data which gives a indication on the maximum available space for actuator fitment. The constraint is shown below,

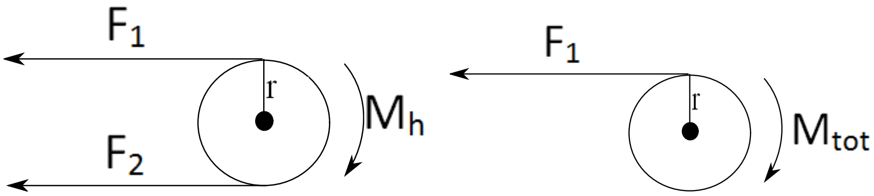

(a) Bending moment free body diagram (b) Equivalent bending moment free body diagram

Figure 7.13 – Bending moment free body diagram

$$l_0 = 340mm \tag{7.7.6}$$

which can be related to the required moment arm length by recalling equation 7.7.2 and shown below.

$$r = 19.4mm \tag{7.7.7}$$

This results in the maximum obtainable hinge moment for a singular actuator as expressed in equation 7.7.8.

$$M_t = F_1 r = 0.681N\text{m} \tag{7.7.8}$$

The number of parallel required actuators, n, can be determine as the maximum required hinge moment is known.

$$n = \frac{M_{h_{req}}}{M_t} \approx 23 \tag{7.7.9}$$

The distance between the parallel actuators, b, should be adequately chosen to ensure room for adequate cooling. The actuator volumetric size can be calculated as shown in equation 7.7.10 with reference to Figure 7.12.

$$V_{actuator} = lwh \tag{7.7.10}$$

With,

$$l = b(n-1) \tag{7.7.11}$$

$$w = l_0 \tag{7.7.12}$$

$$h = 2r \tag{7.7.13}$$

An estimate of the SMA actuator mass is considered solely on the amount of SMA wire in the actuator. No additional sensor or power equipment is considered.

$$M_{actuator} = l_0 \pi r^2 2n\rho \tag{7.7.14}$$

The transient power consumption, corresponding to a required deflection rate requirement, can also be scaled by a factor of n as a result of a n wire actuator. The deflection rate requirement is set to approximately $32° s^{-1}$ which translates to a transient power consumption of 15 Watts per wire as obtained in the power consumption investigation depicted in Figure 7.11.

The volume, mass and transient power consumption for the SMA tab actuator and the equivalent scaled down tab jack actuator can then be evaluated for different values of b. Two cases are considered and the results are tabulated below. The aileron hydraulic jack parameters were scaled down by a factor of 145 for both the mass and volume while no information regarding the transient power consumption could be obtained. For case 1 the results suggests a weight reduction factor of approximately 4.3 in favour of the SMA actuator. Unfortunately the SMA actuator volume is up to 23 times larger than the equivalent jack. For case 2 the weight reduction and transient power consumption stays constant with the volume decreasing but still a factor of approximately 4 times larger than the equivalent jack actuator. It is mentioned that this evaluation is based on a scaled down hydraulic aileron actuator. To reduce the volumetric size of the SMA actuator one can either consider bundled SMA actuators or investigate a smarter configuration to use the available space more efficiently. This is suggested as future work as it is not included in the scope of this thesis. This scalability attempt is a first approximation and should serve as a starting point when launching an in-depth actuator scalability analysis.

		Case 1 (b = 5mm)	Case 2 (b = 1mm)
	Hydraulic Jack	SMA Actuator	SMA Actuator
Volume (m^3)	6.75×10^{-5}	1.5×10^{-3}	2.91×10^{-4}
Mass (kg)	0.088	0.0204	0.0204
Power(Watt)	–	345	345

Table 7.4 – Scaled down hydraulic jack versus scaled up SMA actuator

Chapter 8

Conclusions and Recommendations

This chapter aims to conclude the project by addressing the project goals set out in Chapter 1 based on the results obtained during the completion of the project. A project summary is presented, followed by the findings and conclusions . Finally recommendations are made for further research followed by suggestions on improving the results obtained in this project.

8.1 Summary

This project presented the design, implementation and testing of a feedback control system to control the deflection of an SMA-based control surface actuator.

The design phase consisted of designing an SMA-based control surface actuator, developing an SMA-based control surface actuator model, and controller development. The SMA-based actuator was successfully designed and its dynamics combined with the identified SMA model, which demonstrated successful SMA behaviour, in order to develop an SMA-based control surface actuator model. The developed model captured the dynamics of the actuator sufficiently.

The controller design phase followed and resulted in the successful design of four control algorithms, each designed to meet the set time domain specifications. The controller designs were verified in simulation.

An SMA-based control surface actuator demonstrator, which conformed with the actuator design, was constructed and demonstrated promising SMA-based actuation. The demonstrator was equipped with the necessary electronics to capture the actuator behaviour and to aid in the practical controller verification and data capturing.

A system identification procedure was conducted, which resulted in successfully verifying the theoretical SMA-based control surface actuator model. The constitutive SMA model, thermodynamic model and actuator model were successfully validated.

Two of the control algorithms were tested on the demonstrator and successfully confirmed in simulation. Due to sensor limitations experienced at the later stages of the project, the remaining two control algorithms were not implemented practically. These two controllers were therefore implemented through simulation. Controller evaluation was conducted using the two practically obtained controller results and two controller results obtained through simulation. The evaluation criteria were based on the required time domain specifications.

Additionally, an investigation into the effect of the heat transfer mechanism on the temperature response of an SMA wire was performed. This resulted in valuable information on the obtainable transient response at various altitudes and convection conditions.

8.2 Conclusions

The SMA-based control surface actuator concept was validated by developing a demonstrator. The demonstrator illustrated functional actuation, which led to the conclusion that an SMA-based actuator can achieve control surface actuation.

The successful implementation of four controllers shows that SMAs can be manipulated to obtain controlled actuation.

From the practical results it is concluded that the required control surface deflection is indeed obtainable. Regarding the transient response of the actuator, the prospects do not look so promising. The controller evaluation suggests that the transient response is slightly slower than is required for trailing edge actuation. The primary factor limiting the transient response is the cooling method applied to extract the energy from the system. Before considering an SMA-based actuator for trailing edge actuation, one needs to investigate alternative cooling mechanisms. Only then will an SMA-based actuator demonstrate improved transient response for cyclic trajectory tracking. It might prove beneficial to investigate alternative uses for SMA actuators on conventional aircraft, albeit for other less demanding control surfaces or structural applications.

The overall project can be considered a success as it demonstrated the SMA-based control surface actuator concept by constructing a functional demonstrator, and developing an SMA-based control surface actuator model to aid in controller development to evaluate the key performance parameters of an SMA-based actuator. The information presented, although it did not produce the sought-after outcome, will serve as a basis for future investigation into SMA-based actuators in aerospace engineering.

8.3 Improvements and Recommendations

First of all, it should be noted that the prototype constructed in the project is by no means optimal. By making use of smarter configurations, it is possible to meet any deflection requirement with the availability of enough SMA wire. The force experienced in the SMA wire is also configuration dependent, which emphasises the importance of a suitable configuration for the specific application.

Most of the models describing SMA behaviour require some form of parameter estimation. It is important to conduct a thorough estimation on a suitable rig, preferably a tensile testing machine, as this will directly influence the accuracy of the theoretical model with respect to the practical results.

The incorporation of sensors into the actuator system needs to be done accurately. As experience has shown in this project, the temperature sensors need extra attention. Thermocouples are not recommended. Instead some form of surface-mount temperature sensor should be considered. The stress sensors should also be incorporated into the actuator structure and not form part of the SMA wire path.

Topics for future research and recommendations are illustrated below.

- The implementation of the feedback linearisation and temperature controller on a practically feasible system is suggested to compare the practically obtained and simulation results. This is recommended to establish whether the non-linear controller is indeed superior to the others.

- It would be beneficial to investigate two-wire control for an SMA-biased configuration. The ability to actively cool an element can drastically improve the transient response.

- Rather than using an SMA-biased actuator, it could prove useful to investigate a spring-biased SMA actuator. This would simplify the modelling and control system design of the actuator considerably. It would, however, require an efficient heat-removal system.

- The primary factor limiting the transient response of any SMA actuator is the cooling method applied to remove the energy from the system. To ensure transient response improvements, it is essential to investigate alternative cooling mechanisms.

- It is recommended that the change in SMA parameters relating to the temperature dynamics be investigated. Not modelling the change in resistance and specific heat with temperature will limit the accuracy of the SMA-based actuator model.

- An important SMA-based actuator characteristic not addressed in this project is its response to extensive cyclic loading and fatigue characteristics. This is an essential part of research if an SMA-based actuator were ever to be considered in high-risk actuating environments. The SMA-based actuator would need to ensure a certain amount of cycles before degrading its response, or for that matter before resulting in wire failure. This research would produce crucial information regarding the actuator redundancy.

Appendix A

Heat Equations

A.1 Heat Conduction Relationship Derivation

This appendix illustrates the derivation of a thermal heat conduction relationship as presented in section 3.4 for the specific application.

A.1.1 Lumped System Analysis

In order to derive a suitable relationship we treat the SMA wire as a lumped system, which entails that its internal temperature remains essentially uniform throughout the wire. The temperature distribution is only a function of time and not of position, hence the name lumped system analysis. This is a valid assumption as the diameter of the SMA wire is relatively small compared to its length; this simplifies the current heat transfer solving the heat transfer problem without sacrificing a significant amount of accuracy.

A.1.1.1 Analysis Assumptions

In order to implement the lumped system analysis the following assumptions were made. It is assumed that the SMA actuator geometry complies with the criteria for lumped system analysis (validated at a later stage). The cross-sectional area of the SMA wire is assumed constant throughout the length of the wire. The SMA wire is heated with a uniformly distributed heat source. Only convectional heat loss from the SMA wire surface to the surrounding medium, at constant temperature, is considered.

A.1.1.2 Relationship Derivation

The energy balance equation is shown below,

$$\underbrace{\left\{\begin{array}{c}\text{Rate of heat generation}\\\text{inside the wire}\end{array}\right\}}_{\dot{E}_{gen}}-\underbrace{\left\{\begin{array}{c}\text{Rate of heat convection}\\\text{to the surroundings}\end{array}\right\}}_{\dot{Q}_{loss}}=\underbrace{\left\{\begin{array}{c}\text{Rate of change of energy}\\\text{content of the wire}\end{array}\right\}}_{\dot{E}_{storage}}$$

with,

$$\dot{E}_{gen} = i^2 R \tag{A.1.1}$$

$$\dot{Q}_{loss} = hA(T - T_\infty) \tag{A.1.2}$$

$$\dot{E}_{storage} = \rho c_p V \frac{dT}{dt} \tag{A.1.3}$$

where ρ, c_p, V, h, A, T, T_∞, R and i are the material density, the specific heat capacity of the SMA, the wire volume, the convectional heat transfer coefficient, the wire surface area, the wire temperature, the ambient temperature, the wire resistance and the wire current respectively. Equations A.A.1, A.A.2 and A.A.3 are then plugged into the energy balance to yield the heat conduction relationship, illustrated below as in section 3.4.

$$\rho c_p V \frac{dT}{dt} = -hA(T - T_\infty) + i^2 R \tag{A.1.4}$$

Appendix B

Strain Gauge Design

Load cells were required to measure the stress experienced within the SMA wires during the actuator application. The stress measurements were required as one of the inputs to the control system. Apart from the temperature and angular position measurements, the stress measurement would serve as a secondary measurement to indicate the current compositional state of the SMA wire. Stress was measured by using a strain gauge, a resistive metal film that changes resistance with elongation or flexure. The strain gauges were mounted on an aluminium bracket exposed to an axial force. This axial force, the force experienced by the SMA wire, would result in a change in strain in the mounting bracket, which in turn leads to a change in length of the strain gauge. This change in length is coupled to a change in resistance which, if connected to the correct circuitry, can be interpreted as a signal for an analog-to-digital converter. A strain gauge is typically applied in conjunction with a Wheatstone bridge, an electrical circuit used to measure the voltage difference between two terminals, after which the signal is amplified accordingly and exposed to the necessary signal conditioning. The mechanical design is discussed first, followed by the electronic design and some interesting practical observations.

B.1 Mechanical Design

Mounting brackets were required to transfer and then convert the applied force into a significant strain that the strain gauges would react to. Initially a mounting bracket under uni-axial tension was considered. In this case the strain gauge would be mounted on a flat rectangular plate subjected to axial loads. This configuration was found incapable of inducing enough strain to result in a large enough resistance change in the strain gauge. For this configuration enormous gains would be required in the amplification stage. This would result in the amplification of noise, which is not ideal. Therefore a mounting bracket in the form of a U was designed. The advantage of such a configuration is evident in the way in which strain is induced in the strain gauge. An additional bending force is present along with the axial force, creating a larger strain resolution. This design would induce enough strain to deliver noticeable voltage changes over the

Wheatstone bridge, resulting in lower gain values in the amplification stage. The free body diagram of the strain gauge mounting bracket is illustrated below.

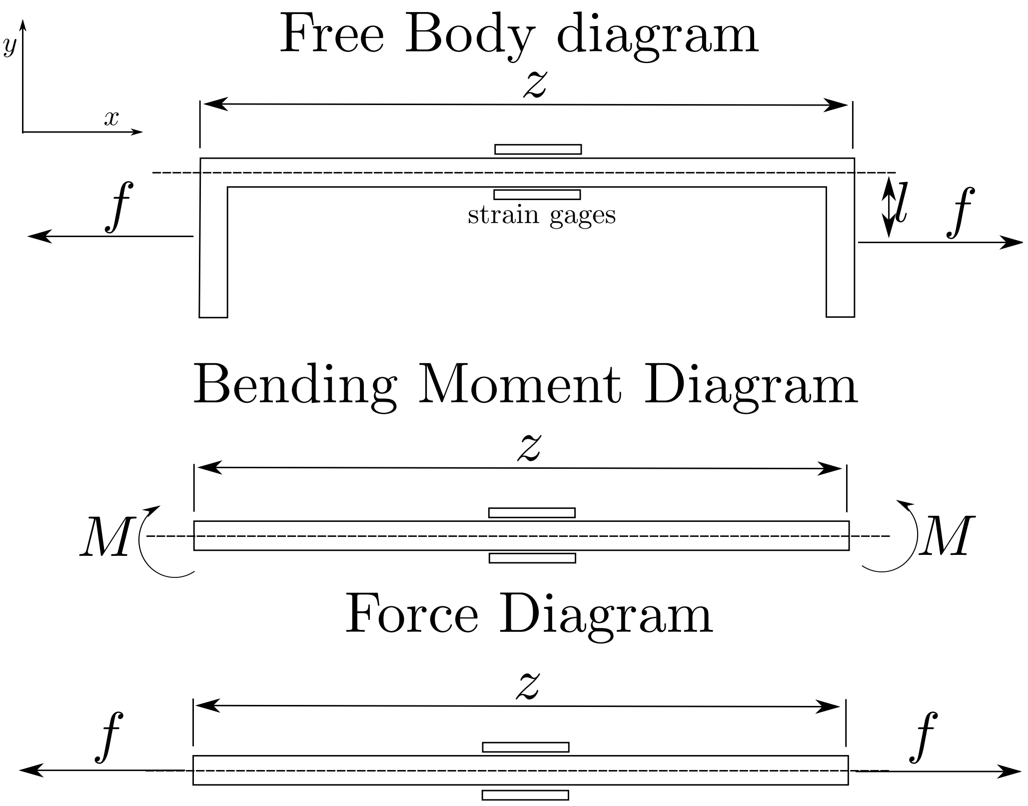

Figure B.1 – Strain gauge free body diagram

The above U bracket illustrates the side view of the mounting mechanism. Two strain gauges would be applied as shown, in the centre of the bracket, while the SMA wire will be attached to the bracket ends as indicated by the symbol f, the force in the SMA wire. The bottom strain gauge would experience tension, while the top strain gauge would be under compression. In order to evaluate the strain induced by the configuration, the free body diagram is split in two by applying the super-positioning principle. A bending moment diagram, illustrating the moments acting on the strain gauge, and an axial force diagram, indicating the axial forces acting on the strain gauge, are obtained. The strain gages will deform as a result of axial and moment forces. The strain from the axial forces is easily obtained by applying Hooke's law.

$$\epsilon_{axial} = \frac{\sigma}{E} = \frac{f}{EA} \tag{B.1.1}$$

where f is the axial force, A the cross-sectional area and E the Young's modulus of the U bracket material. According to Mechanics of Engineering Materials , the fundamental relationship between the bending stress, moment and geometry of a member is as follows:

$$\frac{M}{I} = \frac{\sigma}{y} = \frac{E}{R} \tag{B.1.2}$$

where M, I, y and R are the bending moment, second moment of inertia of the member, distance from the neutral axis to the point of question and radius of curvature of the neutral axis respectively. The neutral axis is merely the transverse axis, for a cross-sectional member, where the strain is zero. The radius of curvature is the radius of the circumferential arc formed when a beam is subjected to pure bending. The relationship relating the strain of a member, because of a bending moment, to its position and radius of curvature is as follows:

$$\epsilon_{moment} = \frac{y}{R} \tag{B.1.3}$$

Substituting the radius of curvature obtained from equation B.1.2 into equation B.1.3 and recalling that $I = \frac{bh^3}{12}$ for a rectangular cross section the bending strain could be represented as follow.

$$\epsilon_{moment} = \frac{My}{EI} = \frac{12My}{Ebh^3} \tag{B.1.4}$$

where b and h are the width and height of the cross-section of interest. The total strain subjected to the bottom strain gauge is as follows:

$$\epsilon_{tot} = \epsilon_{moment} + \epsilon_{axial} \tag{B.1.5}$$

$$\epsilon_b = \frac{12fly}{Ebh^3} + \frac{f}{EA} = \frac{f}{E}[\frac{12ly}{bh^3} + \frac{1}{A}] \tag{B.1.6}$$

while the total strain in the top strain gauge is indicated below. The difference, because of the negative strain induced by the bending moment, is shown below.

$$\epsilon_t = -\frac{12fly}{Ebh^3} + \frac{f}{EA} = \frac{f}{E}[-\frac{12ly}{bh^3} + \frac{1}{A}] \tag{B.1.7}$$

with

$$M = fl \tag{B.1.8}$$

These strain relationships can now be incorporated into the bridge setup equations to relate change in resistance to a change in output voltage and bridge sensitivity.

B.2 Electronic Design

The electronics consisted of a Wheatstone bridge, an instrumentation amplifier and a second-order Butterworth filter. The basic setup is illustrated in Figure B.2. A Wheatstone bridge is typically used to detect small changes in resistance. The change in resistance is induced by the change in length of the strain gauge. Strain gauges are typically characterised by their gauge factor coefficient, GF, which is an indication of the strain gauge sensitivity. The gauge factor is related to the change in resistance and strain experienced by a strain gauge through the following relationship:

$$\frac{\delta R}{R} = GF\epsilon \tag{B.2.1}$$

Initially a 1-bridge setup was considered. In such a case one of the legs in the Wheatstone bridge is replaced by a strain gauge, while the other three are replaced with fixed resistors. The 1-bridge setup accuracy is greatly influenced by temperature variations as the slightest resistance change, caused by these temperature variations, would result in a considerable error in the amplification stage. If the leads attaching the strain gauge to the bridge are of a considerably length, temperature effects are bound to occur as the resistance of the leads will fluctuate with temperature. It was also found that the smallest of temperature changes, whether the result of temperature variation or self-heating, influenced the fixed resistors resistance in the bridge configuration considerably. Even the smallest of resistance changes would results in inaccurate data, which doomed the 1-bridge setup as unsuitable for this specific application.

The shortcomings of the 1-bridge setup led to the application of the 2-bridge setup. Therefore 2 strain gages were substituted at the positions of resistors 2 and 4. A 2-bridge setup can either be applied with two active gages or one active and one passive gauge. For this application 2 active gages were applied as this results in increased sensitivity, which in turn requires less amplification, thus minimizing the amplification of unwanted effects such as temperature deviations. Typical bridge outputs for strain gauge applications are in the order of 2mV per volt of excitation for full-scale deformation.

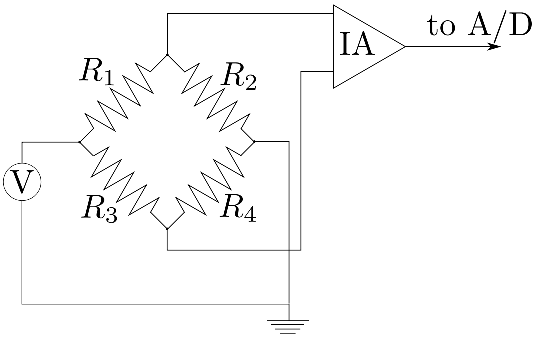

Figure B.2 – Wheatstone bridge setup

The typical input output relationship for a Wheatstone bridge is illustrated in equation B.2.2.

$$E_O = \frac{R_1R_4 - R_3R_2}{(R_1 + R_2)(R_3 + R_4)}E_i \qquad \text{(B.2.2)}$$

where E_i and E_O are the excitation voltage applied across the bridge and the voltage difference between the two terminals respectively. In the specific configuration resistors R_2 and R_4 change their value by δR_2 and δR_4 as a result of the applied strain. In such a case the relationship changes to:

$$E_O = \frac{R_1(R_4 + \delta R_4) - R_3(R_2 + \delta R_2)}{(R_1 + R_2 + \delta R_2)(R_3 + R_4 + \delta R_4)}E_i \qquad \text{(B.2.3)}$$

For the specific case all the resistors in the bridge are equal, simplifying the relationship further.

$$E_O = \frac{RR + R\delta R_4 - RR - R\delta R_2}{(2R + \delta R_2)(2R + \delta R_4)} E_i = \frac{R(\delta R_4 - \delta R_2)}{(4R^2 + 2R(\delta R_2 + \delta R_4) + \delta R_4 \delta R_2)} E_i \tag{B.2.4}$$

As the specific setup was adapted to operate accordingly, the input-output relationship differs from this point onwards from the conventional methods. Usually one would expect equal resistance changes for the 2-bridge setup. In this setup that is not the case, as the change in resistance for both gages differs. Both gages experience strain as a result of the bending force, one a positive and the other a negative change, caused by the respective elongation and contraction, depending on which side of the U-bracket the strain gauge is situated. This is as the usual case . The setup differs in the sense that both strain gages experience a positive strain as a result of the axial force acting on the bracket. Adding the respective strains, caused by the bending and axial forces, results in different strains. Understanding the input-output relationship therefore required distinguishing between the axial and bending strains. The following was defined:

$$\delta R_{4a} = \delta R_{2a} \tag{B.2.5}$$

$$\delta R_{4b} = -\delta R_{2b} \tag{B.2.6}$$

which is the change in resistance caused by the axial and the bending forces respectively. Substituting these newly defined values into equation B.2.4 yields the following relationship:

$$E_O = \frac{R(\delta R_{4a} + \delta R_{4b} - (\delta R_{2a} - \delta R_{2b}))}{4R^2 + 2R((\delta R_{2a} - \delta R_{2b}) + (\delta R_{4a} + \delta R_{4b})) + (\delta R_{4a} + \delta R_{4b})(\delta R_{2a} - \delta R_{2b})} E_i \tag{B.2.7}$$

$$E_O = \frac{R(2\delta R_b)}{4R^2 + 2R(2\delta R_a) + (\delta R_{4a} + \delta R_{4b})(\delta R_{2a} - \delta R_{2b})} E_i \tag{B.2.8}$$

Dividing by R^2 then yields the following.

$$E_O = \frac{\frac{2\delta R_b}{R}}{4 + \frac{4\delta R_a}{R} + \frac{(\delta R_{4a} + \delta R_{4b})(\delta R_{2a} - \delta R_{2b})}{R^2}} E_i \tag{B.2.9}$$

Assuming that $\frac{(\delta R_{4a} + \delta R_{4b})(\delta R_{2a} - \delta R_{2b})}{R^2} << 1$ and $\frac{4\delta R_a}{R} << 1$ the relationship reduces further.

$$E_O = \frac{\frac{\delta R_b}{R}}{2} E_i \tag{B.2.10}$$

Recalling equation B.2.2 and assuming that $\delta R_b >> \delta R_a$, which is suitable as δR_a is only 3 percent of δR_b, the following relationship could be developed.

$$E_O = \frac{GF\epsilon_b}{2} E_i \tag{B.2.11}$$

We have now developed the input-output voltage relationship for the specific strain gauge setup. On the basis of this knowledge the suitable amplification was chosen, after which the signal was put through the necessary signal conditioning. It is now possible to combine equations B.2.11 and B.1.6 to develop the input-output relationship:

$$E_O = \frac{GF(\frac{f}{E}[\frac{12ly}{bh^3} + \frac{1}{A}])}{2} E_i \tag{B.2.12}$$

which can be interpreted as a linear relationship namely,

$$E_O = KE_i \tag{B.2.13}$$

with.

$$K = \frac{GF(\frac{f}{E}[\frac{12ly}{bh^3} + \frac{1}{A}])}{2} \tag{B.2.14}$$

The Wheatstone bridge output voltage varies linearly, depending on the force the mounting bracket is exposed to in the presence of a constant voltage input over the bridge.

B.3 Load Cell Calibration

After the load cell design, electronics implementation and the completion of the load cell bracket, load cell calibration was conducted. The calibration procedure consisted of systematically loading the load cell with known weights, while recording its raw data signal for a specified duration through the data acquisition system. This enables the identification of the linear curve relating the recorded voltage to the measured weight. Having calibrated both load cells it was subjected to the following loading sequence to illustrate its functionality. The weight adjustments were made by hand therefore causing the spiky mesurements during the transitional areas.

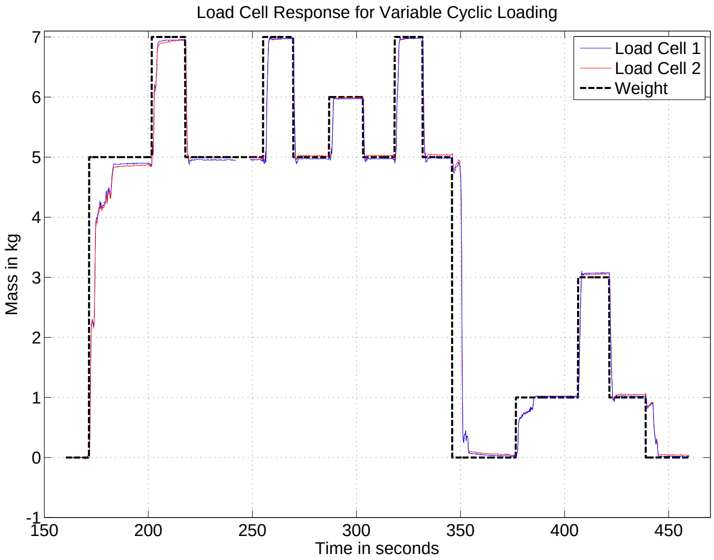

Figure B.3 – Load cell response

Bibliography

[1] Jaquet, C.: *Control Surfaces in Confined Spaces: The optimisation of trailing edge tabs to reduce control surface hinge moments.* Master's thesis, Stellenbosch University, 2010.

[2] D. Grant, V.H.: Design of shape memory alloy actuator with high strain and variable structure control.

[3] R.B. Gorbet, D.W.: A dissipativity approach to stability of a shape memory alloy position control system. *IEEE Transactions on Control Systems Technology*, vol. 6, pp. 554–562, 1998.

[4] K.K. Ahn, B.N.: Position control of shape memory alloy actuators using safe tuning fuzzy pid controller. *International Journal of Control, Automation, and Systems*, vol. 6, pp. 756–762, 2006.

[5] C.A. Dickenson, J.W.: Feedback control using shape memory alloy actuators. *Journal of Intelligent Material Systems and Structures*, vol. 9, pp. 242–250, 1998.

[6] R.B. Gorbet, K.A. Morris, D.W.: Passivity-based stability and control of hysteresis in smart actuators. *IEEE Transactions on Control Systems Technology*, vol. 9, pp. 5–16, 2001.

[7] N. Lechevin, C.R.: Quasipassivity-based robust nonlinear control synthesis for flap positioning using shape memory alloy micro-actuator. In: *American Control Conference*. 2005.

[8] Y.L. Han, Q.S. Li, A.L.A.L.P.L.: Structural vibration control by shape memory alloy damper. *Earthquake Engineering and Structural Dynamics*, vol. 32, pp. 483–494, 2003.

[9] C.J. Lee, C.M.: Analytical dynamic model and experimental robust and optimal control of shape-memory-alloy bundle actuators. *American Society Of Mechanical Engineers*, 2002.

[10] P. Barooah, N.R.: Closed loop control of a shape memory alloy actuation system for variable area fan nozzle.

[11] S. Majima, K. Kodama, T.H.: Modelling if shape memory alloy actuator and tracking control system with the model. *IEEE Transactions on Control Systems Technology*, vol. 9, pp. 54–59, 2001.

[12] R.D. Howe, D.A. Kontarnis, W.P.: Shape memory alloy actuator controller design for tactile displays. *Proceedings of the 34th Conference on Decision & Control*, pp. 3540–3544, 1995.

[13] Y.H. Teh, R.F.: A new control system for fast motion control of sma actuator wires.

[14] S.M. Dutta, F.G.: Differential hysteresis modelling of a shape memory alloy wire actuator. *IEEE Transactions on Mechatronics*, vol. 10, pp. 189–197, 2005.

[15] S. Sana, V.R.: Robust control of input limited smart structural systems. *IEEE Transactions on Control Systems Technology*, vol. 9, pp. 60–68, 2001.

[16] G. Song, B. Kelly, B.A.: Active position control of shape memory alloy wire actuated composite beam. *Smart Materails and Structures*, vol. 9, pp. 711–716, 2000.

[17] S.B. Choi, Y.M. Han, J.K.C.C.: Force tracking control of a flexible gripper featuring shape memory alloy actuators. *Mechatronics*, vol. 11, pp. 677–690, 2001.

[18] Y. Kai, G.C.: Design and control of novel embedded sma actuators. *Istanbul University Engineering Faculty Journal of Elecrical & Electronics*, vol. 2, pp. 513–520, 2002.

[19] K. Arai, S. Aramaki, K.Y.: Feedback linearizarion of shape memory alloy. *SICE anual conference*, 95.

[20] Moallem, M.: Nonlinear position control of a flexible beam using shape memory alloy actuators. In: *15th Triennial World Congress, Barcelona, Spain*. 2002.

[21] N.G. Bizdoaca, A. Petrisor, E.B.: Conventional control and fuzzy control algorithms for shape memory based tendons robotic structures. *SWEAS Transactions on Systems and Control*, vol. 3, pp. 115–124, 2008.

[22] S.S. Ge, K.P. Tee, I.V.E.T.: Tracking and vibration control of flexible robots using shape memory alloys. *IEEE Transactions on Mechatronics*, vol. 11, pp. 690–698, 2006.

[23] M. Moallem, V.T.: Tracking control of an antagonistic shape memory alloy actuator pair. *IEEE Transactions on Control Systems Technology*, vol. 17, pp. 184–190, 2009.

[24] Parker, S.P.: *McGraw-Hill Dictionary of Scientific and Technical Terms 6th Edition*. McGraw-Hill Companies, Inc, 2003.

[25] Olander, A.: An electrochemical investigation of solid cadmium-gold alloys. *Journal of the Amercan Chemical Society*, vol. 54, pp. 3819–3833, 1932.

[26] George B. Kauffman, I.M.: The story of nitinol: The serendipitous discovery of the memory metal and its applications. *The Chemical Educator*, vol. 2, pp. 1–21, 1996.

[27] Darjan, C.: Shape memory alloys. 2007.

[28] Constantinos Mavroidis, Charles Pfeiffer, M.M.: *Automation, Miniature Robotics and Sensors for Non-Destructive Testing and Evaluation*. 1999.

[29] G. Airoldi, T. Ranucci, G.R.: Mechanical and electrical properties of a niti shape memory alloy. *Journal de Physique IV*, vol. 1, pp. 439–444, 1991.

[30] Ashish Khandelwal, V.B.: Model for shape memory alloy behavior: An overview of model. *International Journal of Structural Changes in Solids*, vol. 1, pp. 111–148, 2009.

[31] A. Paiva, M.S.: An overview of constitutive models for shape memory alloys. *Mathematical Problems in Engineering*, vol. 2006, pp. 1–30, 2005.

[32] Pai, A.: *A Phenomenological Model of Shape Memory Alloys Including Time-Varying Stress*. Master's thesis, University of Waterloo, 2007.

[33] L.C. Brinson, A. Bekker, S.H.: Deformation of shape memory alloys due to thermo-induced transformation. *Journal of Intelligent Material Systems and Structures*, vol. 7, 1996.

[34] Mihalcz, I.: Fundamental characteristics and design method for nickel-titanium shape memory alloy. *Periodica Polytechnica Mechanical Engineering*, vol. 45, pp. 75–86, 2001.

[35] M. Huang, L.B.: A multivariant model for single crystal shape memory alloy behaviour. *Journal of the Mechanics and Physics of Solids*, vol. 46, pp. 1379–1409, 1997.

[36] K. Tanaka, S Kobayashi, Y.S.: Thermomechanics of transformation pseudoelasticity and shape memory effect in alloys. *International Journal of Plasticity*, vol. 2, pp. 59–72, 1986.

[37] J.G. Boyd, D.L.: A thermodynamical constitutive model for shape memory materials: Part 1. the monolithic shape memory alloy. *International Journal of Plasticity*, vol. 12, pp. 805–542, 1996.

[38] C. Laing, C.R.: One-dimensional thermomechanical constitutive relations for shape memory materials. *Journal of Intelligent Material Systems and Structures*, vol. 1, pp. 207–234, 1990.

[39] L.C. Brinson, A.B.: Temperature-induced phase transformation in a shape memory alloy: Phase diagram based kinetics approach. *Journal of the Mechanics and Physics of Solids*, vol. 45, pp. 949–988, 1996.

[40] L.C. Brinson, M.H.: Simplifications and comparisons of shape memory alloy constitutive models. *Journal of Intelligent Material Systems and Structures*, vol. 7, 1996.

[41] J.L. Meriam, L.K.: *Engineering Mechanics: Dynamics*. Jonh Wiley & Sons, Inc, 2003.

[42] J. Uchil, K.K. Mahesh, K.G.K.: Electrical resistivity and strain recovery studies on the effect of thermal cycling under constant stress r-phase in niti shape memory alloy. *Physica*, vol. B 324, pp. 419–428, 2002.

[43] G. Wang, X. Jiang, D.N.: Measurement of specific heat, latent heat and phase transformation temperatures of shape memory alloys. *High Temperature-High Pressures*, vol. 37, pp. 91–107, 2008.

[44] Cengel, Y.A.: *Heat and Mass Transfer: A Practical Approach*. McGraw Hill, 2006.

[45] Jean-Jacques E. Slotine, W.L.: *Applied Nonlinear Control*. Prentice Hall, 1991.

[46] Intorduction to flexinol. August 2009.
Available at: `http://www.dynalloy.com/`

[47] Technical characteristics of flexinol.
Available at: `http://www.dynalloy.com/pdfs/TCF1140.pdf`